Technische Universität München
TUM School of Computation, Information and Technology

Modelling and Design of a Monolithic Complementary Metal-Oxide-Semiconductor Compatible Front-End-of-Line Fin Field-Effect Transistor Micro-Electro-Mechanical-System

Richard Hudeczek

Vollständiger Abdruck der von der TUM School of Computation, Information and Technology der Technischen Universität München zur Erlangung des akademischen Grades eines

Doktors der Ingenieurwissenschaften

genehmigten Dissertation.

Vorsitz:		Prof. Dr. Franz Kreupl
Prüfer*innen der Dissertation:	1.	Prof. Dr. Thomas F. Eibert
	2.	Prof. Dr. Amelie Hagelauer

Die Dissertation wurde am 15.03.2023 bei der Technischen Universität München eingereicht und durch die TUM School of Computation, Information and Technology am 04.09.2023 angenommen.

Abstract

In recent years, the market of wireless communication, radar, applications for car-to-car communication, the internet of things and industry 4.0 has lead to a skyrocketing demand for high spectral purity signal generation. Maintaining stable radio frequency signals is key to the new communication standards enabling high-order modulation schemes, and thus high data transfer rates. High quality factor resonators are required to meet this ever-rising demand. These can hardly be attained by current complementary metal-oxide-semiconductor process-compatible devices such as conventional LC-based structures which suffer from severe inductive cross-coupling and large device footprints. To fill in the gap, modern micro-electro-mechanical-system devices, like the resonant body transistors, offer excellent quality factors at high frequencies. Furthermore they can be fabricated monolithically in the front-end-of-line of the complementary metal-oxide-semiconductor stack with no additional post-processing. Resonant body transistors are constructed from a periodic series of planar driving field-effect transistors which resonate mechanically upon electrical excitation which leads to a modulation of the current in the sensing field-effect transistors.

The thesis aims to gain insights into the fundamental electromechanical behaviour of a particular resonant body transistor, the so-called resonant fin transistor. The device promises exceptional figures of merit such as a quality factor of 49 000 at a resonant frequency of 32 GHz. These figures of merit are investigated by simulations and characterisations of fabricated micro-electro-mechanical-systems, to evaluate the viability of its commercial application.

In the first part of this thesis, the anisotropic material parameters of complementary metal-oxide-semiconductor technologies are discussed with respect to their importance for this kind of device with regard to a later theoretical modelling approach.

The theoretical investigation in the second part is carried out using the finite-element method, which provides the electromechanical framework for the simulation of the resonator. It links the principles of electrostatic actuation of the mechanical eigenmodes to the piezoresistive modulation of the charge carrier mobility. Simulations of the front-end-of-line at a fixed quality factor of 49 000, however, deliver a strongly degraded transconductance several orders of magnitude lower than anticipated.

In the third part, the mechanical properties of a phononic crystal mirror in the back-end-of-line are assessed using both analytic and finite-element approaches in a one-, two- and three-dimensional setup. Here, the importance of band gaps within the mechanical dispersion relation, which are matched to both frequency and the wave vector of the cavity mode, is discussed

in the presence of highly anisotropic mechanical materials. The investigation indicates the absence of a matched band gap leads to a much lower quality factor of the resonant fin transistor by several orders of magnitude than originally reported in the literature. The performance of the resonant fin transistor is also assessed in a combined study of both the front-end-of-line and back-end-of-line showing an insufficient overall performance making it unsuitable for circuit applications from a theoretical standpoint.

The final part of this work describes the layout and design process of a resonant fin transistor on a 16 nm fin field-effect transistor technology node. Due to the high complexity, new manufacturing techniques are developed and verified. After a successful integration of the resonant fin transistor, which was confirmed by scanning electron microscope imaging and high frequency silicon wafer measurements, the overall resonator functionality of the resonator could not be confirmed. The experimental result thus substantiates the theoretical investigation and confirms the accuracy of the finite-element method for the analysis of novel micro-electro-mechanical-systems.

Zusammenfassung

In den letzten Jahren hat die Entwicklung des Marktes für drahtlose Kommunikation, Radartechnik, Anwendungen für Auto-zu-Auto Kommunikation, das Internet der Dinge und die Industrie 4.0 eine massive Nachfrage nach spektral reiner Signalgenerierung ausgelöst. Die Erzeugung stabiler Hochfrequenzsignale ist für die neuen Kommunikationsstandards, die hochwertige Modulationsschemata ermöglichen und somit hohe Datenübertragungsraten gewährleisten, von entscheidender Bedeutung. Um dem kontinuierlich steigenden Bedarf gerecht zu werden, sind Resonatoren mit hohem Gütefaktor erforderlich. Diese werden jedoch mit den aktuellen komplementären Metalloxid-Halbleiter kompatiblen Resonatoren wie beispielsweise traditionelle LC-basierte Strukturen kaum erreicht, da diese unter starker induktiver Kreuzkopplung und großen Bauteilabmessungen leiden. Um diese Lücke zu schließen, bieten moderne Mikro-Elektromechanische-Systeme wie zum Beispiel Resonanzkörpertransistoren hervorragende Gütefaktoren bei hohen Frequenzen. Des Weiteren können sie monolithisch im Front-End-of-Line des komplementären Metalloxid-Halbleiter Prozesses gefertigt werden, ohne dass weitere Nachbearbeitungsschritte erforderlich sind. Resonanzkörpertransistoren bestehen aus einer periodischen Reihe von planaren Antriebsfeldeffekttransistoren, die bei elektrischer Anregung in eine mechanische Schwingen versetzt werden, was wiederum zu einer Modulation des Stroms in den Sensorfeldeffekttransistoren führt.

Die Arbeit zielt darauf ab, tiefere Einblicke in das grundlegende elektromechanische Verhalten eines speziellen Resonanzkörpertransistors, des sogenannten resonanten Fin-Transistors, zu gewinnen. Der Resonator verspricht hervorragende Leistungsmerkmale wie zum Beispiel eine Güte von 49 000 bei einer Resonanzfrequenz von 32 GHz. Diese Kennzahlen werden durch Simulationen und Messungen des gefertigten Mikro-Elektromechanischen-Systems untersucht, um die Realisierbarkeit einer kommerziellen Nutzung zu evaluieren.

Im ersten Teil dieser Arbeit werden die anisotropen Materialparameter von komplementären Metalloxid-Halbleiter-Technologien im Hinblick auf ihre Bedeutung für diese Art von Resonator und im Zusammenhang mit einer späteren theoretischen Modellierung diskutiert.

Die theoretische Untersuchung im zweiten Teil wird mithilfe der Finiten-Elemente-Methode durchgeführt, die das elektromechanische Rahmenwerk für die Simulation des Resonators bereitstellt. Sie verknüpft die Prinzipien der elektrostatischen Anregung der mechanischen Eigenmoden mit der piezoresistiven Modulation der Ladungsträgerbeweglichkeit. Die Simulationen im Front-End-of-Line bei einer festen Güte von 49 000 liefern jedoch eine stark degradierte Transkonduktanz, die mehrere Größenordnungen niedriger ausfällt als ursprünglich

erwartet.

Im dritten Teil der Arbeit werden die mechanischen Eigenschaften eines phononischen Kristallspiegels im Back-End-of-Line mithilfe analytischer und Finite-Elemente-basierter Ansätze in ein, zwei und drei Dimensionen betrachtet. Hier wird die Bedeutung von Bandlücken innerhalb der mechanischen Dispersion, die sowohl mit der Frequenz als auch dem Wellenvektor der resonanten Mode übereinstimmen, in der Anwesenheit hoch anisotroper mechanischer Materialien diskutiert. Die Untersuchung deutet auf ein Fehlen einer passenden Bandlücke hin was zu einer um mehrere Größenordnungen geringeren Güte des resonanten Fin-Transistors führt als ursprünglich in der Literatur berichtet wurde. Die Funktionalität des Resonators wird auch in einer kombinierten Studie von dem Front-End-of-Line und Back-End-of-Line bewertet, welche jedoch eine unzureichende Funktionalität aufzeigt und den Resonator deshalb aus theoretischer Sicht für Schaltungsanwendungen als ungeeignet identifiziert.

Der Abschluss dieser Arbeit beschreibt den Layout- und Designprozess eines resonanten Fin-Transistors auf einem 16 nm Fin-Feldeffekttransistor-Technologieknoten. Aufgrund der hohen Komplexität werden neu entwickelte Fertigungstechniken vorgestellt und verifiziert. Trotz einer erfolgreichen Integration des resonanten Fin-Transistors, welche durch Rasterelektronenmikroskopie und hochfrequente Siliziumwafer Messungen überprüft wurde, konnte die Funktionalität des Resonators letztendlich nicht bestätigt werden. Das experimentelle Ergebnis untermauert die theoretischen Resultate und bestätigt die Genauigkeit der Finiten-Elemente-Methode zur Untersuchung neuartiger Mikro-Elektromechanischer-Systeme.

Contents

1 Introduction **1**

2 CMOS Compatible Front-End-of-Line Micro-Electro-Mechanical-Systems **7**

2.1 The CMOS Layer 7

2.1.1 The Front-End-of-Line 8

2.1.2 The Back-End-of-Line 10

2.2 A Fully Integrated CMOS Front-End-of-Line MEMS 11

2.2.1 An Introduction to Phononic Crystals 11

2.2.2 The Resonant Body Transistor 13

2.2.3 The Resonant Fin Transistor 17

3 Linear Elastic Solid Mechanics in Anisotropic CMOS Materials **23**

3.1 Hooke's Law 23

3.2 Voigt's Notation 26

3.3 Common Elastic Properties 27

3.4 Crystallographic Reference Frame 28

3.5 Tensor Basis Transformation 29

3.6 Isotropic Cubic Materials 30

3.7 Anisotropic Cubic Materials 32

3.7.1 Young's Modulus 33

3.7.2 Poisson's Ratio 34

3.7.3 Shear Modulus 37

3.7.4 Elastic Wave Velocities 39

4 The Finite-Element Method **43**

4.1 Geometry Discretisation 43

4.2 Shape Functions 46

4.3 Construction of the Finite-Element Equations 49

4.4 Mechanical Eigenmodes 52

4.5 Viscous Damping and Frequency Domain Response 53

4.6 Modal Superposition 55

5 Electromechanical Modelling of the Resonant Fin Transistor **57**
5.1 Resonant Eigenmodes 58
5.1.1 Periodic Structures 58
5.1.2 Eigenmodes of the Resonant Fin Transistor 61
5.1.3 Index Guiding 64
5.1.4 Resonant Mode Shapes 67
5.2 Frequency Domain Response 70
5.3 Extended Simulation Setups 77
5.3.1 Symmetry Simplifications 77
5.3.2 Finite Number of Parallel Gates 81
5.3.3 Extended 14-Fin Unit Cell 85
5.4 Equivalent Isotropic Materials 87
5.4.1 Transient Response 90
5.4.2 Finite 2D Cavity 93
5.5 Transconductance Modelling 94
5.5.1 Piezoresistive Effect in Monocrystalline Silicon 94
5.5.2 FinFET Mobility Variation 101
5.5.3 Mechanical Transconductance 105

6 Confinement Characteristics of a Back-End-of-Line Phononic-Crystal **113**
6.1 The One-Dimensional Phononic Crystal 113
6.2 The Two-Dimensional Phononic Crystal 121
6.3 Combined Simulation of the Phononic Crystal and Resonant Cavity 127
6.3.1 SiO_2-based Back-End-of-Line 127
6.3.2 SiCO:H-based Back-End-of-Line 132
6.4 The Three-Dimensional Phononic Crystal 136
6.5 Fundamental Limits of the Quality Factor 143

7 Design and Characterisation of the Resonant Fin Transistor **149**
7.1 Device Layout and Fabrication 149
7.2 Process Adaptations and DC Characterisation 155
7.3 Measurements of the Resonant Fin Transistor 161

8 Conclusion and Outlook **167**

Bibliography **171**

Acknowledgements **191**

List of Publications of the Author **193**

Acronyms

1D	one-dimensional
2D	two-dimensional
3D	three-dimensional
BEOL	back-end-of-line
CMOS	complementary metal-oxide-semiconductor
DOF	degree of freedom
DUT	device under test
FEM	finite-element method
FEOL	front-end-of-line
FET	field-effect transistor
FinFET	fin field-effect transistor
IC	integrated circuit
MEMS	micro-electro-mechanical-system
MOS	metal-oxide-semiconductor
NMOS	n-channel metal-oxide-semiconductor
PMOS	p-channel metal-oxide-semiconductor
Q-factor	quality factor
RBT	resonant body transistor
RF	radio frequency
RFT	resonant fin transistor

1

Introduction

In 1947 W. Shockley, J. Bardeen and W. Brattain developed the first working transistor at the Bell Laboratories [Bardeen and Brattain 1948]. The invention revolutionised electronics as transistors became omnipresent. Some years later, in 1954, C. S. Smith discovered the piezoresistive effect in silicon, which ultimately led to the creation of the first semiconductor sensors [Smith 1954]. They outperformed at that time prevalent metal-based solutions and nowadays they still shape and advance the scope of modern integrated circuits (ICs) [Fischer et al. 2015].

Early implementations of the piezoresistive effect were used in strain and acceleration gauges where a mechanical deformation leads to a measurable change in conductivity of the material, also giving them the nowadays widely used name micro-electro-mechanical-systems (MEMSs). While the basic principles remained unchanged over the last decades since their invention, the breadth of implementation and complexity increased. In the consumer market, MEMSs are found in many applications nowadays. Every mobile device contains MEMS serving different purposes as microphones [Bogue 2013], gyroscopes [Serrano 2013; Patel and McCluskey 2012; Fischer et al. 2015] or multi-axis accelerometers [Bogue 2013]. In weather stations for home application, MEMS are integrated as pressure, humidity or thermal sensors [Setiono et al. 2019; Randjelović et al. 2008; Huang et al. 2015; André et al. 2017; Jaeger et al. 2000]. Their range of applications is not limited to sensing as they can also manipulate their surroundings and vice versa. MEMS in micro-mirror arrays mould the flow of light in projectors or heads-up display applications as small-scale integration and high actuation speeds over a broad light spectrum are required [Qu 2016].

With the meteoric rise of 6G, radar, car-to-car communication, the internet of things and industry 4.0, the need for a higher spectral purity signal generation is also rising [Wikstrom et al. 2020; Reichardt et al. 2012; Lacaita et al. 2007]. Consequently, stable radio frequency (RF) signals with high spectral purity are vital to enabling these new communication standards, which is challenging to achieve with conventional LC-based solutions [Stillmaker and Baas 2017; Lee et al. 2005]. MEMSs are promising candidates to fill the gap in frequency generation and filtering as their operating frequency and quality factor (Q-factor) is

far superior to existing solutions [Wikstrom et al. 2020; Reichardt et al. 2012; Lacaita et al. 2007; Nguyen 2007; Nguyen 2005; Ostman et al. 2006].

Modern solidly mounted MEMS resonators are typically divided into two device classes: bulk acoustic-wave (BAW) and surface acoustic-wave (SAW) devices. Surface acoustic-wave resonators use interdigital transducers to create lateral mechanical waves from electric signals and vice versa. The mechanical waves travel along the surface of a piezoelectric material, such as $LiTaO_3$ or $LiNbO_3$ [Wu et al. 2016; Zhu et al. 2016; Kourani et al. 2019; Gao et al. 2020; Gao et al. 2016; Shao et al. 2019; Jiang et al. 2019; Hsu and Lin 2018]. Using interference of mechanical waves created by multiple transducers, it is possible to design efficient filters or delay elements within ICs. However, their frequency is typically limited to a few hundred megahertz which strongly depends on the ratio of the surface wave velocity and the interdigital transducer pitch [Hashimoto 2012].

The bulk acoustic-wave resonators create a vertical standing wave within the piezoelectric material, using a top and bottom electrode rather than laterally spaced electrodes at the device surface. Typical piezoelectric materials involved are AlN, GaN or ZnO [Popa 2015; Krishnaswamy et al. 2006; Loebl et al. 2004]. Their natural frequency is limited by the thickness of the active material, which defines the wavelength of the standing mechanical wave. Bulk acoustic-wave resonators can be manufactured using bulk or surface machining, both of which are costly procedures and generally considered unfriendly for integration to complementary metal-oxide-semiconductor (CMOS) technologies [Fischer et al. 2015; Fedder et al. 2008; Qu 2016]. They can be further differentiated into film bulk acoustic-wave resonators (FBARs) and solidly mounted resonators (SMRs) [Liu et al. 2020]. Film bulk acoustic-wave resonators are fabricated using released piezoelectric films, decoupling them acoustically from their surroundings [Razafimandimby et al. 2013; Popa 2015; Yang, Lu, et al. 2018; Yang et al. 2016; Reddy and Mohan 2012; Bi and Barber 2008; Krishnaswamy et al. 2006]. Their resonant frequencies are in the megahertz to low gigahertz range, allowing their deployment within several 4G and 5G applications. However, their manufacturing requires extensive processing steps during the release of the thin film structure.

A novel approach avoids the complex processing steps by mounting the thin film directly to the substrate as a solidly mounted resonator. To minimise acoustic losses in the carrier structure, they rely on acoustic Bragg mirrors embedded in the substrate [Bi and Barber 2008]. They are constructed from alternating layers with a high acoustic impedance mismatch, such as tungsten and SiO_2. Under careful optimisation of the involved layer thicknesses, an acoustic mirror at the resonant frequency of the MEMS can be created [Ruby 2007]. Since bulk acoustic-wave and surface acoustic-wave are manufactured using deposition and lift-off techniques and CMOS incompatible materials, they are commonly manufactured as stand-alone devices on external chips. The required bonding of the external MEMS to the main IC severely limits the performance [Fischer et al. 2015; Qu 2016; Fedder et al. 2008].

Monolithically integrated resonators greatly benefit the application, such as reduced system

complexity, form factor and cost, as they can be processed natively within the CMOS process and thereby improve signal integrity by removing the need for off-chip frequency generation. CMOS-compatible monolithic MEMS are typically classified into three main process categories: pre-CMOS, inter-CMOS and post-CMOS, based on the order they are fabricated in conjunction with the CMOS flow [Fedder et al. 2008]. In the first type, also called "MEMS-first", the devices are fabricated before the CMOS process in the recess edge of the silicon wafer. The inter-CMOS or "MEMS-in-the-middle" process interleaves CMOS fabrication steps with polysilicon deposition and micro-machining. Pre-CMOS and inter-CMOS were originally designed for accelerometers and gyroscopes. However, dedicated foundries are required due to the particular procedure, which is one of the main drivers for the increased cost associated with those options. The post-CMOS or "MEMS-last" process offers more flexibility and reduced manufacturing cost because the MEMS is fabricated independently after the CMOS flow. This category can be further divided into additive and subtractive post-CMOS MEMS. The additive process deposits CMOS-compatible materials on top of the finished IC. The subtractive process etches existing material to build the MEMS but usually forces stricter design rule checks on the underlying CMOS IC [Fischer et al. 2015; Qu 2016; Peroulis et al. 2012; Qu 2016; Lu 2009]. Although they are compatible with the CMOS flow, their manufacturing is costly and challenging [Pachkawade et al. 2013; Valle et al. 2021].

A promising candidate for monolithically integrated MEMS is the unreleased resonant body transistor (RBT), which contrary to suspended MEMS which often times feature airgaps is in full contact with the supporting structure in all directions [Razafimandimby et al. 2013; Weinstein 2009; Bahr et al. 2018]. It combines a mixture of capacitive actuation and active field-effect transistor (FET) sensing and potentially achieves exceptional transconductances and Q-factors. Furthermore, its resonant frequencies are over tens of gigahertz due to its small mechanical feature size while perfectly compatible with the standard CMOS flow. On a modern fin field-effect transistor (FinFET) platform, it allegedly achieved the largest ever reported Qf product of 1.57×10^{15}.

To further assess the potential of the RBT on a 16 nm FinFET technology node, a thorough theoretical investigation of the performance using the finite-element method (FEM) and subsequent on-wafer characterisations of the fabricated devices are carried out in this thesis.

In Chapter 2 the fundamentals of the CMOS process are introduced and an overview of the back-end-of-line (BEOL) and front-end-of-line (FEOL) is given. The focus is after that shifted to the novel class of existing RBT devices in planar technologies. Their operation is based on a mechanical eigenmode within the FEOL confined by index guiding of the substrate wafer and BEOL phononic crystal. The differential electrostatic actuation and active FET sensing lead to transconductances in the low micro siemens range, which is improved by several orders of

magnitude by moving from a planar FET to a vertical FinFET technology.

In Chapter 3 the mechanical properties of typical CMOS materials are introduced to enable a subsequent use in the FEM. Here the focus is geared towards cubic anisotropic materials such as silicon and copper, which exhibit a varying mechanical response depending on their crystallographic orientation. The main elastic parameters, namely Young's modulus, shear modulus and Poisson's ratio, and the wave propagation response in the crystallographic frame, which are required for later modelling of the resonant fin transistor (RFT), are introduced.

In Chapter 4 the mechanical equations of motion used in the FEM are derived from the Lagrange equations. Additional concepts, which are required for the investigation of a resonant structures, such as damping, eigenmodes and various solution methods, are also discussed.

In Chapter 5 the FEOL of the RFT is modelled with the FEM on a simplified three-dimensional (3D) periodic unit cell. In the first part, the resonant eigenmodes and index guiding properties are discussed in dependence on the underlying wafer orientation. After establishing a well-guided RFT mode, the simulation setup is calibrated to capacitive measurements of the structure. To further reduce the computational complexity symmetry simplifications are discussed in the presence of anisotropic materials and varying Poisson's ratios. Different geometrical FinFET variations are compared for their simulated electromechanical frequency domain response at various electrical bias and drive conditions. Also discussed is the performance of a larger simulation volume using multiple parallel resonant gates or a larger number of fins with a different wiring scheme. In the second part, the transconductance of the RFT is modelled using the piezoresistive effect of silicon for various wafer orientations and simulation setups. Ultimately the impact of a varying Q-factor on the transconductance of the simulated RFT is discussed, as discrepancies to the reported values in the literature exist.

In Chapter 6 the phononic crystal properties of the BEOL in one-dimensional (1D) and two-dimensional (2D) simulations using equivalent isotropic materials are addressed. Here the formation of acoustic band gaps tailored to the RFT frequency and propagation wave vector are discussed for different BEOL stack variants. Using a 2D approximation, the full RFT is simulated, including the complete CMOS layer and the impact of a matched band gap on the Q-factor of the RFT. Most simplifications are dropped in a final 3D investigation of the BEOL, including all mechanical anisotropic effects. Their impact on the band structure and gap formation is discussed concerning the performance of the RFT. The chapter is concluded with an analysis of the fundamental Q-factor limits, which further substantiate the observed discrepancies with existing literature.

In Chapter 7 the design and fabrication of the RFT in a 16 nm FinFET Technology node are covered. Here the required process adaptations for the successful structure fabrication are verified with on-wafer measurements and a scanning electron microscope. Ultimately the measurement limits and performance of the RFT are compared to the initial theoretical analysis. The lacking functionality of the RFT, which could ultimately not be verified, is in line with the foregone theoretical investigations, and thus challenges existing literature.

2

CMOS Compatible Front-End-of-Line Micro-Electro-Mechanical-Systems

Contents

2.1 The CMOS Layer 7
2.1.1 The Front-End-of-Line 8
2.1.2 The Back-End-of-Line 10
2.2 A Fully Integrated CMOS Front-End-of-Line MEMS 11
2.2.1 An Introduction to Phononic Crystals 11
2.2.2 The Resonant Body Transistor 13
2.2.3 The Resonant Fin Transistor 17

The electrical and mechanical properties of the commonly used complementary metal-oxide-semiconductor (CMOS) layer for standard integrated circuits (ICs) design are a key building block for the design of novel mechanical resonators. After the introduction of planar field-effect transistor (FET) and fin field-effect transistor (FinFET) technologies and their interconnection in the back-end-of-line (BEOL), the new class of fully monolithic front-end-of-line (FEOL) resonators and their compatibility with the CMOS process are discussed. Here the working principle and performance numbers of a resonant body transistor (RBT) on an advanced FinFET node are introduced.

2.1 The CMOS Layer

Current CMOS implementations contain two regions, the FEOL and BEOL, as sketched in Figure 2.1(a). The FEOL houses all silicon-based devices, like active FETs, but also passives such as diodes, resistors and metal-oxide-semiconductor (MOS) capacitors. Multiple metal layers in the BEOL interconnect these devices. In addition to the wiring between the different FEOL devices, the BEOL includes metal-based passives like inductors, resistors and capacitors.

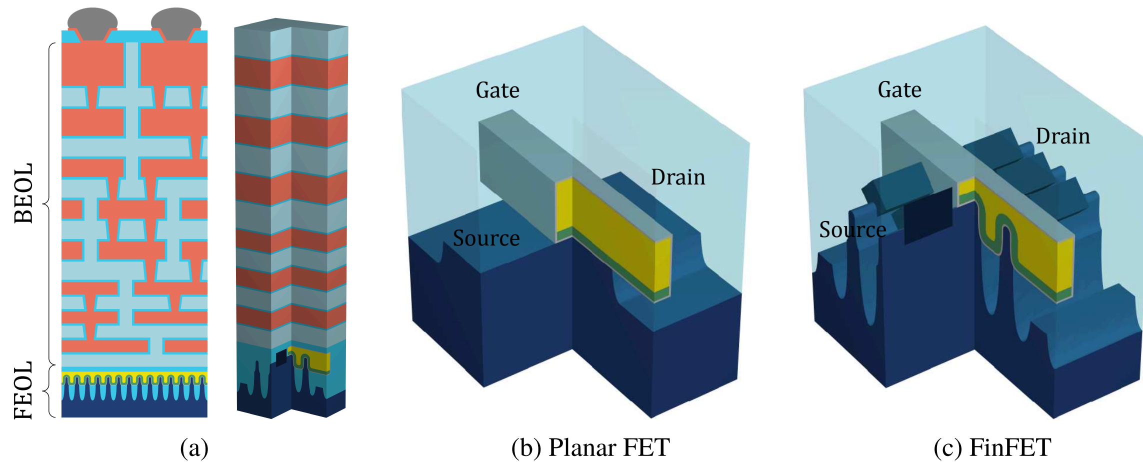

Figure 2.1: (a) Illustration of a CMOS layer with the FEOL and BEOL. Comparison of a (b) planar FET and (c) tri-gate FinFET technology node.

2.1.1 The Front-End-of-Line

Starting from the bottom up, the choice of the wafer substrate material determines the later use case of the devices. In current foundry scale applications crystallographically rotated p-type doped silicon wafers are dominant for conventional ICs [Thompson et al. 2004; Saitoh et al. 2008; Jaeger et al. 2013; Gallon et al. 2004]. Other semiconductor solutions geared toward specific applications also exist. For high-power and high-electron-mobility transistors (HEMTs), III/V semiconductors are the preferred choice over silicon. For released micro-electro-mechanical-system (MEMS), differently oriented silicon wafers with beneficial mechanical properties are also available and for low device leakage and power consumption silicon-on-insulator wafers prevailed [Xu et al. 2016; André et al. 2017; Chandrahalim et al. 2007; Gallon et al. 2004].

Using a combination of subtractive and additive processing techniques the FETs are fabricated directly on the wafer. In older semiconductor technologies the devices and their arrangement were planar, with the conductive channel being planar beneath the gate, as sketched in Figure 2.1(b). The feature sizes of the FETs were in the range of 3 µm down to 22 nm [TSMC 2021; Global Foundries 2021; Samsung 2021]. Historically the feature size or node of the technology refers to a fraction of the tightest manufacturable pitch between adjacent gates, typically the half pitch. It substantially influences the IC performance as it mandates the possible current densities and IC footprint, to name a few [Mendiratta and Tripathi 2020]. Following Moore's law and the need for higher integration densities, planar FETs started suffering from several undesired effects.

Classical constant electric field scaling worked well down to the 130 nm node. Here lateral dimensions, layer thicknesses and supply voltages are scaled by the same ratio, resulting in reduced power consumption and increased speed of the CMOS technologies. Increased leakage currents of thin gate oxides could be mitigated by using thicker dielectrics or materials with a

higher permittivity known as high-κ dielectrics. Even with these material innovations, further scaling of planar technologies beyond 28 nm or 22 nm was limited. Shorter gate lengths lead to increased leakage currents and drain voltage-dependent threshold voltages, also known as drain-induced barrier lowering (DIBL), as a result of the reduced electrostatic control.

Planar FETs were replaced by vertical tri-gate devices, as sketched in Figure 2.1(c), also known as FinFETs. The three-dimensional (3D) FinFET structure controls the electron channel from three sides, which improves electrostatic control and enabled additional scaling for the 16 nm and beyond technology nodes [Dennard et al. 1974; ITRS 2021]. Since the gate surrounds the channel on three sides of the fin, it allows the gate to regain complete control over the channel regardless of the length. All scaling issues of the planar FETs are alleviated, enabling continued shrinking in newer technology node generations down to 3 nm [Robertson 2005; Loubet et al. 2017; Parvais et al. 2009]. At the same time, it also offers higher performance for the same lateral device footprint as the current density strongly increases in comparison to planar FETs [Tang et al. 2001; Jurczak et al. 2009; Subramanian et al. 2006]. Since the gate has complete control over the channel behaviour, current FinFET implementations have lightly doped channels which offer better threshold voltage matching in the event of random doping fluctuations [Jurczak et al. 2009]. To reduce the amount of dopant diffusion and leakage current between the channel and the gate, high-κ dielectrics, such as HfO_2 [Kavalieros et al. 2006; ITRS 2021], were introduced. While they also enabled continued technology node shrinks due to the thinner required layer thickness, the saturation current of the FET, which is directly proportional to the equivalent dielectric thickness, was also improved [Sze 2014].

In 1954 C. S. Smith discovered a resistivity change in monocrystalline semiconductors, such as silicon or germanium, when applying an external force. In the presence of stress, the charge carrier density changes following a volumetric change of the specimen, which causes a shift of the conduction and valence band [Smith 1954]. It was later used to further improve the carrier mobility by additional high-strain layers on-top of the FET. By applying either a tensile or compressive strain along the direction of the channel, the electron or hole mobility of n-channel metal-oxide-semiconductor (NMOS) and p-channel metal-oxide-semiconductor (PMOS) devices could be improved. This technique yields an improved current at the same bias voltage, increasing the current density even further [Smith 1954; Thompson et al. 2004; Jurczak et al. 2009; Collaert et al. 2016; Verheyen et al. 2006; Liow et al. 2007; Kavalieros et al. 2006].

Although FinFETs provide solutions to many complications present in planar technologies, they come with unique problems and challenges. Since the fabrication of semiconductor fins is a complicated task requiring several etching steps, the surface roughness of the fin top and side facets can be suboptimal. This leads to an increased carrier scattering in the channel. Hence, the etching procedures must be tuned precisely and optimised to mitigate this issue [Lee et al. 2011]. A further drawback originates from the tall aspect ratio, which reduces the thermal conductivity, and thus intensifies the self-heating of the FinFET. This reduced thermal

conductivity negatively impacts the reliability of interconnects to the BEOL and the electrical performance [Liu, Wang, et al. 2014].

In newly emerging technology nodes, the FinFETs will soon be superseded by the gate-all-around field-effect transistors (GAAFETs), also known as ribbon FETs, with even better leverage of the vertical integrability as multiple channels are stacked vertically, all of which are entirely surrounded by the gate [Bae et al. 2018; Loubet et al. 2017].

2.1.2 The Back-End-of-Line

The metallisation layer of the CMOS layer, the BEOL as sketched in Figure 2.1(a), is, in its most straightforward description, responsible for the interconnection of the aforementioned FEOL device. For this purpose, patterned metal and oxide layers are alternately deposited on the FEOL. So-called "vias" handle the vertical connections between different metal layers. On the surface, the BEOL offers the possibility to interconnect with packages or other chips by bonding or bumping [Fischer et al. 2015; Lu 2009; ITRS 2021].

To interpose the delicate FEOL dimensions to the comparatively large IC interconnects, the layer thicknesses and pattern dimensions increase throughout the BEOL, as sketched in Figure 2.1(a). The lower metal layers have thicknesses in the sub-100 nm range and smaller associated track widths required to interconnect the small FEOL devices. The track width specifies the dimensions and spacings of adjacent wires, which is enforced by the design rule check. For layers further away from the FEOL, the thicknesses and track widths are typically larger. Also, the track directions, the dominant direction of the wires, are generally orthogonal in these higher layers, which maximises structural integrity and reduces parasitic capacitances. The final layers on top of the BEOL have a thickness in the micrometre range to reduce the sheet resistance and provide higher structural integrity for the wafer packaging.

Originally the BEOL was constructed from SiO_2 and aluminium. With the decrease in node size of the FEOL and the subsequent rise in switching speeds, the BEOL had to be modified to keep pace [Meindl et al. 2003]. Hence, aluminium was replaced with copper due to its lower sheet resistance, thus significantly improving the performance [Nitta et al. 2003; Davis et al. 2001]. With further tightening bounds for the interconnection delay, SiO_2 with the comparatively large permittivity of 3.8 was insufficient as it limited the switching speed [Grill 2003; Gambino 2012]. It was thus replaced with a low-κ oxide, such as SiCO:H, with a permittivity of $2 - 2.8$. SiCO:H is a high porosity variant of carbon-doped amorphous SiO_2 fabricated using plasma-enhanced chemical vapour deposition [Gambino 2012; McGahay 2010; Narayanan et al. 2002].

The improvements from using copper and SiCO:H are accompanied by more intricate integration methods. In combination with copper SiCO:H suffers from material diffusion resulting in reduced breakdown voltages and leakage currents [McGahay 2010]. This behaviour is mitigated by an additional plasma annealing step which increases the integrity of the brittle SiCO:H layer surface by forming a thin layer of SiO_2. Further deposition of a thin

copper seed layer with a subsequent fabrication of the entire metal layer alleviates the issue completely [Gambino 2012; McGahay 2010; Narayanan et al. 2002]. Furthermore, copper cannot be patterned by reactive ion etching, which was widely used for aluminium, requiring the introduction of a "dual damascene" process, increasing complexity [Gambino 2012]. In contrast to aluminium, copper is also a highly anisotropic mechanical material which puts additional stress on the interconnects. These material properties degrade mechanical reliability, especially in combination with porous SiCO:H, resulting in an increased failure of vias and higher complexity packaging methods to bypass this issue [Basavalingappa et al. 2017; Gambino 2012]. Moreover, contamination of the FEOL with copper atoms must be prevented as deep trap states in the silicon, introduced by the copper atoms, may lead to a complete device failure [Brotherton et al. 1987].

2.2 A Fully Integrated CMOS Front-End-of-Line MEMS

While the electrical performance of the BEOL is a well-researched field, its periodic arrangement of the different layers sparked interest in the field of monolithic MEMS design as it also exhibits unique mechanical properties [Ionescu 2010; Weinstein and Bhave 2010; Bahr et al. 2014; Bahr et al. 2015; Bahr et al. 2016; Bahr et al. 2018]. In contrast to released MEMS, where mechanical losses occur predominately at the anchor points, unreleased monolithic devices are in direct contact with their surrounding. Without appropriate mechanical confinement, they would suffer from pronounced radiation losses, which impede their performance [Bahr et al. 2015]. One mitigation approach leverages the periodic arrangement of the BEOL layers to create a phononic crystal mirror which contributes to the mechanical confinement and leads to high quality factors (Q-factors) of the monolithic devices [Bahr et al. 2016; Bahr et al. 2015; Khelif and Adibi 2016].

2.2.1 An Introduction to Phononic Crystals

Phononic crystals are artificial materials are constructed from mechanical scatterers arranged in a periodic matrix. Such a structure possesses a band structure similar to the photonic band structure in photonic crystals or the electronic band structure in semiconductors [Khelif and Adibi 2016; Joannopoulos et al. 2008]. It describes the possible vibrational eigenmodes for the different wave propagation directions supported by the structure. These supported eigenmodes are strongly affected by the lattice's elastic properties, periodicity and shape of the scatterers.

The propagation of mechanical waves within the periodic phononic crystal can be described based on Floquet-Bloch theorem [Khelif and Adibi 2016]. Used on the smallest irreducible unit cell of the periodic lattice, which is known as the Brillouin zone, the vibrational eigenmodes of complex systems can be computed using the finite-element method (FEM) by solving the discretised eigenvalue equation

$$[\mathbf{K} - \lambda \mathbf{M}]\boldsymbol{\phi} = 0, \tag{2.2.1}$$

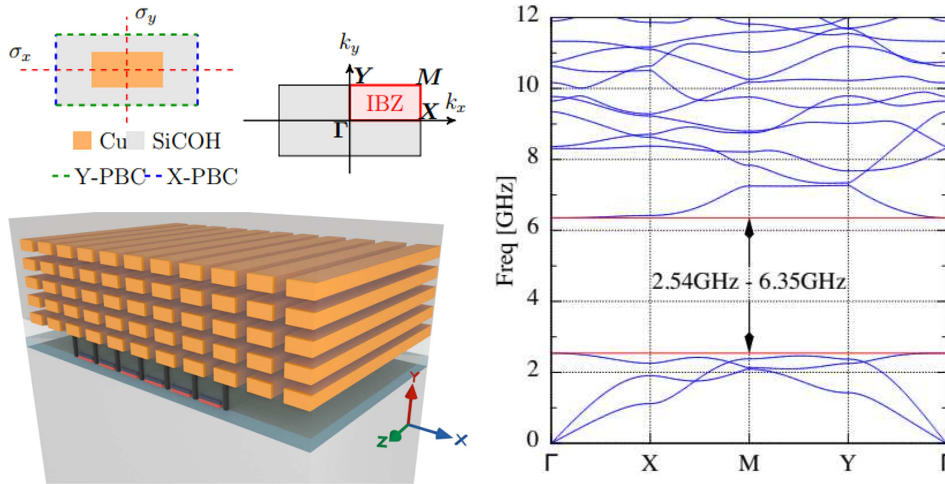

Figure 2.2: Phononic crystal made from parallel copper wires with the respective unit cell and Brillouin zone. The corresponding mechanical band structure and band gap are plotted on the right. (Reprinted from [Bahr 2016].)

where $\lambda = \omega^2$ is an eigenvalue of the system with the angular eigenfrequency ω. The corresponding mechanical displacement eigenvector is given by $\boldsymbol{\phi}$. $\mathbf{K}$ and $\mathbf{M}$ are the acoustic stiffness and mass matrices, respectively [Bathe 2014; Chopra 2012; Liu 2003; Rao 2010]. The solutions of (2.2.1) along the perimeter of the irreducible Brillouin zone yield the band structure of the structure, as shown exemplarily in Figure 2.2 for a square copper matrix embedded in SiO_2. The bands describe the dispersion relation of the vibrational eigenmodes concerning their propagation direction within the phononic crystal. If the acoustic impedance $Z = \rho c$, where ρ is the density and c the speed of sound, of the scatterers and their surrounding medium are strongly mismatched, the structure may exhibit so-called band gaps for specific frequency ranges. Within these band gaps mechanical wave propagation is partially or fully prohibited, regardless of the incident wave vector and the phononic crystal acts as a perfect mechanical mirror [Khelif and Adibi 2016].

The formation of the band gaps follows from a destructive interference of the scattered waves known as the Bragg mechanism. The first gap is typically observed at the frequency $\omega = c/a$, where c is the wave velocity and a the lattice period [Khelif and Adibi 2016; Joannopoulos et al. 2008]. The attenuation strength increases with the number of unit cell repetitions and is strongest close to the centre frequency of the band gap [Hudeczek and Baumgartner 2020; Khelif and Adibi 2016; Goettler et al. 2010]. Construction of a wide high-frequency gap is often challenging since the gap width scales inversely with the lattice pitch, which is again limited by the manufacturing resolution [Bahr et al. 2015; Khelif and Adibi 2016; Joannopoulos et al. 2008].

Phononic crystals have been successfully deployed in the reduction of anchor losses in released MEMS structures [Hamelin et al. 2019], improved confinement in surface acoustic-wave devices [Shao et al. 2019; Jiang et al. 2019; Ziaei-Moayyed et al. 2010] and as biological sensors [Lucklum et al. 2010]. They were also demonstrated in the BEOL stack of a conventional

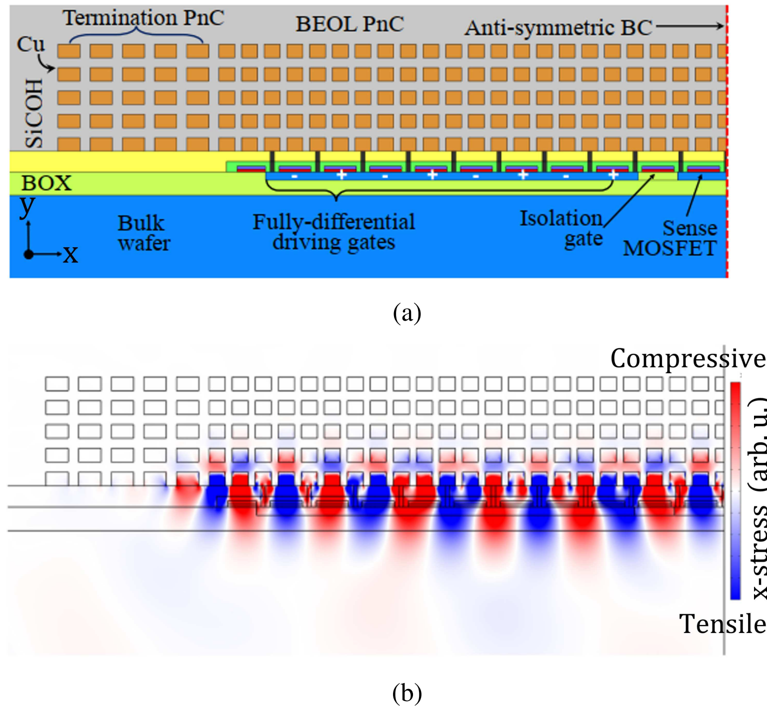

Figure 2.3: (a) 2D FEM simulation setup and (b) corresponding y-stress patterns for the resonant mode. (Adapted from [Bahr 2016].)

CMOS process in recent years. With adequate patterning of the stack, a phononic crystal with a directional band gap was found, which enabled the manufacturing of the first entirely unreleased FEOL MEMS with strongly increased figures of merit compared to existing released solutions [Bahr et al. 2018; Weinstein 2009].

2.2.2 The Resonant Body Transistor

This relatively novel class of unreleased CMOS MEMSs, also known as RBTs, leverages the full potential of the piezoresistive effect with a combination of electrostatic actuation and active FET sensing enabled by the phononic crystal. This class of MEMSs promises increased transduction, resonant frequencies in the double-digit gigahertz realm and increased Q-factors above 1000. Additionally the full compatibility with the CMOS process is maintained and additional performance improvements are expected with further technology node shrinks [Weinstein and Bhave 2010].

RBTs can be manufactured from a periodic arrangement of FET transistors in the FEOL, forming a waveguide with distinct mechanical eigenmodes [Bahr 2016; Bahr et al. 2016]. The cross-section of the left half of a RBT design, showing the FEOL cavity and BEOL mirror, is sketched in Figure 2.3(a). The mechanical target mode of the devices features a stress pattern with opposing signs in neighbouring FETs of the cavity as plotted in Figure 2.3(b).

Since the waveguide is not released and in contact with the surrounding material in all directions, the eigenmodes could quickly radiate away reducing the performance [Bao 2015;

Choudhary and Iniewski 2013; Bahr et al. 2014]. Therefore, a vertical confinement of the mechanical mode is required in order to minimise losses and improve the Q-factor, which can be achieved with the help of a matched phononic crystal manufactured in the BEOL. The best-performing waveguide modes favour the wave vector $k_y = \pi/a$, where a is the pitch of the FETs, which ensures a solid mechanical coupling of adjacent FETs. Hence the phononic crystal must feature a preferably absolute band gap, as sketched in Figure 2.2, for the desired waveguide mode frequency and wave vector.

However, such patterning as required for the phononic crystal is only possible in the BEOL. To ensure confinement against substrate losses, the waveguide mode may not couple to the bulk modes of the substrate material. Bulk modes feature the well-known linear dispersion relation

$$\omega = \mathbf{k}c, \tag{2.2.2}$$

where c is the mechanical wave velocity in the substrate and $\mathbf{k}$ is the wave vector [Khelif and Adibi 2016; Joannopoulos et al. 2008]. A continuum of states exists for all frequencies above the so-called sound cone (2.2.2) and potential waveguide modes may couple to those available states and radiate away, reducing the Q-factor, and thus the performance. To prevent undesired mechanical substrate losses the resonant frequency of the RBT must be designed with regard to the dispersion relations of the surrounding materials. Thus, the frequency of the RBT must be sufficiently small to ensure confinement via total internal reflection at the material interfaces [Khelif and Adibi 2016; Hsu and Lin 2018].

The mechanical eigenmode of the RBTs cavity, formed by the FETs, is driven by internal electrostatic transduction which is achieved by wiring adjacent FETs as MOS capacitors, which are biased in strong inversion [Bahr 2016]. The mechanical eigenmode is actuated by modulating the voltage across the MOS capacitors, which leads to a deformation of the individual FETs. Such actuation proved to be highly efficient, albeit having a dielectric material within the capacitor structure, due to the lower spatial separation of the electrodes and higher permittivities involved [Bahr 2016; Weinstein and Bhave 2007]. This driving principle is applied to the cavity through differentially wired MOS capacitors within the waveguide. This connection scheme allows the creation of a strong deformation profile matched to the wave vector of the desired propagating eigenmode when actuated electrically at the mechanical eigenfrequency of the cavity [Bahr 2016; Bahr et al. 2016].

Whereas released MEMS often rely on capacitive sensing, RBTs use the piezoresistive effect of silicon to sense the deformation of the eigenmode as a modulation of the carrier mobility within the cavity FETs. At the centre of the cavity, shown in Figure 2.3(a), the sensor is constructed from a differentially wired pair of active FETs. The mechanical eigenmode, actuated by the driving MOS capacitors, creates a stress profile within the channels, and thus modulates the carrier mobility at the eigenmode frequency. Here the opposing signs of stress also lead to a differential modulation. This type of sensing promises excellent performance

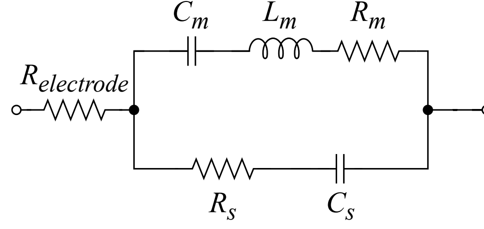

Figure 2.4: Modified Butterworth-Van Dyke model for a capacitive MEMS resonator. (Adapted from [Choudhary and Iniewski 2013].)

at gigahertz frequencies which has been successfully demonstrated for FETs on different technology platforms [Weinstein and Bhave 2007; Bahr et al. 2014; Bahr et al. 2018].

The figure of merit of the RBT is the mechanical transconductance

$$G_m = \frac{i_{sense}}{v_{drive,diff}} = |Y_{dd21} - Y_{dd12}| \tag{2.2.3}$$

which links the required differential actuation voltage $v_{drive,diff}$ at the drive MOS capacitors to the resulting differential current i_{sense} at the active sense FETs. This working mode is different from most established MEMS which typically operate solely within the voltage domain. The RBT on the other hand converts an input voltage to an output current [Hager et al. 2021; Hudeczek et al. 2022; Zhu et al. 2016; Razafimandimby et al. 2013; Hamelin et al. 2019]. The transconductance is obtained from the differential admittance parameters for the forward Y_{dd21} and reverse Y_{dd12} directions. Since the device is only functional in the forward direction by construction, all parasitic effects, as introduced by the wiring, are removed leading to a self-de-embedded transconductance [Weinstein and Bhave 2007; Bahr 2016].

This behaviour of the RBT, which converts a modulated voltage at the input to a modulation of the output current, provides additional challenges when modelled in circuits. Capacitive devices, such as film bulk acoustic-wave resonators, convert an actuation voltage at the input into a voltage swing at the output of the device. Such operation is typically represented by a modified Butterworth-Van Dyke (MBVD) model, as depicted in Figure 2.4 [Larson and Bengzon 2013; Hodge et al. 2017; Choudhary and Iniewski 2013; Jaffe and Smith 1957]. The circuit mimics the electrical and mechanical behaviour using a motional (L_m, R_m, C_m) and a static arm (R_s, C_s). The motional inductance L_m, motional resistance R_m and motional capacitance C_m describe the electromechanical behaviour of the devices including acoustic losses. The static arm describes the electrical capacitance of the device C_s and the corresponding dielectric losses R_s. Lastly the contact resistances are modelled by the series resistance $R_{electrode}$ [Choudhary and Iniewski 2013].

This model is often times used in circuit applications, due to the low implementation effort, to model the impedance response of the MEMS in close spectral vicinity to the main resonance. Although it was proposed to be also applicable for RBTs [Srivastava et al. 2021], which are based on an active sensing approach, it was shown that the conversion from an alternating voltage at

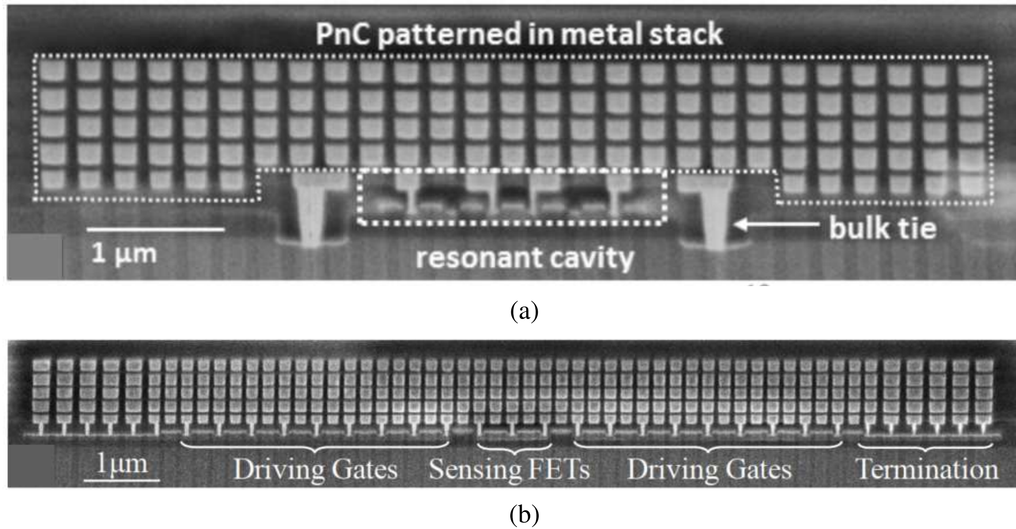

Figure 2.5: Iterations of the RBT manufactured on IBM's 32 nm silicon-on-insulator node. The RBTs resonate at (a) 2.8 GHz with a Q-factor of 252 and (b) 3.252 GHz with a Q-factor of 11 620. (Adapted from [Bahr et al. 2014; Bahr et al. 2016].)

the device input to an alternating current at the output of the device prevents a direct use of the modified Butterworth-Van Dyke model without major modifications [Hager et al. 2021; Bahr 2016]. Furthermore, the modified Butterworth-Van Dyke model is only a simplified representation and a more rigorous approach, like FEM modelling, is required to obtain physical insights into the operation principles [Hudeczek et al. 2022].

Initial concepts of the RBT were built on IBM's 32 nm silicon-on-insulator (SOI) planar technology. The first designs had a short cavity size with only one pair of driving and sensing FETs, as shown in Figure 2.5(a). This early implementation delivered a transconductance of G_m = 0.5 µS at 2.8 GHz with a Q-factor of 252 [Bahr et al. 2014]. However, this performance is comparable to existing surface acoustic-wave and bulk acoustic-wave solutions, with the added benefit of being monolithically embedded in the FEOL of the CMOS layer without complex processing steps. The phononic crystal, which enables the large Q-factor, is built from parallel copper wires in the BEOL, which is designed to have a directional band gap with a bandwidth of 3.81 GHz and a centre gap frequency of 4.45 GHz. Thus the resonant frequency lies within the forbidden frequency range of the phononic crystal. A second, supposedly optimised structure, as shown in Figure 2.5(b), uses a larger cavity size with an increased number of driving MOS capacitors and achieves a resonant frequency of 3.252 GHz with a strongly increased Q-factor of 11 620. Surprisingly the optimised structure performs worse, with a transconductance of only G_m = 96 nS, turning it unusable for oscillator applications in IC design [Hudeczek et al. 2022; Bahr et al. 2016].

A shortcoming of the early RBT designs was the unfavourable orientation of the individual FETs within the cavity. Due to the use of planar technology, the mechanical deformation was mainly vertical, creating only low stress of a few hundred 100 kPa to low MPa in the channels of the sense FETs. The low stress resulted from a low coupling between adjacent drive FETs

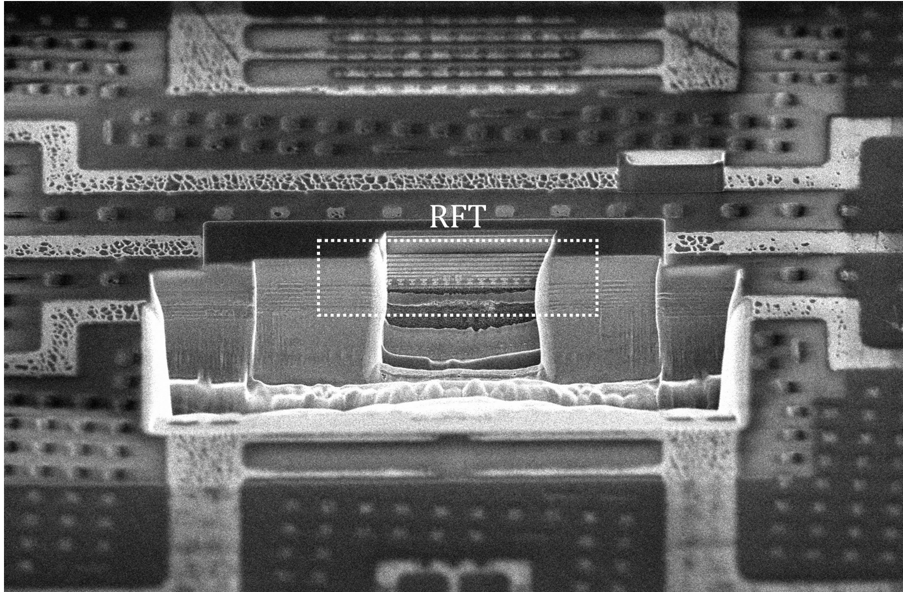

Figure 2.6: Focused ion beam scanning electron microscope picture of a RFT including top-level wiring.

[Bahr et al. 2014; Bahr et al. 2016]. Furthermore, this technology's smallest possible device pitch between adjacent FETs of 165 nm limits the resonant frequency, which is inversely proportional to the pitch. The above mentioned issues lead to a promising, but still small, transconductance.

2.2.3 The Resonant Fin Transistor

A more recent variation of the RBT, which was manufactured on a 14 nm FinFET technology node from Global Foundries, is promising a greatly increased mechanical transconductance, Q-factor and resonant frequency, while maintaining all of the benefits of the planar RBT [Bahr 2016]. The so-called resonant fin transistor (RFT) was reported with a transconductance of $G_m = 14\,\mathrm{mS}$ marking an increase of several orders of magnitude over the planar RBT designs. At the same time it operates at a much larger frequency of 32 GHz and a Q-factor of 49 000 making it the one of the best performing resonator MEMS to the current date, which is typically quantified by the frequency product $Qf = 1.57 \times 10^{15}\,\mathrm{Hz}^{-1}$ [Bahr 2016].

This performance increase is mainly achieved through the change to a FinFET technology as sketched in Figure 2.1(c). In Figure 2.6 a cross-section of a RFT, which was fabricated in this work on a 16 nm FinFET node, is shown. The RFT is integrated in the same manner as the RBT on the planar technology nodes where the resonant mechanical cavity is fabricated in FEOL of the CMOS stack. However, the periodic waveguide is now formed by hundreds of adjacent FinFETs, as shown in Figure 2.7(a). The FEOL cavity is split into two different types of unit cells which are responsible for driving and sensing the mechanical mode. All unit cells, in contrast to the RBT, share a common gate which spans over all fins in the cavity. The drive unit cells are connected as MOS capacitors in a differential manner to the two electrical drive phases drive-plus (DP) and drive-minus (DM), as sketched in Figure 2.7(b). They are responsible to drive the mechanical eigenmode by electrostatic transduction which was also used for the RBT

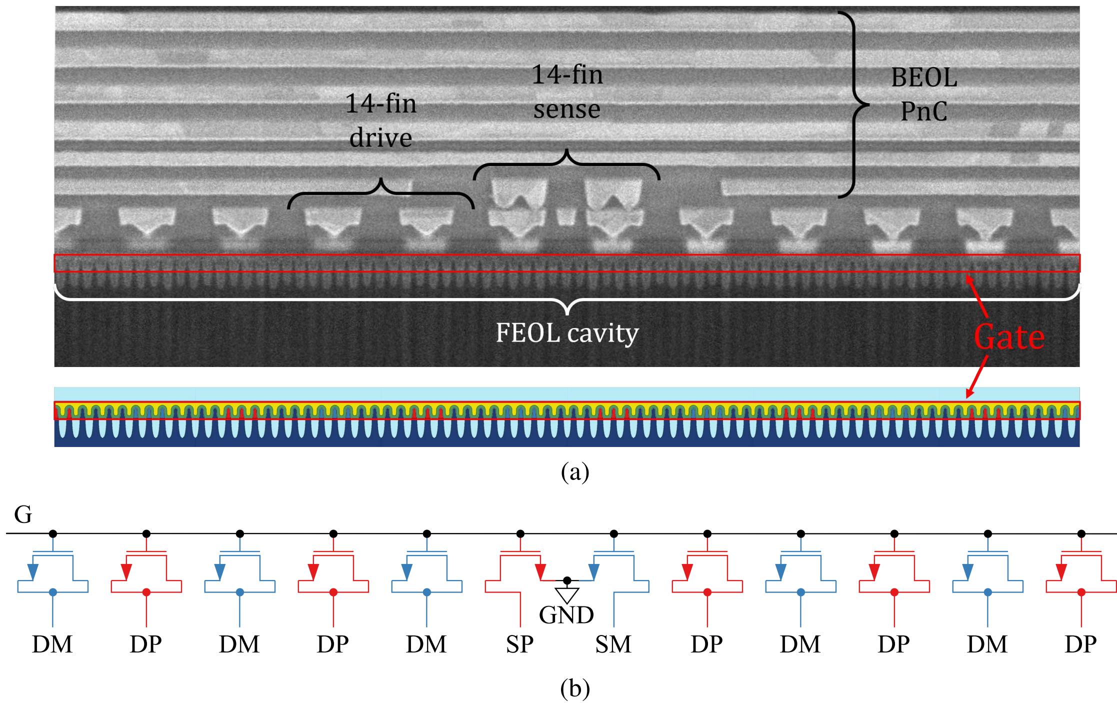

Figure 2.7: (a) Scanning electron microscope image of the RFT cavity in the gate region with the BEOL phononic crystal (PnC), the FEOL cavity and sketch of the fins. (b) Schematic of the FEOL cavity where each transistor is matched to three fins in (a). The connections are marked as: drive-plus (DP), drive-minus (DM), sense-plus (SP), sense-minus (SM), ground (GND) and gate (G).

[Bahr 2016; Bahr et al. 2018]. The actuated mechanical eigenmode propagates through all fins within the cavity, also the sense unit cell, which is built from a differential pair of active FinFETs connected to the sense-plus (SP) and sense-minus (SM) phases. These will pick up the mechanical deformation of the fins as a modulation of the carrier mobility which depends on the direction and magnitude of stress on the FinFET channels [Thompson et al. 2004; Ma et al. 2013; Sze 2014]. In a research environment the different connections (drive-plus, drive-minus, sense-plus, sense-minus and gate) are routed via the BEOL to the surface of the wafer where they are directly connected to measurement equipment, which is discussed in Chapter 7. In a productive implementation, for example as resonant fin oscillator, these connections would be routed internally to other CMOS devices [Hager et al. 2021].

With the transition to a FinFET technology the feature size, and thus the pitch of the periodic structure is reduced to 48 nm. This leads to an increase of the resonant frequency to 32 GHz [Bahr et al. 2018]. Similar to the RBT, adjacent FinFETs will contract and expand in a breathing motion as sketched in Figure 2.8(a) for two adjacent fins. The corresponding dispersion relation of this differential eigenmode is plotted in Figure 2.8(b). For the waveguide to support the propagation of the differential eigenmode, the mode must be guided at the Y-point, which lies at the wave vector $k_y = \pi/a$, where a is the fin pitch.

The guiding of the mechanical mode at this frequency is challenging and relies both on a matching phononic crystal in the BEOL, as marked in Figure 2.7(a), as well as total internal reflection at the boundary to the silicon substrate. Contrary to the RBT, which featured a

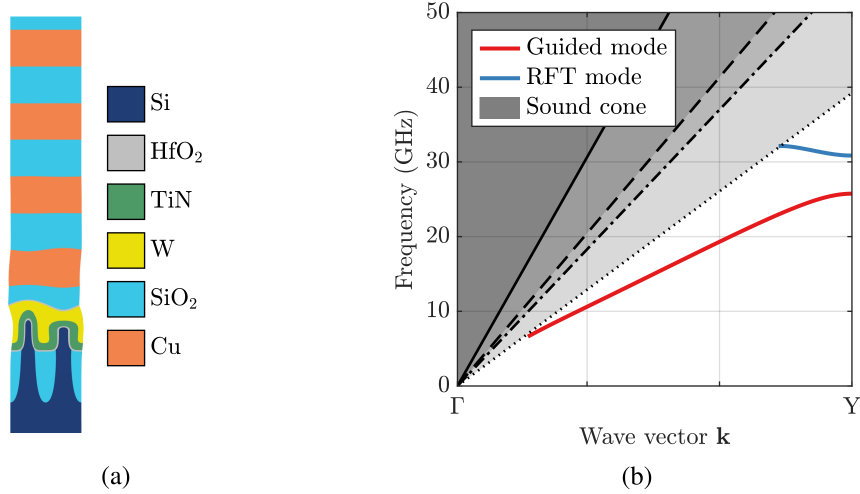

Figure 2.8: (a) Deformation profile of the RFT eigenmode, with a matched BEOL phononic crystal. (b) Mechanical dispersion relation of the RFT and substrate.

phononic crystal with an omnidirectional band gap (compare Figures 2.2 and 2.5), this is not feasible at the required frequency due to limitations of the FinFET technologies. For an omnidirectional band gap at this frequency sufficiently small lateral patterning of the BEOL is prevented by the design rule checks of the semiconductor foundries [Bahr et al. 2018]. Those rules are designed for a yield oriented BEOL regarding the electrical performance and typically do not consider the use as a mechanical mirror. Nevertheless, the unpatterned BEOL stack, with the correct layer thicknesses, was reported to feature a partial band gap matching the frequency and wave vector of the RFT eigenmode, which follows a 2D FEM simulation [Bahr et al. 2018; Bahr et al. 2014]. Consequently, the deformation strongly decays within the first few layers of the phononic crystal, as sketched in Figure 2.8(a), which leads to good confinement of the mode.

The guiding effect of the substrate is unchanged between the RBT and RFT, as silicon allows shielding of the cavity up to several tens of gigahertz at the required wave vector. This effect is shown in Figure 2.8(b) for a typical band structure of the RFT cavity with the dispersion relations of the so-called sound cone of the substrate. Propagating modes occurring at the Y-point of the Brillouin zone, where they can couple to the adjacent fins must reside well beneath the sound cones of the substrate material at the Brillouin zone edge. Hence the common gate forms a well-defined waveguide for the RFT mode to propagate through, enabling the strongly increased Q-factor [Bahr et al. 2018].

While the smaller technology node size enabled the RFT's superior performance, the electrical connections to the cavity are more complex at those scales. Ideally, all driving fins of the RFT are connected alternately to one of the two electrical phases, as sketched for the mechanical phases (marked by + and -) and electrical phases (drive-plus and drive-minus) in Figures 2.9(a) and 2.9(c). Connecting the fins in this manner gives the smallest possible unit cell, containing only two adjacent fins, and thus yields the highest performance as all of the fins are actuated. Analogously the sense unit cell at the centre of the cavity also consists of two differentially

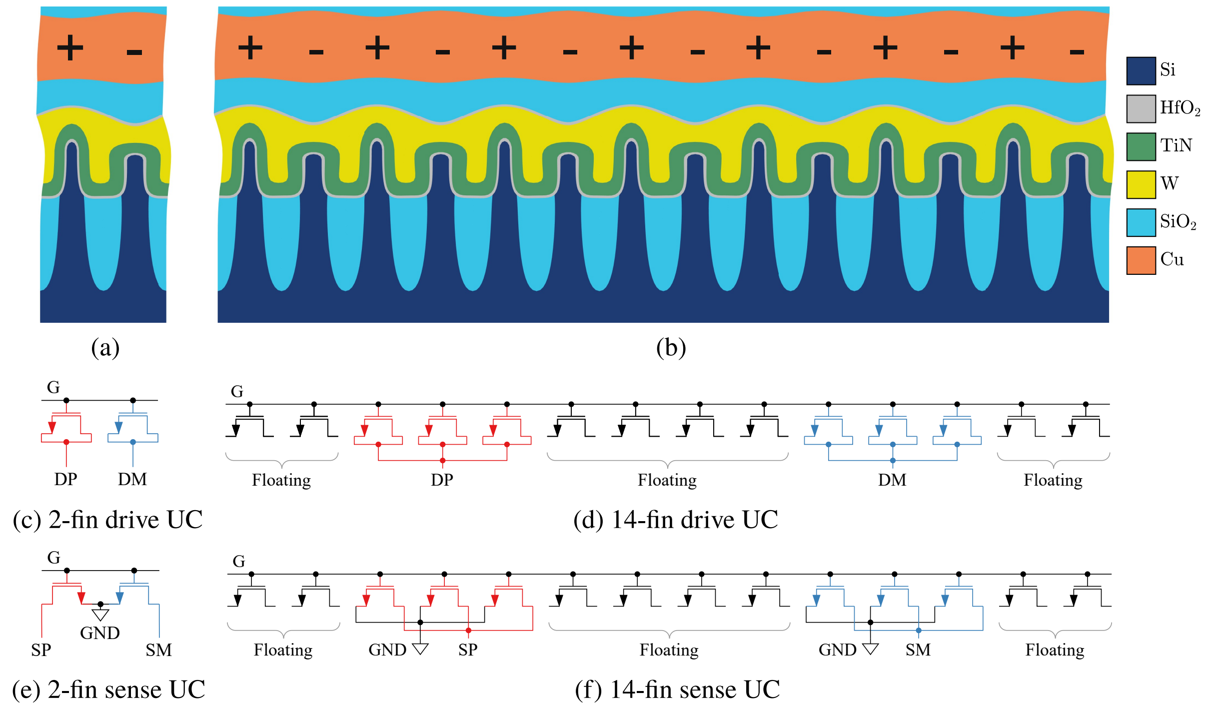

Figure 2.9: (a) Cross-section of the idealised 2-fin unit cell (UC) with the respective (c) drive and (e) sense wiring. (b) Fabricated 14-fin unit cell (UC) with triple fin contacts and intermediate floating fins with the respective (d) drive and (f) sense wiring. The fin deformation sketched in (a) and (b) represents the mechanical RFT mode which is not to scale and + and - denote the mechanical phase of each fin. The connections are marked as: drive-plus (DP), drive-minus (DM), sense-plus (SP), sense-minus (SM), ground (GND) and gate (G).

wired fins, as shown in Figure 2.9(e). However, this type of single fin contact is prohibited in all major foundry FinFET technologies by the design rule check which ensures a yield and reliability-oriented device layout in the FEOL, which is prohibitive for the best RFT integration.

To bypass this design rule check limitation, a different connection scheme is required [Bahr et al. 2018]. Rather than connecting adjacent fins to separate phases, fin groups of three are jointly connected to the same potential. Each group is separated by four electrically floating fins to the neighbouring groups to account for the minimum contact spacing requirements, which is shown in Figure 2.10. This cavity layout is the tightest possible integration in a productive foundry setting that allows sufficient driving of the RFT mode by using the seventh spatial harmonic of the cavity [Bahr et al. 2018]. Hence the size of the unit cell is increased to 14 fins as sketched in Figures 2.9(b), 2.9(d) and 2.9(f) for the mechanical phase (marked by + and -) and electrical drive and sense unit cells, respectively. This scheme is expected to reduce the performance compared to the 2-fin integration, as within each three-fin contact, only two fins match the phase from a mechanical point of view. The mechanical phase of the third fin is the opposite of the electrical phase, and thus impedes a stronger actuation. The same concept applies to the sensing unit where two fins are in phase and one fin is out of phase. Hence two fins within each contact group cancel one another, resulting in only two active fins within each 14-fin unit cell. Nevertheless, the reduction in drive and sense efficiency appears to be inconsequential,

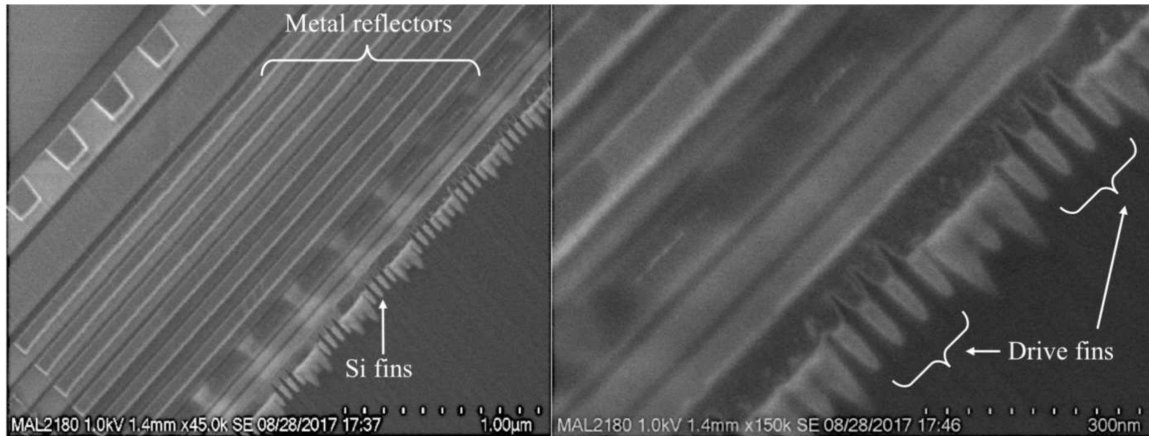

Figure 2.10: Scanning electron microscope image of the RFT in the contact region showing the BEOL phononic crystal and 14-fin unit cell configuration RFT. (Reprinted from [Bahr et al. 2018].)

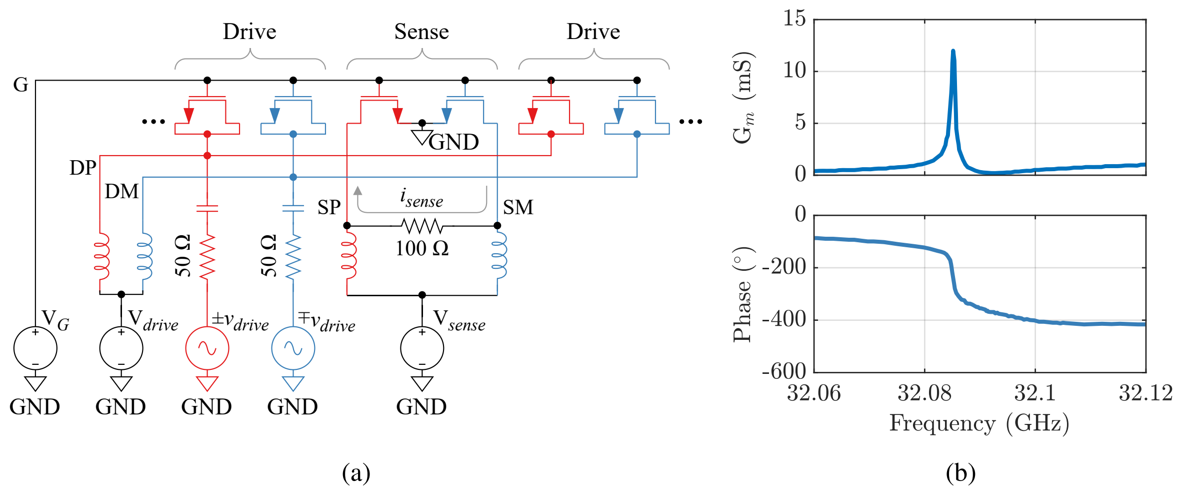

Figure 2.11: (a) Schematic of the differential RFT wiring. The connections are marked as: drive-plus (DP), drive-minus (DM), sense-plus (SP), sense-minus (SM), ground (GND) and gate (G). (Adapted from [Bahr et al. 2018; Weinstein 2018].) (b) Measured mechanical transconductance and phase of the RFT. (Adapted from [Bahr et al. 2018].)

given the reported performance metric of the device [Bahr et al. 2018].

The respective circuit to drive and sense the RFT is sketched in Figure 2.11(a). Note that different variations of this circuit are found in the literature, which share some of the same authors, however, with contradictory designs of the sense unit mechanics [Weinstein 2018; Bahr et al. 2018; Srivastava et al. 2021; Bahr 2016]. The depicted variant is based on the most plausible description of an active FET based sensing approach, although the authors often times switch between active and capacitive sensing approaches without justification.

To drive and sense the mechanical mode the common gate is biased at a constant voltage of $V_G = 0.8\,\mathrm{V}$. In order to detect a modulation of the carrier mobility and consequently the sense current, the sense transistors are supplied with a source bias of $V_{sense} = 200\,\mathrm{mV}$. This results in a current of $I_{sense} = 118\,\mu\mathrm{A}$ within the transistors without going into saturation. Upon the mechanical deformation of the sense FinFETs, the carrier mobility, and thus the current is

modulated [Bahr et al. 2018; Thompson et al. 2004; Ma et al. 2013]. Since opposing signs of stress lead to either an increase or a reduction of the carrier mobility, a sense current i_{sense}, modulated at the frequency of the mechanical eigenmode, is measured.

The remaining FinFETs are responsible for driving the mechanical eigenmode. They are therefore connected as individual MOS capacitors, which is achieved by shorting the source and the drain together. All driving MOS capacitors are biased at a constant voltage of $V_{drive} = 40\,\text{mV}$, leading to small initial stress in the structure. It causes a small deformation of the drive fins through the electrostatic force between the gate and the FinFET channels. The differential eigenmode is then actuated with a drive power of $v_{drive} = -20\,\text{dBm}$, which causes a displacement from the equilibrium position. If the frequency of the electrical actuation and the eigenmode coincide, the deformation amplitude within the fins grows and applies an approximately 40 MPa stress orthogonal to the channel direction within the sense FinFETs [Bahr et al. 2018]. The resulting mechanical eigenmode propagates through the cavity to the sense transistors resulting in an increased modulation of the output current due to the stress dependency of the carrier mobility [Bahr et al. 2018]. The resulting measured and de-embedded mechanical transconductance (2.2.3) is plotted in Figure 2.11(b). It features a well defined and clean resonance with a peak transconductance of 14 mS [Bahr et al. 2018].

Although a further publication concerning a theoretical implementation of the RFT exists the working principle is contradictory to the original publication [Srivastava et al. 2021]. Given the originally exceptional performance and claimed broad application range, the lack of a replication of the original results and missing reports of a successful circuit implementation are dubious.

Consequently, to confirm the high figures of merit and potentially unlock the full capabilities of the RFT, the functionality and behaviour of the RFT must be further investigated. To fully assess the potential of the RFT, 3D FEM modelling of the mechanics in the FEOL and BEOL is required to cover the mechanical anisotropic behaviour of silicon and its impact on the mobility variation [Hager et al. 2021; Hudeczek et al. 2022]. Further, the performance of the phononic crystal mirror, especially in the absence of lateral patterning and the presence of strongly anisotropic mechanical materials such as copper, can have a potentially detrimental effect on the Q-factor [Hudeczek and Baumgartner 2020]. Here, an assessment of the RFT in the context of an oscillatory circuit for IC applications is essential [Hager et al. 2021; Hudeczek et al. 2022]. In the context of manufacturability, the transfer to a comparable FinFET technology node and subsequent characterisation is required to confirm the reported data by Bahr et al. [Bahr et al. 2018; Hudeczek et al. 2021].

3

Linear Elastic Solid Mechanics in Anisotropic CMOS Materials

Contents

3.1 Hooke's Law 23
3.2 Voigt's Notation 26
3.3 Common Elastic Properties 27
3.4 Crystallographic Reference Frame 28
3.5 Tensor Basis Transformation 29
3.6 Isotropic Cubic Materials 30
3.7 Anisotropic Cubic Materials 32
3.7.1 Young's Modulus 33
3.7.2 Poisson's Ratio 34
3.7.3 Shear Modulus 37
3.7.4 Elastic Wave Velocities 39

To enable the modelling of the resonant fin transistor (RFT) using the finite-element method (FEM) the fundamental mechanical properties of anisotropic cubic materials deployed in the complementary metal-oxide-semiconductor (CMOS) process are introduced. The RFT's mechanical response is mainly described by Young's and the shear modulus, Poisson's ratio and the wave-carrying properties of the involved materials.

3.1 Hooke's Law

Hooke's law describes the deformation of a material subjected to an external force. This force is directly proportional to the displacement from the equilibrium position for small displacements. In that sense, the response of a material is described by the linear constitutive stress-strain

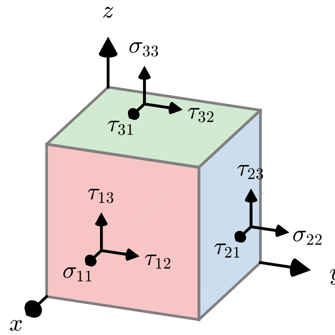

Figure 3.1: Components of the Cauchy stress tensor in 3D. Principal stresses are indicated by σ_{ii} and shear stresses by τ_{ij}. (Adapted from [Roesler 2007].)

relation[1]

$$\sigma_{ij} = C_{ijkl}\varepsilon_{kl}, \quad i,j,k,l = 1,2,3 \tag{3.1.1}$$

where the second-order stress $[\sigma]$ and strain $[\varepsilon]$ tensors relate via the fourth-order elasticity tensor $[C]$. To calculate the strains from given a stress, the inverse of Hooke's law

$$\varepsilon_{ij} = S_{ijkl}\sigma_{kl} \tag{3.1.2}$$

can be used, which links stress to strain via the compliance tensor $[S] = [C]^{-1}$ [Nye 1985; Vannucci 2018; Roesler 2007; Kaselow 2004; Wortman and Evans 1965].

The stress within a material depends on the loaded area and the applied force. For a force F acting on a surface A, normal stress is denoted by

$$\sigma = \frac{F_\perp}{A} \tag{3.1.3}$$

and

$$\tau = \frac{F_\parallel}{A} \tag{3.1.4}$$

signifies shear stress. For an infinitesimal small material element in three dimensions, as sketched in Figure 3.1, the general nomenclature

$$\sigma_{ij} = \frac{F_j}{A_i}, \quad i,j = 1,2,3 \tag{3.1.5}$$

is used, where the first index indicates the normal vector of the surface and the second index represents the direction of the force. Following the so-called classical continuum, an infinitesimal element cannot transfer moments leading to a symmetric stress tensor where $\sigma_{ij} = \sigma_{ji}$ [Roesler 2007; Vannucci 2018]. The resulting six independent components are thus

[1] The Einstein notation is used when an index appears more than once [Einstein 1916]. It implies summation over all possible index values, in which case the summation symbol is dropped from the equation: $\sigma_{ij} = \sum_{k=1}^{3}\sum_{l=1}^{3} C_{ijkl}\varepsilon_{kl} = C_{ijkl}\varepsilon_{kl}$.

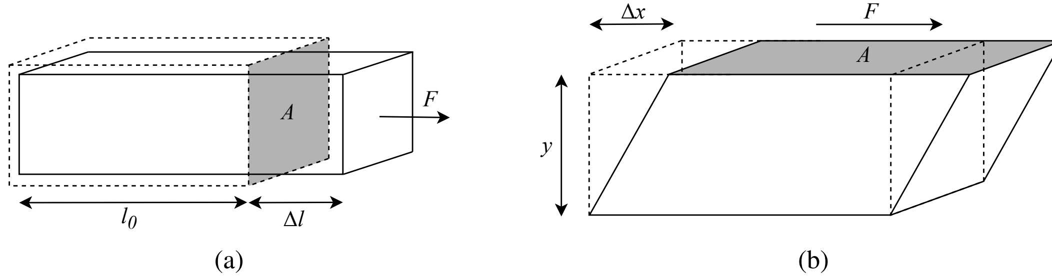

Figure 3.2: Load cases for (a) normal and (b) shear stress for a force F acting on the surface A. (Adapted from [Roesler 2007].)

written as

$$[\sigma] = \begin{bmatrix} \sigma_{11} & \tau_{12} & \tau_{13} \\ \tau_{21} & \sigma_{22} & \tau_{23} \\ \tau_{31} & \tau_{32} & \sigma_{33} \end{bmatrix} = \begin{bmatrix} \sigma_{11} & \sigma_{12} & \sigma_{13} \\ \sigma_{21} & \sigma_{22} & \sigma_{23} \\ \sigma_{31} & \sigma_{32} & \sigma_{33} \end{bmatrix} \tag{3.1.6}$$

with $\tau_{ij} = \sigma_{ij}$. Here the diagonal elements describe normal stresses, and the off-diagonal elements shear stresses.

If a component is subjected to stress, it may either be displaced rigidly or non-rigidly. Rigid-body displacements govern translations and rotations of the whole body without causing internal deformations of the component. Non-rigid deformations result in strains within the body, causing changes in lengths and angles, as sketched in Figure 3.2. Changes in lengths, known as normal strains, relate the difference in elongation Δl from the equilibrium length l_0 via

$$\varepsilon = \frac{\Delta l}{l_0}. \tag{3.1.7}$$

Analogously the shear strains describe changes in angles and are given by

$$\gamma = \frac{\Delta x}{y}, \tag{3.1.8}$$

which are caused by deformations Δx parallel to the surface, which is perpendicular to y. The general notation for arbitrary small strains within a body is

$$\varepsilon_{ij} = \frac{1}{2}\left(\frac{\partial u_i}{\partial x_j} + \frac{\partial u_j}{\partial x_i}\right), \quad i, j = 1, 2, 3 \tag{3.1.9}$$

where u_i denotes a small displacement and x_i the three principal axes, respectively. This notation assumes $\varepsilon_{ij} = \gamma_{ij}/2$, which ensures the symmetry of the stress tensor $\varepsilon_{ij} = \varepsilon_{ji}$ and correct transformational behaviour. The stress tensor is thus written as

$$[\varepsilon] = \begin{bmatrix} \varepsilon_{11} & \gamma_{12}/2 & \gamma_{13}/2 \\ \gamma_{21}/2 & \varepsilon_{22} & \gamma_{23}/2 \\ \gamma_{31}/2 & \gamma_{32}/2 & \varepsilon_{33} \end{bmatrix} = \begin{bmatrix} \varepsilon_{11} & \varepsilon_{12} & \varepsilon_{13} \\ \varepsilon_{21} & \varepsilon_{22} & \varepsilon_{23} \\ \varepsilon_{31} & \varepsilon_{32} & \varepsilon_{33} \end{bmatrix} \tag{3.1.10}$$

which also has a total of six independent components.

The stiffness tensor $[C]$, which describes all linear elastic relations between stress and strain of material, has $3^4 = 81$ components. Due to the symmetric behaviour of both $[\sigma]$ and $[\varepsilon]$, the elastic modulus fulfils the relations

$$C_{ijkl} = C_{jikl} = C_{ijlk} = C_{klij}, \quad i, j, k, l = 1, 2, 3 \tag{3.1.11}$$

which reduces the 81 components to a maximum of 21 independent magnitudes by minor symmetry operations [Roesler 2007; Vannucci 2018].

3.2 Voigt's Notation

Due to the cumbersome handling of higher-order tensors and their respective visualisation, Voigt's notation can be used to simplify the tensor notation. It introduces a mapping relation for the matrix indices

$$11 \rightarrow 1,\ 22 \rightarrow 2,\ 33 \rightarrow 3,\ 23 \rightarrow 4,\ 13 \rightarrow 5,\ 12 \rightarrow 6 \tag{3.2.1}$$

which collapses any pair of tensor indices into a single index such as $\sigma_{ij} \rightarrow \sigma_\alpha$, $\varepsilon_{ij} \rightarrow \varepsilon_\alpha$ and $C_{ijkl} \rightarrow C_{\alpha\beta}$ [Roesler 2007; Zhang et al. 2014; Wortman and Evans 1965; Vannucci 2018]. Consequently, a second-order tensor takes the form of a column vector and a fourth-order tensor of a quadratic matrix.

Using Voigt's notation, the second-order stress and strain tensors are rewritten as [Wortman and Evans 1965; Vannucci 2018]

$$[\sigma_\alpha] = [\sigma_{11}\ \sigma_{22}\ \sigma_{33}\ \tau_{23}\ \tau_{13}\ \tau_{12}]^T \quad \text{and} \quad [\varepsilon_\alpha] = [\varepsilon_{11}\ \varepsilon_{22}\ \varepsilon_{33}\ \gamma_{23}\ \gamma_{13}\ \gamma_{12}]^T\ . \tag{3.2.2}$$

The prefactor of this notation for the strain components γ_{ij} is required to satisfy the stress-energy density relation

$$F = \frac{1}{2}\sigma_{ij}\varepsilon_{ij}, \quad i, j = 1, 2, 3 \tag{3.2.3}$$

arising from the symmetric stress and strain properties in Hooke's law [Roesler 2007; Vannucci 2018].

Therefore, Hooke's law is simplified to the well-established matrix form

$$\begin{bmatrix} \sigma_1 \\ \sigma_2 \\ \sigma_3 \\ \tau_4 \\ \tau_5 \\ \tau_6 \end{bmatrix} = \begin{bmatrix} c_{11} & c_{12} & c_{13} & c_{14} & c_{15} & c_{16} \\ & c_{22} & c_{23} & c_{24} & c_{25} & c_{26} \\ & & c_{33} & c_{34} & c_{35} & c_{36} \\ & & & c_{44} & c_{45} & c_{46} \\ & sym & & & c_{55} & c_{56} \\ & & & & & c_{66} \end{bmatrix} \begin{bmatrix} \varepsilon_1 \\ \varepsilon_2 \\ \varepsilon_3 \\ \gamma_4 \\ \gamma_5 \\ \gamma_6 \end{bmatrix} \tag{3.2.4}$$

with its respective inverse

$$\begin{bmatrix} \varepsilon_1 \\ \varepsilon_2 \\ \varepsilon_3 \\ \gamma_4 \\ \gamma_5 \\ \gamma_6 \end{bmatrix} = \begin{bmatrix} s_{11} & s_{12} & s_{13} & s_{14} & s_{15} & s_{16} \\ & s_{22} & s_{23} & s_{24} & s_{25} & s_{26} \\ & & s_{33} & s_{34} & s_{35} & s_{36} \\ & & & s_{44} & s_{45} & s_{46} \\ & sym & & & s_{55} & s_{56} \\ & & & & & s_{66} \end{bmatrix} \begin{bmatrix} \sigma_1 \\ \sigma_2 \\ \sigma_3 \\ \tau_4 \\ \tau_5 \\ \tau_6 \end{bmatrix} \tag{3.2.5}$$

where the stress, strain, stiffness and compliance matrices are represented using Voigt's notation. To ensure the conservation of the stress-energy density (3.2.3), prefactors must be added to the components of the compliance matrix as [Turley and Sines 1971; Vannucci 2018; Brannon 2018; Nye 1985]:

$$s_{\alpha\beta} = \begin{cases} S_{ijkl}, & \text{if both } \alpha \text{ and } \beta \text{ are } 1, 2 \text{ or } 3 \\ 2S_{ijkl}, & \text{if either } \alpha \text{ or } \beta \text{ are } 4, 5 \text{ or } 6 \\ 4S_{ijkl}, & \text{if both } \alpha \text{ and } \beta \text{ are } 4, 5 \text{ or } 6. \end{cases} \tag{3.2.6}$$

A different convention, which does not rely on additional prefactors in the compliance matrix, is Kelvin-Mandel's notation [Dellinger et al. 1998]. It applies the same prefactor of $\sqrt{2}$ to both shear stress and shear strain components which allows the specific prefactors of the compliance matrix to be omitted. Consequently, the compliance and stiffness tensors transform identically. Whereas this notation enables the use of vector algebra conventions, it is strictly prohibited in Voigt's notation. However, Voigt's notation and the engineering convention are well established in the literature and commercially available software and are thus used in this work.

3.3 Common Elastic Properties

Following the definitions of stress and strain, Hooke's law takes the simple form

$$\sigma = E\varepsilon \tag{3.3.1}$$

for small displacements, where E is the so-called Young's modulus. It quantifies the stiffness of a material in a particular direction. For the generalised case, it is found from

$$E_\alpha = \frac{\sigma_\alpha}{\varepsilon_\alpha} = \frac{1}{s_{\alpha\alpha}}, \quad \alpha = 1,2,3 \tag{3.3.2}$$

which relates normal strains to normal stresses in a material.

The orthogonal directions of a body will either contract or expand if it is strained uniaxially. Poisson's ratio

$$\nu = -\frac{\varepsilon_{tran}}{\varepsilon} \tag{3.3.3}$$

quantifies this phenomenon which relates the strains of two orthogonal directions ε and ε_{tran}. In the generalised form, it is obtained by

$$\nu_{\alpha\beta} = -\frac{\varepsilon_\beta}{\varepsilon_\alpha} = -\frac{s_{\beta\alpha}}{s_{\alpha\alpha}} = -\frac{s_{\alpha\beta}}{s_{\alpha\alpha}}, \quad \alpha \neq \beta, \quad \alpha,\beta = 1,2,3 \tag{3.3.4}$$

where importantly the relation $\nu_{\alpha\beta} \neq \nu_{\beta\alpha}$ holds [Wortman and Evans 1965; Brantley 1973; Ting and Chen 2005; Vannucci 2018; Turley and Sines 1971]. Poisson's ratio obtains scalar values in the range $-1.0 < \nu_{\alpha\beta} < 0.5$, where an incompressible material will have a constant volume with $\nu = 0.5$. Auxetic materials, a material class with special mechanical properties, may have negative values, and thus exhibit counter-intuitive behaviour. If an auxetic material is subjected to an external load, the transversal directions expand, whereas in a material with a positive Poisson's ratio transversal contraction occurs [Vannucci 2018; Yu et al. 2017].

If material is subjected to pure shear forces, Hooke's equation takes the form

$$G = \frac{\gamma}{\tau} \tag{3.3.5}$$

where G is the shear modulus which describes the shear stiffness of a material. In the general form, it is found via

$$G_\alpha = \frac{\sigma_\alpha}{\varepsilon_\alpha} = \frac{1}{s_{\alpha\alpha}}, \quad \alpha = 4,5,6 \tag{3.3.6}$$

which links shear stresses and shear strains [Roesler 2007; Wortman and Evans 1965].

3.4 Crystallographic Reference Frame

To describe arbitrary orthonormal cubic crystal bases and their relative rotation to the principal crystal axes [100], [010] and [001], a geometric reference frame is required. Here Miller's convention defines directions and planes in a crystallographic system that can be used to describe material properties. Square brackets $[hkl]$ describe a specific direction in crystal space. Angled brackets $\langle hkl \rangle$ denote a family of directions which are covered by the material symmetries, such as $\langle 100 \rangle := [100], [010], [001], [\bar{1}00], [0\bar{1}0], [00\bar{1}]$ where $\bar{1} = -1$. Round brackets (hkl) indicate a specific crystal plane and braces $\{hkl\}$ describe the corresponding family of planes

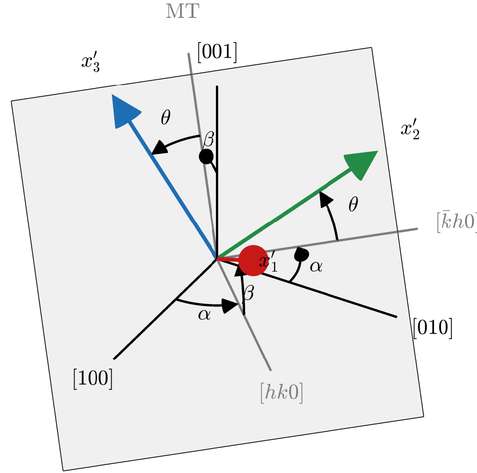

Figure 3.3: Definition of the reference frame convention proposed in [Turley and Sines 1971].

such as {100} := (100), (010), (001), $(\bar{1}00)$, $(0\bar{1}0)$, $(00\bar{1})$. In cubic crystals, $[hkl]$ is the normal direction to its corresponding plane (hkl), which may not be generalised to other material classes [Vannucci 2018; Roesler 2007].

As proposed by J. Turley and G. Sines, one reference frame notation is based on the Eulerian angles α, β and θ [Turley and Sines 1971; Healy et al. 2020]. They define a new reference frame concerning the principal crystal axes as sketched in Figure 3.3. The new orthonormal frame, indicated by the primed basis vectors $x_1' = [hkl]$, x_2' and x_3' is created by a counter-clockwise yaw α of the new frame around [001], followed by a subsequent pitch β around the zone axis $[\bar{k}h0]$. Furthermore, the meridional tangent (MT) is given by the direction of x_3' after the pitch is executed. Lastly, the counter-clockwise roll θ of x_2' and x_3' around x_1' in the (hkl) plane is measured from the zone axis $[\bar{k}h0]$ or the meridional tangent (MT).

A major benefit of this construction lies in its simplicity to describe orientations of crystallographic frames and the fact that all reference frames with a common yaw α share the same zone axis, favouring elastic properties comparisons in various crystal planes [Turley and Sines 1971; Healy et al. 2020]. Using the Miller indices of the plane normal direction x_1', each coordinate frame is constructed by deriving α and β from the plane normal direction $[hkl]$. The subsequent counter-clockwise rotation θ of the basis is signified as $(hkl)^\theta$ for the remainder of this work. In the particular case $\theta = 0°$, the superscript is omitted [Turley and Sines 1971].

3.5 Tensor Basis Transformation

A major drawback of the matrix representation in Voigt's notation is the impracticability of basis transformations due to the additional prefactors [Roesler 2007]. To circumvent this problem transformations are carried out in tensor notation. Here a fourth-order tensor $[T]$ can be

transformed into a new basis by using the general equation for tensor basis transformations

$$T'_{ijkl} = a_{im}a_{jn}a_{kp}a_{lq}T_{mnpq}, \quad i,j,k,l,m,n,p,q = 1,2,3 \tag{3.5.1}$$

where a_{im} is the direction cosine between the ith and mth axis of the primed (new) and non-primed (old) coordinate system [Turley and Sines 1971; Thomas 1966; Knowles and Howie 2014; Mainprice and Casey 1990]. Analogously, a second-order tensor $[t]$ is transformed via

$$t'_{ij} = a_{ik}a_{jl}t_{kl}, \quad i,j,k,l = 1,2,3. \tag{3.5.2}$$

Although specific transformation matrices exist for Voigt's notation, they have to be assembled individually for each property of Hooke's law, which follows from the used prefactors in (3.2.6) [Zienkiewicz et al. 2013; Bao and Huang 2003]. Hence, when applying Voigt's notation, subsequent basis transformations are carried out using the respective tensor rotations given in (3.5.1) and (3.5.2) [Roesler 2007; Vannucci 2018].

3.6 Isotropic Cubic Materials

In the special case of isotropic elastic materials, all components of the stiffness tensor are invariant under arbitrary rotations [Roesler 2007; Vannucci 2018; Healy et al. 2020]. One example of a CMOS-compatible material with almost isotropic properties is tungsten, which is used both for vias and gate material [Roesler 2007; Gambino 2012]. By imposing additional rotational conditions, the remaining 21 components of the stiffness tensor are reduced to three quantities, and the compliance matrix takes the simple form

$$[c] = \begin{bmatrix} c_{11} & c_{12} & c_{12} & & & \\ c_{12} & c_{11} & c_{12} & & & \\ c_{12} & c_{12} & c_{11} & & & \\ & & & c_{44} & & \\ & & & & c_{44} & \\ & & & & & c_{44} \end{bmatrix} \tag{3.6.1}$$

where the shear component follows from

$$c_{44} = \frac{c_{11} - c_{12}}{2}. \tag{3.6.2}$$

As all other components vanish, only two independent quantities c_{11} and c_{12} remain [Roesler 2007; Vannucci 2018]. The same applies to the inverse $[s] = [c]^{-1}$, taking a similar

form

$$[s] = \begin{bmatrix} s_{11} & s_{12} & s_{12} & & & \\ s_{12} & s_{11} & s_{12} & & & \\ s_{12} & s_{12} & s_{11} & & & \\ & & & s_{44} & & \\ & & & & s_{44} & \\ & & & & & s_{44} \end{bmatrix} \tag{3.6.3}$$

with $s_{44} = 2(s_{11} - s_{12})$ and the unique quantities s_{11} and s_{12}. Both matrices may be divided into four 3×3 sub-matrices, each describing a different effect: The upper right and lower left sub-matrix relate shear stresses to normal strains. However, as all components vanish, there is no coupling in-between those in isotropic materials. The lower right sub-matrix relates shear stresses and shear strains. Considering the diagonal appearance, only components of the same direction couple. The remaining sub-matrix in the upper left governs the relations between normal strains and normal stresses. As it is fully occupied, normal stresses cause both transversal and longitudinal strains [Roesler 2007; Vannucci 2018].

Returning to the definition of isotropic material properties, Young's modulus (3.3.2) is thus given by

$$E = \frac{1}{s_{11}}. \tag{3.6.4}$$

Poisson's ratio (3.3.4) may be obtained via

$$\nu = -\frac{s_{12}}{s_{11}} \tag{3.6.5}$$

and the shear modulus is given by

$$G = \frac{1}{s_{44}}, \tag{3.6.6}$$

which are all constant in an isotropic material. Young's and the shear modulus are required to describe the propagation of elastic waves through continuous isotropic media. Generally, an isotropic bulk material supports a longitudinal wave, also known as a pressure wave, in any direction. Its speed of propagation is given by the relation

$$c_l = \sqrt{\frac{E}{\rho}}, \tag{3.6.7}$$

which depends exclusively on Young's modulus and material density ρ. Note that this wave is pseudo-polarised along its propagation direction [Rosenbaum 1988; Kaselow 2004; Gross and Seelig 2018]. Two transversal waves accompany it, also referred to as shear waves. Their respective wave speed is obtained via

$$c_t = \sqrt{\frac{G}{\rho}} \tag{3.6.8}$$

Table 3.1: Anisotropy factor A, elastic constants c_{11}, c_{12} and c_{44} and density ρ for selected CMOS materials.

Material		A	c_{11} (GPa)	c_{12} (GPa)	c_{44} (GPa)	ρ (kg m^{-3})
Cu	[a]	3.22	168.0	121.0	75.0	8960
Si	[b, c, a]	1.57	165.7	63.9	79.6	2330
Al	[a]	1.23	108.0	61.0	29.0	2700
W	[a, d]	1.01	523.3	204.5	161.7	19 280
SiCO:H	[e]	1.00	6.6	2.5	2.1	1100
SiO_2	[f, g]	1.00	78.5	16.0	31.2	2200
HfO_2	[e, g]	1.00	278.0	156.9	61.0	9800
TiN	[e]	1.00	227.5	97.5	65.0	4300

[a] [Roesler 2007] [b] [Wortman and Evans 1965] [c] [Dismukes et al. 1964]
[d] [Featherston and Neighbours 1963] [e] [Zizka et al. 2016] [f] [Tomar et al. 2003] [g] [Robertson 2005]

which considers the shear stiffness of the material and density [Rosenbaum 1988; Kaselow 2004; Gross and Seelig 2018]. Their polarisation directions are orthogonal to one another while also being orthogonal to the direction of propagation. As all mechanical properties are invariant with crystallographic orientation, the wave speeds are also independent of the direction.

3.7 Anisotropic Cubic Materials

Numerous materials used in the CMOS process, for example, silicon and copper, crystallise into a cubic lattice. As a consequence, the mechanical properties vary spatially and are thus anisotropic. The cubic crystal lattices possess rotational symmetries of 90° multiples around the $\langle 100 \rangle$ axes. Moreover, additional rotational symmetries of 180° and 120° multiples exist for the $\langle 110 \rangle$ and $\langle 111 \rangle$ axes, respectively. As the elasticity tensor must be invariant with the added symmetry constraints, (3.6.2) is no longer valid since

$$c_{44} \neq \frac{c_{11} - c_{12}}{2}. \tag{3.7.1}$$

The elasticity tensor and compliance tensor thus maintain the form given in (3.6.1) and (3.6.3), however, now with three independent components c_{11}, c_{12} and c_{44} and s_{11}, s_{12} and s_{44}. The anisotropy factor

$$A = \frac{2(s_{11} - s_{12})}{s_{44}} \tag{3.7.2}$$

quantifies the mechanical difference between an isotropic and an anisotropic material, where $A = 1$ indicates isotropy and $A > 1$ anisotropy [Roesler 2007; Vannucci 2018].

The mechanical properties of selected CMOS materials, both isotropic and anisotropic, are listed in Table 3.1. Elemental copper, for example, which is used as interconnect in the back-end-of-line (BEOL), has the largest anisotropy factor of currently deployed CMOS materials. Also, the silicon substrate exhibits strong anisotropic behaviour, which influences the mechanical and electrical behaviour of CMOS devices in the front-end-of-line

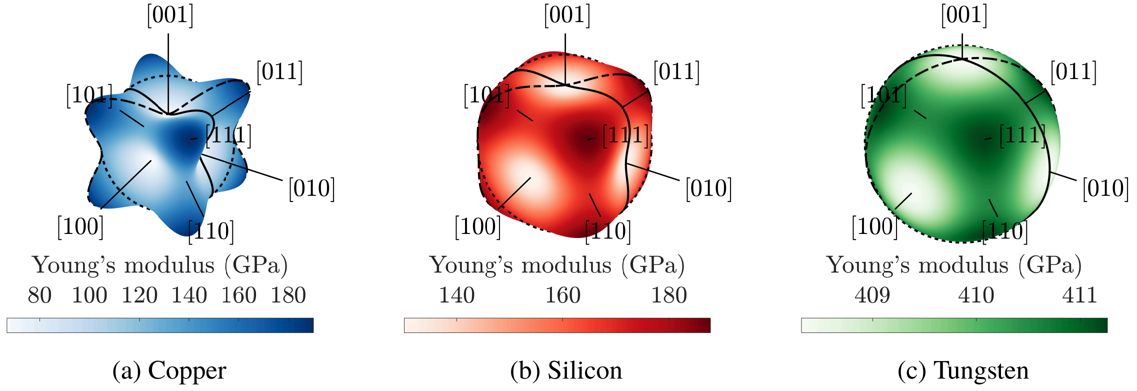

(a) Copper (b) Silicon (c) Tungsten

Figure 3.4: Young's modulus in crystal space for (a) copper, (b) silicon and (c) tungsten. The projections of (100), (110) and (111) planes are indicated by the solid, dash-dotted and dotted lines respectively.

(FEOL) [Thompson et al. 2004]. Moreover, it is a well-established material for released monolithic micro-electro-mechanical-system (MEMS) devices, like gyroscopes, accelerometers and resonators, which often exploit the anisotropic mechanical behaviour [Zhou et al. 2018; Sieberer et al. 2019; Ziaei-Moayyed et al. 2010; Wang et al. 2011]. All remaining materials used in the CMOS process are assumed to be of isotropic nature.

3.7.1 Young's Modulus

As discussed in the previous section, the material properties in anisotropic cubic materials vary with the crystallographic direction. Following the added symmetry implications on the material tensors, the inverse of Young's Modulus (3.3.2) in an arbitrary direction $[hkl]$ is found via

$$\frac{1}{E_{[hkl]}} = s'_{11} = s_{11} - (2s_{11} - 2s_{12} - s_{44})\left(\alpha^2\beta^2 + \alpha^2\gamma^2 + \beta^2\gamma^2\right) \tag{3.7.3}$$

where s'_{11} is the first component of the compliance matrix. It is transformed into a new basis with help of the direction cosines

$$\alpha = \cos([hkl],[100]), \quad \beta = \cos([hkl],[010]) \quad \text{and} \quad \gamma = \cos([hkl],[001]) \tag{3.7.4}$$

between the direction of interest $[hkl]$ and the three principal axes [100], [010] and [001] of the cubic lattice [Wortman and Evans 1965; Brantley 1973; Hopcroft et al. 2010; Zhang et al. 2014; Muramatsu and Kitamura 1993; Ting and Chen 2005; Nye 1985; Roesler 2007].

Its magnitude is shown for selected cubic CMOS materials for all directions of the unit sphere in Figure 3.4. It is obtained by sweeping the direction $[hkl]$ in (3.7.3) over the whole unit sphere. Monocrystalline copper and silicon, which are depicted in Figures 3.4(a) and 3.4(b) with $A = 3.22$ and $A = 1.57$, exhibit varying magnitudes of Young's modulus in different directions [Roesler 2007]. The unit sphere is deformed following a clear cubic symmetry. Considering the lowest-order Miller directions, Young's modulus assumes its maxima along $\langle 111 \rangle$, its minima

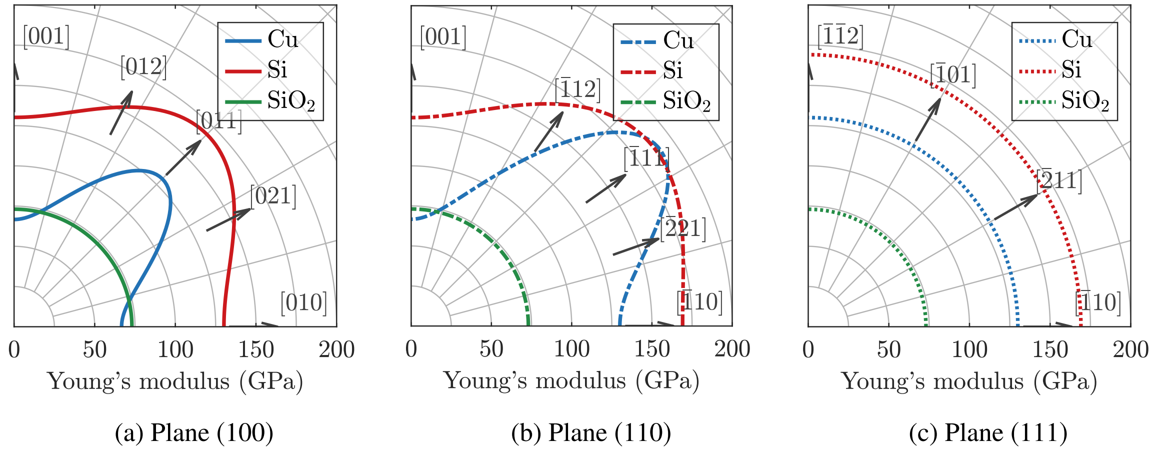

(a) Plane (100)
(b) Plane (110)
(c) Plane (111)

Figure 3.5: Projections of the Young's modulus of copper, silicon and SiO_2 in the crystal planes (a) (100), (b) (110) and (c) (111) in polar coordinates.

along $\langle 100 \rangle$ and features intermediate saddle points in the $\langle 110 \rangle$ directions. Lastly, shown for reference in Figure 3.4(c) is tungsten, an almost isotropic cubic material with $A = 1.01$. Thus Young's modulus is almost invariant with direction, and thus nearly forms a sphere in crystal space.

For several applications it is necessary to consider Young's modulus within a specific crystal plane. The projections of Young's modulus for the planes (100), (110) and (111), as indicated by the solid, dash-dotted and dotted black lines in Figure 3.4, are given in Figure 3.5. Note that the cubic symmetry makes it sufficient to visualise only one quadrant of each plane. Looking at the (100) plane in Figure 3.5(a) the minima and saddle point values are easily identified. SiO_2 is shown as an example of an isotropic material for the reason that tungsten is a very stiff material with $E = 411$ GPa making a visual comparison difficult. Furthermore, as previously mentioned, the maximum and minimum values in cubic materials of E are always found in the $\langle 111 \rangle$ and $\langle 100 \rangle$ directions, both visible in the (110) plane shown in Figure 3.5(b).

Interestingly, E is invariant in the $\{111\}$ planes, as shown by the dotted iso-contour circles in the surface plots in Figure 3.4 and their respective projections in Figure 3.5(c). This follows from the relations of the direction cosines $\alpha + \beta + \gamma = 0$ and $\alpha^2 + \beta^2 + \gamma^2 = 1$, which all directions in $\{111\}$ satisfy. This consequently leads to a constant value for $\alpha^2\beta^2 + \alpha^2\gamma^2 + \beta^2\gamma^2 = \frac{1}{4}$ in (3.3.2) [Qin et al. 2019]. This isotropic behaviour in the $\{111\}$ family of planes is beneficial for several application types of released MEMS as the lateral stiffness for a $\langle 111 \rangle$-oriented silicon wafer is constant [Wortman and Evans 1965; Qin et al. 2019; Kim et al. 2001; Brantley 1973].

3.7.2 Poisson's Ratio

Poisson's ratio was a singular value in the isotropic case, but it varies in anisotropic cubic materials. Here it strongly impacts the MEMS deformation under various crystallographic orientations, which must be considered in the modelling [Patel and McCluskey 2012;

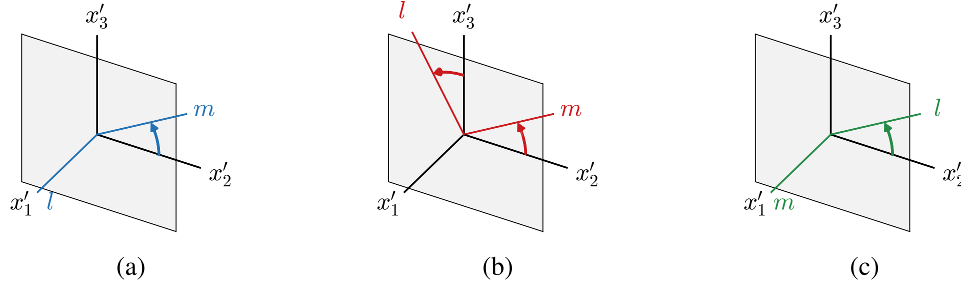

Figure 3.6: Different load scenarios for the definition of Poisson's ratio in the presence of a pull l and orthogonal observation m. For (a) out-of-plane pull and in-plane observation, (b) in-plane pull and in-plane observation and (c) in-plane pull and out-of-plane observation. The shaded grey rectangle marks the observation plane.

Hudeczek et al. 2022]. For an arbitrary plane spanned by two orthogonal basis vectors x'_2 and x'_3 with the plane normal vector x'_1, following the notation by J. Turley and G. Sines, three different load cases are sketched in Figure 3.6: In the first case, shown in Figure 3.6(a), the pull l is perpendicular out-of-plane along the plane normal x'_1, whereas the transversal m may assume any direction in-plane [Wortman and Evans 1965]. In this case, both directions are orthogonal by construction. In the second case, depicted in Figure 3.6(b), both the direction of the pull and its transversal direction are in-plane. However, the orthogonality of both vectors needs to be maintained at all times. The last case describes the opposite of the first case, with the pull being in-plane and the transverse direction out-of-plane (compare Figure 3.6(c)), which visualises the inequality present in (3.3.4). For all scenarios, Poisson's ratio in a particular crystallographic direction can be computed with

$$\nu_{[hkl]} = -\frac{s_{12} + (s_{11} - s_{12} - s_{44}/2)\left(\alpha_1^2\alpha_2^2 + \beta_1^2\beta_2^2 + \gamma_1^2\gamma_2^2\right)}{s_{11} + (2s_{11} - 2s_{12} - s_{44})\left(\alpha_1^2\beta_1^2 + \beta_1^2\gamma_1^2 + \alpha_1^2\gamma_1^2\right)} \tag{3.7.5}$$

where α_1, β_1 and γ_1 are the direction cosines for the direction of pull l and α_2, β_2 and γ_2 for the respective transversal observation direction m, as sketched in Figure 3.6.

Poisson's ratio is plotted for several selected crystal planes in Figure 3.7 [Wortman and Evans 1965; Qin et al. 2019; Healy et al. 2020; Rosenbaum 1988]. The projections are obtained by sweeping the respective load l and observation m directions in (3.7.5) in the observation plane $[hkl]$, according to the three cases show in Figure 3.6. In Figure 3.7(a), the first load case (compare Figure 3.6(a)) in (110) is plotted for a fixed load direction l along the plane normal direction and a rotating observation m in the plane. Poisson's ratio for copper and silicon varies strongly in this plane and the maxima occur at the zenith in [001] and the minima along $[\bar{1}10]$. By moving the transversal observation direction m towards the zone axis $[\bar{1}10]$, Poisson's ratio will decrease until it reaches its minimum. In the case of copper, auxetic behaviour is observed close to the zone axis, where Poisson's ratio is negative under the specified loading conditions [Huang et al. 2014]. Analogously, the load case described in Figure 3.6(b)

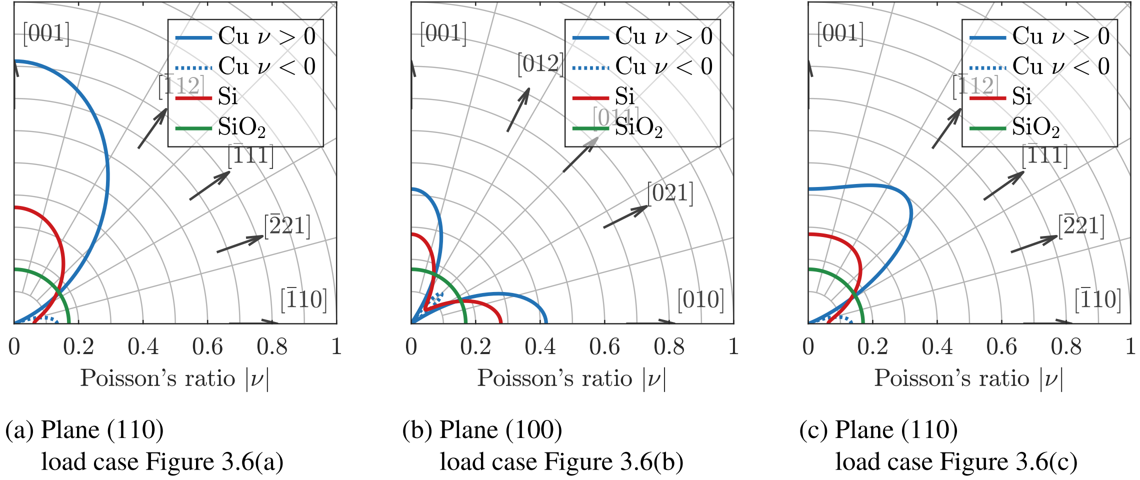

(a) Plane (110)
load case Figure 3.6(a)

(b) Plane (100)
load case Figure 3.6(b)

(c) Plane (110)
load case Figure 3.6(c)

Figure 3.7: Poisson's ratio projections in copper, silicon and SiO_2 for various load cases and crystal planes in polar coordinates.

is shown for (100) in Figure 3.7(b). In this instance both the observation m and load direction l are rotated together in the observation plane, while maintaining orthogonality between m and l. In this loading scenario, the minima are again observed in $\langle 110 \rangle$, where copper exhibits auxetic behaviour. The inequality $\nu_{ij} \neq \nu_{ji}$ is signified in Figure 3.7(c) for the third load case (compare Figure 3.6(c)) in (110), where the load and transversal directions are switched in comparison to Figure 3.7(a).

The visualisation of the isotropic behaviour of Poisson's ratio in the $\{111\}$ family of planes is omitted but can be proven analogously to Young's modulus. Since $\alpha_1^2\alpha_2^2 + \beta_1^2\beta_2^2 + \gamma_1^2\gamma_2^2 = \frac{1}{6}$, following from $\alpha_1\alpha_2 + \beta_1\beta_2 + \gamma_1\gamma_2 = 0$ in the $\{111\}$ planes, ν is invariant from the directions in this plane [Qin et al. 2019].

While this representation only allows an investigation of Poisson's ratio for a single plane at a time, obtaining the global extrema requires a different approach. To obtain the maxima and minima over the whole unit sphere the plane's normal direction of the first load case (compare Figure 3.6(a)) is swept over the whole unit sphere [Healy et al. 2020]. For each normal direction all possible in-plane observation directions are calculated from (3.7.5) and the maximum ν_{max} and minimum ν_{min} values for each plane are mapped to the respective normal direction of the plane as plotted in Figure 3.8. The surfaces in Figures 3.8(a) and 3.8(d) and Figures 3.8(b) and 3.8(e) are associated with the positive values $\nu_{max} > 0$ and $\nu_{min} > 0$ of respectively copper and silicon. Copper exhibits auxetic behaviour, as shown in Figure 3.8(c) for $\nu_{max} < 0$, for plane normal directions deviating less than 22° from $\langle 110 \rangle$. Silicon, however, has purely positive Poisson's ratios, following from a smaller anisotropy factor. Interestingly all cubic materials obtain their extremal values, minimum and maximum, in the $\{110\}$ planes. Furthermore, all materials exhibit isotropic Poisson's ratios in $\{111\}$ following from $\nu_{max} = \nu_{min}$ in those planes.

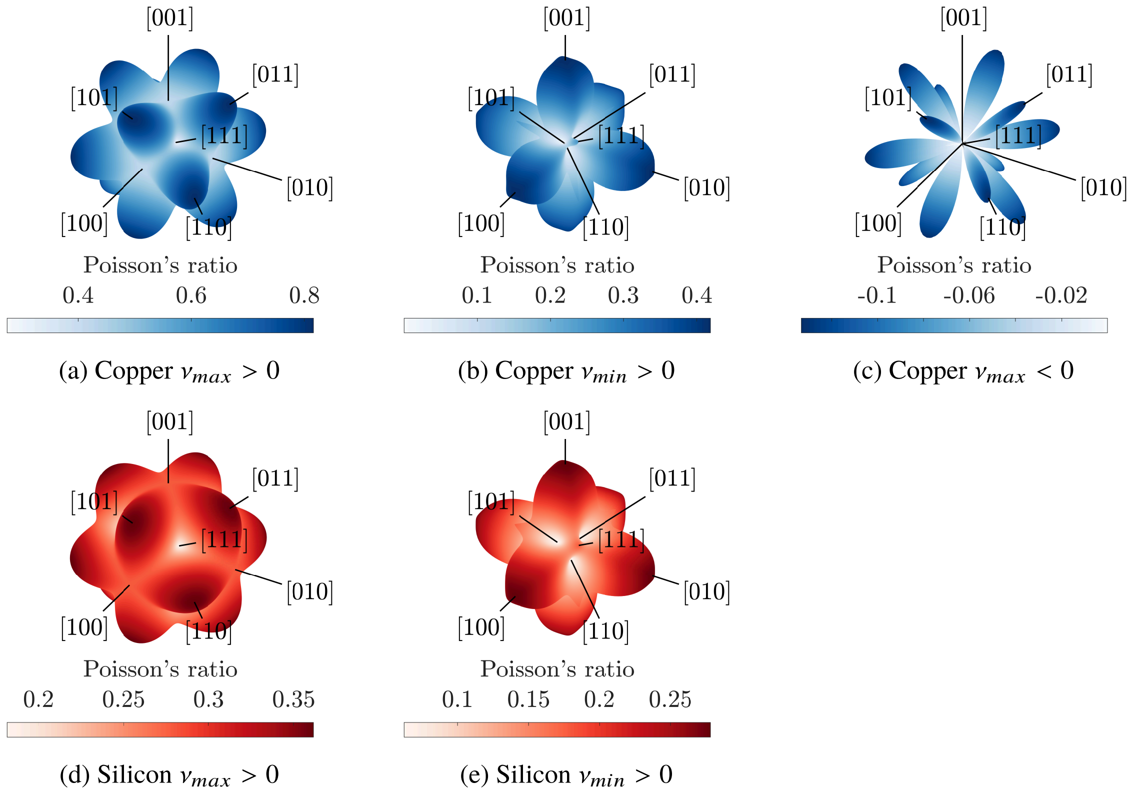

(a) Copper $\nu_{max} > 0$ (b) Copper $\nu_{min} > 0$ (c) Copper $\nu_{max} < 0$

(d) Silicon $\nu_{max} > 0$ (e) Silicon $\nu_{min} > 0$

Figure 3.8: Extremal values of Poisson's ratio in (a) to (c) copper and (d) to (e) silicon. The Miller directions indicate the plane's normal direction (x_1' in Figure 3.7) the Poisson's ratio is evaluated on.

3.7.3 Shear Modulus

The shear modulus is the last property required to describe an anisotropic cubic material. Similar to Young's modulus, the inverse of the shear modulus is given by

$$\frac{1}{G_{[hkl]}} = s_{44} + 4\left(s_{11} - s_{12} - \frac{s_{44}}{2}\right)\left(\alpha_1^2\alpha_2^2 + \beta_1^2\beta_2^2 + \gamma_1^2\gamma_2^2\right) \tag{3.7.6}$$

which depends on the respectively transformed shear compliance in a particular observation and corresponding orthogonal direction [Wortman and Evans 1965; Qin et al. 2019; Roesler 2007]. Analogous to Poisson's ratio, the shear modulus can be calculated for different crystallographic planes as shown in Figure 3.9. However, since the shear modulus is symmetric with $G_{ij} = G_{ji}$ there is no necessity to investigate the load scenario sketched in Figure 3.6(c). The shear modulus varies strongly depending on the observation plane and load scenarios. Its isotropic nature in the {111} planes is not shown but follows the same derivation as used for Poisson's ratio [Shrikanth et al. 2020].

The global extremal values of the shear modulus, as given in Figure 3.10, may be obtained by following the same procedure as outlined in Section 3.7.2 for Poisson's ratio, where the extremal values of each plane are mapped to the respective normal direction. The shear modulus reaches its maximum G_{max} in all planes associated with the plane normals rotating in {100}, which

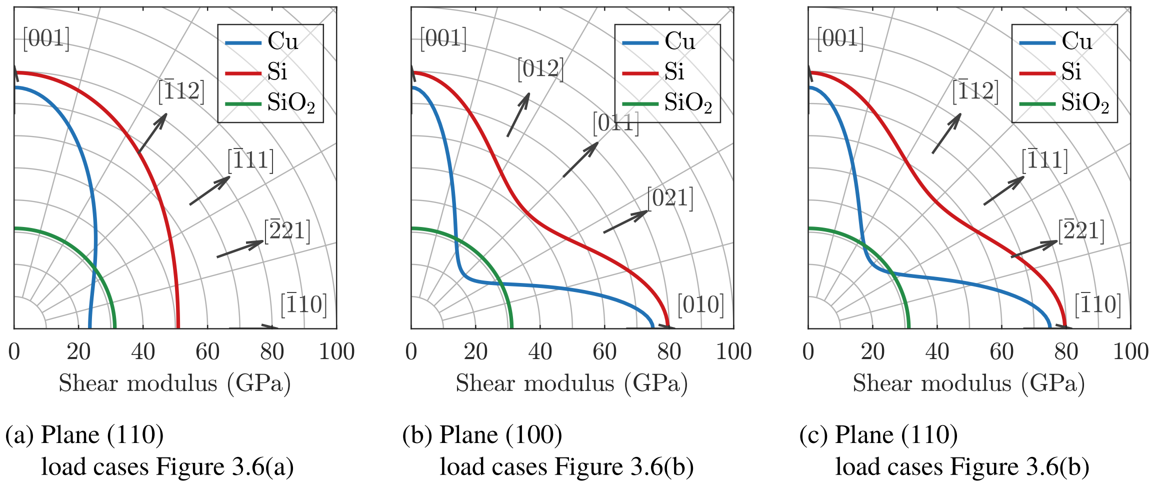

(a) Plane (110)
load cases Figure 3.6(a)

(b) Plane (100)
load cases Figure 3.6(b)

(c) Plane (110)
load cases Figure 3.6(b)

Figure 3.9: Shear modulus of copper, silicon and SiO_2 in different crystallographic planes for the load cases shown in Figure 3.6(a) and Figure 3.6(b) in polar coordinates.

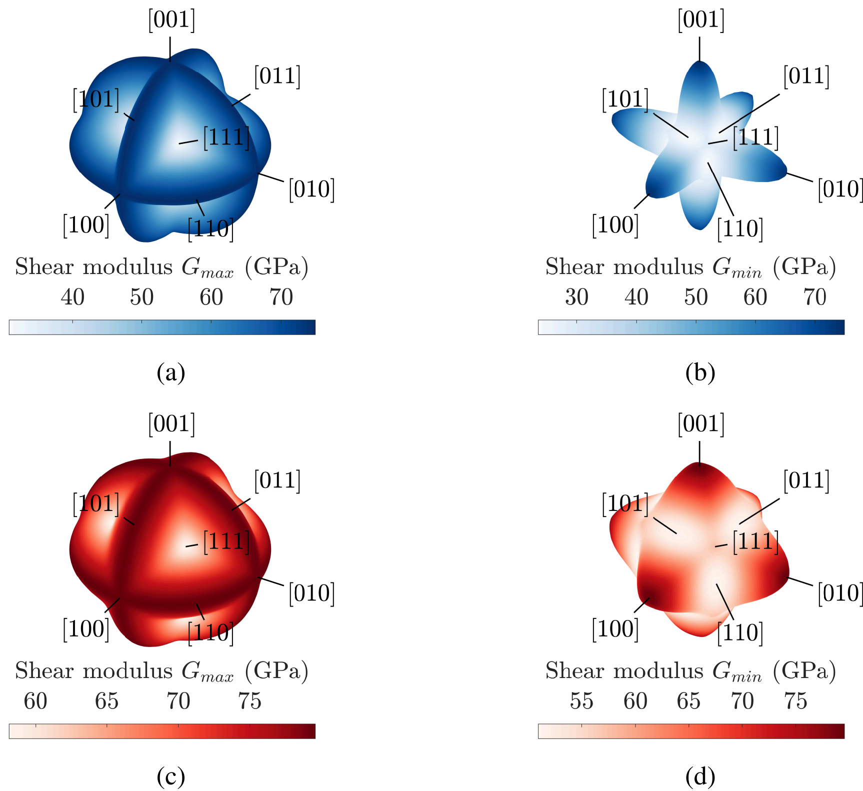

(a)

(b)

(c)

(d)

Figure 3.10: Extremal values of the shear modulus in (a) and (b) for copper and in (c) and (d) for silicon. The Miller directions indicate the normal direction $\mathbf{x}_1'$ for the planes on which the shear modulus is evaluated.

occurs for both copper and silicon, as shown in Figures 3.10(a) and 3.10(c). Furthermore, the smallest values G_{min}, as depicted in Figures 3.10(b) and 3.10(d), occur exclusively in the {110} planes. Moreover, within the {100} and {111} planes, the maximum and minimum shear moduli are identical for the first load case.

3.7.4 Elastic Wave Velocities

The elastic material properties are also required to describe mechanical wave phenomena. The Christoffel equation

$$[M_{ij} - c_p^2 \delta_{ij}] p_j = 0, \quad i,j = 1,2,3 \tag{3.7.7}$$

describes the propagation of elastic waves through an anisotropic medium where δ_{ij} is the Kronecker delta, c_p is the phase velocity and p_j are the components of the polarisation vector. The Christoffel matrix for a monochromatic wave is given by

$$M_{ij} = k_k C_{iklj} k_l, \quad i,j,k,l = 1,2,3 \tag{3.7.8}$$

where k_k are the components of the wave vector [Mainprice and Casey 1990; Mensch and Rasolofosaon 1997; Jaeken and Cottenier 2016; Healy et al. 2020; Svitek et al. 2014; Rosenbaum 1988]. The solution to this eigenvalue problem yields three eigenvalues which describe the phase velocities of the supported waves in anisotropic media. The corresponding eigenvectors denote the respective polarisation directions. They are associated with the plane pressure wave, known as P-wave or longitudinal wave, which is accompanied by two shear waves, called S1-wave and S2-wave or transversal waves, respectively. Note that the polarisation vector of the longitudinal wave points along the propagation direction, making it pseudo-polarised. The polarisation directions of the transversal waves are orthogonal to the propagation direction [Jaeken and Cottenier 2016; Ting 2006a; Mainprice and Casey 1990; Svitek et al. 2014].

Contrary to an isotropic material, which only supports shear waves at a single propagation velocity, albeit at any polarisation, an anisotropic material supports two mechanical wave velocities for the same direction of propagation. Their speeds vary for different propagation directions and are directly related to Young's and the shear modulus resulting in a similar spatial dependence (see Figure 3.4), as shown in Figure 3.11. A pressure wave inside an anisotropic cubic material, as plotted for copper and silicon in Figures 3.11(a) and 3.11(d), will thus have its largest phase velocity along $\langle 111 \rangle$ as the material's stiffness is extremal in those directions, with its lowest speed occurring along $\langle 100 \rangle$, respectively.

The propagation speed of the first shear wave plotted for copper and silicon in Figures 3.11(b) and 3.11(e) is closely related to the maximum shear stiffness G_{max}, and thus has its largest phase velocity in all directions in the $\{100\}$ planes, with the slowest velocity along $\langle 111 \rangle$. The second shear wave, on the other hand, reaches its fastest speed along the principal crystal axes $\langle 100 \rangle$ and will propagate at the slowest velocity along $\langle 110 \rangle$ as it is related to the lowest shear stiffness G_{min}, as shown in Figures 3.11(a) and 3.11(d) for copper and silicon [Ting 2006a; Jaeken and Cottenier 2016]. Thus they are also referred to as fast and slow shear waves, as one shear wave propagates faster than the other. For shear waves propagating along the principal axes where $G_{max} = G_{min}$, both shear waves propagate at the same speed [Ting 2006b; Kaselow 2004]. Moreover, shear waves propagate significantly slower than pressure waves in the same direction

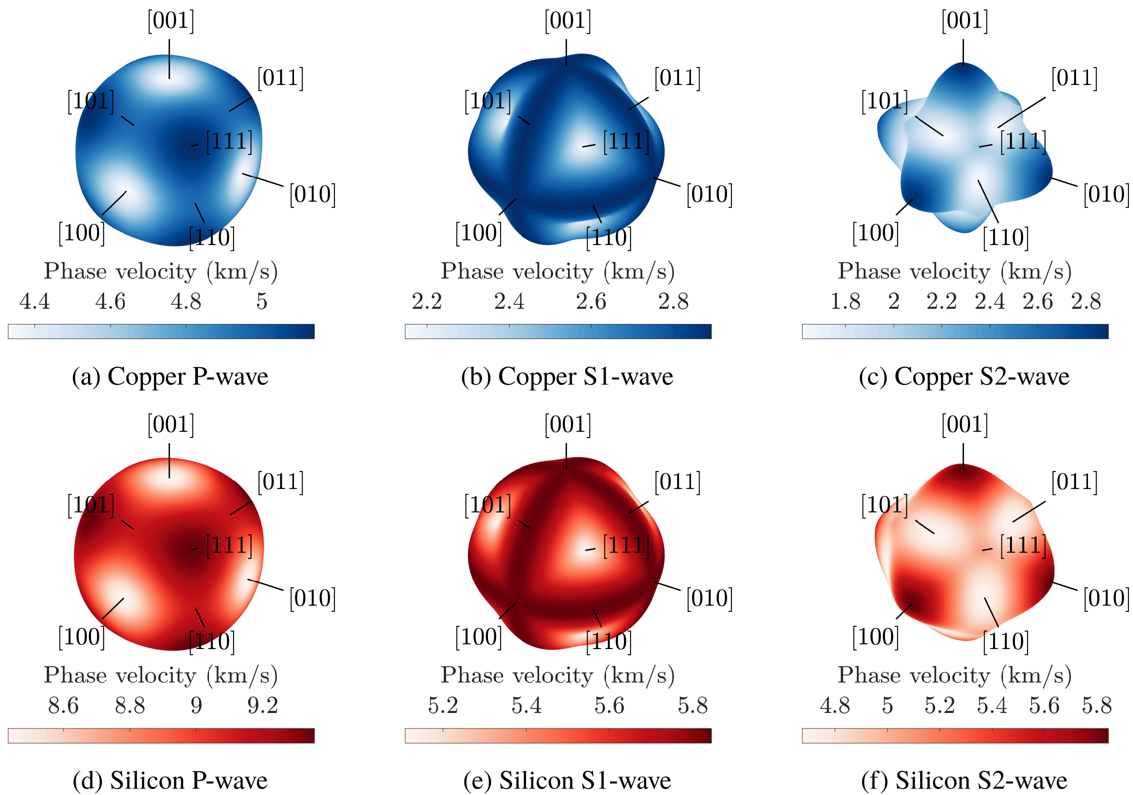

(a) Copper P-wave (b) Copper S1-wave (c) Copper S2-wave

(d) Silicon P-wave (e) Silicon S1-wave (f) Silicon S2-wave

Figure 3.11: Phase velocities pressure and shear waves in (a) to (c) for copper and in (d) to (f) Silicon.

as the material displacement is perpendicular to the direction of propagation which impedes the energy transfer [Hirose and Lonngren 2010; Graff 1975; Rosenbaum 1988; Rose 2014; Chen 2015; Svitek et al. 2014].

Summary

Hooke's law describes the fundamental properties of linear elastic materials. They are required to model the mechanical response of the RFT, which is constructed from several anisotropic mechanical materials. Therefore, the main material properties, namely Young's and the shear modulus and Poisson's ratio were introduced. Whereas in isotropic materials, all mechanical properties are invariant with the crystallographic orientation, anisotropic materials, like silicon and copper, exhibit a strongly varying response.

Following the cubic crystal symmetry, Young's modulus, which quantifies the longitudinal stiffness of a material, obtains its extremal values along $\langle 001 \rangle$ and $\langle 111 \rangle$, marking the respective minima and maxima. Furthermore, it is isotropic in the $\{111\}$ planes, which holds for all material properties of anisotropic cubic materials. In the case of pronounced anisotropic behaviour, as it occurs in copper, Poisson's ratio, which relates two orthogonal strains, may exhibit counter-intuitive auxetic behaviour for directions close to $\langle 110 \rangle$.

Analogously to Young's modulus, the shear modulus measures the shear stiffness of a material

subjected to an external shear force. Both also relate to the sound wave velocities in bulk media, which support the propagation of one longitudinal wave and two transversal waves in any direction. Here the sound velocities are linked to Young's modulus, in the case of longitudinal waves and the maximum and minimum shear modulus to the fast and slow transversal waves, respectively. For the two distinct propagation directions, $\langle 001 \rangle$ and $\langle 111 \rangle$, both shear waves propagate at the same wave speed.

4

The Finite-Element Method

Contents

4.1 Geometry Discretisation 43
4.2 Shape Functions 46
4.3 Construction of the Finite-Element Equations 49
4.4 Mechanical Eigenmodes 52
4.5 Viscous Damping and Frequency Domain Response 53
4.6 Modal Superposition 55

To obtain the mechanical response of a complex system the principles of the finite-element method (FEM) are discussed. Here the elementwise discretisation, the field variable interpolation and corresponding shape functions are introduced. Using the strain displacement and local element matrices, the elemental and global finite-element equations of motion are assembled from the Lagrange equations and discussed with regard to different analysis methods.

4.1 Geometry Discretisation

For some mechanical problems, especially in structural mechanics, the behaviour can be described analytically or may be approximated using empirical data [Chopra 2012]. With an increasing complexity, however, finding an analytical solution is a tedious, if not a hopeless effort [Chopra 2012; Liu 2003; Bathe 2014; Zienkiewicz et al. 2013; Rao 2010]. Hence, numerical methods like the finite-difference time-domain (FDTD) method or FEM try to bridge the gap by discretizing a large complex structure into smaller idealised pieces. Based on simplified problem descriptions in thee well defined pieces, the overall problem may be solved numerically. Both finite-difference time-domain and FEM methods can be applied in several interdisciplinary fields such as structural solid mechanics, electromagnetics and optics, fluids, plasmas, micro-electro-mechanical-system (MEMS) devices and many more.

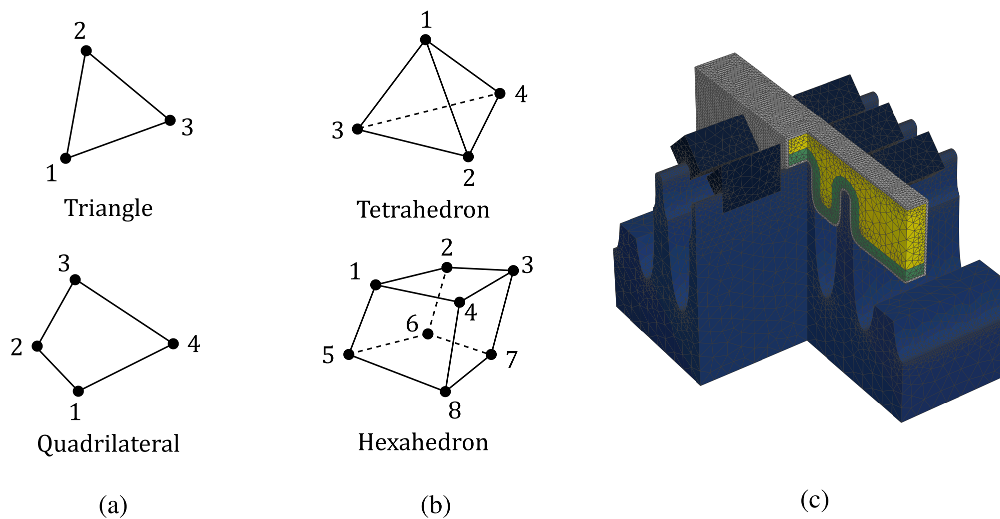

Figure 4.1: Discretisation in (a) 2D and (b) 3D elements adapted from [Rao 2010]. A FinFET structure meshed with COMSOL using tetrahedral elements is depicted in (c).

For this work COMSOL[1], a commercially available multi-physics FEM simulation software, was used. It not only enables the simulation of structural problems but it can also handle coupled multi-physics problems such as electromechanical devices. Excellent derivations of the FEM can be found in the literature [Zienkiewicz et al. 2013; Bathe 2014; Liu 2003; Rao 2010; Larson and Bengzon 2013; Felippa 2004] and only a brief summary is given in this work.

At the core of the FEM, as implied by its name, lies the discretisation of the geometry into smaller elements, which is commonly referred to as meshing. During the meshing procedure the geometry is approximated in a predefined and consistent manner using finite elements. The shape of these elements must be selected with regard to the dimensionality and form of the whole geometry. Whereas for a one-dimensional (1D) problem, the only possible element is a linear segment bounded by two nodes, two-dimensional (2D) structures can be discretised with triangles, quadrilaterals or generalised polygons, as sketched in Figure 4.1(a). Carrying on to 3D problems the simplest possible discretisation element, with the least number of nodes, is the tetrahedron which is depicted in Figure 4.1(b). However, it is also possible to use prisms, brick-type elements or generalised quadrilaterals. The meshing procedure is generally not limited to a single element type but may use different elements as long as compatibility is maintained. This alludes that elements are connected to neighbouring elements at the nodes and may not overlap or form gaps inside the structure.

An exemplary mesh of a FinFET structure, using tetrahedral elements only, is shown in Figure 4.1(c). To improve the accuracy of the solution, thin structures like the high-κ oxide surrounding the gate in a FinFET process, require a finer mesh resolution, while larger domains within the structure may be approximated using larger elements. Although a finer mesh yields a higher accuracy it adversely impacts the computational performance as the required memory

[1]COMSOL Multiphysics® v. 5.5. `www.comsol.com`

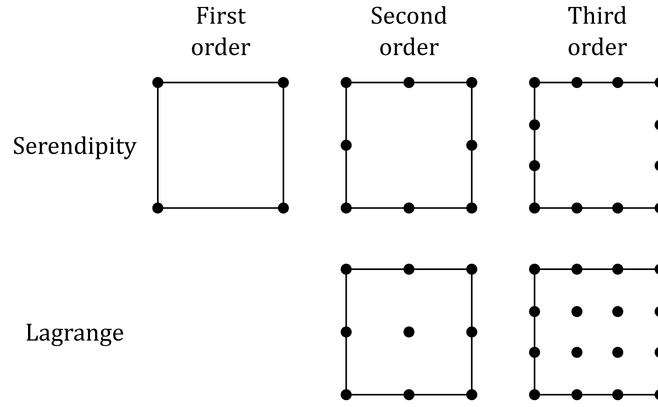

Figure 4.2: First, second and third order Serendipity and Lagrange elements for a 2D quadrilateral.

and the solution time scale with the degrees of freedom (DOFs).

The DOFs in a structural mechanics problem are typically given by the number of nodes. For each node the displacement vector is written as

$$\vec{D}_i = \begin{bmatrix} d_{i,1} \\ d_{i,2} \\ \vdots \\ d_{i,n_f} \end{bmatrix} \overset{n_f=3}{=} \begin{bmatrix} u_i \\ v_i \\ w_i \end{bmatrix}, \tag{4.1.1}$$

where $d_{i,j}$ are the mechanical displacement components. For a 3D structural problem the DOFs of a single node are typically $n_f = 3$ as the displacement field variable may move along all three main axes. The displacement components along the three main axes, in this case the x-axis, y-axis and z-axis, are then typically given by the three field variables u_i, v_i and w_i [Liu 2003; Rao 2010; Felippa 2004].

Several nodes are combined into an element as shown for a 2D quadrilateral element in Figure 4.2 [Ho and Yeh 2006]. In the FEM often two types of elements are used. Serendipity elements possess only nodes on the edges, whereas Lagrange elements also feature nodes within the element which is computationally more demanding as the number of nodes, and thus the total DOFs are increased. The FEM computes the field variables for the nodes of the elements. To describe the displacement of the whole element the individual displacement vectors of each node (4.1.1) are collected in the elemental displacement vector

$$\vec{D}^{(e)} = \begin{bmatrix} u_1 & v_1 & w_1 & u_2 & v_2 & w_2 & \cdots & u_{n_d} & v_{n_d} & w_{n_d} \end{bmatrix}^T, \tag{4.1.2}$$

where n_d is the number of nodes and the superscript $^{(e)}$ signifies an element local coordinate system [Liu 2003; Rao 2010]. To find the value of the field variables not only at the nodes but at any given point within the element so-called shape or basis functions are required.

4.2 Shape Functions

Using shape functions the displacement vector at any point in the element

$$\vec{U}(x,y,z,t) = \sum_{i=1}^{n_d} [\widetilde{N}_i(x,y,z)]\vec{D}_i(t) = [N(x,y,z)]\vec{D}^{(e)}(t) \tag{4.2.1}$$

is interpolated from the nodal displacements $\vec{D}^{(e)}(t)$ using the matrix of shape functions $[N(x,y,z)]$ [Liu 2003; Rao 2010; Bathe 2014; Larson and Bengzon 2013].

The matrix of shape functions

$$[N(x,y,z)] = \begin{bmatrix} [\widetilde{N}_1(x,y,z)] & [\widetilde{N}_2(x,y,z)] & \cdots & [\widetilde{N}_{n_d}(x,y,z)] \end{bmatrix} \tag{4.2.2}$$

contains the diagonal sub-matrices

$$[\widetilde{N}_i(x,y,z)] = \begin{bmatrix} N_{i,1}(x,y,z) & & & \\ & N_{i,2}(x,y,z) & & \\ & & \ddots & \\ & & & N_{i,n_f}(x,y,z) \end{bmatrix} \tag{4.2.3}$$

where for 3D problems $n_f = 3$ and typically $N_{i,1} = N_{i,2} = N_{i,3} = N_i$ [Liu 2003; Rao 2010].

The shape functions $N_i(x,y,z)$ must adhere to four conditions: Firstly they must be of unity value at their respective home node i and vanish at all other nodes, which is the interpolation condition. Secondly, they must vanish outside any element boundary that does not contain node i, which is called the local support condition. Thirdly, they must fulfil the inter-element compatibility condition which requires continuity between adjacent elements containing the same node i. Lastly the completeness condition mandates that the interpolation is able to represent any linear displacement field or constant value [Zienkiewicz et al. 2013; Liu 2003; Felippa 2004].

The shape functions can be calculated by assuming that the displacement vector at any point within the element

$$\vec{U}^h(x,y,z) = \sum_{i=1}^{n_d} p_i(x,y,z)\alpha_i = \vec{p}^T(x,y,z)\vec{\alpha} \tag{4.2.4}$$

can be approximated from a linear combination of n_d linearly-independent basis functions $p_i(x,y,z)$. The coefficient α_i for each basis function is defined as

$$\vec{\alpha} = \begin{bmatrix} \alpha_1 & \alpha_2 & \cdots & \alpha_{n_d} \end{bmatrix}^T. \tag{4.2.5}$$

The required monomials for a 3D problem can be constructed from the Pascal's pyramid and

are written as

$$\vec{p}(x,y,z) = \begin{bmatrix} 1 & x & y & z & xy & yz & zx & x^2 & y^2 & z^2 & \cdots & x^p & y^p & z^p \end{bmatrix}^T \tag{4.2.6}$$

up to a order p with a total of n_d terms [Liu 2003]. Consequently, the element order in Figure 4.2 defines the order of the monomials, and thus the interpolation type. Here the order of the element should be chosen upon the requirements of the finite-element problem. In solid mechanics, which includes rotations of objects, linear interpolation causes larger errors compared to quadratic shape functions, which reduce the error. This, however, comes at an increased computational cost due to the larger number of nodes, and thus total DOFs [Bauchau and Han 2013].

The coefficients α_i are calculated from

$$\vec{D}^{(e)} = [P]\vec{\alpha} \tag{4.2.7}$$

by enforcing the approximated displacements in (4.2.4) to be equal to the nodal displacements $\vec{D}^{(e)}$ at the respective nodes. Here

$$[P] = \begin{bmatrix} \vec{p}^T(x_1,y_1,z_1) \\ \vec{p}^T(x_2,y_2,z_2) \\ \vdots \\ \vec{p}^T(x_{n_d},y_{n_d},z_{n_d}) \end{bmatrix} \tag{4.2.8}$$

is the so-called momentum matrix, which is of the size $n_d \times n_d$, which can be written as

$$[P] = \begin{bmatrix} p_1(x_1,y_1,z_1) & p_2(x_1,y_1,z_1) & \cdots & p_{n_d}(x_1,y_1,z_1) \\ p_1(x_2,y_2,z_2) & p_2(x_2,y_2,z_2) & \cdots & p_{n_d}(x_2,y_2,z_2) \\ \vdots & \vdots & \ddots & \vdots \\ p_1(x_{n_d},y_{n_d},z_{n_d}) & p_2(x_{n_d},y_{n_d},z_{n_d}) & \cdots & p_{n_d}(x_{n_d},y_{n_d},z_{n_d}) \end{bmatrix} \tag{4.2.9}$$

in its expanded form. Assuming the inverse of the momentum matrix exists the coefficients $\vec{\alpha}_i$

$$\vec{\alpha}^T = [P]^{-1}\vec{D}^{(e)} \tag{4.2.10}$$

can be calculated. Substituting this equation in (4.2.4) allows for the calculation of an approximated displacement

$$\vec{U}^h(x,y,z) = [N(x,y,z)]\vec{D}^{(e)} \tag{4.2.11}$$

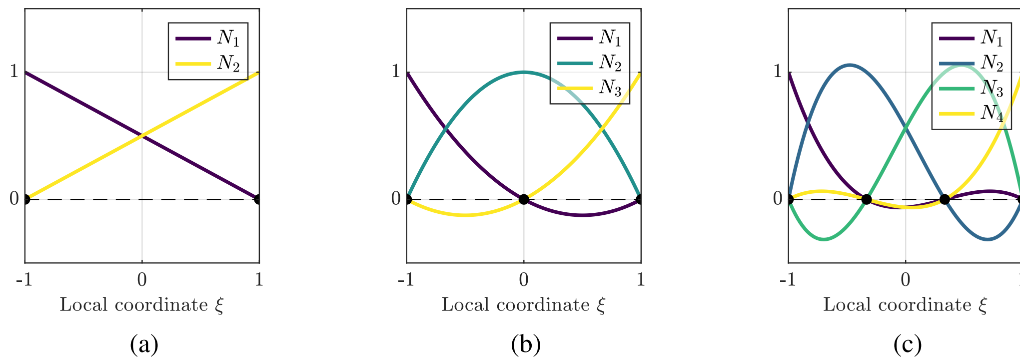

Figure 4.3: 1D (a) linear, (b) quadratic and (c) cubic shape functions in the local element coordinate frame.

at any point within the element. The matrix of shape functions is defined as

$$\begin{aligned}[N(x,y,z)] = \vec{p}^T(x,y,z)[P]^{-1} &= \left[\vec{p}^T(x,y,z)[P]_1^{-1} \quad \vec{p}^T(x,y,z)[P]_2^{-1} \quad \cdots \quad \vec{p}^T(x,y,z)[P]_{n_d}^{-1}\right] \\ &= \left[[\widetilde{N}_1(x,y,z)] \quad [\widetilde{N}_2(x,y,z)] \quad \cdots \quad [\widetilde{N}_{n_d}(x,y,z)]\right]\end{aligned} \tag{4.2.12}$$

where $[P]_i^{-1}$ is the ith column of $[P]^{-1}$ [Liu 2003; Bathe 2014; Rao 2010]. Using this methodology the shape functions of the elements can be calculated. They are plotted some lower orders in Figure 4.3 and Figure 4.4 for 1D and 2D elements in their local element coordinate systems (ξ) and (ξ, η). While this is a general approach to derive the shape functions for an element, shortcut methods are widely deployed in finite-element software as they are less computation intensive [Zienkiewicz et al. 2013; Larson and Bengzon 2013; Rao 2010].

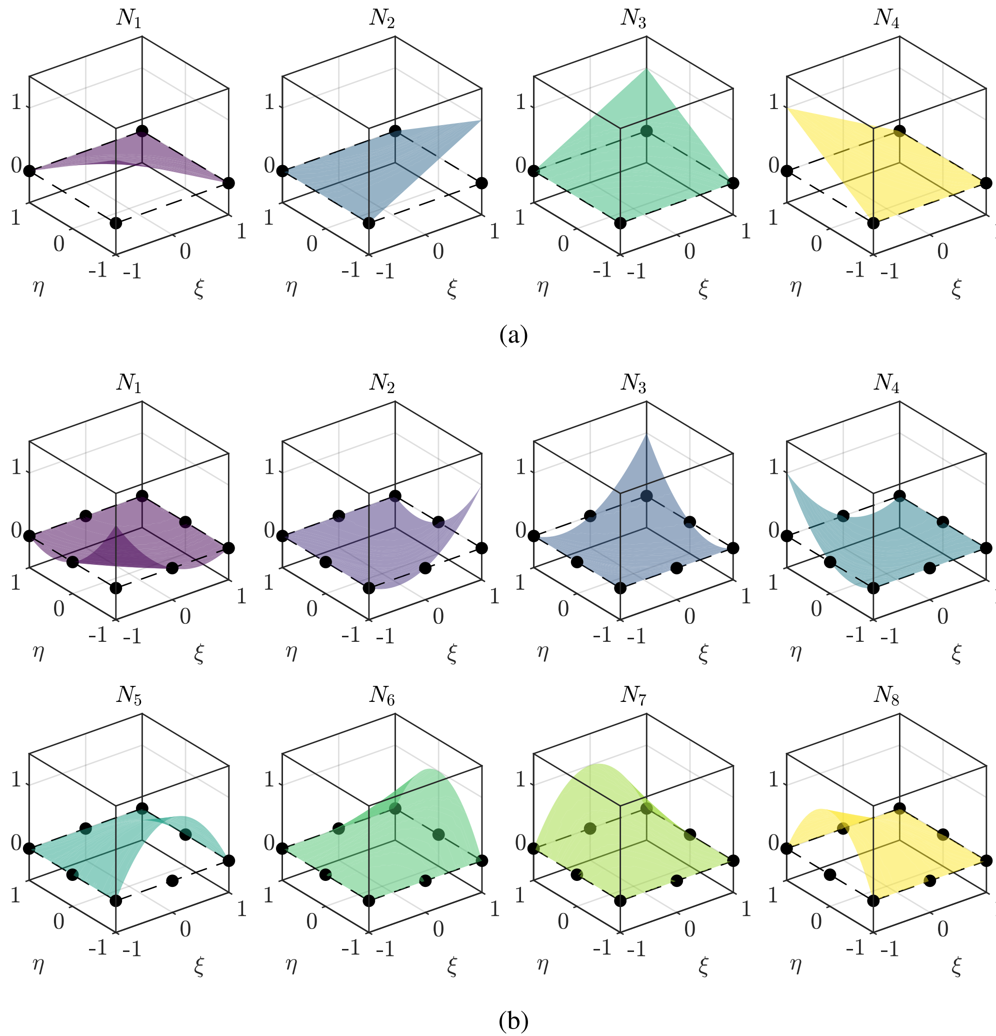

Figure 4.4: 2D (a) linear and (b) quadratic serendipity shape functions for quadrilateral elements in the local element coordinate frame.

4.3 Construction of the Finite-Element Equations

Following the discretisation of a geometry into elements and the derivation of the element shape functions the equations of motion can be derived. Therefore the strains

$$\vec{\varepsilon} = [B]\vec{D}^{(e)} \tag{4.3.1}$$

and stresses

$$\vec{\sigma} = [c]\vec{\varepsilon} = [c][B]\vec{D}^{(e)} \tag{4.3.2}$$

are expressed using the strain displacement matrix $[B]$ and the elasticity matrix $[c]$, which was derived in Chapter 3. The strain displacement matrix writes as

$$[B] = \begin{bmatrix} B_1 & B_2 & \cdots & B_{n_d} \end{bmatrix} \tag{4.3.3}$$

where

$$[B_i] = \begin{bmatrix} \frac{\partial N_i}{\partial x} & 0 & 0 \\ 0 & \frac{\partial N_i}{\partial y} & 0 \\ 0 & 0 & \frac{\partial N_i}{\partial z} \\ \frac{\partial N_i}{\partial y} & \frac{\partial N_i}{\partial x} & 0 \\ 0 & \frac{\partial N_i}{\partial z} & \frac{\partial N_i}{\partial y} \\ \frac{\partial N_i}{\partial z} & 0 & \frac{\partial N_i}{\partial x} \end{bmatrix}. \tag{4.3.4}$$

is calculated from the shape functions and (3.1.9) [Zienkiewicz et al. 2013; Liu 2003].

Using these expressions the equations of motion can be calculated using either the Eulerian or Lagrangian formulation. In solid mechanical problems, with small deformations, the finite-element equations are commonly derived from the Lagrange equations as deformations are assumed to be volume preserving. They are given by the Lagrange equation

$$\frac{\mathrm{d}}{\mathrm{d}t}\frac{\partial L}{\partial \dot{D}} - \frac{\partial L}{\partial D} + \frac{\partial R}{\partial \dot{D}} = 0 \tag{4.3.5}$$

where a dot indicates the first derivative with respect to time and

$$L = T - V + W \tag{4.3.6}$$

is the Lagrangian function with the kinetic energy T, the potential energy V, the external work W and the dissipation function R [Rao 2010; Larson and Bengzon 2013; Zienkiewicz et al. 2013]. Applied to a single element they can be written as

$$T^{(e)} = \frac{1}{2}\iiint_V \rho \dot{\vec{U}}^T \dot{\vec{U}} \mathrm{d}v, \tag{4.3.7}$$

$$V^{(e)} = \frac{1}{2}\iiint_V \vec{\varepsilon}^T \vec{\sigma} \mathrm{d}v, \tag{4.3.8}$$

$$R^{(e)} = \frac{1}{2}\iiint_V \mu \dot{\vec{U}}^T \dot{\vec{U}} \mathrm{d}v \tag{4.3.9}$$

and

$$W^{(e)} = \iiint_V \vec{U}^T \vec{f}_b \mathrm{d}v + \iint_S \vec{U}^T \vec{f}_s \mathrm{d}s \tag{4.3.10}$$

where V is the element volume, S the element surface, $\dot{\vec{U}}$ the velocity vector of the nodal field variables, ρ the density and μ the damping coefficient. The external forces on the element body and surfaces are given respectively by $\vec{f}_b$ and $\vec{f}_s$ [Rao 2010; Bathe 2014; Liu 2003].

By substitution of (4.2.1), (4.3.1) and (4.3.2) in (4.3.7) to (4.3.10), the Lagrange components

can be rewritten as

$$T^{(e)} = \frac{1}{2}\dot{\vec{D}}^{(e)T}[M^{(e)}]\dot{\vec{D}}^{(e)}, \tag{4.3.11}$$

$$V^{(e)} = \frac{1}{2}\vec{D}^{(e)T}[K^{(e)}]\vec{D}^{(e)} \text{ and} \tag{4.3.12}$$

$$R^{(e)} = \frac{1}{2}\dot{\vec{D}}^{(e)T}[C^{(e)}]\dot{\vec{D}}^{(e)}. \tag{4.3.13}$$

From these the local element mass matrix

$$[M^{(e)}] = \iiint_V \rho[N]^T[N]\mathrm{d}v \tag{4.3.14}$$

the local element stiffness matrix

$$[K^{(e)}] = \iiint_V [B]^T[C][B]\mathrm{d}v \tag{4.3.15}$$

and the local element damping matrix

$$[C^{(e)}] = \iiint_V \mu[N]^T[N]\mathrm{d}v \tag{4.3.16}$$

are derived. Similar expressions for the elemental nodal body forces

$$\vec{F}_b^{(e)} = \vec{D}^{(e)T} \iiint_V [N]^T \vec{f}_b \mathrm{d}v \tag{4.3.17}$$

and the surface forces

$$\vec{F}_s^{(e)} = \vec{D}^{(e)T} \iint_S [N]^T \vec{f}_s \mathrm{d}s \tag{4.3.18}$$

can be calculated [Rao 2010; Bathe 2014; Larson and Bengzon 2013].

To obtain the set of equations for not just a single element but the complete global structure, which contains all connected elements, the local element matrices are expanded to the global matrix size. The expanded matrices take the form

$$T^{(g)} = \sum_{e=1}^{E} T^{(e)\prime}, \tag{4.3.19}$$

$$V^{(g)} = \sum_{e=1}^{E} V^{(e)\prime}, \tag{4.3.20}$$

$$R^{(g)} = \sum_{e=1}^{E} R^{(e)\prime} \text{ and} \tag{4.3.21}$$

$$\vec{F}^{(g)}(t) = \vec{F}_c^{(g)}(t) + \sum_{e=1}^{E} \left(\vec{F}_s^{(e)\prime}(t) + \vec{F}_b^{(e)\prime}(t)\right) \tag{4.3.22}$$

where the prime indicates a sparse matrix or vector which is expanded to the global matrix size. The subscript $^{(g)}$ marks the global matrix formulation, E is the total number of elements and $\vec{F}_c^{(g)}(t)$ the force vector of concentrated nodal forces in the global form. This procedure also yields, analogously to (4.3.11) to (4.3.16), the global formulations of the mass $[M^{(g)}]$, stiffness $[K^{(g)}]$ and damping $[C^{(g)}]$ matrices [Rao 2010].

Substitution of the global matrices into the Lagrange equations (4.3.5) and (4.3.6) yields the differential equations of motion for the entire geometry

$$[M^{(g)}]\ddot{\vec{D}}(t) + [C^{(g)}]\dot{\vec{D}}(t) + [K^{(g)}]\vec{D}(t) = \vec{F}^{(g)}(t) \tag{4.3.23}$$

where, $\dot{\vec{D}}(t)$ and $\ddot{\vec{D}}(t)$ are the velocity and acceleration of the nodal field variables. The discretised equations of motion are commonly written for simplicity as

$$\mathbf{M}\ddot{\mathbf{D}} + \mathbf{C}\dot{\mathbf{D}} + \mathbf{K}\mathbf{D} = \mathbf{F} \tag{4.3.24}$$

which implies the global matrix formulation and time dependencies of the force and displacement vectors [Larson and Bengzon 2013; Zienkiewicz et al. 2013; Rao 2010; Liu 2003].

4.4 Mechanical Eigenmodes

Using the FEM, the mechanical eigenmodes of a structure can be found by solving the equilibrium equation of a free undamped dynamic vibration

$$\mathbf{M}\ddot{\mathbf{D}} + \mathbf{K}\mathbf{D} = 0 \tag{4.4.1}$$

for the nodal displacements. The solution for the displacement is assumed of the form

$$\mathbf{D} = \boldsymbol{\phi} e^{j\omega t} \tag{4.4.2}$$

where $\boldsymbol{\phi}$ is the amplitude vector of the nodal displacements and ω is the vibration frequency. One can rewrite (4.4.1) to obtain the eigenvalue equation

$$[\mathbf{K} - \lambda\mathbf{M}]\boldsymbol{\phi} = 0 \tag{4.4.3}$$

where $\lambda = \omega^2$ is an eigenvalue of the system. To find a non-zero solution to the eigenvalue equation the determinant

$$\det(\mathbf{K} - \lambda\mathbf{M}) = 0 \tag{4.4.4}$$

must vanish.

Expanding the above equation leads to a polynomial of order equal to the DOFs with the roots $\lambda_1, \lambda_2, \ldots, \lambda_{n_d}$ known as the eigenvalues of the structure. They relate to the natural

frequencies of vibration, which are supported by the structure's geometry and material properties. Each eigenvalue λ_i is associated with a corresponding eigenvector $\boldsymbol{\phi}_i$ describing the nodal displacements of the eigenmode. By construction, all eigenvectors are orthogonal. However, in some cases several eigenvalues may coincide. In this case multiple eigenvectors which satisfy (4.4.3), and thus have the same eigenvalue, may exist [Bathe 2014; Chopra 2012; Liu 2003; Rao 2010].

The eigenvalues can also be obtained for a damped structure with the characteristic equation

$$-\omega^2\mathbf{MD} + j\omega\mathbf{CD} + \mathbf{KD} = 0 \tag{4.4.5}$$

which can be solved by splitting the equation into two first-order equations [Zienkiewicz et al. 2013; Chen and Taylor 1989]. However, depending on the analysis following the eigenmode simulation, it is possible to neglect damping during the initial eigenvalue calculation and consider it at a later stage in the investigation [Lesieutre 2001; Comsol 2019].

4.5 Viscous Damping and Frequency Domain Response

Several approaches exist to introduce damping in solid mechanic finite-element problems with one common approach using Rayleigh damping, a form of proportional viscous damping [Lesieutre 2001; Chopra 2012; Larson and Bengzon 2013; Alipour and Zareian 2018; Chopra and McKenna 2015; Liu 2003; Comsol 2019]. Using the Rayleigh damping formulation, the damping matrix

$$\mathbf{C} = \alpha\mathbf{M} + \beta\mathbf{K} \tag{4.5.1}$$

is constructed from a linear combination of the known mass and stiffness matrices from the finite-element formulation. The pre-factors α and β are real-valued scalars found from experiments or calculations, with the units 1/s and s, respectively. Knowing the damping ratios of two eigenmodes of the system

$$\zeta_n = \frac{\alpha}{2}\frac{1}{\omega_n} + \frac{\beta}{2}\omega_n \tag{4.5.2}$$

at their respective frequency ω_n the prefactors α and β can be calculated by solving [Lesieutre 2001; Chopra and McKenna 2015; Alipour and Zareian 2018; Rao 2010]

$$\frac{1}{2}\begin{bmatrix} 1/\omega_i & \omega_i \\ 1/\omega_j & \omega_j \end{bmatrix}\begin{bmatrix} \alpha \\ \beta \end{bmatrix} = \begin{bmatrix} \zeta_i \\ \zeta_j \end{bmatrix}. \tag{4.5.3}$$

The damping ratios for the individual modes can be obtained from empirical measurements such as the ring-down method [Polunin et al. 2015]. With this method, the quality factor (Q-factor) of a mode can be determined from the decay rate during a transient measurement, which relates

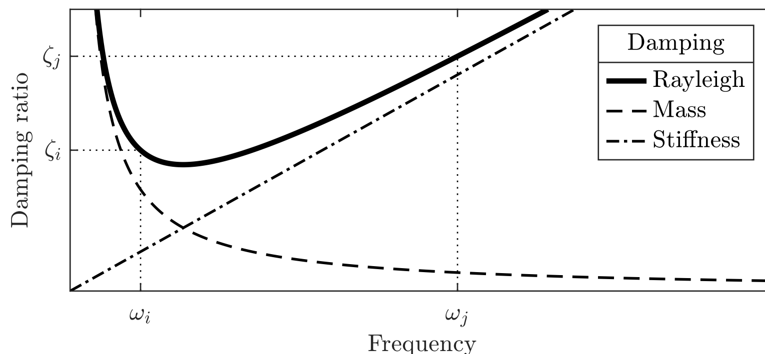

Figure 4.5: Rayleigh damping formalism using a linear combination of mass and stiffness dependent damping.

to the damping ratio via [Chopra 2012; Brand et al. 2015]

$$\zeta = \frac{1}{2Q}. \tag{4.5.4}$$

Using this approach, the Rayleigh damping coefficients can be computed as plotted in Figure 4.5. Both the mass and stiffness terms vary with frequency and the sum yields the total damping. The total damping is bounded at the two known frequencies ω_i and ω_j to the known values ζ_i and ζ_j. In a classical application, the under-damping in the region of interest, between ω_i and ω_j, is commonly considered the conservative approach, as over-damping may be undesirable [Chopra 2012]. Note that in the case of a rigid body mode, the Rayleigh damping formulation introduces unreasonable non-zero damping. Furthermore, modes outside the bounded region are overdamped and will not respond in an oscillatory manner in an unforced motion. Despite the drawbacks inherent to the model, Rayleigh damping may provide accurate results when being considered over a narrow frequency range [Lesieutre 2001; Chopra 2012]. Using Rayleigh damping the simulations can be adjusted by setting different macroscopic damping values to mimic the behaviour of the structure.

To obtain the mechanical response of a structure for different excitation frequencies, the differential finite-element equation (4.3.24) must be considered with a time-varying structural response

$$\mathbf{D} = \mathbf{D}_0 e^{j\omega t} \tag{4.5.5}$$

where $\mathbf{D}_0$ is the maximum deflection. The equilibrium equation thus takes the form

$$-\omega^2 \mathbf{MD} + j\omega \mathbf{CD} + \mathbf{KD} = \mathbf{F} \tag{4.5.6}$$

after substituting the derivatives [Marfurt 1984; Zhao et al. 2017; Brand et al. 2015]. The solution to this equation yields a complex-valued displacement, and thus provides both amplitude and phase information [Comsol 2018; Soares and Mansur 2005]. This method is generally computation-intensive, especially in weakly damped systems with tight frequency resolution requirements, as all possible DOFs of the complete structure must be considered.

4.6 Modal Superposition

The modal superposition principle can be applied to bypass the problem of the high computational cost associated with the frequency domain response which considers all DOFs. The system may be simplified if only a few major resonant eigenmodes contribute to the overall structural response. Rather than solving the frequency spectrum with (4.5.6) for all possible DOFs, the response can be approximated using a superposition of some uncoupled structural eigenmodes. Here a few modes may already be sufficient to describe the overall structural response and the DOFs can be strongly reduced in the process [Zienkiewicz et al. 2013; Rao 2010].

Starting from the eigenvalue equation (4.4.3), a set of orthogonal eigenmodes which fulfil

$$\boldsymbol{\phi}_i^T \mathbf{M} \boldsymbol{\phi}_j = 0, \quad \text{and} \quad \boldsymbol{\phi}_i^T \mathbf{K} \boldsymbol{\phi}_j = 0, \quad i \neq j. \tag{4.6.1}$$

can be computed [Comsol 2019]. For representation purposes the eigenvectors $\boldsymbol{\phi}_i$ are gathered in the matrix of eigenmodes $\mathbf{\Phi}$, where each column of represents an eigenvector. It then writes in matrix form with the mass matrix as

$$\mathbf{\Phi}^T \mathbf{M} \mathbf{\Phi} = \begin{bmatrix} m_1 & & & \\ & m_2 & & \\ & & \ddots & \\ & & & m_{n_d} \end{bmatrix} = \mathbf{\Psi}. \tag{4.6.2}$$

Since the amplitudes of the eigenmodes are arbitrary, they can be normalised using the mass matrix normalisation, so each $m_i = 1$ of the modal mass matrix, and thus $\mathbf{\Psi} = \mathbf{I}$, where $\mathbf{I}$ is the identity matrix. Analogously, the corresponding stiffness matrix can be normalised according to

$$\mathbf{\Phi}^T \mathbf{K} \mathbf{\Phi} = \begin{bmatrix} m_1\omega_1^2 & & & \\ & m_2\omega_2^2 & & \\ & & \ddots & \\ & & & m_{n_d}\omega_{n_d}^2 \end{bmatrix} = \mathbf{\Omega} \tag{4.6.3}$$

where the diagonal entries represent the squares of the modal angular natural frequencies after mass matrix normalisation [Comsol 2019].

At the core of the modal superposition principle lies the assumption that the total displacement within a structure can be written as a linear combination of the independent modal eigenvectors

$$\mathbf{D} \approx \sum_{i=1}^{n} q_i \boldsymbol{\phi}_i \tag{4.6.4}$$

where q_i is the amplitude vector of the ith mode. In matrix form, the equation can be written as

$$\mathbf{D} = \mathbf{\Phi q} \tag{4.6.5}$$

where $\mathbf{q}$ is a vector containing the modal amplitudes. Substitution of (4.6.5) in (4.3.24) yields

$$\mathbf{MU\ddot{q}} + \mathbf{CU\dot{q}} + \mathbf{KUq} = \mathbf{F} \tag{4.6.6}$$

and further left-hand side multiplication with $\mathbf{\Phi}^T$ gives

$$\mathbf{\Psi\ddot{q}} + \mathbf{\Phi}^T\mathbf{C\Phi\dot{q}} + \mathbf{\Omega q} = \mathbf{F}_m \tag{4.6.7}$$

where $\mathbf{F}_m = \mathbf{\Phi}^T\mathbf{F}$ is the modal load. The equation may further be simplified as $\mathbf{\Psi}$ and $\mathbf{\Omega}$ are diagonal matrices. Assuming orthogonality of all eigenvectors, the damping term $\mathbf{\Phi}^T\mathbf{C\Phi}$ can be expressed by a diagonal matrix ζ_r containing an individual damping ratio for each contributing eigenmode, which is not possible with viscous damping alone. The equation of motion thus reduces to

$$\mathbf{\ddot{q}} + 2\zeta_r\boldsymbol{\omega_r}\mathbf{\dot{q}} + \boldsymbol{\omega_r}\mathbf{q} = \mathbf{F}_m \tag{4.6.8}$$

where all linear equations are decoupled, which provides faster computation times compared to the fully coupled expression [Rao 2010]. The selection and number of modes must be carefully considered as they substantially impact the solution's accuracy [Lesieutre 2001; Comsol 2019; Zienkiewicz et al. 2013; Rao 2010].

Summary

By simplifying a complex geometry into smaller parts its mechanical behaviour can be solved numerically with the FEM where otherwise no analytic solution is feasible. During the discretisation the geometry is constructed from nodes which are connected into elements. For these elements it is possible to derive the differential equations of motion which are interpolated at arbitrary points within the respective elements using shape functions. For solid mechanical problems the finite-element equations are typically derived from the Lagrange equations.

The resulting equations of motion allow for the calculation of different characteristics of the structure, such as the resonant eigenmodes and frequency domain response. For the latter, damping is crucial, which may be introduced via viscous Rayleigh damping as it allows for a fine control of the mechanical response.

5

Electromechanical Modelling of the Resonant Fin Transistor

Contents

5.1 Resonant Eigenmodes 58
  5.1.1 Periodic Structures 58
  5.1.2 Eigenmodes of the Resonant Fin Transistor 61
  5.1.3 Index Guiding 64
  5.1.4 Resonant Mode Shapes 67
5.2 Frequency Domain Response 70
5.3 Extended Simulation Setups 77
  5.3.1 Symmetry Simplifications 77
  5.3.2 Finite Number of Parallel Gates 81
  5.3.3 Extended 14-Fin Unit Cell 85
5.4 Equivalent Isotropic Materials 87
  5.4.1 Transient Response 90
  5.4.2 Finite 2D Cavity 93
5.5 Transconductance Modelling 94
  5.5.1 Piezoresistive Effect in Monocrystalline Silicon 94
  5.5.2 FinFET Mobility Variation 101
  5.5.3 Mechanical Transconductance 105

To model the mechanical response of the resonant fin transistor (RFT) the resonant eigenmodes in the front-end-of-line (FEOL) are investigated on a simplified unit cell using the finite-element method (FEM). The wave guiding properties of the substrate and frequency domain response of the structure under electric excitation are modelled for varying crystallographic orientations. The mechanical performance of the finite device is then estimated using larger simulation volumes and different connection schemes. For a later circuit application the electro mechanical performance of the RFT is modelled using the piezoresistive effect of silicon, yielding an estimated mechanical transconductance .

5.1 Resonant Eigenmodes

To describe the mechanical behaviour of the RFT and assess its performance and limitations, an understanding of the mechanical eigenmodes of the structure is essential. They can be found analytically for simple problems with a small degree of freedom (DOF). For complex problems, however, numerical methods prevail due to their greater flexibility or the lack of analytic descriptions. Amongst different approaches such as plane-wave-expansion (PWE) and finite-difference time-domain (FDTD), the finite-element method (FEM) method is widely used for mechanical problems, ranging from structural buildings and earthquake science [Chopra 2012] to mechanical engineering [Rao 2010; Liu 2003; Bathe 2014] and further to the micro and nano-scale for micro-electro-mechanical-system (MEMS) design [Choudhary and Iniewski 2013; Bao and Huang 2003; Graczykowski et al. 2012; Shi et al. 2021; Baghelani et al. 2011; Zhou et al. 2018; Sviličić et al. 2015].

5.1.1 Periodic Structures

A description of the mechanical eigenmodes is essential to describe the resonant behaviour of the RFT. Those eigenmodes can be found using the FEM as discussed in Section 4.4. It solves the differential equations of motion for complex structural problems by discretizing the geometry into smaller finite elements.

With an increasing simulation volume, the DOFs and, consequently, the solution times increase in a non-linear manner [Pardo et al. 2012]. Many problems may be further simplified to counteract the long simulation times and improve convergence and solution speed by exploiting the geometrical symmetries and boundary conditions. A periodic structure with a large number of repetitions, such as the RFT with 154 consecutive periodic fin field-effect transistors (FinFETs), may be assumed as infinitely extended in a very simplistic assumption. However, scattering events at the abrupt termination of a finite structure will lead to increased losses [Bahr et al. 2015]. By exploiting the periodicity of the cavity, the computational effort can be drastically lowered since it can be reduced to a small subsection or unit cell of the periodic structure with a lower DOF than the complete structures.

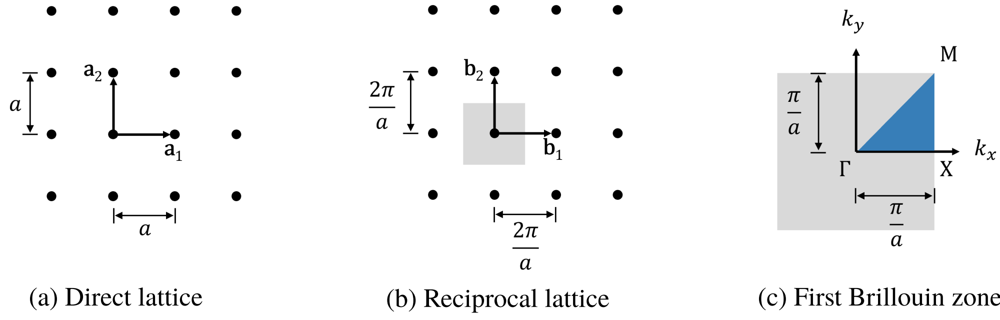

(a) Direct lattice (b) Reciprocal lattice (c) First Brillouin zone

Figure 5.1: (a) 2D direct lattice with the primitive basis vectors. (b) Reciprocal lattice with the primitive basis vectors and the Brillouin zone marked in grey. (c) First Brillouin zone (grey) and irreducible Brillouin zone (blue) with the high symmetry points.

With the help of Floquet-Bloch boundary conditions the DOFs of periodic structures can be reduced, allowing for a computationally more efficient modelling. Any periodic structure in one-, two-, or three-dimensions may be described by a Bravais lattice. It is formed by a collection of points with their respective locations given by

$$\mathbf{R} = l\mathbf{a}_1 + m\mathbf{a}_2 + n\mathbf{a}_3 \tag{5.1.1}$$

where $\mathbf{a}_1$, $\mathbf{a}_2$ and $\mathbf{a}_3$ are the three primitive basis vectors of the lattice. The lattice is also invariant under any translation by the integer coefficients l, m and n. It is defined in the real space of the structure and is commonly referred to as the direct lattice. An exemplary two-dimensional (2D) square lattice, with spacing a is shown in Figure 5.1(a). Commonly wave propagation phenomena are studied on the reciprocal lattice with the primitive lattice vectors

$$\mathbf{b}_1 = 2\pi \frac{\mathbf{a}_2 \times \mathbf{a}_3}{\mathbf{a}_1 \cdot (\mathbf{a}_2 \times \mathbf{a}_3)}, \tag{5.1.2}$$

$$\mathbf{b}_2 = 2\pi \frac{\mathbf{a}_3 \times \mathbf{a}_1}{\mathbf{a}_1 \cdot (\mathbf{a}_2 \times \mathbf{a}_3)} \text{ and} \tag{5.1.3}$$

$$\mathbf{b}_3 = 2\pi \frac{\mathbf{a}_1 \times \mathbf{a}_2}{\mathbf{a}_1 \cdot (\mathbf{a}_2 \times \mathbf{a}_3)} \tag{5.1.4}$$

for a three-dimensional (3D) lattice, which are constructed from the direct lattice vectors [Jiménez et al. 2021]. Similarly to the direct lattice the reciprocal lattice vectors follow

$$\mathbf{G} = l'\mathbf{b}_1 + m'\mathbf{b}_2 + n'\mathbf{b}_3 \tag{5.1.5}$$

where l', m' and n' are integers. The direct and reciprocal lattice vectors follow the condition $\mathbf{G} \cdot \mathbf{R} = 2\pi N$, where N is an integer value. The reciprocal lattice of a square direct lattice is depicted in Figure 5.1(b), marked in grey is the first Wigner-Seitz cell which is also known as the Brillouin zone.

In a periodic structure such as a phononic crystal or a periodic waveguide all material

properties, namely the density

$$\rho(\mathbf{r} + \mathbf{R}) = \rho(\mathbf{r}) \tag{5.1.6}$$

and elastic moduli

$$c_{\alpha\beta}(\mathbf{r} + \mathbf{R}) = c_{\alpha\beta}(\mathbf{r}), \tag{5.1.7}$$

are considered periodic on the direct lattice [Khelif and Adibi 2016; Jiménez et al. 2021]. Assuming the displacements to be plane waves

$$\mathbf{u}(\mathbf{r}, t) = \mathbf{u}(\mathbf{r})e^{j\omega t} \tag{5.1.8}$$

where ω is the angular frequency, the Floquet-Bloch theorem allows to rewrite the displacements as

$$\mathbf{u}(\mathbf{r}) = \mathbf{u_k}(\mathbf{r})e^{j\mathbf{k}\cdot\mathbf{r}}. \tag{5.1.9}$$

Here $\mathbf{k}$ is the Bloch wave vector and $\mathbf{u_k}(\mathbf{r} + \mathbf{R}) = \mathbf{u_k}(\mathbf{r})$ is a periodic function on the direct lattice which is valid for all lattice vectors $\mathbf{R}$ [Khelif and Adibi 2016; Jiménez et al. 2021; Joannopoulos et al. 2008].

To obtain the dispersion relation, also known as the band structure, which describes most of the mechanical properties of the structure, it is sufficient to solve the eigenvalue problem on the perimeter of the Brillouin zone. It leads to an infinite number of allowed frequencies $\omega_n(\mathbf{k})$ at a given wave vector, where n is an integer numbering the bands. The Brillouin zone typically posses further symmetries which can be exploited to reduce computational cost even further. The newly derived unit cell is referred to as the irreducible Brillouin zone, which is marked in blue in Figure 5.1(c) with the so-called high symmetry points Γ, X and M. The obtained dispersion relation for all wave vectors on the perimeter of the irreducible Brillouin zone is also known as band structure.

Although the lattice vectors of the direct lattice can point in any direction, without being parallel, only rectangular lattices are considered in this work. Depicted in Figure 5.2 are examples of selected one-dimensional (1D), 2D and 3D Brillouin zones with the respective high-symmetry points which are indicated by capital letters [Setyawan and Curtarolo 2010]. As indicated by grey lines, the first Brillouin zones may be further reduced by exploiting symmetry planes giving rise to the irreducible Brillouin zone. It is marked for all reciprocal Wigner-Seitz cells in colour with their respective high symmetry points. Note the different naming conventions for some high symmetry points for the different lattice types and dimensions.

In the following study of the eigenmodes and band structures, it is sufficient to obtain the solutions on the perimeter of the irreducible Brillouin zones as those reflect all extremal values obtained inside the Brillouin zone, reducing the required simulation resources [Khelif and Adibi 2016; Joannopoulos et al. 2008; Setyawan and Curtarolo 2010].

In the later band structure studies, it is sufficient to obtain the solutions on the perimeter of the irreducible Brillouin zone as those reflect all extremal values obtained inside the Brillouin

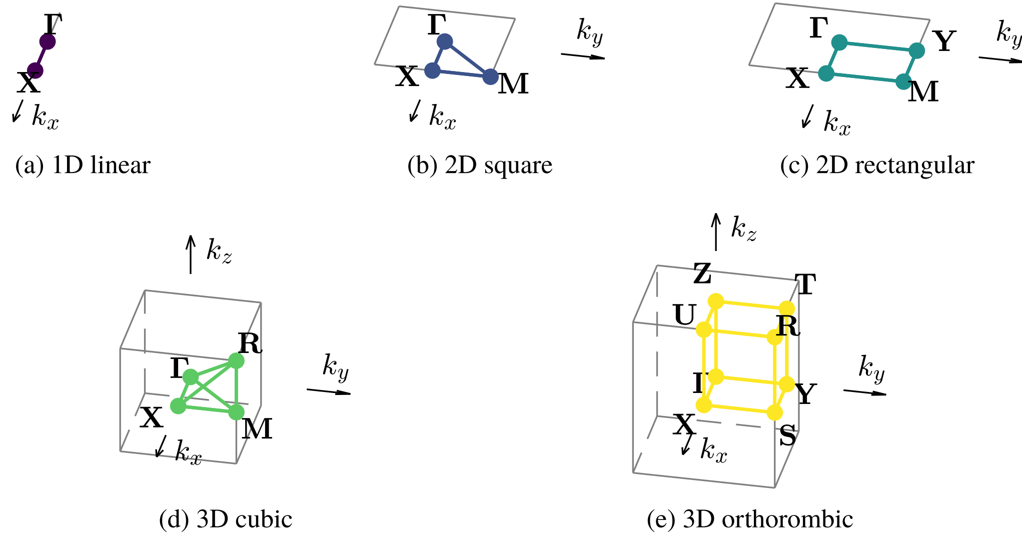

(a) 1D linear (b) 2D square (c) 2D rectangular

(d) 3D cubic (e) 3D orthorombic

Figure 5.2: Wigner-Seitz cells for different unit cell configurations with their respective irreducible Brillouin zone and high symmetry points.

zone [Khelif and Adibi 2016; Joannopoulos et al. 2008; Setyawan and Curtarolo 2010].

5.1.2 Eigenmodes of the Resonant Fin Transistor

As fabricated by Bahr et al. the RFT features 154 consecutive fins which can be approximated using just a single FinFET with periodic Floquet-Bloch boundary conditions, effectively reducing the required DOFs down to 1/154 [Bahr et al. 2018]. To further reduce complexity and separate the resonant behaviour from the phononic crystal, the back-end-of-line (BEOL) mirror is removed from the simulation. Instead, it is modelled with a solid oxide slab made from SiO_2 or SiCO:H. The respective differential unit cells, spanning two adjacent FinFETs, are sketched in Figures 5.3(a) and 5.3(b). Note that only a single fin is considered in the finite-element eigenmode analysis. The corresponding Brillouin zone is depicted in Figure 5.3(c). The FinFETs are modelled to typical 16 nm technology node dimensions comparable to Global Foundries' 14 nm node [Bahr et al. 2018]. The fins can be divided into an active transistor part, covered by the high-κ dielectric and the gate conductor and the inactive part below the fin, where the gaps between fins are filled by thermally stable SiO_2. The gate stack is created from a thin high-κ HfO_2 layer and a work-function material such as TiN. The common gate of the cavity is made from tungsten, a very stiff, near-isotropic material. Vertically above the gate, where the BEOL is usually manufactured, the previously mentioned SiO_2 and SiCO:H slabs are used for the simulation. The depicted structures are modelled for a gate length of 36 nm and a technology-typical gate pitch.

To reflect the RFT's periodic structure, they are constructed with Floquet-Bloch boundary conditions along the y-axis. On the facets perpendicular to the x-axis, symmetric boundary conditions are used. They suppress out-of-plane movements, which leads to the assumption of an infinite number of parallel gates within the RFT. The impact of a finite number of gates is

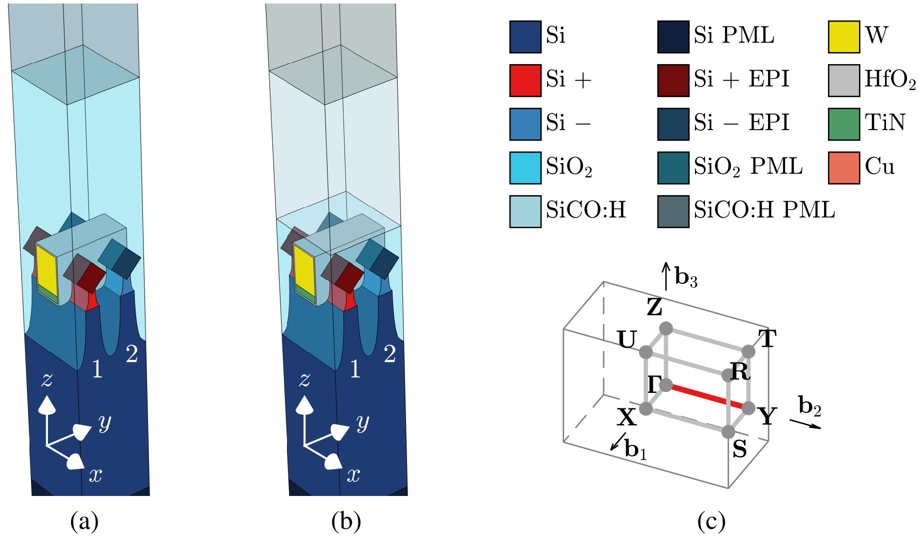

Figure 5.3: Ideal 2-fin unit cells with (a) a SiO_2 and (b) a SiCO:H slab on top of the RFT cavity. (c) Brillouin zone of the unit cells. ((a) Adapted from [Hudeczek et al. 2022].)

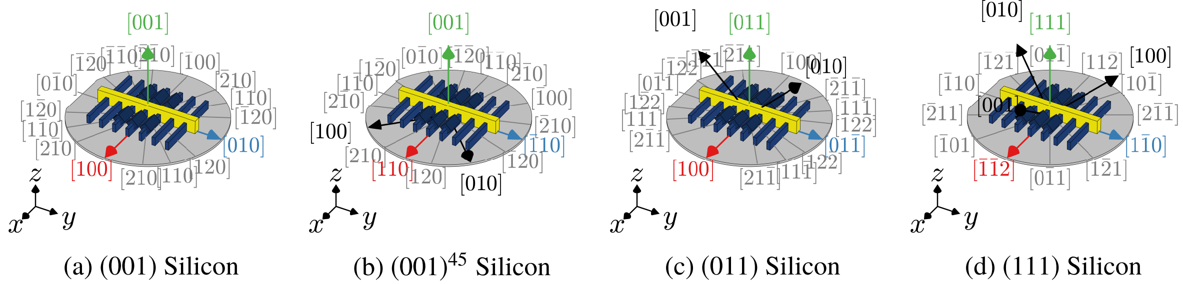

Figure 5.4: Different wafer orientations with their respective surface-normal, channel and gate directions. (Adapted from [Hudeczek et al. 2022].)

discussed later in Section 5.3.2. Layers of perfectly matched layers terminate the unit cells along the z-axis. Those regions absorb all incoming mechanical waves which is a valid assumption as no reflections in the far distance are expected due to the presence of a thick silicon wafer and BEOL oxide slab [Joannopoulos et al. 2008; Khelif and Adibi 2016].

As discussed in Chapter 3, monocrystalline silicon exhibits anisotropic mechanical properties. Therefore, several wafer orientations are modelled to study their impact on the performance of the RFT. As sketched in Figure 5.4, the four investigated directions are commonly deployed in integrated circuit (IC) or MEMS design. The first orientation, as illustrated in Figure 5.4(a), covers the case of a non-rotated standard silicon wafer (100), where the channel points along the principle axis [100]. Therefore, the RFT's spatial coordinates align with the silicon wafer's principle crystallographic axes. The second orientation $(001)^{45}$, shown in Figure 5.4(b), is rotated counter-clockwise by 45° around the wafer's normal direction [001]. Here the FinFETs' channels point along [110], which is considered the best orientation for standard complementary metal-oxide-semiconductor (CMOS) ICs, due to the beneficial susceptibility to uniaxial stress along the channel, as discussed in more detail in Section 5.5.1 [Thompson et al. 2004; Saitoh et al. 2008; Jaeger et al. 2013; Gallon et al. 2004]. The third configuration (011),

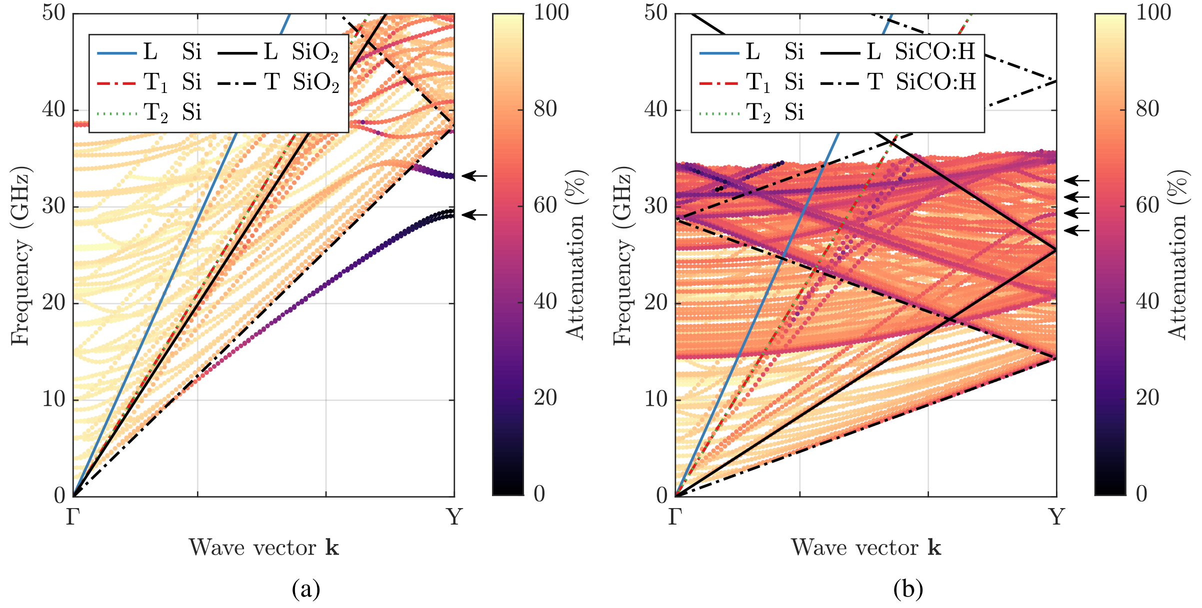

Figure 5.5: FEM simulated band structure along Γ−Y for a top confinement with (a) SiO_2 and (b) SiCO:H on a (001) oriented wafer. Note that (b) was limited to 250 modes for each computed wave vector.

depicted in Figure 5.4(c) is added for completeness and is not commonly used. As sketched in Figure 5.4(d), the last wafer is (111) oriented with the channel pointing along $[\bar{1}\bar{1}2]$. This behaviour is considered beneficial for several types of released MEMS as all material properties are isotropic in the wafer plane, as discussed in Section 3.7.

Resonant modes, with wave vectors along the y-axis parallel to the cavity, are relevant for the device's operation. Therefore, the band structure along Γ−Y has to be considered as modes with a wave vector matched to the Y-point may couple to the adjacent fins and thereby propagate through the whole cavity [Khelif and Adibi 2016; Joannopoulos et al. 2008]. Note that the original publication by Bahr et al. investigates modes within Γ−X as a 2D approximation with the respective Brillouin zone convention shown in Figure 5.2(b) has been considered [Bahr et al. 2018]. The dispersion of a single FinFET is computed with the FEM on a (001) wafer for both oxide variants and shown in Figure 5.5. The colour code quantifies the attenuation

$$\alpha = \frac{\Im(\omega)}{\Re(\omega)} \tag{5.1.10}$$

of each mode calculated from the real $\Re$ and imaginary $\Im$ part of the complex-valued eigenfrequencies ω [Muzar and Stotz 2019]. Note that the attenuation is normalised to the largest observed value within each simulation. For the first unit cell variant with a SiO_2 slab, plotted in Figure 5.5(a), four guided modes with a low attenuation are observed at the Brillouin zone edge at Y, as marked by the arrows. These modes are well confined within the gate leading to a low attenuation, and thus large quality factor (Q-factor). Contrary to the SiO_2 slab, the low-κ SiCO:H oxide does not support well-guided modes, as shown in Figure 5.5(b). Although four similar modes can be identified, as marked by the arrows, their frequency is shifted, and

Table 5.1: Resonant frequencies and Q-factors of the four marked guided modes in Figure 5.5.

Mode	SiO_2 slab		SiCO:H slab	
	f (GHz)	Q-factor	f (GHz)	Q-factor
1	29.076	2.8×10^9	27.457	68
2	29.585	6.0×10^9	29.258	190
3	33.104	9.6×10^9	30.922	37
4	33.291	1.2×10^9	32.617	131

they are largely attenuated.

This behaviour is consequently reflected in the Q-factor

$$Q = \frac{\Re(\omega)}{2\Im(\omega)} \tag{5.1.11}$$

which is calculated from the complex-valued eigenfrequencies ω [Lifshitz and Roukes 2000; Brand et al. 2015; Chopra 2012]. The respective values are listed in Table 5.1 for all marked modes. Interestingly the observed Q-factors for the SiO_2 slab are more than several billion, whereas the SiCO:H slab only supports values in the low tens to hundreds. The huge values result from the neglected damping within the structure, as the accurate description of material damping is challenging. Therefore, the Q-factor is a direct measure of confinement of the mode as it quantifies all energy being deposited in the perfectly matched layers, which terminate the finite vertical directions of the simulation volume. A large Q-factor indicates a well confined mechanical mode in the FEOL cavity as only little energy is lost into the perfectly matched layers. Hence the confinement and guiding properties of the RFT cavity are strongly affected by the choice of the oxide material within the BEOL. The large difference in the observed Q-factors of the two oxide variants follows from the mechanical differences (see Table 3.1) and shielding capabilities.

5.1.3 Index Guiding

Since the BEOL phononic crystal is neglected and the RFT cavity is solely confined by a solid silicon or oxide slab. The shielding capabilities of those slabs is defined by the sound wave dispersion relation

$$\omega = \mathbf{k}c \tag{5.1.12}$$

of the respective materials, where c is the wave velocity of either the longitudinal or transversal waves [Khelif and Adibi 2016; Dobrzyński et al. 2018; Joannopoulos et al. 2008]. As discussed in Section 3.7.4 the sound wave velocities depend on the crystal orientation and propagation direction in cubic crystals. Consequently, the wafer orientations lead to different dispersion relations for both longitudinal and transversal waves within the bulk materials, based on the sound velocities in Table 5.2. The values have been obtained using the Christoffel equation

Table 5.2: Mechanical wave velocities in anisotropic bulk silicon and isotropic SiO_2 and SiCO:H along the gate direction for longitudinal (L) and transversal (T) waves. The sound cone (SC) frequencies are given for the Y point matched to the FinFET pitch.

Material	Orientation	**k**-vector	c_l (m s^{-1})	c_{t1} (m s^{-1})	c_{t2} (m s^{-1})	SC f_{max} @ Y L (GHz)	SC f_{max} @ Y T (GHz)
Silicon	(001)	[010]	8440.7	5844.9	5844.9	87.924	64.379
	$(001)^{45}$	$[\bar{1}10]$	9357.0	5844.9	4678.5	97.469	48.739
	(011)	$[01\bar{1}]$	9357.0	5844.9	4678.5	97.469	48.739
	(111)	$[1\bar{1}0]$	9357.0	5844.9	4678.5	97.469	48.739
SiO_2	isotropic		5848.1	3687.5	3687.5	60.918	38.412
SiCO:H	isotropic		2453.7	1377.3	1377.3	25.559	14.347

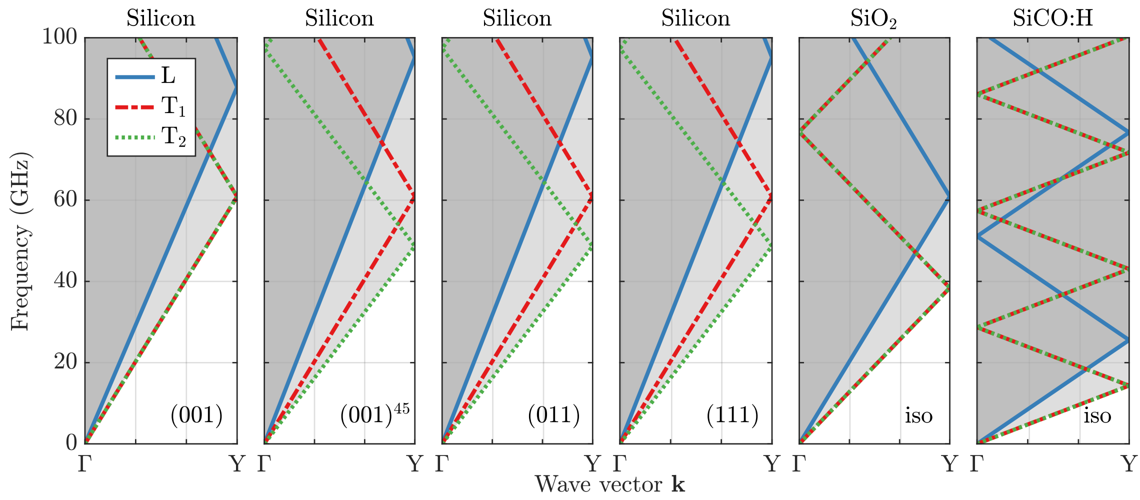

Figure 5.6: Bulk dispersion relations in anisotropic silicon and isotropic (iso) SiO_2 and SiCO:H along the gate direction $\Gamma-\mathrm{Y}$ for longitudinal and transversal waves.

(3.7.7) for the respective polarisations and propagation directions along $\Gamma-\mathrm{Y}$. The respective bulk dispersion relations of anisotropic silicon, SiO_2 and SiCO:H are shown in Figure 5.6 for both longitudinal and transversal waves. The longitudinal wave dispersion relation is marked in blue, with the two transversal dispersion relations marked in red and green, respectively. The extent of the Brillouin zone is matched to the FinFET pitch of the RFT, with the respective directions of propagation in crystal coordinates listed in Table 5.2. A folding of the bands is observed at the high symmetry points, which follows from the finite extent of the Brillouin zone [Hudeczek and Baumgartner 2020; Graczykowski et al. 2014; Ku et al. 2010].

For the wafer orientation (001), only one shear wave velocity exists for both transversal waves. However, for (011), $(001)^{45}$ and (111) silicon, two distinct shear wave velocities occur for propagation along $\Gamma-\mathrm{Y}$, leading to a subsequent splitting in the dispersion relation. A continuum of states exists for all shear waves with a frequency above the slow shear wave dispersion as indicated by the shaded region, which also applies to longitudinal and fast shear waves. These regions are commonly referred to as the sound cones of the material. Any

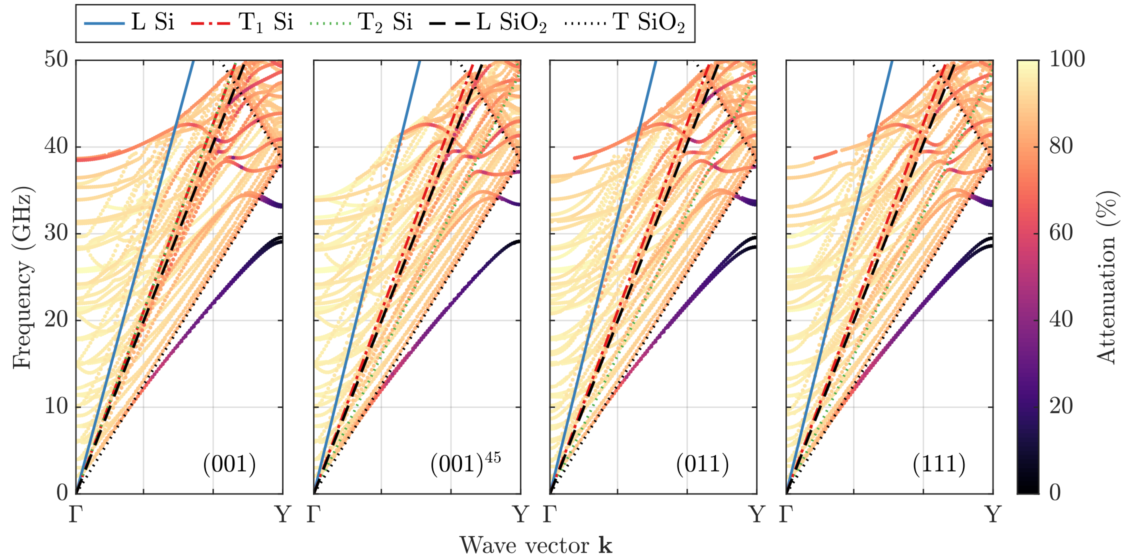

Figure 5.7: Band structure and evolution of the guided modes along Γ−Y for different silicon wafer orientations.

resonant mode within the cavity of the RFT with a frequency above one of the sound cones of the underlying silicon wafer cannot be confined by index guiding as it may couple to the bulk modes [Khelif and Adibi 2016; Dobrzyński et al. 2018; Joannopoulos et al. 2008].

However, as the sound cone frequencies of all silicon orientations at the Y-point, as listed in Table 5.2, are larger than the required 32 GHz for the RFT mode, the silicon wafer is capable of shielding the resonant mode at any of the investigated wafer orientations. The differentiator if a mechanical mode is confined to the FinFETs is the choice of the BEOL oxide slab on top of the cavity. Whereas the sound cone of SiO_2 is sufficiently large to confine modes up to a frequency of 38.412 GHz, the sound cone of SiCO:H only allows shielding up to a frequency of 14.347 GHz, for this specific fin pitch. The lower frequency follows from the much lower stiffness of the high porosity low-κ oxide, which thus has a much lower sound velocity. Consequently, only SiO_2 is capable of shielding the resonant mode if no BEOL metals are considered [Hsu and Lin 2018; Jiang et al. 2019; Khelif et al. 2010].

The respective dispersion relations for the RFT on all four silicon wafer orientations with a SiO_2 slab are shown in Figure 5.7. The guided modes are well below the calculated sound cone frequencies for all orientations. Above the sound cone of SiO_2 many highly attenuated modes are found, which allow the cavity modes to couple to the SiO_2 slab. Similarly, the sound cone of silicon can also be discerned from the band structure of the RFT. However, the sound cone of SiO_2 is the limiting factor. Consequently, the underlying wafer orientation choice does not impede the index guiding properties, and stable guided modes are found for all orientations.

Consequently, the RFT can be built without a phononic crystal on an older technology node with a SiO_2-based BEOL excluding the copper layers. However, this is not sufficient for modern radio frequency (RF) stacks which are built with SiCO:H as dielectric material, and therefore, a phononic crystal is mandatory to ensure proper mechanical confinement. This issue signifies

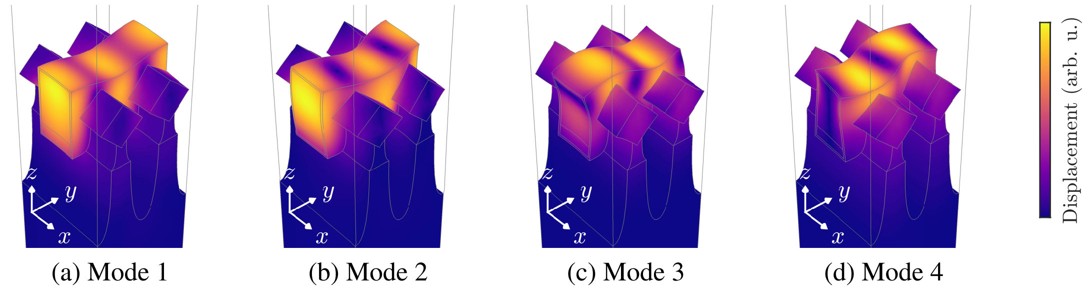

Figure 5.8: Displacement amplitudes for the guided modes at the Brillouin zone edge Y on a (001) wafer with a SiO_2 BEOL slab. The respective unit cell and band structure are shown in Figure 5.3(a) and Figure 5.5(a).

the importance of a matched phononic crystal mirror for low-κ BEOL stacks, as the successful operation of RFT is unlikely at these low observed Q-factors. Hence, the RFT is initially modelled with a SiO_2 slab as it supports the formation of guided modes without a phononic crystal.

Note that the calculated Q-factors of several billion in the case of a SiO_2 slab is an upper limit which just includes the mode guiding related losses [Hamelin et al. 2019; Zhou et al. 2018]. Additional loss mechanisms such as thermoelastic dissipation, the Akhiezer effect, and the Landau-Rumer regime were neglected as their impact is discussed later in Section 6.5. The simulation shows that the low-κ oxide slab does not feature well-guided modes, as shown in Figure 5.5(b), but rather a continuum of highly attenuated and, thereby, lossy modes. However, the four previously observed modes are still distinguishable at a drastically lower Q-factor of several tens, as given in Table 5.1. Moreover, the frequency of the respective modes is shifted to lower frequencies following the choice of the BEOL material and the respective index guiding properties. The lack of guided modes stems from the lower sound velocities within SiCO:H, compared to SiO_2, resulting in worse index guiding characteristics.

5.1.4 Resonant Mode Shapes

Although the RFT may support several guided modes, as marked in Figure 5.5(a), not all of them can be actuated electrostatically. Their general effectiveness for the resonator can be assessed via the displacement profiles of the guided modes, which gives more insight into their behaviour. The eigenvectors, which represent the possible deformations of the structure, can be obtained with the FEM. They are shown in Figure 5.8 for the first four guided modes on a (001) wafer with a SiO_2 BEOL slab. The mode shapes are unfolded along the Floquet-Bloch boundary conditions to cover two adjacent fins for representation purposes, although only one was initially simulated. They are deformed according to the eigenvector obtained from the simulation where the colour code represents the strength of the deformation

$$d = \sqrt{u^2 + v^2 + w^2} \tag{5.1.13}$$

which is calculated from the displacement components u, v and w, which act along the x-, y- and z-axis, of the eigenvector [Jiménez et al. 2021; Bathe 2014; Liu 2003]. Note that the amplitude is arbitrary and not to scale, which follows from normalising mode displacements during computation.

Due to the electrical excitation driving the metal-oxide-semiconductor (MOS) capacitors, only modes with a deformation profile matched to the electromechanical actuation forces can be driven. For a mode to be suitable for the operation of the RFT, the deformation of the eigenmode must match the electromechanical actuation pattern. The electromechanical force within the FEOL is created between the channel and gate in the different FinFETs. Therefore, the actuation pattern is symmetric around each individual fin. The force leads to a deformation of the gate oxide, and thus a breathing motion of the fins.

Therefore, only the third mode (compare Figure 5.8(c)) can be coupled electrostatically [Bahr et al. 2018; Hudeczek and Baumgartner 2020; Hudeczek et al. 2022]. It offers a strong symmetric displacement concerning the individual fins, creating a strong breathing deformation of the FinFET channels. Moreover, it is well confined to the gate plane. Its frequency of 33.104 GHz on a (100) wafer and its mode shape agrees with the literature-reported values [Bahr et al. 2018].

The three remaining modes cannot be coupled to electrostatically as their deformation profile does not match the actuation pattern. The first mode, shown in Figure 5.8(a), exhibits strong symmetric displacements within the gate spanned by the yz-plane. However, it is asymmetric concerning the individual fins leading to a waving motion that cannot be driven electrostatically. The second and fourth mode, depicted in Figures 5.8(b) and 5.8(d), are similar to the first and third mode. However, they feature additional out-of-plane movements along the channel direction along the x-axis, manifesting in an undesired waving motion of the gate along the channel. Following the necessity of a mechanical mode with a symmetric deformation profile concerning each fin and a symmetric displacement confined to the gate plane, they cannot be driven, leaving only the third mode as a viable option to serve as the RFT mode [Bahr et al. 2018; Hudeczek and Baumgartner 2020; Hudeczek et al. 2022].

The deformation profile of the third mode for the three spatial displacements directions u, v and w is shown in Figure 5.9. The mode has small, although symmetric, displacements along the channel direction, with the largest displacements occurring along the y- and z-axis, respectively.

To quantify the deformation within the channel the pressure

$$p = -\frac{1}{3}\sigma_{ii} \quad i = 1, 2, 3 \tag{5.1.14}$$

is introduced as an intermediate figure of merit which is calculated from the stress tensor [Fowler and Ng 2021; Roesler 2007; Gross and Seelig 2018]. Using this figure of merit, all directional dependencies of the stress are obfuscated and shear contributions are neglected. However, it allows for quick identification and assessment of the resonant modes. It is plotted in

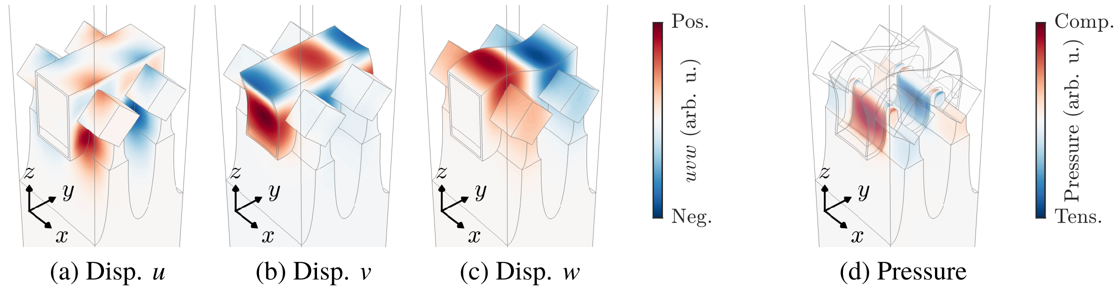

Figure 5.9: Separated displacement components (a) u, (b) v and (c) w for the third guided mode shown in Figure 5.8(c). (d) Differential pressure within the FinFET channels.

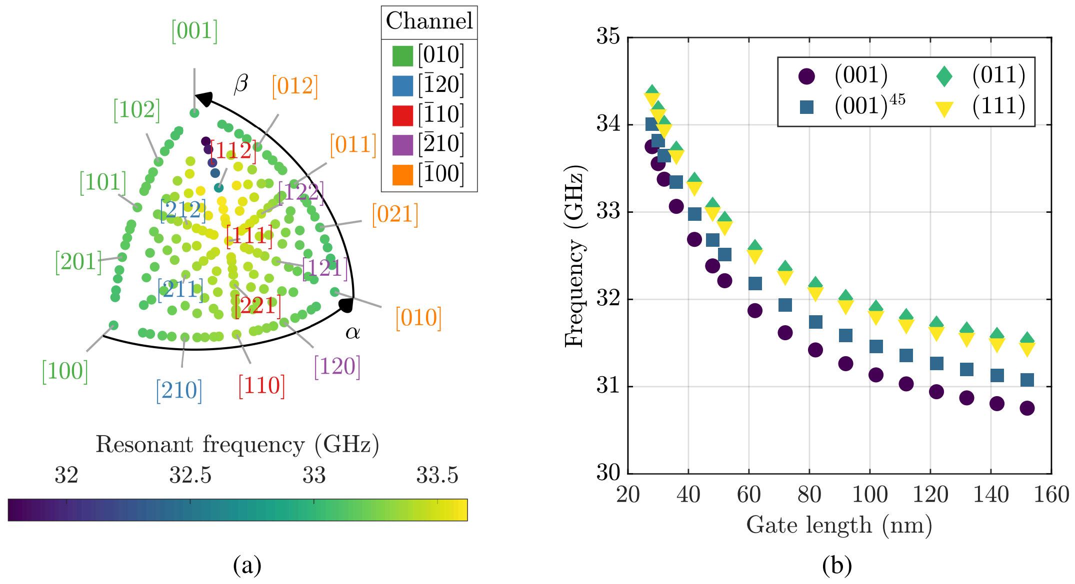

Figure 5.10: (a) Variation of the resonant frequency of a reference device with a gate length of 36 nm for different non-rotated wafer orientations in the first octant in the crystal space. (b) The resonant frequency shift with increasing gate length for the different wafer orientations. ((b) Adapted from [Hudeczek et al. 2022].)

Figure 5.9(d), highlighting the differential deformation between adjacent FinFETs. Moreover, the pressure is concentrated in the channels following the breathing motion of the fins within the gate plane.

The silicon wafer orientation not only influences the sound cone for index guiding, as described in Section 5.1.3, but also directly affects the mechanical response. The changed mechanical properties with the different crystallographic orientations of the underlying anisotropic silicon wafer manifest in a frequency shift of the guided modes, as shown in Figure 5.7.

The RFT will thus have an altered resonant frequency response depending on the substrate choice. Following the cubic symmetry of monocrystalline silicon, a broad overview of the possible frequencies for the previously identified resonant mode of the RFT is given in Figure 5.10(a) for the first octant of possible wafer orientations. Here the colour code indicates the resonant frequency of the RFT mode for each wafer orientation. The naming convention of the wafer normal direction follows the reference frame by J. Turley and G. Sines,

as discussed in Section 3.4, which is swept across the first octant up to the 5th Miller index order [Turley and Sines 1971]. Following the notation in Section 3.4, a counter-clockwise rotation is given by α and the successive pitch of the reference frame by β. Note that only non-rotated wafers with $\theta = 0°$ have been considered. Consequently, several groups of normal directions share the same channel direction, derived from the zone axis $[\bar{k}h0]$, as indicated by the colour of the normal direction. The corresponding gate direction is orthogonal to the wafer normal and channel direction and can be found from the cross-product of those directions.

Interestingly the largest resonant frequencies are obtained for the group sharing the common channel direction $[\bar{1}10]$, or generally due to the cubic symmetry $\langle\bar{1}10\rangle$, for normal wafer orientations between [111] and [223]. For a further increasing β, however, the frequency drops quickly by almost 2 GHz within only $\Delta\beta = 19.4°$ between [112] and [115]. Due to the cubic silicon symmetry, the possible resonant frequencies range from $31.764 - 33.622$ GHz, however, rotated wafers have not been considered, which might add additional possible resonant frequencies.

Since the RFT is ultimately only fabricated on a single wafer type, typically $(001)^{45}$ in a productive IC foundry setting, the frequency is fixed in that regard. Moreover, the RFT is envisioned as a fully integrated device in the IC process. Hence, the frequency shift with other wafer orientations is inconsequential for a later application. Nevertheless, the four commonly presiding orientations (001), $(001)^{45}$, (011) and (111) are further assessed for comparison. While the overall shift in frequency with the substrate choice may be disregarded, a general tune-ability of the frequency on the same substrate is highly beneficial [Lopez et al. 2009].

Typically the resonant frequency of a MEMS relies on the spatial dimensions. In the case of periodic structures, this is mainly the device pitch, with larger distances resulting in lower resonant frequencies. This property, however, is fixed in most foundries and may not be varied across a single wafer. Therefore, only the cavity width, defined by the gate length, can be adjusted. With an increasing gate length, the resonant frequency drops by 3 GHz, for lengths between 28-152 nm, as plotted in Figure 5.10(b). The trend is the same for all four investigated wafer orientations except for the wafer-dependent offset. The shift follows from the out-of-plane breathing motion of the gate, which affects the shape and frequency of the mode. However, further investigation is required. Nevertheless, this behaviour could prove beneficial as it allows the fabrication of RFTs with different resonant frequencies on the same wafer solely by adjusting the gate length of the device, which adds to the versatility and applicability of the RFT in various scenarios.

5.2 Frequency Domain Response

Since the eigenmodes are normalised during computation, it is impossible to judge their effectiveness within the RFT from an eigenmode simulation alone. A fully coupled frequency domain simulation is required to quantify their performance under electrostatic excitation.

The previous eigenmode assumptions are based on a lossless system which is unreasonable in real-world scenarios as such systems do generally not exist. Hence, in terms of damping, additional friction forces need to be considered. Generally, constructing the damping matrix for a large structure is challenging and often difficult as knowledge of the involved damping processes and material properties is lacking, especially in nanostructures. Collecting meaningful material loss data, the computation and experimental determination of the damping matrix is increasingly challenging for large-scale problems. Hence a more convenient empirical approach is pursued. Rather than assigning loss data to every involved material, which typically depends on the frequency and size of the domain, damping may be introduced instead in the form of a viscous damping ratio ζ in the equilibrium equation. The introduction of a damping ratio leads to lossy complex-valued eigenfrequencies. However, it is often an oversimplification of the involved loss mechanisms [Chopra 2012; Liu 2003; Lesieutre 2001].

With the modal superposition technique, as discussed in Section 4.6, the electromechanical response of the RFT can be modelled. This is achieved by modelling both the electrical actuation with sinusoidal drive signals as well as the mechanical response of the structure. The combined behaviour is assessed in a coupled multi-physics simulation, which is handled by the finite-element software.

To properly reflect the driving voltages' differential nature, the unit cell must contain two adjacent FinFETs, as depicted in Figure 5.3. The RFT is biased with a constant voltage of $V_G = 800\,\mathrm{mV}$ applied directly to the tungsten gate and work function material TiN. Similarly, both fins (Si + EPI & SI + and Si − EPI & SI − in Figure 5.3) are biased at a constant drive voltage $V_{drive} = 40\,\mathrm{mV}$. The individual electrical phases, indicated in red and blue, are driven with an amplitude of $v_{drive} = 30\,\mathrm{mV}$ and a phase shift of 180° between adjacent fins, which results in a differential voltage of $v_{drive,diff} = 60\,\mathrm{mV}$. Using this approach, lead and contact resistances are neglected, resulting in an instantaneous voltage response of the structure [Hager et al. 2021; Hudeczek et al. 2022].

In other literature, the driving force was modelled using a 5 MPa mechanical driving force on the surface boundaries of the FinFET channels [Srivastava et al. 2021]. However, the origin of this value is not described. Furthermore, it does not reflect the actual electromechanical force created within the RFT structure, and thus creates most likely arbitrary results.

All four previously observed guided modes are included in the modal superposition simulation, and their Q-factor is limited to 1000 via Rayleigh damping to increase numerical stability. The pressure response, calculated with (5.1.14) from the stress tensor within the channel, is plotted for the reference device on all four wafer variants in Figure 5.11. The corresponding spectrum obtained from the modal superposition simulation features a prominent resonance peak f_R at the third eigenmode frequency. No response is observed for all other previously determined eigenmodes, resulting from the symmetry-forbidden displacements under electrostatic excitation. Also observed is the frequency shift with varying wafer orientations, as shown in Figure 5.10(a), resulting in different resonant frequencies and absolute peak pressures.

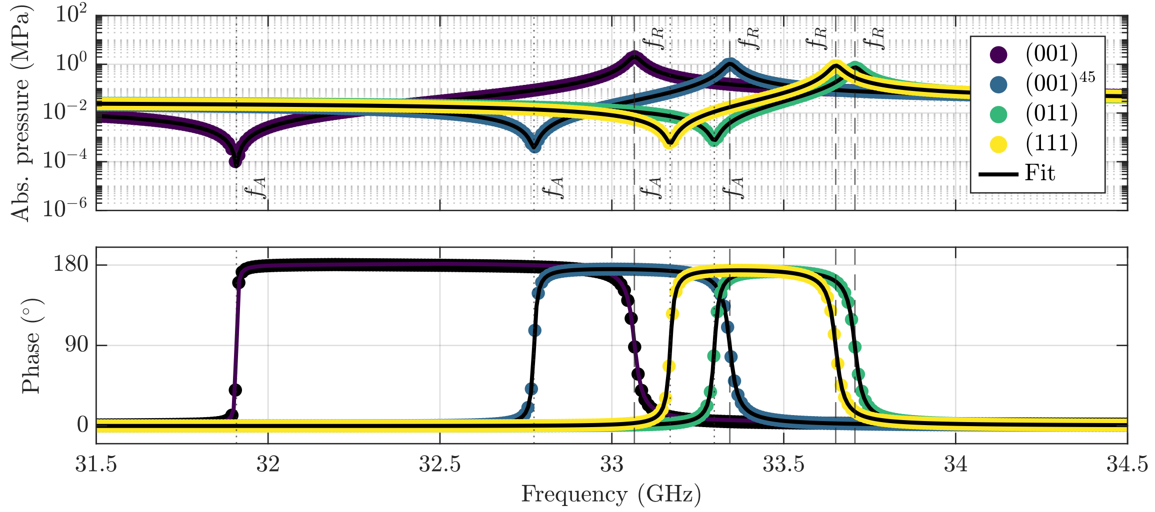

Figure 5.11: Frequency domain response using the modal superposition technique for the reference device with a gate length of 36 nm on the four investigated wafer orientations. (Adapted from [Hudeczek et al. 2022].)

Moreover, each resonance is accompanied by a so-called anti-resonance f_A, where the pressure drops to almost zero, caused by destructive interference in the resonant cavity [Choudhary and Iniewski 2013; Sjövall and Abrahamsson 2008]. From the spectral separation between the resonance and anti-resonance, the electromechanical coupling factor

$$k_{eff}^2 = \frac{\pi^2}{4}\left(\frac{f_A - f_R}{f_R}\right) \tag{5.2.1}$$

is calculated. It describes the conversion efficiency from electrical to mechanical energy and vice versa [Choudhary and Iniewski 2013]. A larger separation of the resonance and anti-resonance hints at an increased coupling efficiency, which is highly desired in MEMS design. It depends mainly on the material composition and geometry of the structure. For the four wafer orientations (001), $(001)^{45}$ and (111) they are 8.64 %, 4.22 %, 2.99 % and 3.53 %, respectively. Putting this value into perspective, it is four to fivefold the value of established MEMS designs [Choudhary and Iniewski 2013; Yang, Lu, et al. 2018; Krishnaswamy et al. 2006; Iqbal and Lee 2018; Zhu et al. 2016; Hui et al. 2013]. However, it is the result of the best-case approximation using a 2-fin unit cell, with each fin being electrically driven, which is not the case in the fabricated design as outlined in Section 2.2.3 [Hager et al. 2021].

The prescribed Q-factor is compared to the Q-factor extracted from a frequency response simulation to verify the simulation setup. The asymmetric shape of the resonance, as shown in Figure 5.11, is common for high Q-factor systems. It can be described analytically with a Fano function

$$F = a + b\frac{2(f - f_R) - q f_{R,BW}}{2(f - f_R) - j f_{R,BW}}, \tag{5.2.2}$$

where a and b are complex-valued pre-factors, f_R the resonant frequency, $f_{R,BW}$ the bandwidth of the resonance and q the Fano parameter which describes the overall symmetry of the resonance

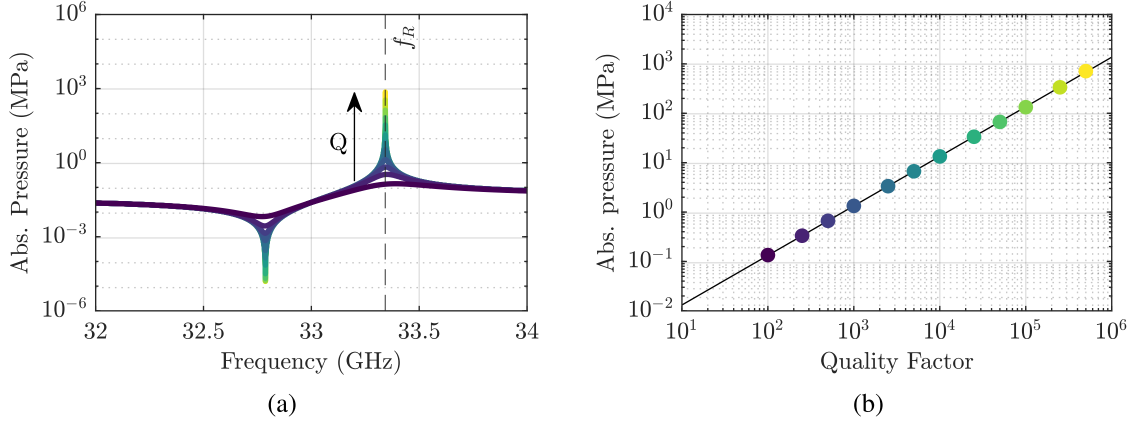

Figure 5.12: (a) The frequency domain response for the reference device with a varying Q-factor. (b) The respective trend of the peak pressure in resonance. (Adapted from [Hudeczek et al. 2022].)

[Fano 1961; Martınez-Argüello et al. 2015]. Fitting the response spectrum enables a subsequent determination of the Q-factor from the resonant frequency and bandwidth via $Q = f_R/f_{R,BW}$. It perfectly matches the prescribed Q-factor of 1000 by the Rayleigh damping formalism. However, this procedure yields only information on the main resonance.

A different method recovers the Q-factor of both the resonance and anti-resonance

$$Q_{R,A} = \frac{\omega_{R,A}}{2} \left| \frac{\partial \varphi}{\partial \omega} \right| \Bigg|_{\omega=\omega_{R,A}} \tag{5.2.3}$$

from the slope of the phase φ transitions [Lakin 1981]. In resonance, it yields the prescribed Q-factor Q_R of 1000. The Q-factor of the anti-resonance Q_A is slightly larger than in resonance, which follows from the under-damping caused by the Rayleigh damping mechanism between the modes of interest. However, little information about the Q-factor of the anti-resonance is found in the literature, as commonly only the spectral position is relevant for the determination of the electromechanical coupling strength [Hodge et al. 2017; Yandrapalli et al. 2019; Yang, Lu, et al. 2018]

Following the linearity of the Rayleigh damping, the Q-factor dependence of the peak pressure is also linear, as shown in Figure 5.12. While at a low Q-factor of 100, the oscillatory behaviour is almost suppressed, the peak pressure scales linearly with the prescribed Q-factor. The linear trend of the absolute pressure in resonance is depicted in Figure 5.12(b). Also, the resonant frequency in a strongly damped system is shifted according to

$$\omega_R' = \omega_R \sqrt{1 - 2\zeta^2}, \tag{5.2.4}$$

where ζ is the Rayleigh damping coefficient discussed in Section 4.5. However, for weakly damped systems with Q-factors above 1000, neither a shift of the resonance nor the anti-resonance is observed [Hirose and Lonngren 2010; Brand et al. 2015; Chopra 2012;

Bachmann et al. 1995].

Moreover, as the RFT has a reported Q-factor of 49 000 and the displacement amplitude is small, the assumption of linear dependence is valid. However, for very small devices, like graphene nanotubes or large displacement amplitudes, non-linear damping mechanisms increase. Since the displacement amplitude is small and the RFT may be considered large, the assumption of a linear damping mechanism is reasonable [Miller et al. 2018; Hudeczek et al. 2022].

Furthermore, this relation can be exploited to further speed up the simulation as the peak pressure at a Q-factor of 1000 may be scaled to an arbitrary Q-factor by

$$p_{new} = p_{1000}\frac{Q_{new}}{1000} \tag{5.2.5}$$

as long as the damping is sufficiently small. Note that this is only valid in resonance since the Q-factor changes the resonance width, and thus the scaling produces meaningless results at all other frequencies [Hudeczek et al. 2022].

In all previous simulations, the n-channel metal-oxide-semiconductor (NMOS) and p-channel metal-oxide-semiconductor (PMOS) were assumed identical. In reality the geometry of the fins is almost unchanged but the material composition of the gate stacks differ. The total capacitance of the stack follows the simplified assumption of a plate capacitance

$$C_{plate} = \frac{A\epsilon_0\epsilon_r}{t_{ox}} \tag{5.2.6}$$

where A is the surface area of the channel in the fin, ϵ_0 the vacuum permittivity, ϵ_r the relative permittivity of the oxide and t_{ox} the thickness of the oxide layer [Zheng et al. 2017; BSIMCMG 2018; Sze 2014]. Since the unit cell is a simplified version of the actual FEOL gate stack, the exact dimensions of the gate oxide thickness are inaccurate. As a result, the capacitance is overestimated for both device types. However, as both PMOS and NMOS devices feature different capacitances, each would require its simulation setup with different spatial properties. However, this would lead to slightly altered resonant frequencies for both device types. However, accurate dimensions of the FEOL configuration are not available. Therefore, both device types are assumed geometrically and material-wise identical for simplicity.

To assess the differences between both device types, the simulations are calibrated to measured capacitance data, for both NMOS and PMOS devices, by introducing an effective permittivity for the high-κ oxide layer. The permittivity of $\epsilon_r = 25$ for HfO_2 is therefore scaled to match the simulation to the measurements, as shown in Figure 5.13. The experimental capacitance was extracted from a two-port RF S-parameter measurement, in-between 25 – 40 GHz, for both NMOS and PMOS devices. It was calculated for a single fin from a larger device with four parallel gates and 30 fins. The scaling factors for the effective permittivities were calculated to $\epsilon_r/\epsilon_{nmos} = 4.05$ and $\epsilon_r/\epsilon_{pmos} = 3.2$ for the NMOS and PMOS, respectively. The adjusted simulated capacitances are in excellent agreement with the experimental data. Both measured

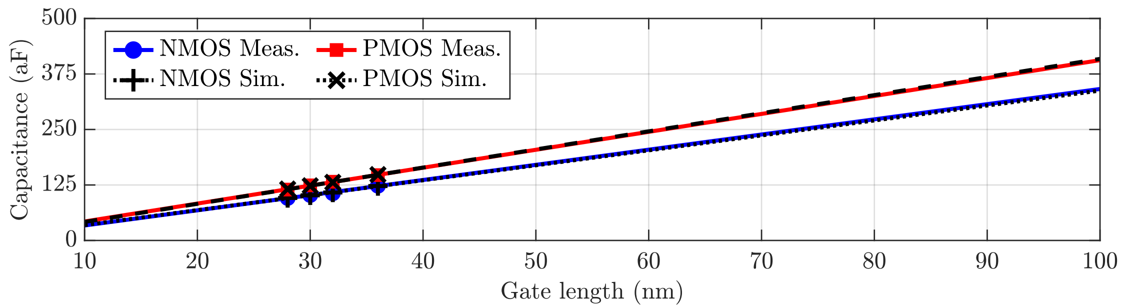

Figure 5.13: Calibrated MOS capacitance for a single simulated fin and single gate structure to measured data for both NMOS and PMOS devices at four typical FinFET gate lengths. (Adapted from [Hudeczek et al. 2022].)

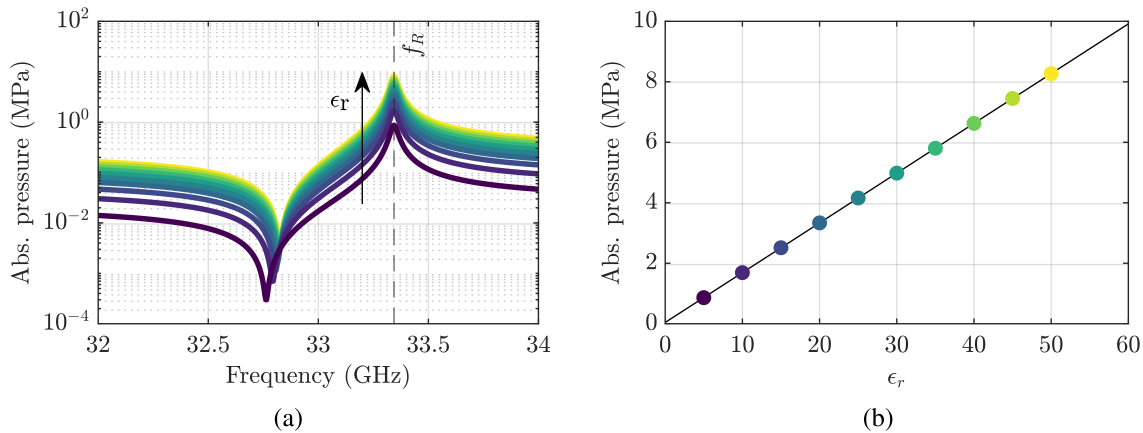

Figure 5.14: (a) The frequency domain response for the reference device with a varying permittivity ϵ_r of the high-κ oxide layer. (b) The respective trend of the peak pressure in resonance. (Adapted from [Hudeczek et al. 2022].)

and simulated data are fitted with linear regression, showing a good agreement of the trend at larger gate lengths. After the adjustment, the PMOS has an almost 25 % increased capacitance over the corresponding NMOS, which follows from the different gate stacks.

The impact of the changed permittivity on the frequency response of the RFT is shown in Figure 5.14(a) for selected values. The resonant frequency of the RFT is unchanged with an altered permittivity, which is reasonable as it solely depends on the geometrical and mechanical material parameters. With an increasing permittivity, the pressure in the FinFETs of the RFT increases. This change is linear, as shown for the peak values in Figure 5.14(b), which are fitted with linear regression. This behaviour arises from the linear dependence of the electrostatic force on the permittivity, which acts on the MOS capacitors [Choudhary and Iniewski 2013]. Interestingly, the frequency of the anti-resonance shifts with an increasing permittivity to higher frequencies. This shift signifies a reduction in electromechanical coupling efficiency, which is commonly affected by the static capacitance of the MEMS [Hager et al. 2021; Choudhary and Iniewski 2013; Hong et al. 2016; Hudeczek et al. 2022]. Following this adjustment, the PMOS offers a 25 % larger pressure than the NMOS at the same voltage bias conditions [Hudeczek et al. 2022].

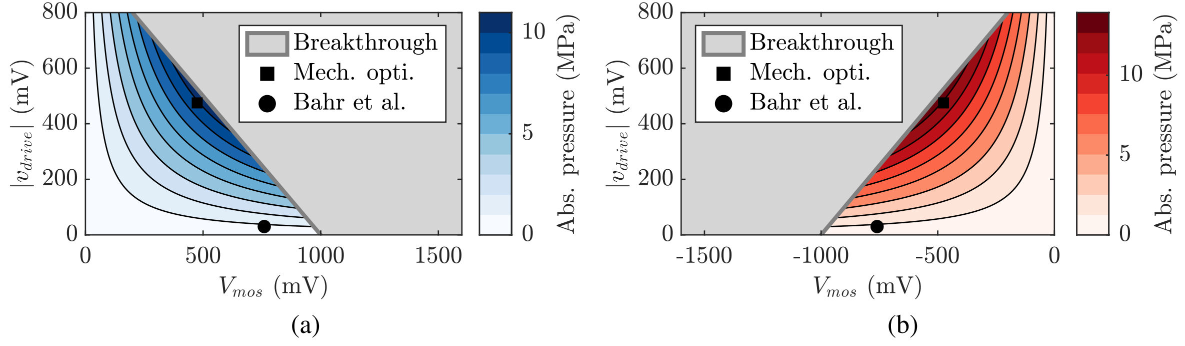

Figure 5.15: Peak pressure in the FinFET channel of (a) NMOS and (b) PMOS RFTs for a constant gate voltage $V_{gate} = 0.8\,\text{V}$ and varying drive bias conditions and amplitudes. The bias condition by Bahr et al. is from [Bahr et al. 2018]. (Adapted from [Hudeczek et al. 2022].)

The simulations up to now used the bias conditions of Bahr et al. which are $V_{gate} = 0.8\,\text{V}$, $V_{drive} = 40\,\text{mV}$ and $v_{drive} = 30\,\text{mV}$ [Bahr et al. 2018]. However, the force within the drive MOS capacitor depends on the bias conditions, which are varied in the following to find the optimal bias voltages. To ensure the nominal operation of the sense transistors, the gate voltage is kept at the voltage of $V_{gate} = 0.8\,\text{V}$ for the NMOS RFT and $V_{gate} = 0\,\text{V}$ for the PMOS RFT, respectively. The absolute pressure inside the channel can be improved by optimizing the drive voltage amplitude and the bias voltage applied to the drive. Here the absolute voltage across the MOS junction within the gate stack

$$V_{mos} = V_{gate} - V_{drive} \tag{5.2.7}$$

is defined. The resulting fin pressure in NMOS and PMOS devices is shown in Figures 5.15(a) and 5.15(b) for varying drive and bias voltages. The larger the absolute bias voltage $|V_{mos}|$ across the gate oxide, the larger the electromechanical force and, consequently, the pressure that acts on the channel. The additional modulated voltage at the drive will thus also provide larger pressures with increasing amplitude since the absolute voltage difference increases. This trend is limited by the breakdown voltage of the gate oxide $V_{gate} - (V_{drive} + |v_{drive}|) > 1\,\text{V}$, as well as the forward bias condition of the well-diodes. However, for both NMOS and PMOS, the gate oxide breakdown condition is reached before the well-diodes open up. Thus, the forbidden voltage region is indicated by the grey-shaded area, where no operation of the RFT is possible. When factoring in an additional 50 mV safety margin on the breakdown condition, the optimum bias point for the highest fin pressure can be found, as marked by a square in Figure 5.15. A mechanical improvement factor of approximately ten over the bias values used by Bahr et al. can be achieved by adjusting the bias point to $V_{drive} = 325\,\text{mV}$ for the NMOS and $V_{drive} = 475\,\text{mV}$ for the PMOS with a modulated amplitude of $v_{drive} = 475\,\text{mV}$ for both [Bahr et al. 2018]. However, to maintain comparability, the following simulations are carried out at the initially proposed bias values.

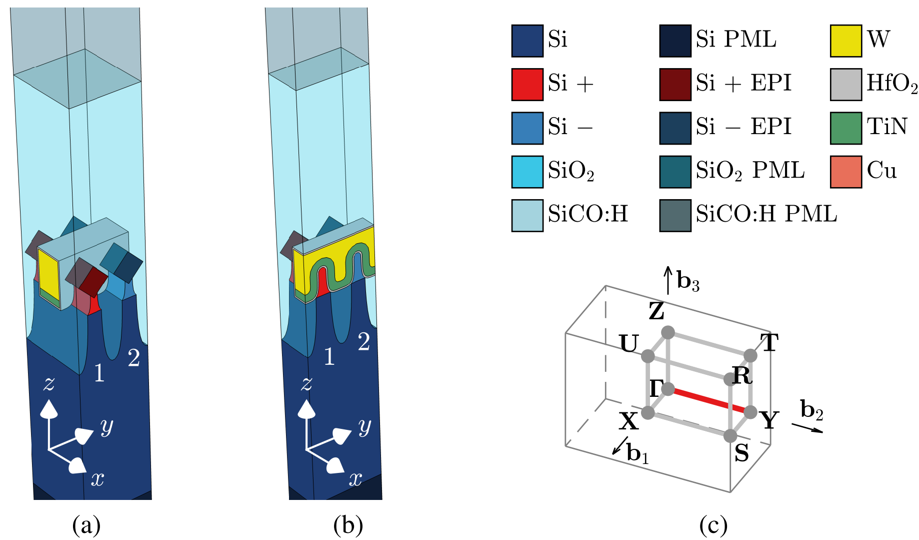

Figure 5.16: Ideal 2-fin unit cells with a SiO_2 BEOL (a) showing the full geometry full-gate and (b) a simplified half-gate variant, exploiting symmetric properties. Also shown in (c) is the respective Brillouin zone. ((a) and (b) adapted from [Hudeczek et al. 2022].)

5.3 Extended Simulation Setups

The previous simulations assumed an idealised connection scheme where every fin is electrically connected. This connection pattern, however, is not viable as closely spaced contacts are not possible with the available lithography and processing. Moreover, the previous simulations reflected an RFT with an infinite number of parallel gates through symmetric boundary conditions. The DOFs must first be reduced to stay within the available computational resources to simulate larger structures. These larger structures include a unit cell extended to 14 fins or a finite number of gates.

5.3.1 Symmetry Simplifications

The used mesh is already optimised for the trade-off between simulation speed and accuracy. A further increase of the meshing resolution, although it would improve the accuracy, would have a detrimental influence on the simulation runtime due to memory and CPU limitations. Hence to maintain the same meshing resolution and sufficiently small DOFs, spatial symmetries of the simulation can be exploited. While the RFT structure was initially already reduced to its smallest periodic subpart, being one fin for the eigenmode and two for the frequency domain simulation, further simplifications are necessary.

The complete RFT is also symmetric concerning the gate plane from a spatial point of view. Therefore, only half of the unit cell can be modelled using symmetric boundary conditions, potentially reducing the DOFs by a factor of two, by cutting along the gate symmetry plane, as shown in Figure 5.16 [Hudeczek et al. 2022]. Whereas the full-gate variant uses Floquet-Bloch boundary conditions in all lateral directions, the reduced half-gate unit cell is only modelled with periodic boundary conditions along the gate direction, whereas the channel direction along

the x-axis is modelled with symmetric boundary conditions. They suppress surface-normal displacements of the boundary facets along the x-axis while only allowing free deformation in the corresponding yz-plane.

While this procedure is allowed from a spatial point of view, it poses a challenge in the presence of anisotropic materials. Following the cubic symmetry of the silicon wafer, the spatial symmetry plane might not coincide with the cubic symmetry of the material properties leading to inaccuracies in the simulation. A lossless simplification should be possible if the spatial and material symmetry planes are identical. This hypothesis is tested with Poisson's ratio for a uniaxial displacement along the y-axis, which is expected to be exerted by the electrostatic force [Hudeczek et al. 2022].

Poisson's ratio is calculated in the xz-plane for the four investigated wafer orientations shown in Figures 5.17(a) to 5.17(d). This representation quantifies the displacements in the plane orthogonal to the loading direction, thus highlighting any asymmetric behaviour caused by the actuation which occurs along the channel direction. The results are plotted in Figures 5.17(e) to 5.17(h). The solid lines are calculated analytically with (3.7.5), while the marker values were simulated with the FEM. While for the first three wafer orientations shown in Figures 5.17(e) to 5.17(g), the gate deforms equally on both sides under uniaxial stress along the gate, the fourth configuration features an asymmetric Poisson's ratio concerning the symmetry plane. Consequently, the fin will deform stronger towards one side of the gate, creating an asymmetric deformation profile. The reduced half-gate unit cell does not capture this behaviour, which suppresses surface-normal displacements. Note that also the selection of the modelled unit cell half will affect the deformation. As the reduced half-gate unit cell is modelled for the left half-space, looking from the notch of the wafer onto the xz-plane, Poisson's ratio is assumed symmetrical to the left side, as indicated by the dashed line and square markers in Figure 5.17(h). For uniaxial displacements along the wafer's normal direction, all Poisson's ratios are symmetric concerning the gate plane, which is not shown.

The displacement profiles of the RFT eigenmodes for the half-gate and full-gate unit cell, as depicted in Figure 5.18 follow the behaviour observed for the Poisson's ratios in Figure 5.17. The RFT modes of the full-gate unit cell on the first three wafers orientations, shown in Figures 5.18(a) to 5.18(c), are symmetric concerning the gate, thereby creating a breathing motion of the gate and fins. Both the resonant frequency and deformation match well with the respective half-gate mode displacements, as depicted in Figure 5.18(e) to 5.18(g). This is in line with the symmetric assumption of Poisson's ratio in those cases.

A mismatch for the displacement and resonant frequency is observed for the (111) wafer, shown in Figure 5.18(d) and Figure 5.18(h). The mode exhibits strong anti-symmetric out-of-plane gate displacements, which force the gate into a wiggling motion. This behaviour is suppressed in the half-gate unit cell, which manifests in a slightly shifted resonant frequency and altered deformation pattern.

No difference between the half-gate and full-gate simulations can be discerned for the first

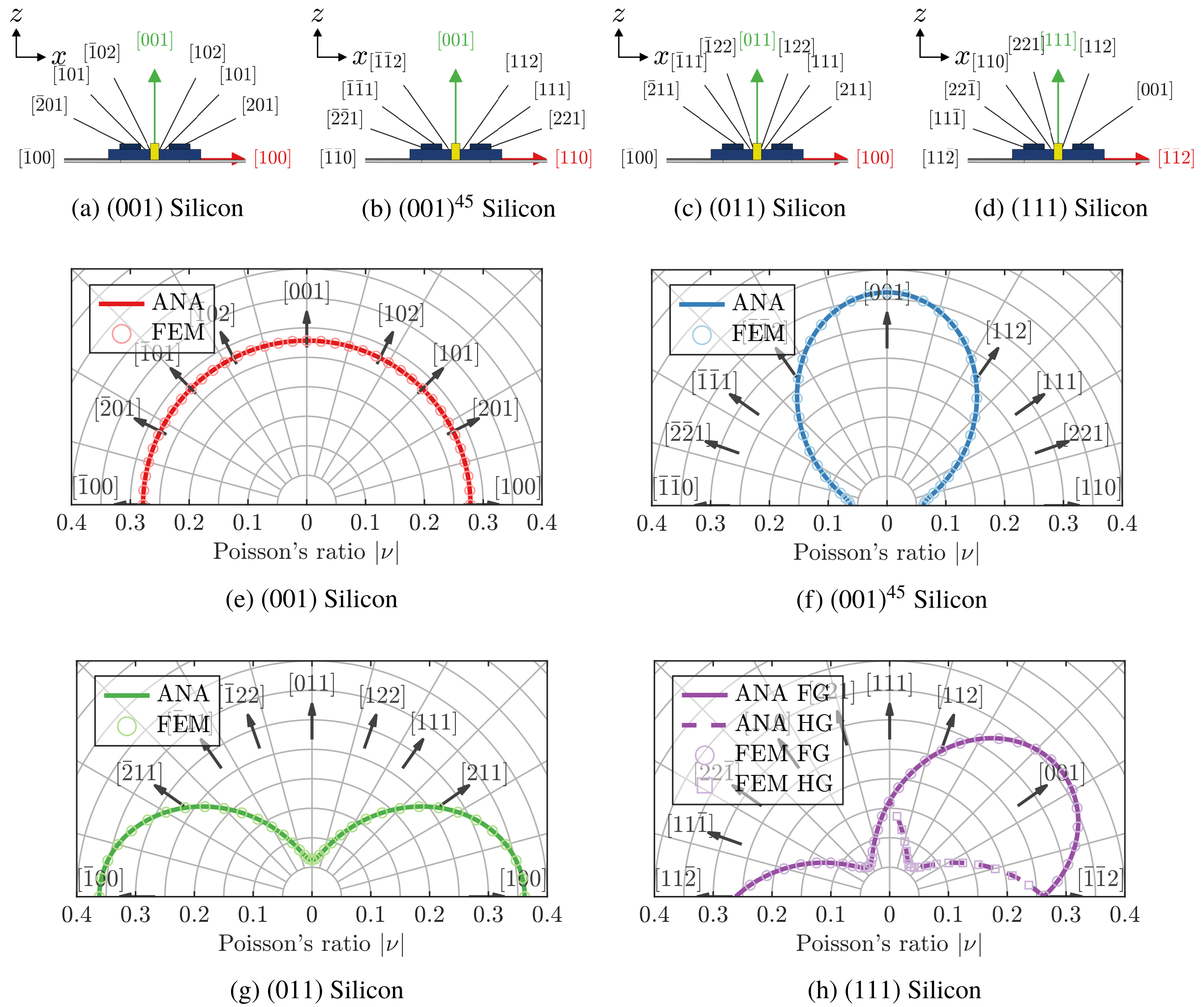

Figure 5.17: Different wafer orientations (a) to (d) used to calculate the Poisson ratio. The corresponding analytic (ANA) solution and FEM simulated values of the Poisson ratio in polar coordinates for the half-gate (HG) and full-gate (FG) assumptions are plotted in (e) to (h).

three wafer orientations. Hence a lossless simplification is possible if the symmetry plane coincides with one of the symmetry planes of the underlying anisotropic wafer material. Note that this assumption suppresses all other true out-of-plane gate modes, as shown in Figures 5.8(b) and 5.8(d). Hence, the gate may only have symmetric rather than anti-symmetric modes concerning the symmetry plane. This behaviour is also observed in the band structure for the half-gate unit cell, as depicted in Figure 5.19 for all four wafers. While previously four dominant guided modes existed (compare Figure 5.7), all out-of-plane gate modes are now suppressed, leaving only the two guided modes shown in Figures 5.8(a) and 5.8(c). Interestingly, the effect of the shear sound cone in anisotropic silicon is also suppressed compared to the full-gate simulation. The limiting sound cone is set by the SiO_2 slab, which is still fully present and unchanged by the simplification, and thus has no further consequences.

The actual extent of the simplification on the frequency response is tested on four wafer orientations at several device gate lengths. For each configuration, the resonant eigenmode

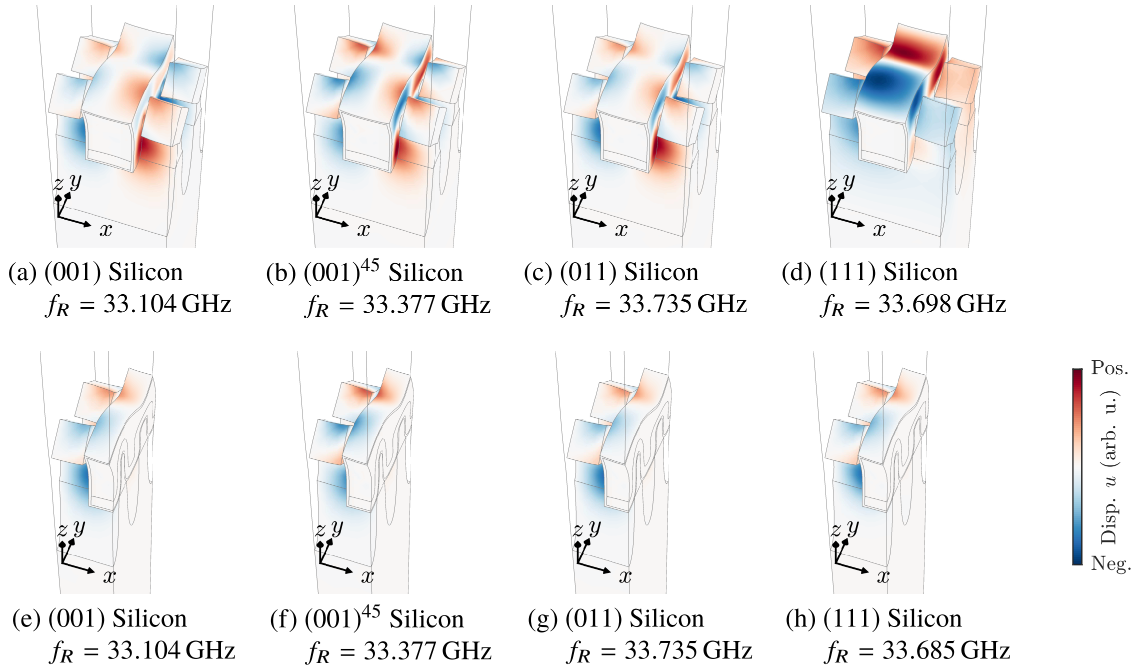

Figure 5.18: Comparison of displacement profiles and resonant frequencies of the RFT mode for the (a) to (d) full-gate and the (e) to (h) half-gate simulations on different orientations.

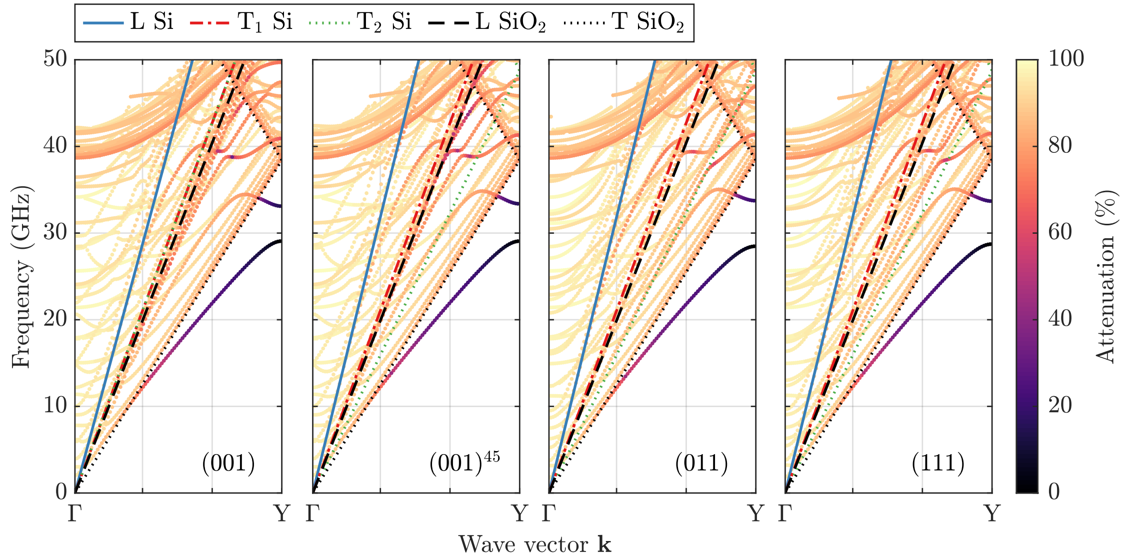

Figure 5.19: Band structure and evolution of the guided modes along Γ−Y for different silicon wafer orientations using a half-gate simulation.

was simulated and used in a subsequent modal superposition simulation. The resulting peak pressures and resonant frequencies are compared in Figure 5.20 between both simulation setups [Hudeczek et al. 2022]. The half-gate and full-gate simulations are almost identical for the first three wafer orientations (001), (001)^{45} and (011), with only minor deviations in the low kilopascal and few hundreds of kilohertz range, as expected from the symmetric Poisson's ratio. The deviations for the fourth wafer orientation (111) are larger, with a more pronounced frequency shift in the megahertz range. However, given the still small absolute change, this may be

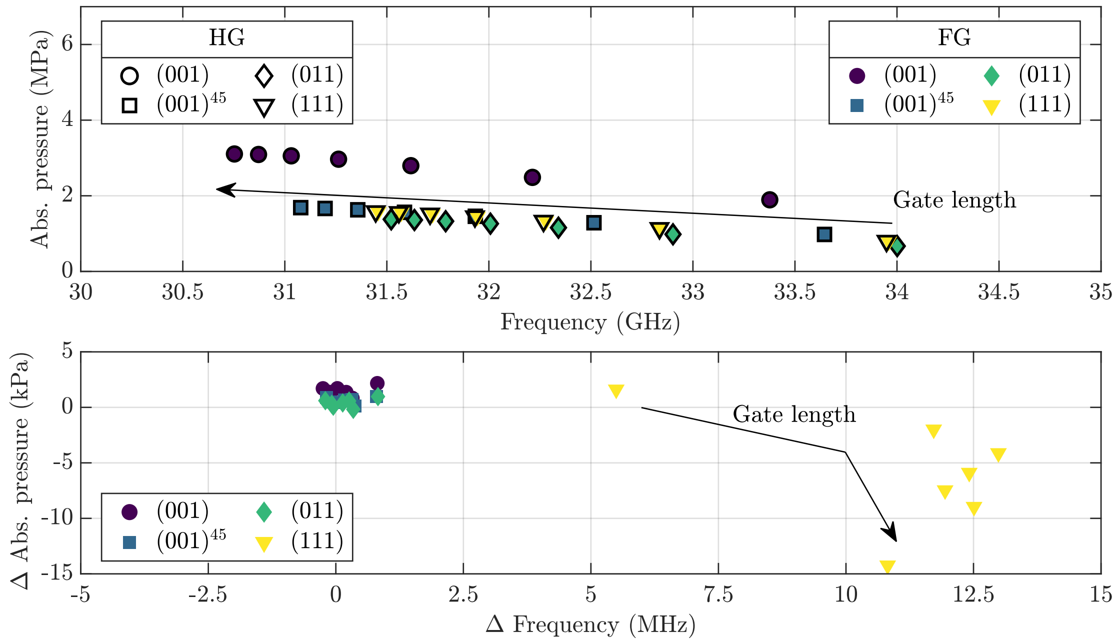

Figure 5.20: A comparison of the full-gate (FG) and half-gate (HG) peak pressures and resonant frequencies for different gate lengths and wafer orientations is shown in the upper plot. The lower plot shows the respective differences in peak pressure and frequency between the half-gate and full-gate simulations.

considered negligible. This is justified as already the full-gate unit cell is only an approximation of the actual FEOL stack, which should lead to a more substantial shift in frequency when compared to the actual fabricated structure. Nevertheless, symmetry simplification reduces the DOFs by a factor of two, reducing the involved simulation times without sacrificing the meshing accuracy.

5.3.2 Finite Number of Parallel Gates

Using the symmetrical simplification, larger simulation volumes can be investigated. In the previous simulations, the RFT was assumed infinite in all lateral directions by using Floquet-Bloch and symmetric boundary conditions. This structure did not accurately represent the fabricated device, which features a finite number of parallel gates surrounded by additional dummy gates for structural integrity. While the cavity length along the gate may still be assumed as infinite, the width is limited by a few parallel gates. Consequently, the impact of a varying number of parallel gates and corresponding protective dummy gates is investigated with a modified unit cell as sketched in Figure 5.21(a). Analogously to the half-gate unit cell only half of the cavity width is modelled with a symmetric boundary condition at the centre. It is based on the 2-fin unit cell but is also finite along the channel direction by introducing an additional perfectly matched layer along the x-axis, which absorbs all incident mechanical waves. The depicted unit cell represents a device with ten parallel gates (G_1 to G_{10}), where G_1 to G_5 are modelled with the chosen symmetry. The simulation also includes three dummy gates, commonly used in this technology to improve device homogeneity. The fins extend till

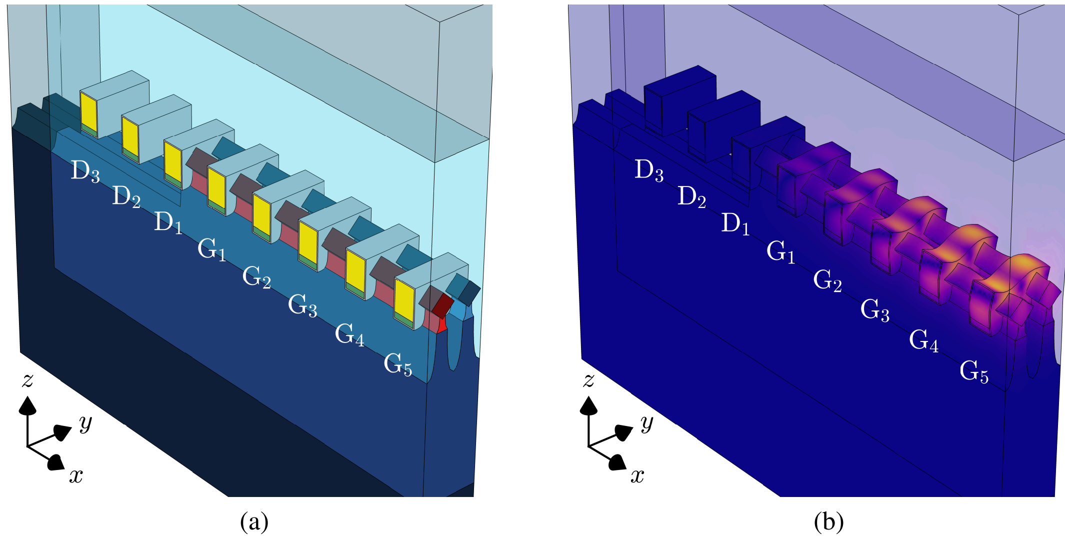

Figure 5.21: (a) The ideal 2-fin unit cell with a finite number of parallel gates G and dummy gates D using a symmetric boundary condition at the centre. (b) Respective displacement profile of the RFT mode in resonance.

the middle of the first dummy gate, which is not electrically active. Due to the increased size and higher DOFs, the structure exhibits a larger number of guided modes in contrast to the previously investigated infinite 2-fin unit cell.

While the structure also supports the RFT mode, as shown for the respective displacement profile in Figure 5.21(b), many parasitic modes at similar frequencies occur with an increasing number of gates. Here the whole structure may be considered as several weakly coupled resonators, where each gate contributes to the overall resonance [Jiménez et al. 2021; Chopra 2012; Khelif and Adibi 2016]. The number of parasitic resonances scales with the number of parallel gates, as plotted in Figure 5.22. The pressure responses for a different gate count are computed for the 20 closest modes to the main resonance on a (001)[45] wafer, and the results are plotted in Figure 5.22. The spectra are normalised and centred around the RFT mode, which was selected using the following criteria: All gates must be in phase, as shown in Figure 5.21(b). Further, the deformation needs to be symmetric around the individual fins, with most deformation occurring orthogonal to the channel in the yz-plane. The largest pressure still occurs for the main resonant mode of the RFT, however, with an increasing number of gates, the number of parasitic resonances increases, as indicated by the markers. With each additional gate, an extra spurious resonance emerges, and the spectral distance to the first spurious resonance decreases. While they are less prominent, they still pose a risk for the RFT as the system may not successfully lock onto the required mode in a later envisioned IC application. Although 20 modes were included in the simulation not all of them can be coupled to electromechanically as discussed in Section 5.1.4.

Although the spectral distance between resonance and anti-resonance shrinks with each additional gate, the electromechanical coupling coefficient remains almost constant as the

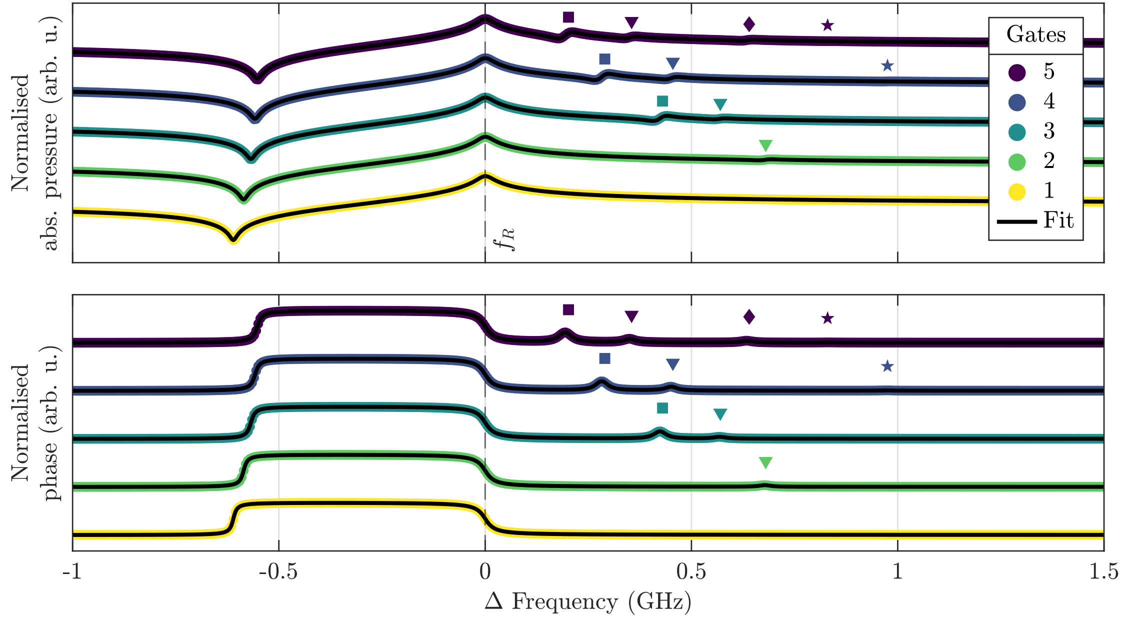

Figure 5.22: Normalised and centred frequency domain response to the main RFT mode for a varying number of parallel gates. Symbols mark spurious modes.

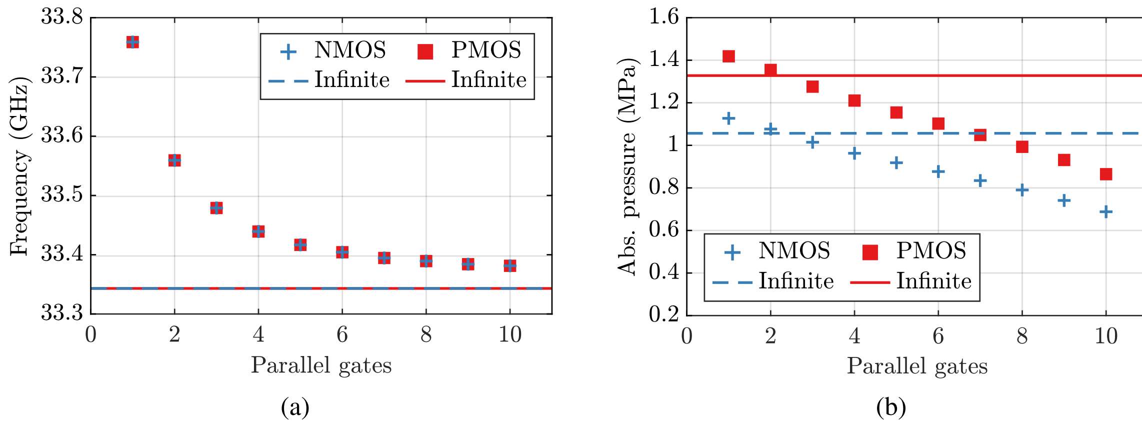

Figure 5.23: (a) The change in resonant frequency for an NMOS and PMOS RFT with the number of gates. (b) The averaged peak pressure within all parallel gates with increasing gate number. ((a) adapted from [Hudeczek et al. 2022].)

resonant frequency shifts to lower frequencies with each additional gate, as shown in Figure 5.23(a). The resonant frequency decreases with an increasing number of gates, but it remains elevated compared to the infinite unit cell. Here reasoning similar to the different gate lengths applies, where a shorter cavity width yields an increased resonant frequency. Interestingly, the number of dummy gates, which was swept from one to three, does not affect the resonant frequency. This follows from the mode shape of the RFT mode, depicted in Figure 5.21(b), which exhibits a strong deformation profile in the centre of the cavity, which levels off towards the last true gate G_1. Hence, as the fins are recessed beneath the dummy gates, no displacement transfer occurs, and the deformation fully decays after the first dummy gate. Unsurprisingly, the NMOS and PMOS feature the same resonant frequency discussed for the

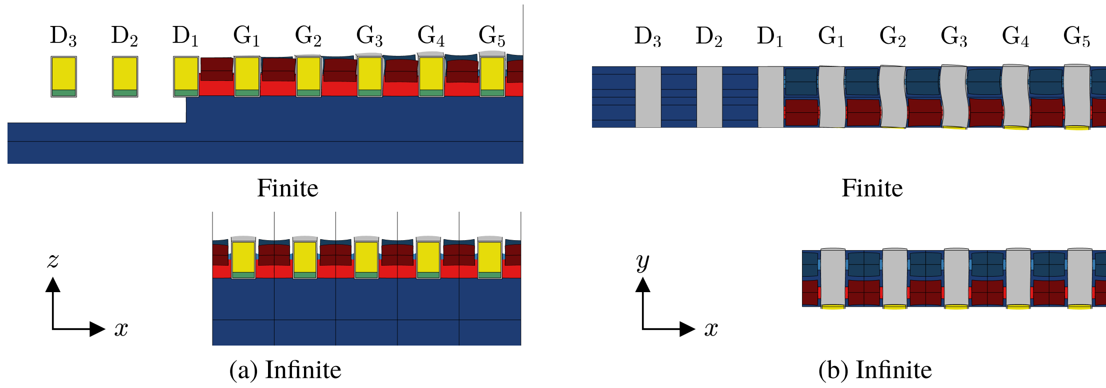

(a) Infinite (b) Infinite

Figure 5.24: Comparison of the displacement profiles of the simulation with a finite number of gates against the infinite unit cell as shown in (a) from the side and (b) from the top. The finite simulation is shown in the top row, and the infinite unit cell, unfolded at the boundary condition, is shown in the bottom row.

effective permittivities in Section 5.2.

Also of interest is the average pressure inside all active gates, as plotted in Figure 5.23(b). While at a single finite gate, the pressure is slightly elevated compared to the infinite 2-fin unit cell, the pressure drops almost linearly with an increasing number of gates. Again the PMOS is offset by the ratio of the permittivities. Note that the pressure is not identical in all gates, as observed for the decaying displacement in Figure 5.21(b), only the averaged pressure from all gates is of interest as the sense transistor is wired with all gates in parallel, effectively averaging the individual contributions [Hudeczek et al. 2022].

The reduction in pressure arises from the mutual obstruction of movement in neighbouring gates. As the RFT mode is differential concerning neighbouring fins and symmetric concerning the gate, as shown in Figure 5.9, the gate is expanding and contracting in a breathing motion. Since this behaviour occurs in all neighbouring gates simultaneously, adjoining gates above the same fin contract and expand in phase, which impedes each other's displacement amplitude.

Looking at the xz-plane cutting through the gates, as shown in the top sketch in Figure 5.24(a), the decreasing amplitude towards the last true gate is visible. For comparison, the displacement profile of the infinite unit cell is shown in Figure 5.24(a) after unfolding the displacement of a single periodic unit cell at the Floquet-Bloch boundary conditions. Similarly, strong out-of-plane deformations can be observed in the xy-plane for the finite simulation. Note that both simulations for the infinite and finite unit cell were carried out on a (001)[45] wafer, which should exhibit symmetric displacements around the individual gates without out-of-plane gate displacements, as discussed in Section 5.3.1. However, due to the mutual obstruction, the gates in the finite simulation in Figure 5.24(b) are forced to expand laterally along the x-axis which does not occur in the infinite periodic unit cell. This behaviour is also present when the full cavity width is modelled without simplifications, as sketched in Figure 5.25 for an RFT with five gates and one dummy gate (D_1 and D_1') on either side. Analogously comparing the half-gate and full-gate unit cells, the symmetric boundary condition at the centre has a negligible impact on the actual eigenmode shape and resonant frequency.

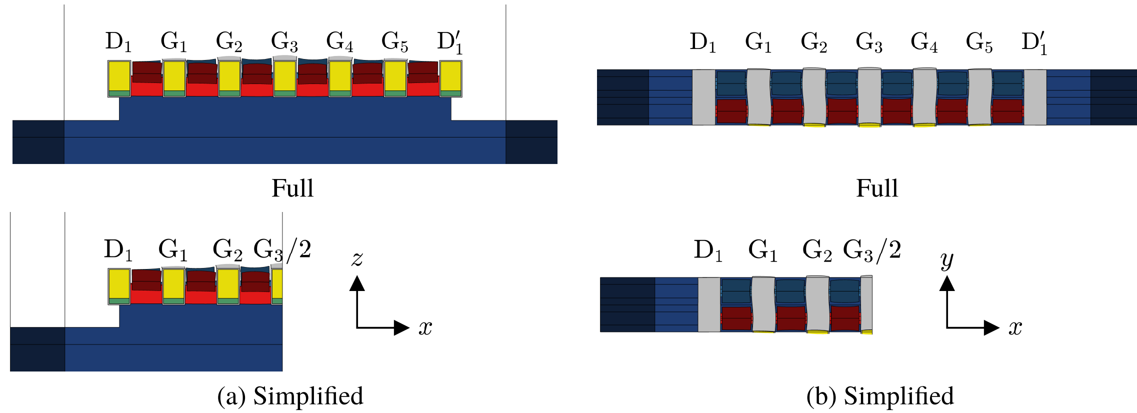

Figure 5.25: Comparison of the displacement profiles of a structure with a finite number of gates without a symmetric boundary condition at the centre to a simulation with only half of the structure as shown in (a) from the side and (b) from the top.

Consequently, fewer parallel gates are preferred to obtain the best performance, with the least spurious modes and the highest fin pressure. However, a larger RFT provides an increased sense current which might be beneficial for the experimental detection, as discussed in Section 5.5.3.

5.3.3 Extended 14-Fin Unit Cell

All previous investigations were centred around the ideal 2-fin unit cell, which cannot be manufactured due to technology constraints. Nevertheless, it provides the upper limit as a best-case approximation, where each fin is contacted separately. Following the foundry design rule checks the tightest possible integration scheme, with distinct electrical phases, requires groups of three adjacent fins to be jointly connected to the same electrical phase. Furthermore, as required by the minimum spacing distance of electrical FEOL contacts combined with the electrical phase requirements, neighbouring electrical phases must be separated by four intermediate electrically floating fins. Consequently, an expanded unit cell with 14 fins, as sketched in Figure 5.26(a), is required to capture the differential electrostatic actuation principle and resulting pressures. In this configuration, fins 3, 4 and 5 are connected to the drive-plus and fins 10, 11 and 12 are connected to the drive-minus, as discussed in Section 2.2.3. Furthermore, the epitaxial source-drain contacts are omitted on the electrically floating fins. Similarly to the 2-fin unit cell, the structure supports the differential RFT mode, as depicted in Figure 5.26(b). However, due to the removal of the intermediate epitaxial contacts, the frequency is shifted by a few megahertz to a lower frequency. Considering the response of a 14-fin unit cell with epitaxial contacts on every fin, the resonant frequencies are almost identical with. Hence the epitaxial contacts are included in the 14-fin unit cell to ease comparability. Moreover, more resonant modes occur due to the increased simulation volume but their spectral distance is in the GHz region, and they are thus neglected in this investigation.

Due to the new connection scheme, the actuation of the resonant eigenmode is expected to be degraded since the electrical polarity does not match the mechanical phase for some

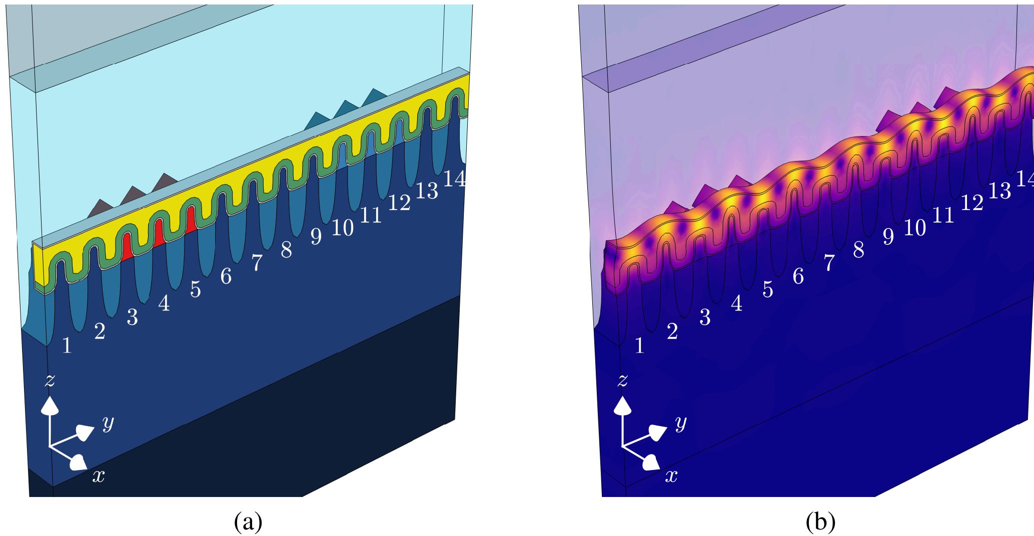

Figure 5.26: (a) Illustration of the fabricated 14-fin unit cell of the RFT. (b) The respective displacement of the resonant eigenmode mode in resonance.

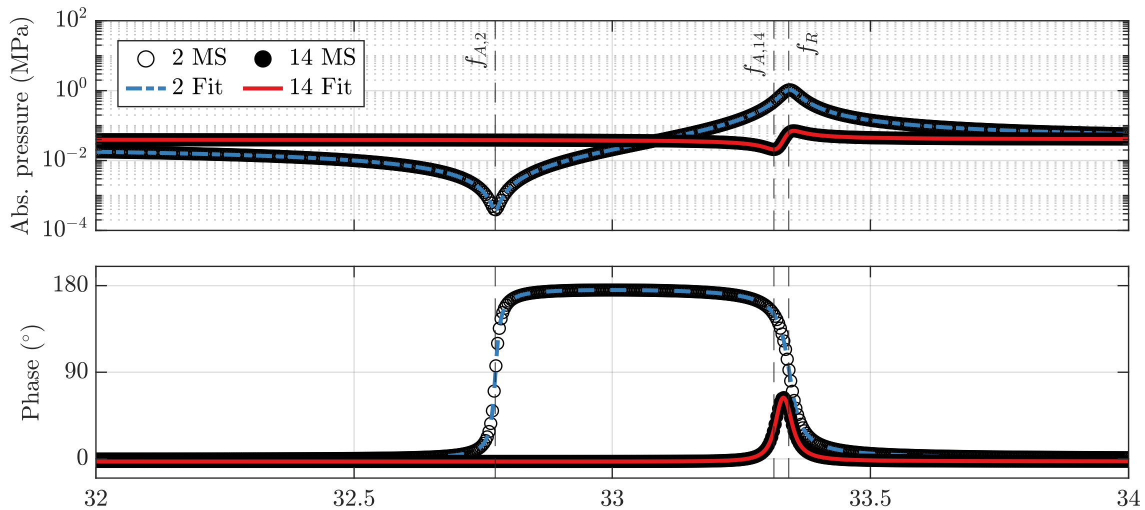

Figure 5.27: Comparison of the frequency domain response for an infinite half-gate simulation of a 2-fin and 14-fin unit cell with their respective Fano fit. (Adapted from [Hager et al. 2021].)

fins [Bahr et al. 2018; Hager et al. 2021; Hudeczek et al. 2022]. This behaviour is also discussed in Section 2.2.3. As a result of the altered connection scheme, the frequency domain response of the 14-fin unit cell is strongly degraded compared to the 2-fin unit cell, as shown in Figure 5.27. While the resonant frequency remains unchanged as expected, the peak pressure and electromechanical coupling are strongly reduced. Whereas the 2-fin unit cell managed a peak pressure of 1.328 MPa, the equivalent 14-fin variant only reached 77.665 kPa, equivalent to a 17-fold reduction, at the same bias conditions. The pressure is evaluated as the average from the fins 3 to 5, as all fins beneath a common contact are connected in parallel. Therefore, the pressures from two fins in each three-fin group cancel each other, leaving only one actively contributing fin. Hence, the resonant mode is only driven by two fins out of 14, resulting in an overall lower peak pressure. Moreover, the coupling efficiency diminishes to only 0.21 % for the

14-fin unit cell, which si calculated from the antiresonance $f_{A,14}$ and resonance frequency f_R with (5.2.1), marking a 20-fold reduction over the ideal 2-fin unit cell with 4.22 ‰ [Hager et al. 2021]. The data is also fitted with a Fano function which yields a Q-factor of 1000 for both unit cells.

Nevertheless, the pressure is only an averaged metric, used as an intermediate figure of merit, and the RFT was modelled at a strongly reduced Q-factor of 1000 which only partially describes the performance of the RFT. The trends, however, may be carried over to full piezoresistive modelling of the transconductance in Section 5.5.3, which gives a better approximation of the actual performance of the RFT.

5.4 Equivalent Isotropic Materials

Although the eigenmode and frequency response yield valuable information on the performance of a MEMS, its transient behaviour must also be considered. While the frequency domain response can be modelled using the modal superposition technique, this is not possible for the time-dependent simulations. This follows from the limitations of the FEM software which does not allow a constant voltage bias, which is required for the gate and FinFETs, during a transient modal superposition simulation. Hence, the transient response of the RFT, subjected to a sinusoidal signal, must be modelled with all DOFs, drastically increasing simulation time and memory consumption.

The symmetry simplifications for those simulations are insufficient, as the number of DOFs must be reduced even further. In those instances, the RFT can be modelled using a 2D approximation. However, as some of the involved materials are mechanically anisotropic, they cannot be fully described using lower-dimension approximations. To circumvent this problem at lower dimensions, equivalent isotropic materials can be constructed for their anisotropic counterpart from the mean of the Reuss and Voigt averages [Mainprice and Humbert 1994; Healy et al. 2020; Man and Huang 2011; Luan et al. 2018; Date and Andrews 1969]. The Voigt averages of Young's and the shear modulus are defined as

$$E_V = [(c_{11} + c_{22} + c_{33}) + 2(c_{12} + c_{23} + c_{31})]/9 \tag{5.4.1}$$

and

$$G_V = [(c_{11} + c_{22} + c_{33}) - (c_{12} + c_{23} + c_{31}) + 3(c_{44} + c_{55} + c_{66})]/15 \tag{5.4.2}$$

which are computed from the components of the compliance tensor. Similarly the Reuss averages are computed from the components of the stiffness tensor where

$$E_R = 1/[(s_{11} + s_{22} + s_{33}) + 2(s_{12} + s_{23} + s_{31})] \tag{5.4.3}$$

Table 5.3: Equivalent isotropic (iso) material properties calculated from the mean of the Reuss and Voigt averages.

Material	ρ (kg m^{-3})	A	c_{11} (GPa)	c_{12} (GPa)	c_{44} (GPa)	c_l (m s^{-1})	c_t (m s^{-1})	**k**
Si	2330	1.57	165.7	63.9	79.6	8433.0	5844.9	[001]
						9356.2	5094.2	[111]
		1.0	186.5	53.5	66.5	8949.2	5344.6	iso
Cu	8960	3.22	168.0	121.0	75.0	4330.1	2893.2	[001]
						5139.4	2130.4	[111]
		1.0	203.3	109.5	46.9	4763.3	2288.2	iso
SiO_2	2200	1.0	78.5	16.0	31.2	5972.1	3765.7	iso
SiCO:H	1100	1.0	6.6	2.5	2.1	2453.7	1377.3	iso

is the Reuss average of Young's modulus and

$$G_R = 15/[4(s_{11} + s_{22} + s_{33}) - 4(s_{12} + s_{23} + s_{31}) + 3(s_{44} + s_{55} + s_{66})] \tag{5.4.4}$$

is the Reuss average of the shear modulus. The Voigt-Reuss-Hill average of the respective modulus is then calculated from the arithmetic mean. Using the averaged moduli the compliance tensor of the averaged material is calculated, which is isotropic [Healy et al. 2020].

The respective values for selected materials are given in Table 5.3. For both silicon and copper, the isotropic approximation overestimates c_{11} while underestimating c_{12} and c_{44}. Consequently, the longitudinal and transversal wave velocities for the isotropic assumption lie within the extremal values observed for anisotropic materials along [001] and [111], as discussed in Section 3.7.4. Therefore, the isotropic approximation yields an averaged response of the anisotropic material.

Using a 2D approximation, the impact of adjacent gates, source-drain contacts and a finite gate length is neglected. The unit cell of the RFT is modelled identical to the gate cross-section of the 3D simulation (compare Figure 5.3) as shown in Figure 5.28. To be consistent with the spatial orientation of the 3D unit cell, shown in for example in Figure 5.16, it is modelled in the yz-plane, with the channel pointing along the x-axis. Fort both configurations, either with a SiO_2 or SiCO:H oxide slab, the band structure is computed in the first irreducible Brillouin zone using only a single fin. They are plotted with the respective sound cones in Figure 5.29. Unsurprisingly both 2D approximations support the RFT mode, as indicated by the arrow. However, as a result of the 2D approximation at a lower frequency as it assumes an infinite gate length. Moreover, the 2D RFT cannot exhibit out-of-plane modes, which may exist using the full-gate unit cell. However, as they cannot be excited for symmetry reasons in the 3D simulation their absence in the 2D simulation is inconsequential, as shown for the half-gate simplification. Lastly, the splitting of the shear sound cones is lifted as only one shear wave may exist in a 2D isotropic approximation.

A comparison of the resonant frequencies and Q-factors between the 2D and 3D simulations is given in Table 5.4. The 2D approximation for both oxide slab variants results in an approximately

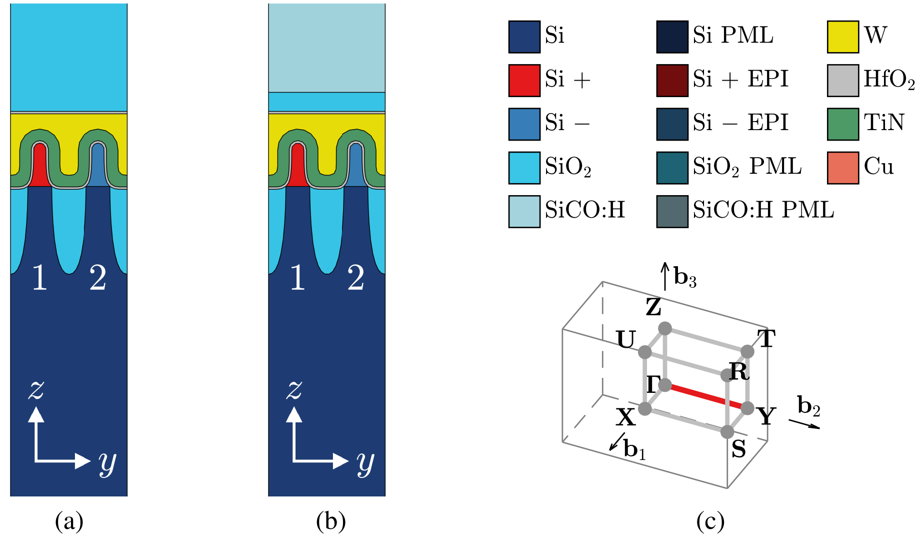

Figure 5.28: Ideal 2D 2-fin unit cells with (a) a SiO_2 and (b) a SiCO:H slab on top of the RFT cavity. (c) Brillouin zone of the unit cells.

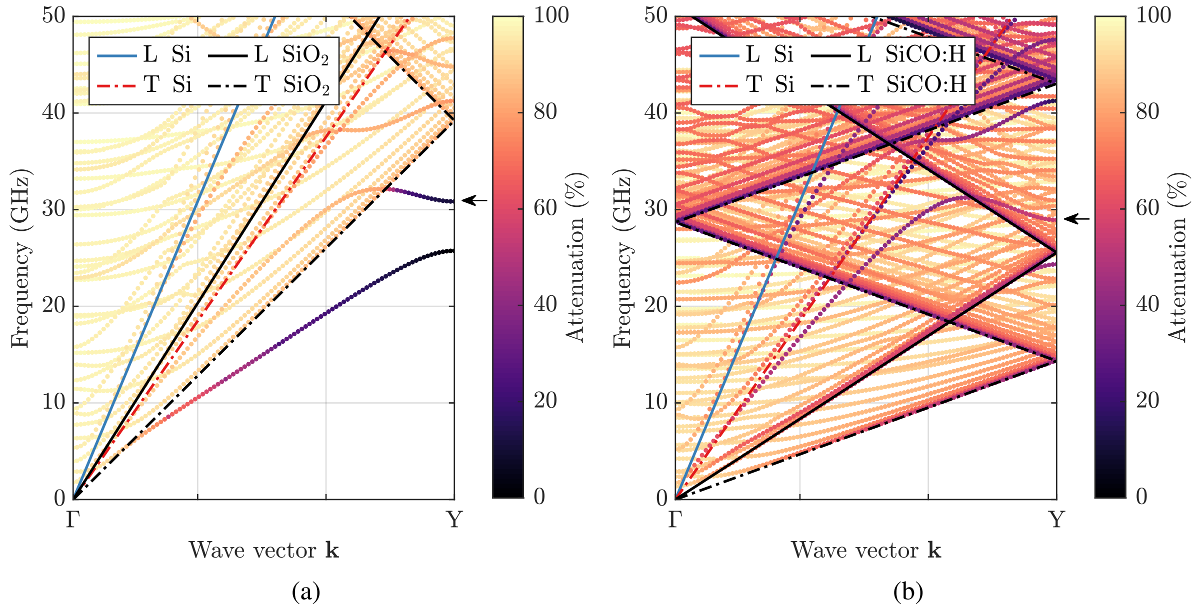

Figure 5.29: FEM simulated band structure along Γ−Y for a top confinement with (a) SiO_2 and (b) SiCO:H using a 2D approximation.

Table 5.4: Resonant frequencies and Q-factors of the 3D and 2D simulations.

Dimension	SiO_2 slab		SiCO:H slab	
	f_R (GHz)	Q-factor	f_R (GHz)	Q-factor
2D	30.847	6.8×10^{10}	28.937	31
3D	33.104	9.6×10^{9}	30.922	37

3 GHz lower resonant frequency than the reference gate length from the 3D simulation. This value matches well with the 3D simulation for longer gate lengths (see Figure 5.10(b)), where the resonant frequency will approach the 2D result for an infinite gate. Again the SiCO:H

Table 5.5: All simulations consisted of a stationary, eigenfrequency and frequency domain modal simulation. The eigenfrequency simulation was executed for 15 Modes, and the RFT mode was used in the subsequent frequency domain simulation. All frequency domain simulations were limited to a Q-factor of 1000 and 401 frequency points.

Dimension	Fins	Assumption	DOFs	Time (sec)	Simulation	f_R (GHz)	Pressure (MPa)
2D	2	infinite gate	9638	11	modal	30.847	8.314
				120	perturb.	30.848	8.112
	14	infinite gate	70 966	39	modal	30.876	0.261
				484	perturb.	30.861	0.255
3D	2	half-gate	90 636	87	modal	33.377	1.328
		full-gate	177 801	185			
	14	half-gate	585 885	490	modal	33.342	0.078
		full-gate	1 144 121	1626			

oxide cannot sustain a confined RFT mode, and the observed Q-factors are similar to their 3D counterpart. The Q-factor of the SiO_2 variant is approximately one order of magnitude larger than that obtained from the 3D variant. However, those values are unrealistic as they are only limited by numerical accuracy. Apart from the lower frequency, the simplified 2D RFT overestimates the pressure within the FinFET channel by a factor of approximately eight in frequency domain simulation at the same bias conditions.

Table 5.5 compares DOFs, simulation time, resonant frequency and fin pressure for the 2D and 3D simulations. For the 2D simulations, which assume an infinitely extended gate, both a modal superposition simulation with only the RFT mode and a harmonic perturbation simulation considering all DOFs was made. While the resonant frequency and obtained peak pressure are comparable for both simulation types, the modal simulation is almost 11 times faster, highlighting the importance of the modal superposition technique for large-scale simulations. The 3D simulations were carried out for the full-gate and simplified half-gate geometry on a (100)[45] wafer. As previously shown, the half-gate simulation yields an identical pressure and resonant frequency. Due to the lower DOFs of the half-gate setup, the simulation completes two to three times faster than the non-simplified geometry. Once more, the overestimated pressure from the 2-fin unit cell, regardless of the dimension, is quite pronounced and highlights the importance of a 3D modelling approach.

5.4.1 Transient Response

The transient response is essential for a later application in a resonant fin oscillator. Using the FEM, the full equilibrium equation (4.3.24) must be considered. Different methods can be applied to find a solution to this transient problem. The two major techniques involve discrete time-stepping and implicit formulations [Liu 2003; Zienkiewicz et al. 2013]. The central difference algorithm, for example, is only conditionally stable. Depending on the used time step, the solution becomes unstable and will not converge. Here the implicit methods, for

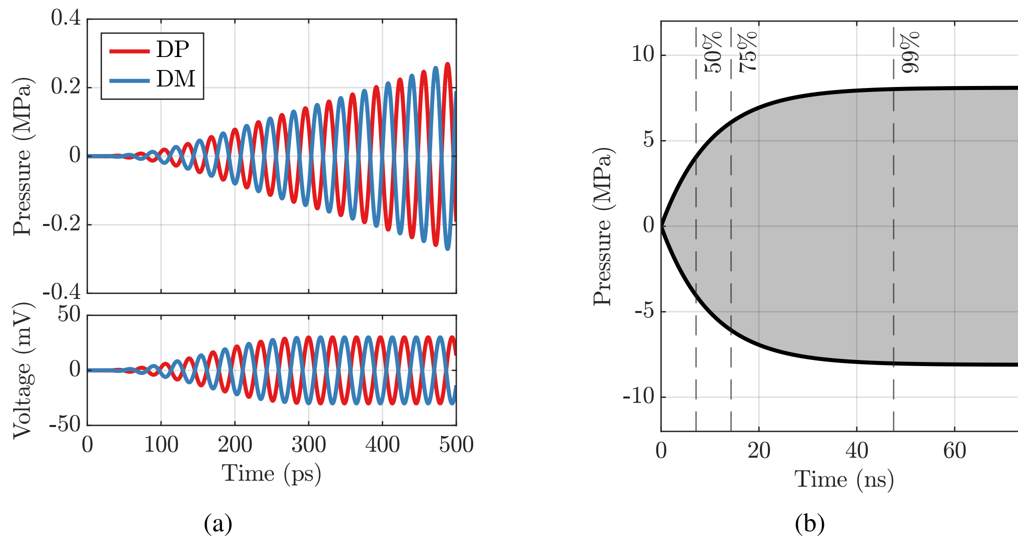

Figure 5.30: (a) Pressure and drive voltage during ramp-up. (b) Complete pressure envelope after settling.

example, the Newmark's or backwards Euler method, offer greater stability and are considered unconditionally stable since they are independent of the time step size. However, accuracy may be lower, especially for fast varying external loads. In those instances, a direct method may offer greater accuracy at the cost of a larger computation time due to the fine time-stepping required. The performance implications may be quite significant as direct methods often need 100 – 1000 fold smaller time-stepping [Liu 2003].

The transient response was simulated for the 2-fin unit cell in 2D. The RFT was damped to a Q-factor of 1000 and driven with an excitation frequency matched to the resonant frequency, using the default bias conditions by Bahr et al. [Bahr et al. 2018]. For this simulation, the indirect methods provided by COMSOL did not succeed, and the direct methods offered better convergence, although at the cost of a strongly increased solution time. The pressure response for the ramp-up and settled region when driven with a sinusoidal signal, 180° out-of-phase between adjacent fins, is plotted in Figure 5.30(a). To quantify the impact of the constant device bias on the transient result, the stationary solution

$$\mathbf{K}\mathbf{D} = \mathbf{F} \tag{5.4.5}$$

was subtracted from the results shown in Figure 5.30 [Rao 2010; Bathe 2014]. To increase numerical stability and prevent discontinuities in the simulation, the drive voltage amplitude is ramped up in an adiabatic manner over the course of ten oscillation periods, as shown in Figure 5.30(a).

As the system is only weakly damped, the resonance amplitude increases slowly, as shown for the envelope in Figure 5.30(b). At the prescribed Q-factor of 1000, the RFT requires 47.3 ns, or

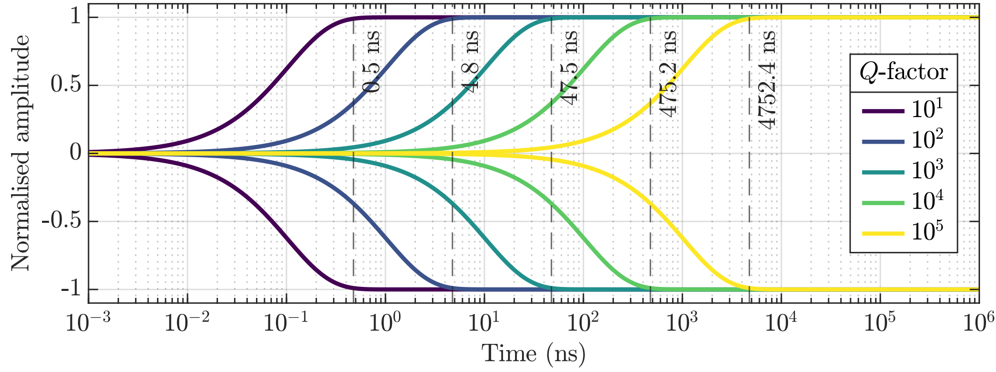

Figure 5.31: Transient ramp-up behaviour of a resonator operating at 30 GHz with different damping ratios. The annotated times mark the 99 % amplitude at the respective Q-factor.

a total of 1459 oscillation periods, to reach 99.9 % of the maximum amplitude. The time

$$t = \log\left(\frac{1}{1-A}\right)\frac{2Q}{\omega_R} \tag{5.4.6}$$

required to reach a specific amplitude A exclusively depends on the resonant frequency and Q-factor [Chopra 2012; Bachmann et al. 1995; Hirose and Lonngren 2010; Brand et al. 2015]. This relation is important as the rise time of the RFT to reach full amplitude influences the circuit design choices. After settling, the pressure amplitude of the transient simulation is identical to the simulated frequency domain simulation in resonance.

The computation of the transient behaviour at high Q-factors is challenging as time steps must be chosen sufficiently small while requiring longer simulation times to capture the complete ramp-up. Thus the behaviour can be estimated using the envelope function

$$\rho(t) = \pm d_{st} e^{-\zeta\omega_R t} \tag{5.4.7}$$

where d_{st} is the maximum static deformation and ζ the damping ratio [Chopra 2012; Brand et al. 2015]. Figure 5.31 shows the rise times of differently damped RFTs, and in general, any resonators at the given Q-factor and resonant frequency. The different envelope amplitudes are calculated at 30 GHz and normalised to their respective maximum. Whereas a resonator with a Q-factor of 10, comparable to well-optimised inductor-based solutions, only requires 0.5 ns to provide its full amplitude, a device with a Q-factor of 1×10^5, requires 4.75 µs to reach 99 % of the equilibrium amplitude [Neihart et al. 2008]. In the wake of faster switching times and responsiveness, the RFT with a supposedly high Q-factor of 49 000 requires 2.47 µs, substantially increasing over existing solutions. This issue must be addressed for later applications, as the device may not be ramped up and down during operation without causing considerable delays. Lastly, the transient response of a MEMS can be used to experimentally obtain the Q-factor of the device during ring-down [Polunin et al. 2015].

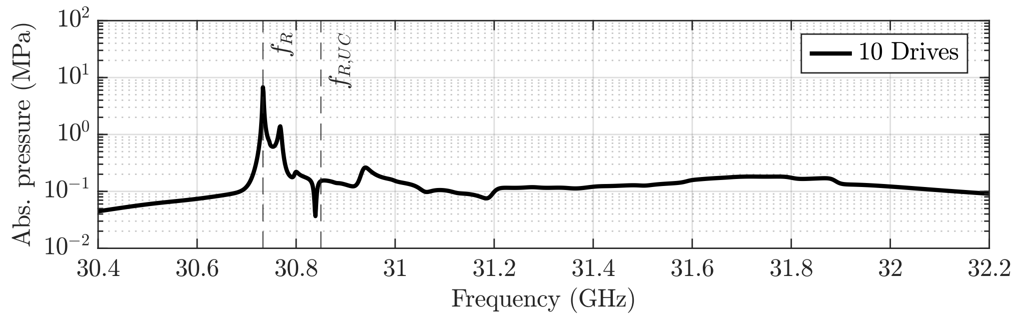

Figure 5.32: Frequency domain response of an RFT with ten drive unit cells and one central sense unit cell, driven at the default bias conditions. $f_{R,UC}$ marks the resonant frequency of the 2 and 14-fin periodic unit cells.

5.4.2 Finite 2D Cavity

As all previously simulated unit cells were only finite in the vertical or lateral directions along the channel, the impact of a finite length of the RFT cavity must also be considered. As a consequence of the infinite simulation setups, the Q-factor is overestimated as losses at the ends are not considered. In this context, however, it is possible to calculate the actual Q-factor of the device in a full-scale finite 2D simulation, which is terminated by perfectly matched layers in all directions. It is based on the 14-fin unit cell wiring scheme and all fins are connected in groups of three with four intermediate floating fins. Consequently, the pressure is evaluated in one of the three connected fins in the sense unit cell at the centre of the cavity, analogously to the 14-fin unit cell. The frequency response spectrum is calculated with a modal superposition simulation for the 100 closest modes in the vicinity of the RFT mode. The response of a cavity with ten drive cells, without any artificial damping, is plotted in Figure 5.32. Here the resonant frequency f_R is at a lower frequency when compared with the infinite cavity assumption $f_{R,UC}$. Furthermore, additional spurious modes occur at a close spectral distance to the RFT mode. The behaviour of only the main resonant mode, without other spurious modes, for different cavity lengths is shown in Figure 5.33(a). With an increasing number of drives, the resonant frequency shifts towards a lower frequency, as shown in Figure 5.33(b), whereas the cavity's absolute peak pressure and Q-factor increase with each additional drive unit cell pair [Hwang et al. 1998]. Due to the complete termination of all dimensions with perfectly matched layers, it is possible to calculate the actual Q-factor of the cavity. The shortest RFT, with two drive unit cells, is only at 1167, whereas, for the longest device with 12 drive units, it increases to 45 488. This Q-factor does not relate to the reported measured Q-factor, despite its similarity, as this simulation does not consider all involved loss mechanisms.

Nevertheless, it can be used to quantify the relative degradation in-between different physical cavity lengths. When limiting the longest device with 12 drive unit cells to a Q-factor of 1000, using Rayleigh damping, the peak pressure is almost identical to the infinite 14-fin unit cell simulation listed in Table 5.5. Since the 14-fin unit cell and finite simulation yield almost the same pressure at the same prescribed Q-factor, the assumption of an infinite cavity length

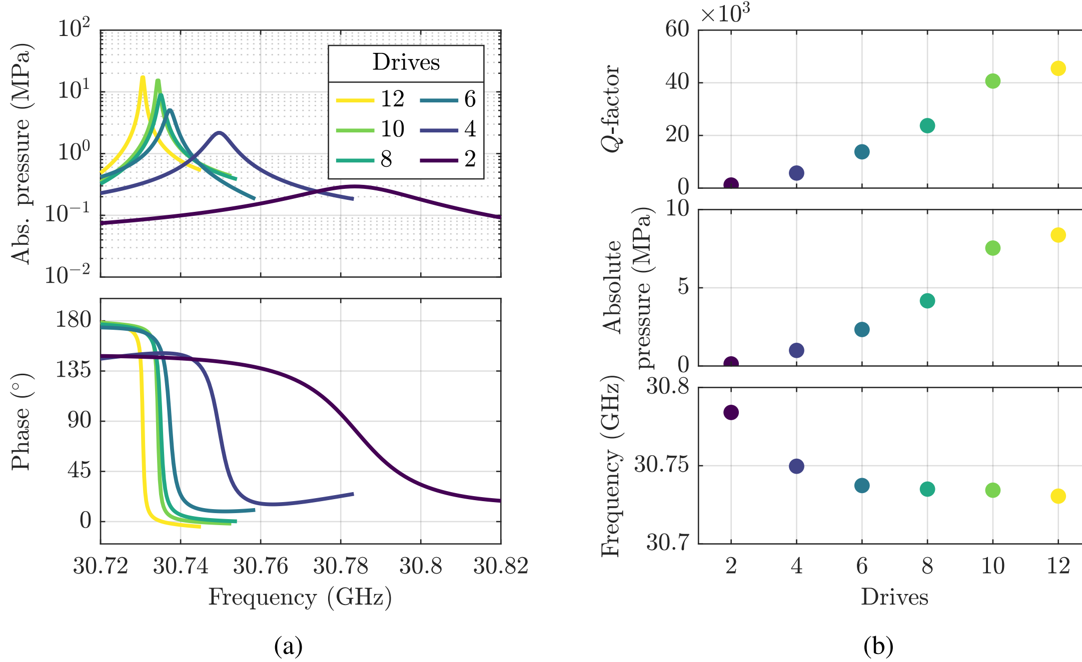

Figure 5.33: The frequency response of the finite RFT using the modal superposition technique at the default bias is given in (a). The corresponding scaling of the Q-factor, absolute pressure and resonant frequency with different cavity lengths is shown in (b).

is justified. With fewer drive unit cells, the influence of the cavity's termination increases, degrading the performance, as shown in Figure 5.33(b).

5.5 Transconductance Modelling

For modelling the drive MOS capacitors, it was sufficient to describe the resonant behaviour using the averaged channel pressure within the individual FinFETs as an intermediate figure of merit. While it is a good approximation of the mechanical performance for different geometries and wafer orientations, it is unsuited describing the sense FinFETs. To adequately describe the performance of the sensing unit, the electronic transport properties in the presence of external stress on the transistor must be modelled [Hudeczek et al. 2022].

5.5.1 Piezoresistive Effect in Monocrystalline Silicon

In semiconductors, the carrier mobility of either electrons or holes depends on several effects, such as the doping concentration, temperature and defect density [Masetti et al. 1983; Sze 2014; Ma et al. 2011]. In monocrystalline semiconductors, such as silicon or germanium, it also depends on the external stress acting on the material [Smith 1954]. In the presence of stress, the charge carrier density changes due to a volumetric change of the specimen, which in turn causes

Table 5.6: Piezoresistance coefficients of n-type and p-type silicon at 300 K [Smith 1954; Kanda 1982; Manku and Nathan 1993].

Silicon	π_{11} (Pa^{-1})	π_{12} (Pa^{-1})	π_{44} (Pa^{-1})
n-type	-102.2×10^{-11}	53.4×10^{-11}	-13.6×10^{-11}
p-type	6.6×10^{-11}	-1.1×10^{-11}	138.1×10^{-11}

a shift of the conduction and valence band [Smith 1954; Kanda 1982]. This resistivity change

$$\frac{\Delta\rho}{\rho_0} \propto \text{Stress} \tag{5.5.1}$$

is directly proportional to the applied stress while being linear up to approximately 20 GPa [Dhar et al. 2007; Sze 2014]. This effect is used in highly sensitive strain sensors. Continuously improving strain engineering is used to boost the performance of CMOS technologies, typically starting around the 90 nm technology nodes. The inexpensive addition of high-stress layers improved the current densities for NMOS and PMOS transistors [Thompson et al. 2004; Saitoh et al. 2008; Jaeger et al. 2013; Gallon et al. 2004].

The description of the piezoresistive effect is empirical and follows analogously to the anisotropic mechanical properties and can be described by a fourth-order piezoresistance tensor. It is given by a 6×6 matrix using Voigt's notation

$$[\pi] = \begin{bmatrix} \pi_{11} & \pi_{12} & \pi_{12} & & & \\ \pi_{12} & \pi_{11} & \pi_{12} & & & \\ \pi_{12} & \pi_{12} & \pi_{11} & & & \\ & & & \pi_{44} & & \\ & & & & \pi_{44} & \\ & & & & & \pi_{44} \end{bmatrix}. \tag{5.5.2}$$

where the components π_{11}, π_{12} and π_{44} were originally obtained through measurements at 300 K. The respective values for n-type and p-type silicon are given in Table 5.6 [Smith 1954; Kanda 1982; Manku and Nathan 1993]. The construction of the piezoresistance tensor follows similar principles as required for the compliance matrix where prefactors

$$\Pi_{ijkl} = \begin{cases} \pi_{\alpha\beta}, & \text{if } \beta \text{ is } 1, 2 \text{ or } 3 \\ \frac{1}{2}\pi_{\alpha\beta}, & \text{if } \beta \text{ is } 4, 5 \text{ or } 6 \end{cases} \tag{5.5.3}$$

are necessary due to the use of Voigt's notation [Kanda 1982].

Following a phenomenological description of the effect, the material resistivity in the presence of arbitrarily oriented small stresses changes according to

$$\frac{\Delta\rho_{ij}}{\rho_0} = \Pi_{ijkl}\sigma_{kl}, \quad i,j,k,l = 1,2,3 \tag{5.5.4}$$

where ρ_0 is the material's resistance without external stress [Manku and Nathan 1993; Ando and Toriyama 2018; Dhar et al. 2007]. Following this description, the carrier mobility variation is given by

$$\frac{\Delta\mu_{ij}}{\mu_0} = -\Pi_{ijkl}\sigma_{kl}, \quad i,j,k,l = 1,2,3 \tag{5.5.5}$$

where μ_0 is the carrier mobility of the material without external stress [Manku and Nathan 1993; Kanda 1982; Kanda 1991; Doll and Pruitt 2013; Yu et al. 2008].

For low doping concentrations, n-type phosphorous and arsenic doping yield an almost identical majority electron carrier mobility with $\mu_P = 1414\,\mathrm{cm^2/Vs}$ and $\mu_{As} = 1417\,\mathrm{cm^2/Vs}$, respectively. The hole mobility using p-type boron doping is $\mu_B = 470.5\,\mathrm{cm^2/Vs}$, which follows from the increased effective mass of holes compared to electrons [Sze 2014; Reggiani et al. 2000; Reggiani et al. 2002; Masetti et al. 1983].

To describe the full extent of the mobility variation within the sense FinFETs the full stress tensor, extracted from the finite-element simulations, must be considered. It enables the subsequent calculation of the alternating current within the sense FinFETs under a constant bias voltage when exposed to the deformation of the RFT mode. As the sense transistors are biased at a constant voltage, the also constant source-drain current is modulated at the RFT mode frequency, following from the changed carrier mobility. Using (5.5.5), the FinFET channel mobility change from source to drain is given by $\Delta\mu_{11} = \Delta\mu_x$ in the spatial frame [Wortman and Evans 1965; Manku and Nathan 1993; Kanda 1982]. Herein the change in channel conductance $\Delta\mu_x$ is referred to as $\Delta\mu$ for the rest of this work, as the current is not sensitive to other matrix elements of the mobility tensor.

The components given in Table 5.6 were originally obtained through measurements at 300 K. However, they also depend on the doping concentration N and temperature T via the relation

$$[\Pi(N,T)] = P(N,T)[\Pi(300\,\mathrm{K})], \tag{5.5.6}$$

where P is the piezoresistance factor [Kanda 1982]. It is given by

$$P(N,T) = \frac{300}{T}\frac{F'_{\mathrm{s}+(1/2)}(E_\mathrm{F}/k_\mathrm{b}T)}{F_{\mathrm{s}+(1/2)}(E_\mathrm{F}/k_\mathrm{b}T)}, \tag{5.5.7}$$

where k_b is the Boltzmann constant, $F_{\mathrm{s}+(1/2)}$ the Fermi integral and $F'_{\mathrm{s}+(1/2)}$ is the derivative as a function of the temperature T and the doping-dependent Fermi energy E_F, [Kanda 1982; Kanda 1991; Doll and Pruitt 2013; Abdelaziz et al. 2014; Oktyabrsky 2022; Zeghbroeck 2021; Sze 2014]. The Fermi energy for n-type and p-type silicon is shown in Figure 5.34 at selected temperatures. With increasing doping concentration, the Fermi energy varies linearly on a logarithmic scale up to densities of $N = 1\times10^{18}\,\mathrm{cm^{-3}}$, where it assimilates to the conduction or valance band energy, depending on the dopant type. The calculation further assumes the silicon is neither intrinsic nor degenerate, with all dopants being ionised [Zeghbroeck 2021].

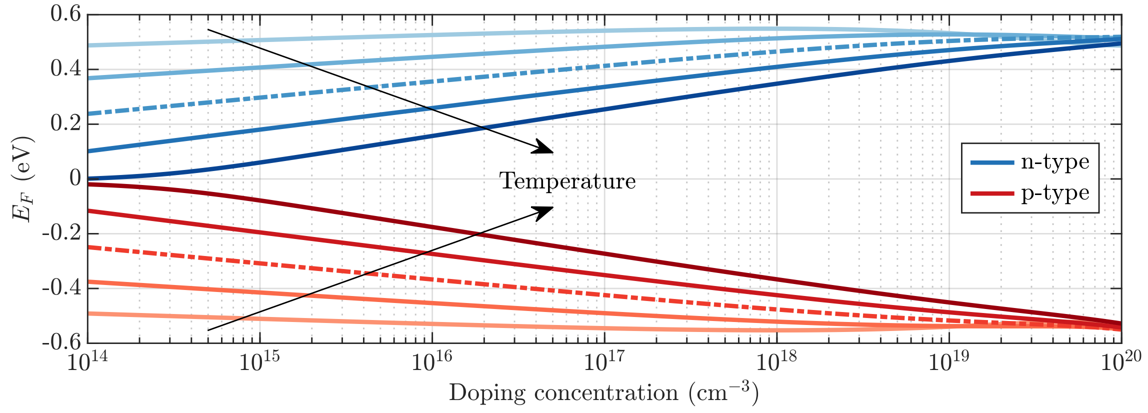

Figure 5.34: Doping dependent Fermi energy for n-type and p-type silicon. The temperature is varied between 100–500 K in 100 K steps, where a dash-dotted line indicates 300 K. (Adapted from [Hudeczek et al. 2022].)

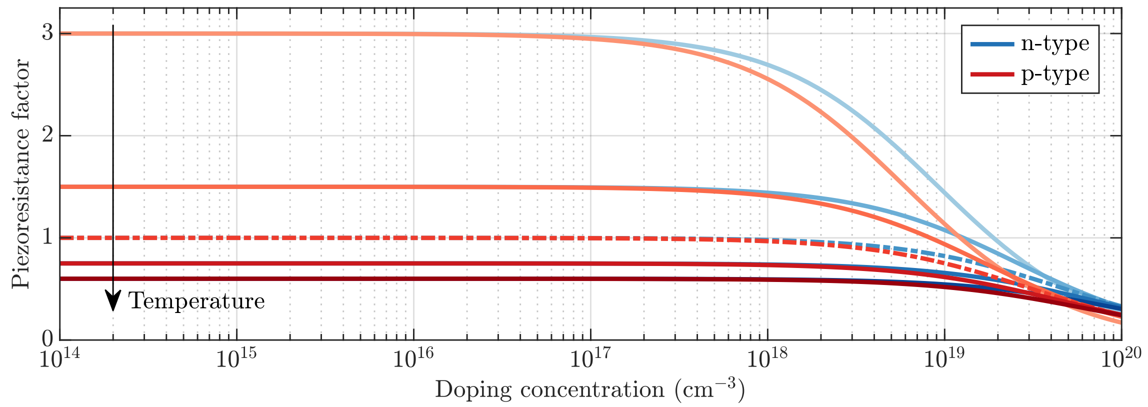

Figure 5.35: Doping dependent piezoresistance factor for n-type and p-type silicon. The temperature is varied between 100 – 500 K in 100 K steps, where a dash-dotted line indicates 300 K. (Adapted from [Hudeczek et al. 2022].)

With increasing temperatures, the Fermi energy assimilates slower to the band edges [Sze 2014; Oktyabrsky 2022; Zeghbroeck 2021].

Considering predominantly carrier phonon scattering rather than ionised impurity scattering, which is a valid assumption for low doping densities ($N < 1 \times 10^{19}\,\mathrm{cm}^{-3}$), the Fermi integrals can be calculated analytically with $s = -1/2$ [Kanda 1982; Doll and Pruitt 2013]:

$$
\begin{aligned}
F_{s+(1/2)}(E_F/k_bT) &= \ln\left(1 + e^{E_F/k_bT}\right) \\
F'_{s+(1/2)}(E_F/k_bT) &= \frac{1}{1 + e^{-E_F/k_bT}}.
\end{aligned}
\tag{5.5.8}
$$

The resulting piezoresistance factor (5.5.7) is plotted for both n-type and p-type silicon in Figure 5.35. It is near-constant and equal for both n-type and p-type silicon for doping densities up to $N = 1 \times 10^{18}\,\mathrm{cm}^{-3}$. For higher doping densities the carrier scattering mechanisms increase and the piezoresistance factor declines. For temperatures as low as 100 K the piezoresistance coefficients (5.5.6), and thus the subsequent effect, is increased by a factor of three. With elevated temperatures, the piezoresistance factor decreases. At room temperature and low

doping densities, it has a unity value.

The approximated results are in good agreement with experimental data for n-type silicon with the scattering exponent $s = -1/2$. For p-type silicon, the approximation is only accurate for doping concentrations below $N = 1 \times 10^{17}\,\mathrm{cm}^{-3}$. At higher doping densities a deviation of $-20\,\%$ at $N = 3 \times 10^{19}\,\mathrm{cm}^{-3}$ was found [Kanda 1982].

In recent literature, it was proposed that the shear coefficient π_{44} for n-type silicon is independent of the carrier concentration up to $1 \times 10^{20}\,\mathrm{cm}^{-3}$, resulting in a slightly modified expression

$$[\pi^{nmos}(P)] = \begin{bmatrix} P\pi_{11} & P\pi_{12} & P\pi_{12} & & & \\ P\pi_{12} & P\pi_{11} & P\pi_{12} & & & \\ P\pi_{12} & P\pi_{12} & P\pi_{11} & & & \\ & & & \pi_{44} & & \\ & & & & \pi_{44} & \\ & & & & & \pi_{44} \end{bmatrix}, \tag{5.5.9}$$

in contrast to p-type silicon, where the full tensor is modified (5.5.6) [Kanda and Matsuda 2007].

However, as the piezoresistive factor provides almost no enhancement within reasonable CMOS doping concentrations and real-world applicable temperature ranges, it is assumed as $P = 1$ for room-temperature devices. Moreover, current CMOS processes only deploy light channel doping with $N = 1 \times 10^{15}\,\mathrm{cm}^{-3}$, staying well within bounds of the accurate region of the piezoresistance factor [Masetti et al. 1983; Reggiani et al. 2002].

In the special case of uniaxial stress applied to a cubic semiconductor, it is possible to define two piezoresistance coefficients: For the longitudinal piezoresistance coefficient

$$\Pi_l = \pi_{11} - 2(\pi_{11} - \pi_{12} - \pi_{44})\left(\alpha_1^2\beta_1^2 + \beta_1^2\gamma_1^2 + \alpha_1^2\gamma_1^2\right) \tag{5.5.10}$$

the stress is parallel to the direction of the electric field and current and α_i, β_i and γ_i are the direction cosines between the direction of interest and the crystal principal axes. Analogously for the transversal piezoresistance coefficient

$$\Pi_t = \pi_{12} + (\pi_{11} - \pi_{12} - \pi_{44})\left(\alpha_1^2\alpha_2^2 + \beta_1^2\beta_2^2 + \gamma_1^2\gamma_2^2\right) \tag{5.5.11}$$

the directions of the applied stress and current flow are perpendicular [Kanda 1982; Kanda 1991]. Both coefficients are plotted for the (100) plane in Figure 5.36 for both n- and p-type silicon. The longitudinal piezoresistance coefficient in Figure 5.36(a) is calculated for the stress rotating together with the current in (100). In this plane, the absolute piezoresistive coefficient for n-type silicon reaches its maxima along ⟨100⟩, with the respective minima along ⟨110⟩. For p-type silicon, the maxima and minima are the opposite, pointing along ⟨110⟩ and ⟨100⟩, respectively. Moreover, the signs of the piezoresistance coefficients are opposing, with n-type silicon being strictly negative and p-type silicon being strictly positive within the {100} planes for the same

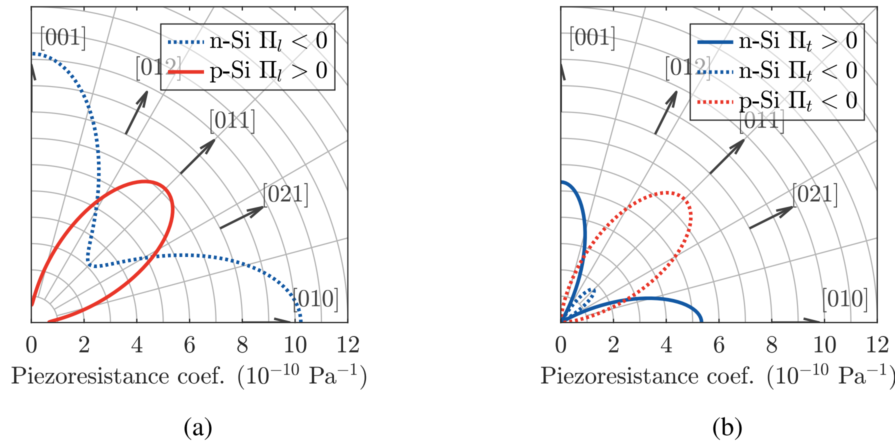

Figure 5.36: Longitudinal and transversal piezoresistance coefficients for n-type and p-type silicon in (100) for (a) uniaxial longitudinal stress and (b) transversal stress along [100] in polar coordinates.

sign of stress.

This effect is leveraged in modern CMOS field-effect transistor (FET) designs where longitudinal stress along the channel can significantly enhance performance. Using a (100)[45] silicon wafer, which is currently to be considered the industry standard for ICs, the FET channels are parallel to the [011] direction. Thus by applying tension on the order of 600 MPa, for example, by using a high tensile stress layer on top of an NMOS FET device, the source-drain current can be enhanced more than 15 % at the same bias conditions. These stress levels can be achieved by appropriate engineering of the nitride-capping layer. Similarly, by compressing the channel of a PMOS FET device by using strained silicon $Si_{1\text{-}x}Ge_x$ for the source-drain implants, the hole mobility increases beyond 50 % [Thompson et al. 2004]. Furthermore, these process adaptations are implementable at a comparatively low cost and can selectively be applied to NMOS and PMOS devices in close vicinity [Ungersboeck et al. 2006; Yang and Cai 2011; Dhar et al. 2007; Chu et al. 2009].

For the transversal piezoresistance coefficient in Figure 5.36(b), with the stress pointing along the plane normal [100], the behaviour is opposite to the longitudinal case. However, for directions close to ⟨110⟩ the sign of the transversal coefficient for n-type silicon inverts. Additionally, the absolute enhancement is lower in comparison to longitudinal strain. Similar to Young's modulus and Poisson's ratio, the longitudinal piezoresistive behaviour is also isotropic in the {111} planes which is not shown.

Calculating the longitudinal coefficient for all directions of the unit sphere shows the global extrema, as plotted in Figure 5.37. The longitudinal piezoresistance coefficient Π_l for n-type silicon, shown in Figure 5.37(a), is purely negative for all crystal directions, with its respective maxima and minima pointing along ⟨100⟩ and ⟨111⟩. For p-type silicon in Figure 5.37(b), the piezoresistance coefficient is purely positive, with the directions ⟨111⟩ and ⟨100⟩ marking the maxima and minima, respectively.

Hence, a PMOS FET built on a {112} wafer with the channel pointing along ⟨111⟩ would

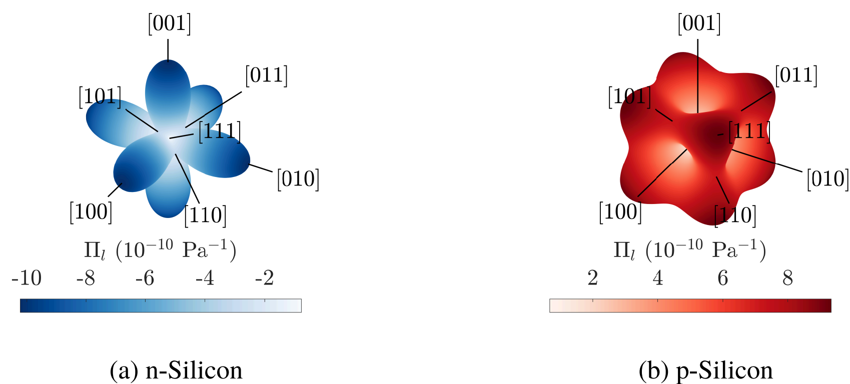

(a) n-Silicon (b) p-Silicon

Figure 5.37: Extremal values of the piezoresistance coefficients for uniaxial longitudinal stress over the full crystal space in (a) n-type and (b) p-type silicon.

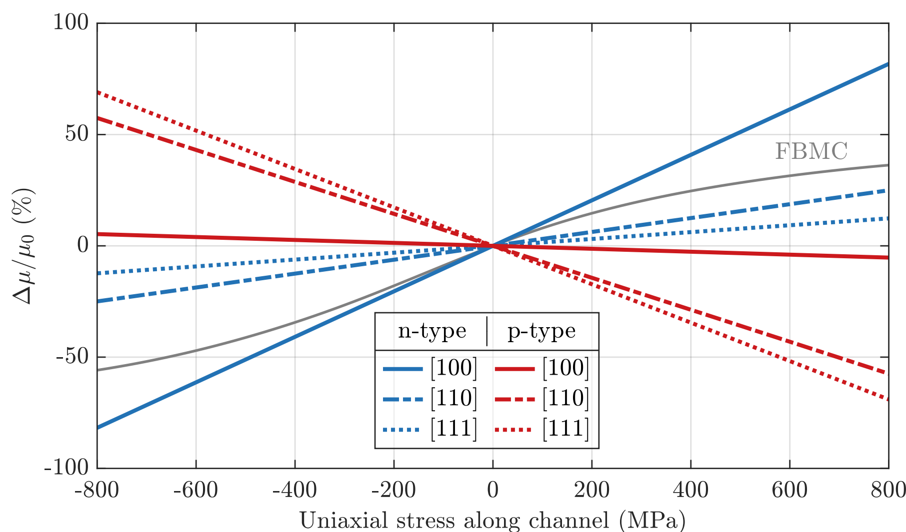

Figure 5.38: Piezoresistive mobility enhancement for uniaxial stress along with the channel directions [100], [110] and [111] for n-type and p-type silicon. The grey line was calculated by [Ungersböck 2007] using a full-band Monte Carlo model (FBMC).

be most susceptible to uniaxial strain along the channel, as mentioned earlier. However, an NMOS FET built on the same substrate orientation and channel direction would see almost no enhancement for the same strain direction. The same applies to devices built on {100} wafers, with channels along ⟨100⟩, where the PMOS FET would not benefit while the NMOS sees its most substantial enhancement. A good trade-off is a $\{100\}^{45}$ wafer where both devices yield satisfactory non-vanishing improvements.

Using (5.5.5), the exact mobility enhancement for the FET channel directions parallel to [100], [110] and [111] can be computed for uniaxial stress along with the same directions, as shown in Figure 5.38. Following Hooke's law, positive values relate to tensile and negative values to compressive stress. For channels oriented along [100], the change in channel mobility μ/μ_0 for the n-type FET sees the largest improvement compared to the other channel directions. On the other hand, p-type devices see only improvements when exposed to compressive

stress. As previously discussed, the largest improvement occurs in the [111] direction. This direction signifies the best waver orientation trade-off as both devices get enhanced for the [110] channel directions, as indicated by the dash-dotted lines. Both device types will see almost no improvement in all other directions.

The change in channel mobility is also compared to data computed with a full-band monte carlo simulation (FBMC), which is discussed in more detail in the literature [Ungersböck 2007; Dhar et al. 2007; Ma et al. 2013]. For small stresses, the piezoresistance model follows the initial linear trend. However, the FBMC solution levels off at larger stresses, giving rise to an increasingly large error in the piezoresistance model. Hence, the piezoresistance model should only be considered for small stresses up to 200 MPa [Bao 2015; Ungersböck 2007; Rochette et al. 2009; Kanda 1982; Manku and Nathan 1993; Smith 1954; Rochette et al. 2009; Ando and Toriyama 2018]. For larger stresses, both tensile and compressive, the piezoresistance model overestimates the carrier mobility due to its linear nature, and the deviations can no longer be neglected. In this case, a more rigorous method like $\mathbf{k} \cdot \mathbf{p}$ perturbation theory is necessary to accurately describe the impact of stress on carrier mobility [Ungersböck 2007; Ungersboeck et al. 2006; Ma et al. 2011; Ma et al. 2013; Dhar et al. 2007; Ward 2012].

As previously noted, the piezoresistance model is empirical and linearly links stresses and mobility changes. In cubic semiconductors, like silicon, the carrier mobility, however, is only linear in the presence of small stresses up to 200 MPa [Ungersböck 2007; Smith 1954; Kanda 1982; Manku and Nathan 1993; Rochette et al. 2009]. With an increasing stress magnitude, the actual mobility will level off, saturate, or even degrade, depending on the crystallographic orientation and stress direction [Ma et al. 2013; Ungersböck 2007]. Consequently, the piezoresistance model will overestimate the mobility change for stresses above 200 MPa. As all previous simulations at the default bias were carried out with a Q-factor of 1000, it is possible to derive a maximum Q-factor with (5.2.5), for which the simulations will yield a pressure below the accuracy limit, as shown in Table 5.7 [Hudeczek et al. 2022]. Following the previous 3D simulations, the largest valid Q-factor for all RFT types, regardless of the gate lengths, unit cells and wafer orientations, is more than 50 000. Although the 2-fin unit cell cannot be manufactured, it is included as a best-case reference. For the more realistic 14-fin unit cell the viable Q-factor limits are over several million. Consequently, the piezoresistance model should yield accurate results for all Q-factors below the maximum Q-factors listed in Table 5.7. For larger values, the mobility variation is overestimated, leading to an exaggerated mechanical transconductance, and thus an overestimated performance figure of merit for the RFT.

5.5.2 FinFET Mobility Variation

From the stress tensors of the channels of the 2-fin unit cell, the mobility variation is calculated using (5.5.5). For each wafer orientation, similar to the mechanical properties, the

Table 5.7: Valid Q-factor range of the piezoresistance model for the infinite unit cells with the resonant peak pressure scaled to 200 MPa [Hudeczek et al. 2022].

MOS type	unit cell fins	gate length (nm)	Q-factor limit (in millions) (001)	$(001)^{45}$	(011)	(111)
NMOS	2	16	0.12	0.23	0.34	0.28
		24	0.10	0.19	0.27	0.23
		150	0.06	0.12	0.15	0.13
	14	16	2.25	3.56	4.23	3.91
		24	1.94	3.22	3.83	3.50
		150	1.33	2.33	2.72	2.40
PMOS	2	16	0.09	0.18	0.27	0.22
		24	0.08	0.15	0.21	0.18
		150	0.05	0.09	0.11	0.10
	14	16	1.79	2.85	3.45	3.18
		24	1.54	2.58	3.11	2.82
		150	1.06	1.86	2.18	1.94

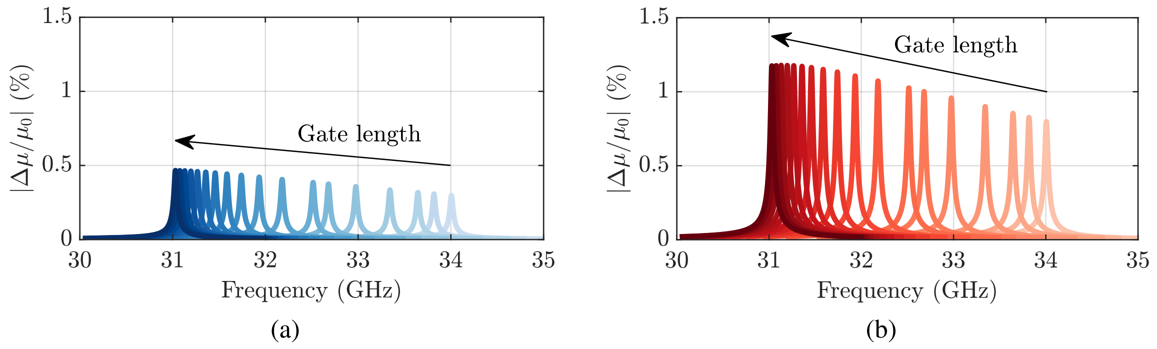

Figure 5.39: Carrier mobility variation for the 2-fin (a) NMOS and (b)PMOS unit cell at a Q-factor of 1000 on a $(001)^{45}$ oriented silicon wafer. ((a) adapted from [Hudeczek et al. 2022].)

piezoresistance tensor must be transformed into the spatial reference frame using the fourth-rank tensor rotation (3.5.1). The resulting mobility variation is shown in Figure 5.39 for the NMOS variant at a Q-factor of 1000, actuated at the default bias condition on a $(001)^{45}$ wafer. For each gate length, the mobility variation reaches its maximum in resonance. Further, the amplitude of the variation increases with increasing gate length. This observation is in line with the behaviour predicted from the averaged pressure figure of merit, which also increased for longer gate lengths, as shown in Figure 5.20. The PMOS variation plotted in Figure 5.39(b) follows the same trend. However, the overall mobility enhancement is almost two-fold compared to the NMOS, which results from the higher susceptibility of the hole mobility to external stress, as discussed in Section 5.5.1.

The calculation is repeated for both device types on all four wafer orientations, with the extracted peak amplitudes plotted in Figure 5.40. Interestingly while the mobility variation for NMOS devices, as depicted in Figure 5.40(a), on the $(001)^{45}$ wafer increases monotonously from

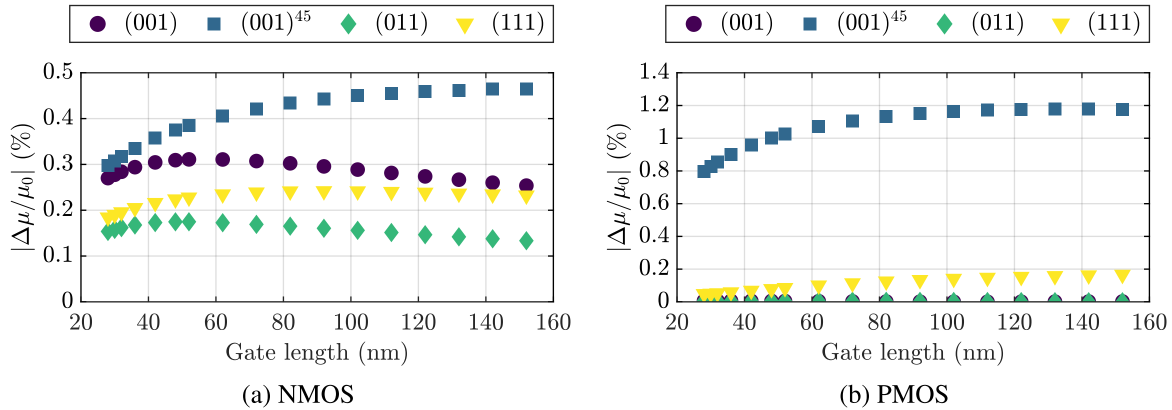

(a) NMOS (b) PMOS

Figure 5.40: Mobility variation in the resonance of the 2-fin unit cell at a Q-factor of 1000 for (a) NMOS and (b) PMOS devices on different silicon substrate orientations. (Adapted from [Hudeczek et al. 2022].)

0.3-0.47 % with larger gate lengths, all other wafer directions level off after reaching a small plateau at relatively small gate lengths. Furthermore, the $(001)^{45}$ wafer orientation provides the best enhancement from all considered orientations, regardless of the RFT gate length. Generally, the mobility enhancement is below 0.5 % for all wafer variants at a Q-factor of 1000 with default bias conditions. The overall low mobility enhancement for the NMOS variant follows from the low susceptibility of electrons to external stress and the low simulated stress components, regardless of the wafer orientation.

The response of the PMOS device to the RFT mode, as shown in Figure 5.40(b), is strongly increased for the $(001)^{45}$ wafer orientation, with a mobility enhancement between 0.8-1.2 %. Interestingly the (001) and (011) wafers offer virtually no enhancement, while the (111) wafer only achieves a maximum enhancement below 0.2 %, regardless of the gate length. This result has a major impact on selecting the underlying wafer orientation, as the PMOS RFT will most likely not work on certain wafer orientations as no mobility modulation occurs. Since the standard IC wafer orientation in modern foundry IC design is $(001)^{45}$, all manufactured NMOS and PMOS devices are enhanced at best.

As previously discussed, a larger number of parallel gates harms the pressure within the sensing unit. This is also reflected in the mobility variation on a $(001)^{45}$ wafer for both NMOS and PMOS devices, as shown in Figure 5.41. Interestingly, whereas the pressure for a single gate device outperformed the infinite unit cell (compare Figure 5.23(b)), the mobility variation is on par with the infinite case. This most likely follows from incorporating the entire stress tensor in the calculation rather than the averaged pressure metric. With an increasing number of gates, the mobility enhancement degrades for both NMOS and PMOS, substantiating the claim of the best performance with a single gate. Analogously to the pressure figure of merit, the number of dummy gates was swept between 1-3 , which did not impact the mobility variation.

The varied internal mobility leads to an increase or decrease in the absolute current of the sense FinFET, depending on the phase of the mechanical modulation. The variation is plotted in Figure 5.42 for the reference NMOS device with a gate length of 36 nm, for varying drain

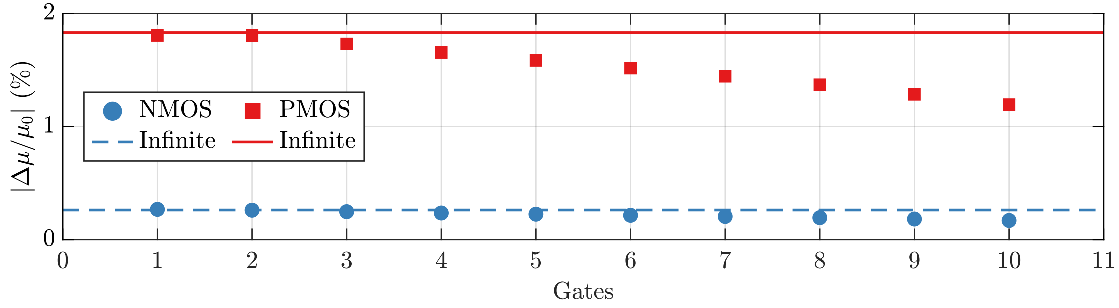

Figure 5.41: Mobility variation in the resonance of the 2-fin unit cell at a Q-factor of 1000 with a changing number of parallel gates on a (001)[45] oriented silicon wafer. (Adapted from [Hudeczek et al. 2022].)

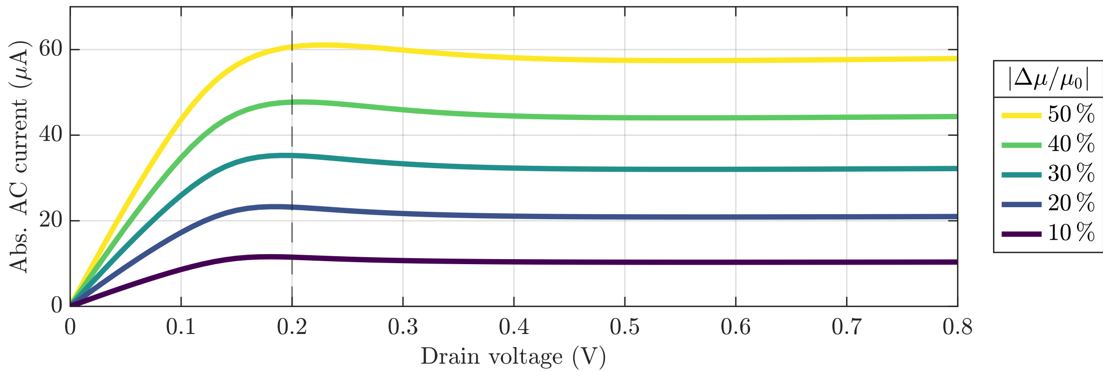

Figure 5.42: Simulated alternating current of the reference NMOS device with different internal carrier mobilities using Spectre [BSIMCMG 2018].

voltages at a constant gate bias $V_G = 0.8$ V. It is calculated from the Spectre FinFET models with a varied internal carrier mobility parameter [BSIMCMG 2018]. The maximum of the modulated current occurs at the transition between the transistor's linear and saturation region, which is slightly shifting towards larger bias values with an increased mobility change. To maximise the current response of the sense transistor, a $V_{sense} = 200$ mV is chosen as it biases the FinFETs in saturation for all conditions. This value is identical to the values reported in the literature [Bahr et al. 2018].

The drain current also depends on the gate length plotted in Figure 5.43(a). The drain current was simulated with a gate voltage of $V_G = 0.8$ V and the previously determined sense bias. Note that for the PMOS the respective voltages $V_G = 0$ V for the PMOS $V_{sense} = 600$ mV are used. The overall current decreases for both NMOS and PMOS with increasing channel lengths, caused by the increased channel resistance at longer gate lengths. Furthermore, the NMOS has an approximately 25 % larger source-drain current which follows from different carrier mobilities and stress optimisations [Thomas 1966; Thompson et al. 2004]. Gate lengths within the grey area are not available in the technology used in this work, and the values are interpolated using an Akima spline.

Also shown in Figure 5.43(b) is the source-drain current for the reference gate length of 36 nm with an increasing number of parallel gates, which is almost linear for both device types.

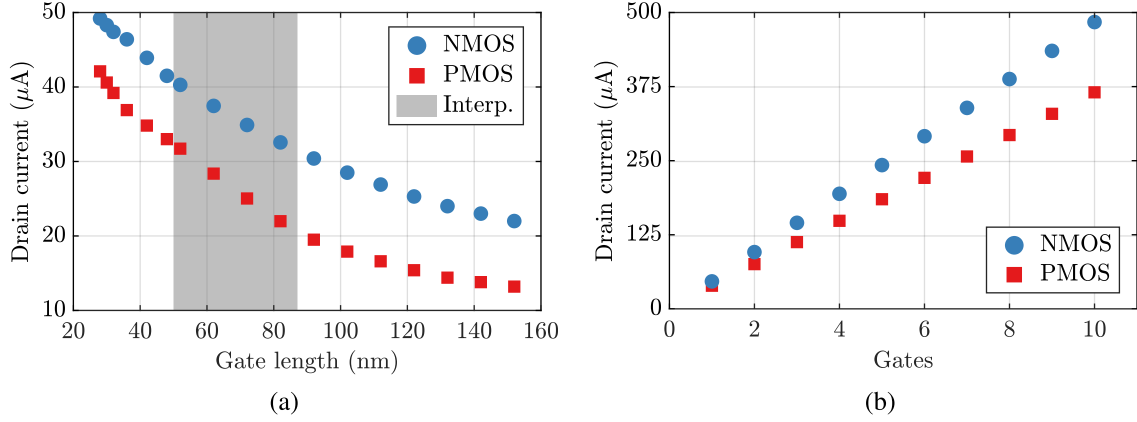

Figure 5.43: (a) The simulated sense drain current for a single fin and single gate FinFET for different gate lengths using Spectre. (b) Scaling of the drain current of the reference FinFET with a single fin with an increasing number of parallel gates. Values within the grey area in (a) are interpolated using an Akima spline. (Adapted from [Hudeczek et al. 2022].)

5.5.3 Mechanical Transconductance

The current modulation is calculated using the simulated carrier mobility enhancements and the sense currents within the sense FinFETs. Focusing only on mobility enhancements due to the piezoresistive effect, the alternating current in the 2-fin unit cell is calculated with

$$i_{sense} = I_{sense} \frac{\Delta\mu_1}{\mu_0} \tag{5.5.12}$$

where I_{sense} is the current from a single gate and a single FinFET [BSIMCMG 2018; Hudeczek et al. 2022].

However, as shown by the previous simulations on the average pressure, the 2-fin unit cell substantially overestimates the pressure. Consequently, the mobility variation must be obtained from the extended 14-fin unit cell configuration to match the expected behaviour of the real device. While the stress tensor was extracted from a single channel in the 2-fin unit cell, the 14-fin variant has two pairs of three adjacent connected fins. Hence, focusing only on one electrical phase, three stress tensors, one for each fin of the common contact, are extracted from the simulation. The overall enhancement of the sense current within a single contact is thus found from the sum of the currents in the three fins

$$i_{\text{sense}} = I_{\text{sense}} \frac{\Delta\mu_3}{\mu_0} + I_{\text{sense}} \frac{\Delta\mu_4}{\mu_0} + I_{\text{sense}} \frac{\Delta\mu_5}{\mu_0} \approx I_{\text{sense}} \frac{\Delta\mu_3}{\mu_0}. \tag{5.5.13}$$

However, in contrast to the 2-fin unit cell where one fin was responsible for one electrical phase, three fins with different mechanical phases contribute to a single electrical phase. Here the outer two fins 3 and 5 share the same mechanical phase, and the phase of the centre fin 4 is the opposite. Thus, while the current may be increased within the two outer fins due to the piezoresistive enhancement, the centre fin has degraded performance or vice versa. Therefore, by assuming a

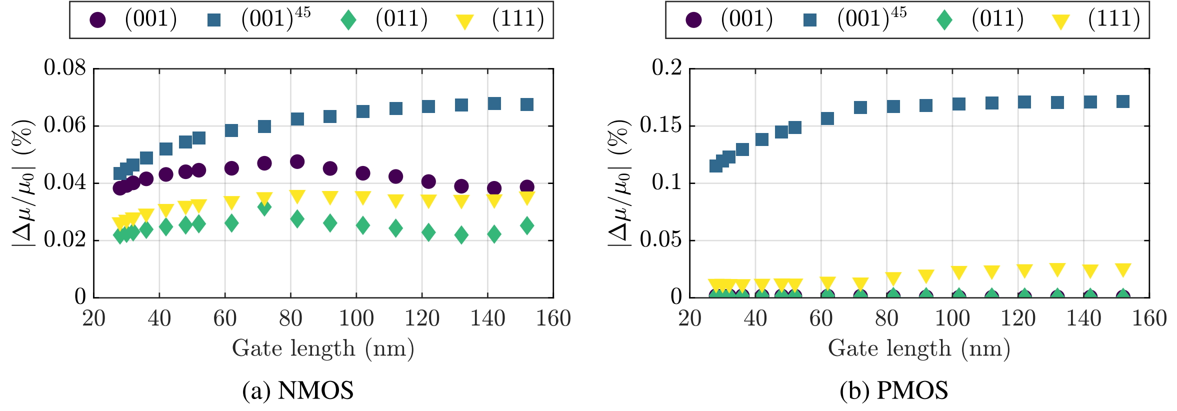

(a) NMOS

(b) PMOS

Figure 5.44: Mobility variation in resonance of the 14-fin unit cell at a Q-factor of 1000 for (a) NMOS and (b) PMOS devices on different silicon substrate orientations. (Adapted from [Hudeczek et al. 2022].)

linear response of the mobility to the piezoresistive effect, the current contributions of two fins will cancel within each electrical contact leaving only on contributing fin [Hudeczek et al. 2022].

The resulting mobility change for the 14-fin unit cell, assuming an average stress tensor over all three fins, is shown in Figure 5.44 for both NMOS and PMOS RFTs. The overall trends are identical as described for the 2-fin unit cell (compare Figure 5.40), however, at a much lower overall enhancement, which is in line with the previously used pressure metric. The performance of the 2-fin unit cell is precisely a factor of seven larger than that of the 14-fin counterpart. This matches with the assumption of only one fin contributing per contact, since only a total of two out of 14 fins are responsible for the mobility variation, whereas all fins of the 2-fin unit cell contribute. Minor deviations between the 2-fin and 14-fin variants can be discerned for some gate lengths, which may be ascribed to slightly different mode shapes and potential meshing inconsistencies. However, their impact is negligible.

Using the differential input amplitude of the drive signal together with the alternating current, the mechanical transconductance

$$G_m = \left| \frac{i_{sense}}{v_{drive,diff}} \right| \tag{5.5.14}$$

of the RFT is calculated [Bahr et al. 2018; Hudeczek et al. 2022]. It is plotted in Figure 5.45 for both NMOS and PMOS devices and the 2-fin and 14-fin unit cells. It was calculated at the default bias and drive voltage conditions for a Q-factor of 1000. For either device type and regardless of the unit cell size, the transconductance is plateauing for small gate lengths up to approximately 50 nm. For longer gates, the transconductance degrades with further increasing channel lengths. In the plateauing region, the increase in mobility, as shown in Figure 5.40 and Figure 5.44, and the decrease in sense current, as depicted in Figure 5.43(a), compensate for each other. As the mobility enhancement levels with further increasing gate lengths, the overall transconductance declines due to the reduced current and, consequently, also the alternating current in the sensing unit. Once again, the 2-fin variant outperforms the 14-fin configuration by a factor of seven. Furthermore, the transconductance of the PMOS is more than twice the value

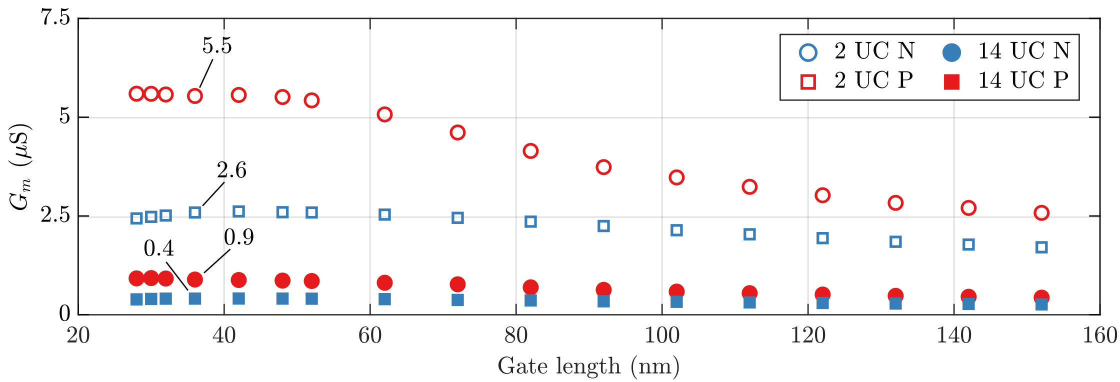

Figure 5.45: Simulated mechanical transconductance for the 2-fin and 14-fin unit cell for both NMOS and PMOS at a Q-factor of 1000. (Adapted from [Hudeczek et al. 2022].)

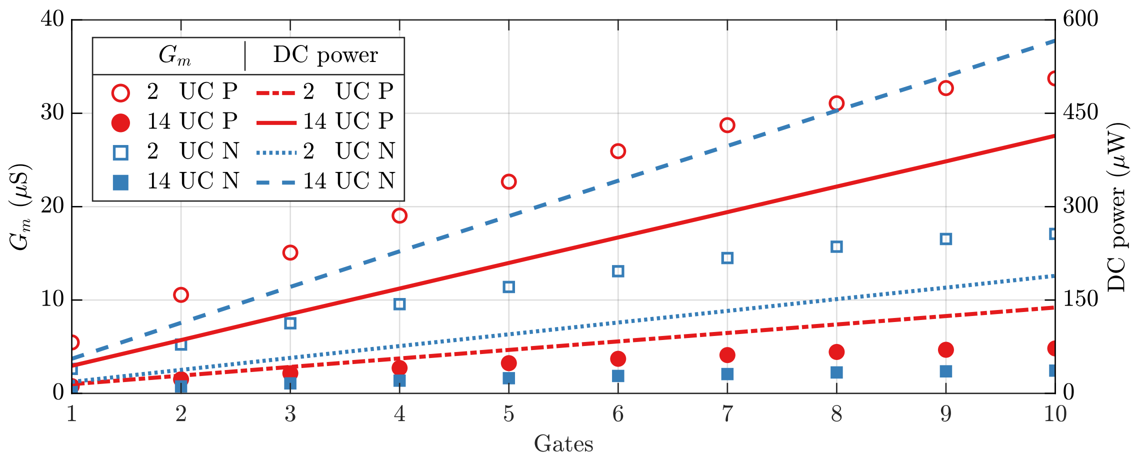

Figure 5.46: Scaling of the transconductance at a Q-factor of 1000 and the required power with the number of parallel gates.

obtained for the NMOS variant, which results from a better susceptibility of the hole mobility to external stress, although the absolute sense current is lower in the PMOS [Hudeczek et al. 2022].

Consequently, the optimum performance for both device types and unit cell sizes is achieved for a comparatively short channel length of 36 nm, with the transconductance in the low to sub-micro siemens range. Note that these values are still simulated at a Q-factor of 1000 and are thus not indicative of the ultimate performance of the RFT.

The absolute transconductance can further be increased with a larger number of parallel gates, as shown in Figure 5.46, however, at the expense of increased power consumption and spurious modes (compare Figure 5.22). Although it was shown that the pressure within the cavity reduces with each additional gate, it is counteracted by the increasing direct current, and thus also the alternating current. Therefore, the transconductance increases with the number of parallel gates before levelling off for many parallel gates. Here a factor of five can be achieved by using ten parallel gates, regardless of the device type and configuration. However, slightly higher values are expected for even more gates.

In conjunction with the transconductance, the power demand rises, which is undesired as it will increase the idle power of the RFT. Comparing the power consumption of the ideal and

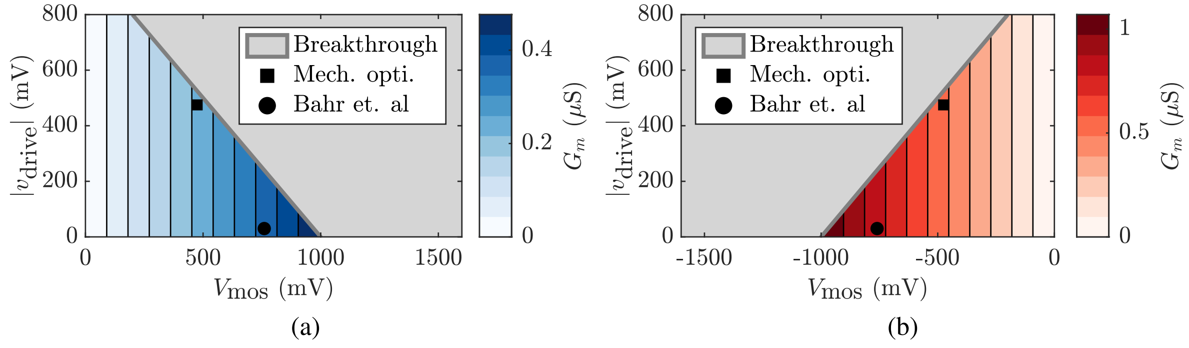

Figure 5.47: Mechanical transconductance at a Q-factor of 1000 for the 14-fin (a) NMOS and (b) PMOS unit cell under varying drive bias conditions and amplitudes with a constant gate voltage $V_{gate} = 0.8$ V. (Adapted from [Hudeczek et al. 2022].)

the actual integration, i.e. the 2-fin and 14-fin unit cells, a further drawback of the extended unit cell configuration is highlighted. While inside the tightest possible integration only two fins determine the power consumption, six fins are required inside the extended implementation, which strongly increases the power consumption. While it remains at a comparatively low level of 44.32 µW and 55.65 µW, for PMOS and NMOS variants with a single gate, it increases to 413.93 µW and 566.64 µW with ten parallel gates. Although the PMOS variant requires lower power than the NMOS, it outperforms the NMOS due to the increased mobility enhancement, and thus increased transconductance.

The optimal transconductance depends on several quantities and may be improved by achieving a larger drain current and subsequent modulated current. However, as shown for the optimal bias condition in Figure 5.42 a sense bias of $V_{sense} = 200$ mV yields the largest possible enhancement. On the other hand, a smaller differential drive amplitude at the same channel pressure would also improve the transconductance. However, with a decreasing alternating drive voltage, the pressure within the FinFET is decreasing (compare Figure 5.15), resulting in a degraded mobility variation and, consequently transconductance. Hence, the optimal bias condition, balancing the largest obtainable modulated sense current at the smallest possible drive voltage, is required. It is shown in Figure 5.47 for both device types. Here the mechanical transconductance improves with an increasing bias voltage applied across the gate oxide, whereas the drive voltage amplitude has a negligible impact on the transconductance. This follows from Figure 5.15, where a linear effect of the drive voltage on the overall pressure within the FinFET channel was observed. Consequently, the linearity of the piezoresistive effect leads to a linear modulation of the sense current with the applied drive voltage. Moreover, the peak pressure increases with a rising voltage V_{mos} between the gate and the FinFET where the optimum transconductance is once more limited by the gate oxide's breakthrough voltage. Here the bias condition chosen by Bahr et al. is close to the optimal condition, leaving sufficient headroom for a larger drive amplitude. The previous bias location marked the largest mechanical performance by using only the pressure figure of merit. However, it performs worse than the bias point

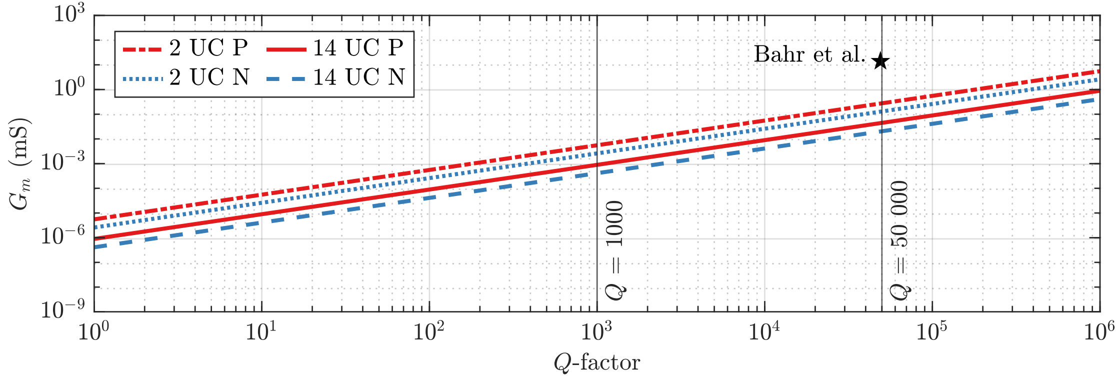

Figure 5.48: Scaling of the mechanical transconductance of the ideal 2-fin and extended 14-fin unit cells with the Q-factor. NMOS and PMOS devices are abbreviated respectively with N and P. The performance reported by Bahr et al. at a Q-factor of 49 000 is marked by a star [Bahr et al. 2018]. (Adapted from [Hudeczek et al. 2022].)

by Bahr et al. when using mechanical transconductance as figure of merit [Bahr et al. 2018; Hudeczek et al. 2022].

Returning to the optimal device with a single gate and a reference gate length of 36 nm, the transconductance obtained at Q-factor of 1000 only reaches 0.9 µS and 0.4 µS for the PMOS and NMOS, respectively. However, the RFT performance was reported for a Q-factor of almost 50 000. Hence, the performance of the best device is scaled to the larger Q-factor with (5.2.5), as plotted in Figure 5.48. At a Q-factor of almost 50 000, the transconductance for the 14-fin unit cells is still in the low micro siemens range with 45 µS for the PMOS and 20 µS for the NMOS RFT, respectively. This value is three orders of magnitude lower than the reported values of 14 mS by Bahr et al. as indicated by the star [Bahr et al. 2018; Hager et al. 2021].

Although the transconductance can be slightly improved with additional gates, this is unlikely given the reported current values by Bahr et al. and insufficient to bridge the remaining gap [Bahr et al. 2018]. The proof-of-concept device is reported with a sense current of I_{sense} = 118 µS, which may be compared to a FinFET with a gate length of approximately 62 nm (compare Figure 5.43(a)) and a single gate from this investigation. For this configuration, the calculated transconductance at a Q-factor of 49 000 reaches an even lower transconductance of 38.22 µS and 18.38 µS for the PMOS and NMOS, respectively. Although no information is given for the device doping, neither of the here simulated devices supports the reported data by Bahr et al. [Bahr et al. 2018; Hudeczek et al. 2022].

Interestingly the reported transconductance of 14 mS and the required carrier mobility enhancement are inconsistent with existing literature [Bahr et al. 2018]. The device, as reported, is biased at a constant voltage of V_{sense} = 200 mV, resulting in sense current or I_{sense} = 118 µA. It was driven with a single-ended port power of −20 dBm which is equal to a differential drive voltage of v_{drive} = 63.2 mV. Following the relation

$$G_m = \frac{i_{sense}}{v_{drive,diff}} = \frac{\Delta\mu I_{sense}}{v_{drive,diff}} \tag{5.5.15}$$

a mobility modulation of 750 % is required in the sense FinFETs. Given that the contribution of two fins cancels the actual mobility enhancement within a single sense contact stems only from a single FinFET. This increases the required mobility modulation by another factor of three. Such stress-induced mobility enhancements within silicon are unreported in literature, with the largest reported enhancements at room temperature being in the 150 % range. However, those values require uniaxial gigapascal pressures which cannot be achieved by an electromechanical actuation, as shown by the simulations [Ungersböck 2007; Smith 1954; Kanda 1982; Manku and Nathan 1993; Rochette et al. 2009]. Furthermore, there are reported stress values of 7 MPa and 40 MPa in literate, as well as the pressure data provided by this analysis, all of which only support sub-per cent mobility enhancements at best [Bahr et al. 2018; Srivastava et al. 2021; Hudeczek et al. 2022; Hager et al. 2021]. Moreover, the stress-induced by the RFT mode is multi-axial, resulting in a probably lower mobility enhancement than uniaxial stress of the same magnitude [Sun, Sun, et al. 2007; Sun, Thompson, et al. 2007; Ma et al. 2013].

It should be noted that the outlined modelling approach neglects effects such as a stress-induced shift of the threshold voltage and altered mobility saturation [Srivastava et al. 2021; Hudeczek et al. 2022]. Given the size of the discrepancy an improvement by more than three orders of magnitude is highly unlikely by a more accurate modelling approach. Since the RFT is fabricated in a technology node a with SiCO:H-based BEOL, an oxide slab is insufficient to confine the resonant mode due to the lower sound dispersion. It was thus replaced with a SiO_2 slab offering excellent confinement by index guiding. Hence the impact of a phononic crystal mirror on the performance of the RFT is investigated in the next chapter to quantify the potential performance benefit of using a matched mechanical mirror.

Summary

The resonant behaviour of the RFT was investigated with the FEM. Using an idealised unit cell, the RFT was simulated without the BEOL phononic crystal on several wafer orientations. The resonant mode was confined by the index guiding properties of the underlying silicon, which varied as a consequence of the anisotropic mechanical response. Since the BEOL was neglected, it was replaced by a SiO_2 or SiCO:H slab, however, the latter is incapable to sustain a well-confined mode within the FEOL due to its mechanical properties.

Following the displacement profiles of the available guided modes, the required RFT mode was identified by symmetry considerations, which results in differential pressure in adjacent FinFET channels. By adjusting the channel length of the FinFETs, the resonant frequency may be tuned by more than 3 GHz, however, it is also affected by the crystallographic orientation of the underlying wafer.

The performance of the resonant mode was assessed with a frequency domain response simulation limited to a Q-factor of 1000. Due to the assumption of small deformations within the cavity, linear viscous Rayleigh damping can be used, which allows a rescaling of the response

in resonance to an arbitrary Q-factor. Since the unit cell is only an approximation of the actual FinFET geometry, the capacitance is calibrated to measurement data. To further reduce the computational cost associated with the FEM simulations, the impact of an anti-symmetric Poisson's ratio on the mirror symmetry of the gate plane was investigated and the impact is negligible for the analysis. Thereby the DOFs can be further reduced which improves the simulation times.

Furthermore, the impact of varying bias and drive voltages on the mechanical performance was addressed, where a balance between actuation and bias voltage must be found. By modelling the fabricated device geometry, the impact of a finite number of parallel resonant gates resulted in a degradation of the peak pressure as they obstructed the displacement of the neighbouring gates. Moreover, with the number of parallel gates, the number of spurious modes is increasing, which poses a risk to the functionality of the RFT. A subsequent simulation of the extended 14-fin unit cell with an adjusted wiring scheme resulted in strong performance degradation and strongly reduced electromechanical coupling efficiency over the 2-fin unit cell.

In the second part, the mechanical transconductance was modelled from the complete stress tensor within the channels of the 2-fin and extended 14-fin unit cells. The subsequent mobility enhancement within the different sense unit was modelled with the piezoresistive effect. External stress on the FinFET channels, caused by the resonant mode, leads to a variation of the carrier mobility, and thus a change in the sense current. This process is the most pronounced for both NMOS and PMOS devices on the commonly used (001)[45] wafer orientation, with the other investigated orientations resulting in much lower or negligible enhancements.

Following the currents in the sense FinFETs, the mechanical transconductance can be calculated from the resulting alternating current caused by a variation of the carrier mobility. At the reported Q-factor of 49 000, more than two orders of magnitude lower mechanical transconductances of 19.6 µS for the NMOS and 44.1 µS for the PMOS were found. This stands in opposition to the reported transconductance of 14 mS by the first proof-of-concept publication. Although several simplifications were made for the simulation setups, all of them resulted in an overestimation of the involved effects, and thus the reported milli siemens transconductances are highly improbable.

6

Confinement Characteristics of a Back-End-of-Line Phononic-Crystal

Contents

6.1 The One-Dimensional Phononic Crystal 113
6.2 The Two-Dimensional Phononic Crystal 121
6.3 Combined Simulation of the Phononic Crystal and Resonant Cavity . 127
6.3.1 SiO_2-based Back-End-of-Line 127
6.3.2 SiCO:H-based Back-End-of-Line 132
6.4 The Three-Dimensional Phononic Crystal 136
6.5 Fundamental Limits of the Quality Factor 143

The phononic crystal properties of the back-end-of-line (BEOL), which are responsible for confining the resonant mode, are modelled using an isotropic one-dimensional (1D) and two-dimensional (2D) as well as an anisotropic three-dimensional (3D) approach. The possible band gaps and their usefulness for successful confinement of the resonant fin transistor (RFT) cavity are addressed for different BEOL stacks. Following the BEOL phononic crystal investigation, the BEOL and front-end-of-line (FEOL) are jointly simulated with the finite-element method (FEM). The performance is lastly put into perspective when anisotropic materials, such as copper, are present in the phononic crystal. A discussion of the reported quality factor (Q-factor) and the fundamental limits caused by the most common loss mechanisms is also given.

6.1 The One-Dimensional Phononic Crystal

As discussed in the previous chapter, the main mechanical mode of the RFT must be confined to the FEOL to maximise the stress in the sense fin field-effect transistor (FinFET) channels and, thereby, the mechanical transconductance. To reduce the overall complexity of the investigation

and study the behaviour of the FEOL, the BEOL phononic crystal was neglected. It was replaced by a solid oxide slab, either SiO_2 or SiCO:H, depending on the BEOL stack-up. Whereas a solid SiO_2 slab was sufficient to shield the mechanical mode via index guiding, and thus to reach a high Q-factor, the SiCO:H slab resulted in a non-functional device as the main resonant mode was radiating away from the cavity.

However, as discussed in Section 2.1, modern BEOL stacks predominantly use the low-κ SiCO:H to improve switching speeds in the integrated circuit (IC) as the RC time constant is reduced compared to the SiO_2 BEOL used in older technology nodes. Therefore, excluding the interconnecting copper layers above the RFT to improve confinement is not possible, as discussed in Section 5.1.3. This problem exists not only in the RFT, but occurs in all other monolithic unreleased micro-electro-mechanical-systems (MEMSs), which are in direct contact with its surrounding, or solidly mounted resonator devices which suffer from the same confinement issues [Bahr et al. 2014; Bahr 2016; Hamelin et al. 2019; Knapp et al. 2018].

Although SiCO:H alone is not sufficient, the periodic structure of alternating metal and oxide layers in the BEOL may exhibit so-called phononic crystal properties that influence wave propagation at certain frequencies and directions. These effects occur for a largely mismatched acoustic impedance

$$Z = \rho c \tag{6.1.1}$$

between the different layers of the stack, where ρ is the material density and c is either the longitudinal or transversal sound velocity in the respective material [Khelif and Adibi 2016; Rose 2014; Jiménez et al. 2021; Pennec and Djafari-Rouhani 2016; Khelif et al. 2010; Joannopoulos et al. 2008]. Whereas a continuous elastic medium supports wave propagation at any frequency, as discussed in Section 3.7.4, an alternating periodic patterning may introduce frequency forbidding regions. Those forbidden frequency ranges are called phononic band gaps, where a wave can not propagate if its frequency and wave vector are enclosed by the phononic band gaps. They are formed by destructive interference within the different layers of the stack [Khelif and Adibi 2016; Joannopoulos et al. 2008; Dobrzyński et al. 2018]. Using appropriate thicknesses of the involved BEOL layers, the centre frequency of the gaps can be shifted. In a typical semiconductor foundry, the thicknesses of the BEOL layers, however, are predefined from routing and electrical boundary conditions as products choose a combination of these available layers based on their requirements which are focused on complexity, performance and cost. Optimizing phononic crystal properties for a monolithic unreleased MEMS in a foundry setting is challenging.

Starting with the SiO_2-based BEOL, to maintain comparability to the previous chapter, the dispersion relation of the phononic crystal can be calculated analytically or with the FEM. Assuming an infinitely extended BEOL with an infinite number of layers, the stack may be reduced to its smallest unit cell, analogously to the modelling of the RFT. The unit cell and corresponding Brillouin zone are illustrated in Figures 6.1(a) and 6.1(c). The orientation of the

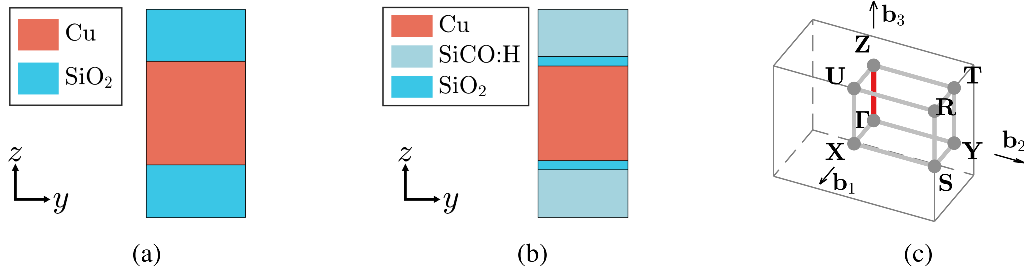

Figure 6.1: The unit cells for calculating the band structure using the interface response theory or FEM of a SiO_2 or SiCO:H base BEOL are depicted in (a) and (b). (c) The corresponding Brillouin zone and vector direction for vertical propagation.

unit cell was chosen following the orientation of the RFT, where the x-axis is parallel to the channel and the y-axis is pointing along the gate direction. Note that the unit cell is illustrated in 2D for visual purposes only.

The band structure for vertical propagation along Γ−Z in this unit cell can be computed analytically using the interface response theory [Djafari-Rouhani and Dobrzynski 1987; Dobrzynski 1990]. It is useful to define the parameters

$$\begin{aligned} C_i &= \cos(2a(i)\alpha(i)) \quad S_i = \sin(2a(i)\alpha(i)) \\ F_i &= c_{11,44}(i)\alpha(i) \qquad \alpha_i = \omega c_{l,t}(i)^{-1} \end{aligned} \tag{6.1.2}$$

where $a(i)$ is the half-layer thickness and $c_{l,t}(i)$ is either the longitudinal or transversal wave velocity of the ith layer, which are given in Table 5.3. $c_{11,44}(i)$ is the elasticity constant for either longitudinal or transversal waves. For the trivial case of a single-layered super-lattice, the interface response theory yields the well-known dispersion relation

$$\cos(\mathbf{k}a_u) = C_1 \tag{6.1.3}$$

for a bulk material as described in Section 5.1.3, on the matter of index guiding. Here $a_u = \sum_{i=1}^{n} a(i)$ is half the length of the unit cell with n layers [Djafari-Rouhani and Dobrzynski 1987; Dobrzynski 1990].

For a two-layered super-lattice, the interface response theory expands to

$$\begin{aligned} \cos(\mathbf{k}a_u) = C_1C_2C_3 + \frac{1}{2}C_1S_2S_3\left(\frac{F_2}{F_3} + \frac{F_3}{F_2}\right) \\ + \frac{1}{2}C_2S_1S_3\left(\frac{F_1}{F_3} + \frac{F_3}{F_1}\right) + \frac{1}{2}C_3S_1S_2\left(\frac{F_1}{F_2} + \frac{F_2}{F_1}\right), \end{aligned} \tag{6.1.4}$$

where the roots to this equation yield the 1D dispersion relation of the phononic crystal. The roots of (6.1.4) for either the wave vector or frequency can be found with the method proposed in [Rose 2014].

The solution to the problem may also be obtained numerically with the FEM. The 1D band

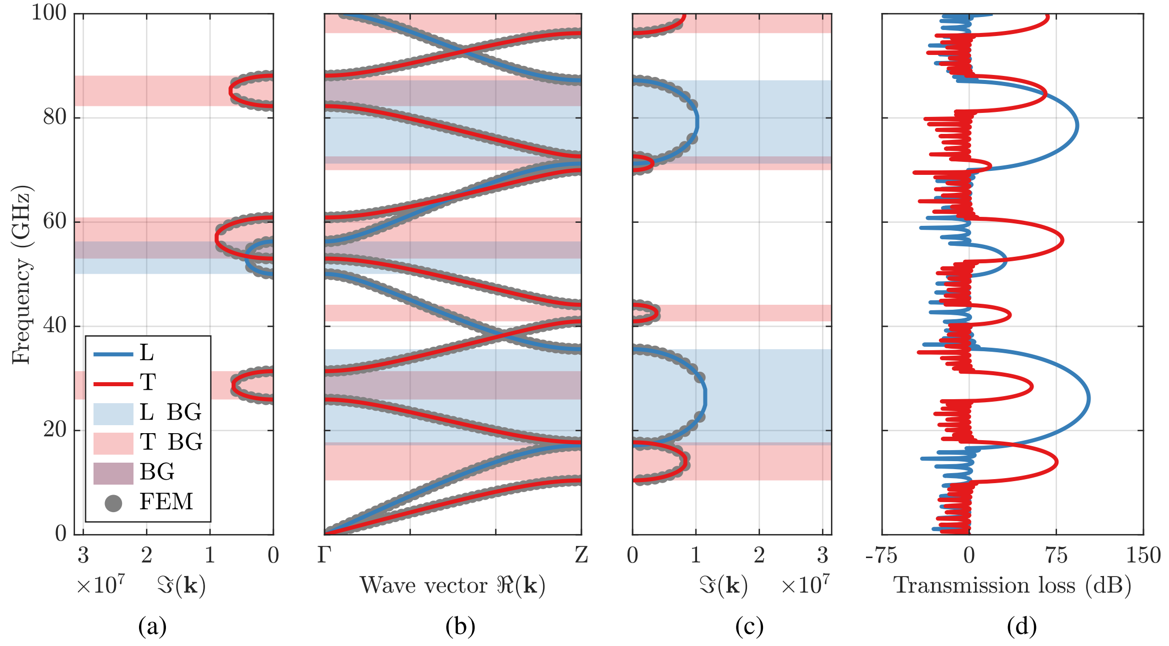

Figure 6.2: Comparison of the 1D band structure of an infinite 1D BEOL, with 50 nm thick copper and SiO_2 layers. The complex-valued band structure in (a) is calculated for the Γ-point with $\mathbf{k} = \Gamma + i\mathbf{k}_{im}$, (b) is computed within Γ−Z, and (c) is computed for the Z-point with $\mathbf{k} = \mathrm{Z} + i\mathbf{k}_{im}$. For a finite BEOL stack, the transmission can be calculated and (d) shows the corresponding transmission loss for a stack with eight metal layer repetitions.

structure is modelled with a 2D unit cell with Floquet-Bloch boundary conditions on all four sides [Hudeczek et al. 2021]. The unit cell depicted in Figure 6.1(a) must be modified with a sufficiently small lateral extension along the y-axis to prevent premature Brillouin zone folding. This effect is also observed for the band structure of the RFT in Section 5.1.2 and the bulk dispersion once the FinFET pitch is considered (see Figure 5.5 and Figure 5.6) [Hudeczek and Baumgartner 2020; Garcıa and Fernández-Álvarez 2015; Yang, Yang, et al. 2018].

It should be noted that copper is a strongly anisotropic material with $A = 3.22$ (see Table 3.1). Therefore, analogously to the 2D modelling of the FEOL, the equivalent isotropic material properties listed in Table 5.3 have to be used in the 1D case.

Both approaches are exercised on a BEOL stack with 50 nm thick copper and SiO_2 layers and the results are compared in Figures 6.2(a) to 6.2(c). Plotted is the real-valued solution within Γ−Z and the complex solutions at the high symmetry points. The solution of the FEM is marked by grey circles, with the analytic solution of the longitudinal and transversal waves given in blue and red, respectively. In contrast to the bulk dispersion, the super-lattice exhibits distinct bands for propagating modes with longitudinal or transversal polarisation. Between the bands, regions without supported eigenmodes exist, marked by the shaded areas. Within these gaps, the propagation of waves, regardless of the wave vector, is suppressed. For some frequency ranges, both longitudinal and transversal waves are blocked, as indicated by the purple areas, which is known as full non-polarised band gap. Some of the gaps are only valid for either longitudinal or transversal waves, which is referred to as a polarised band gap [Hudeczek and Baumgartner 2020;

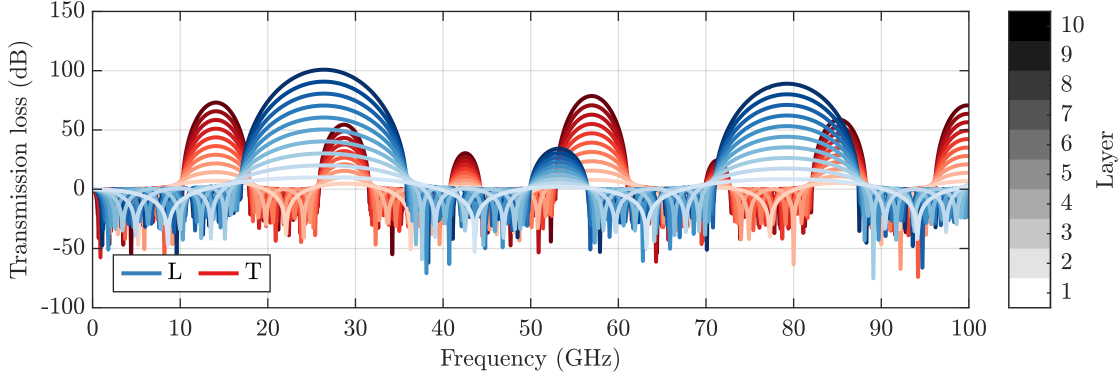

Figure 6.3: Transmission loss for longitudinal and transversal waves for a varying number of BEOL metal layers. The BEOL stack has 50 nm thick copper and SiO_2 layers.

Han et al. 2017; Wang et al. 2015; Achaoui et al. 2010; Sotto et al. 2018].

The analytical solution for (6.1.4) and the results computed with FEM within the band gaps are complex-valued, as shown in Figures 6.2(a) and 6.2(c). In both complex planes, a solution only exists for frequencies within the band gaps, which leads to an exponential decay of mechanical waves propagating through the stack [Jiménez et al. 2021; Khelif and Adibi 2016; Joannopoulos et al. 2008]. Both the analytical solution and the FEM results are in excellent agreement. Note that artificial modes in the complex planes have been filtered from the finite-element solution [Hudeczek and Baumgartner 2021].

The band gaps also manifest in the transmittance spectrum of waves through a finite stack. Using the FEM, a polarised wave is injected in a stack with eight unit cell repetitions. The resulting transmission loss

$$\mathrm{TL} = -20\log_{10}\left(\left|\frac{\mathbf{u}_{out}}{\mathbf{u}_{in}}\right|\right) \tag{6.1.5}$$

is computed from the displacements at the input $\mathbf{u}_{in}$ and output $\mathbf{u}_{out}$ facets of the stack [Pennec et al. 2004; Lu et al. 2018]. The results shown in Figure 6.2(d) exhibit a pronounced spike in the transmission loss for the frequencies within any of the prior calculated longitudinal or transversal band gaps. In those regions, the propagation of waves is strongly suppressed, while at all other frequencies the transmittance reaches unity. The overshoot into the negative values occurs since no damping is present in the simulation. Interestingly, the number of ripples in-between two adjacent band gaps correlates to the number of layer repetitions, as the system behaves like several weakly coupled oscillators [Dobrzyński et al. 2018; Jiménez et al. 2021; Chopra 2012; Khelif and Adibi 2016; Joannopoulos et al. 2008].

Also notable is that the longitudinal and transversal polarisations have different band gaps according to their independent propagation [Ting 2006a]. Unsurprisingly, the strength of the gap directly relates to the imaginary part of the complex-valued band structure as it defines the decay rate of the evanescent modes in the stack [Hudeczek and Baumgartner 2020; Jiménez et al. 2021].

Using a higher number of consecutive layers, the transmission loss of the BEOL, as depicted in Figure 6.3, can be improved by several orders of magnitude. Each additional layer leads to

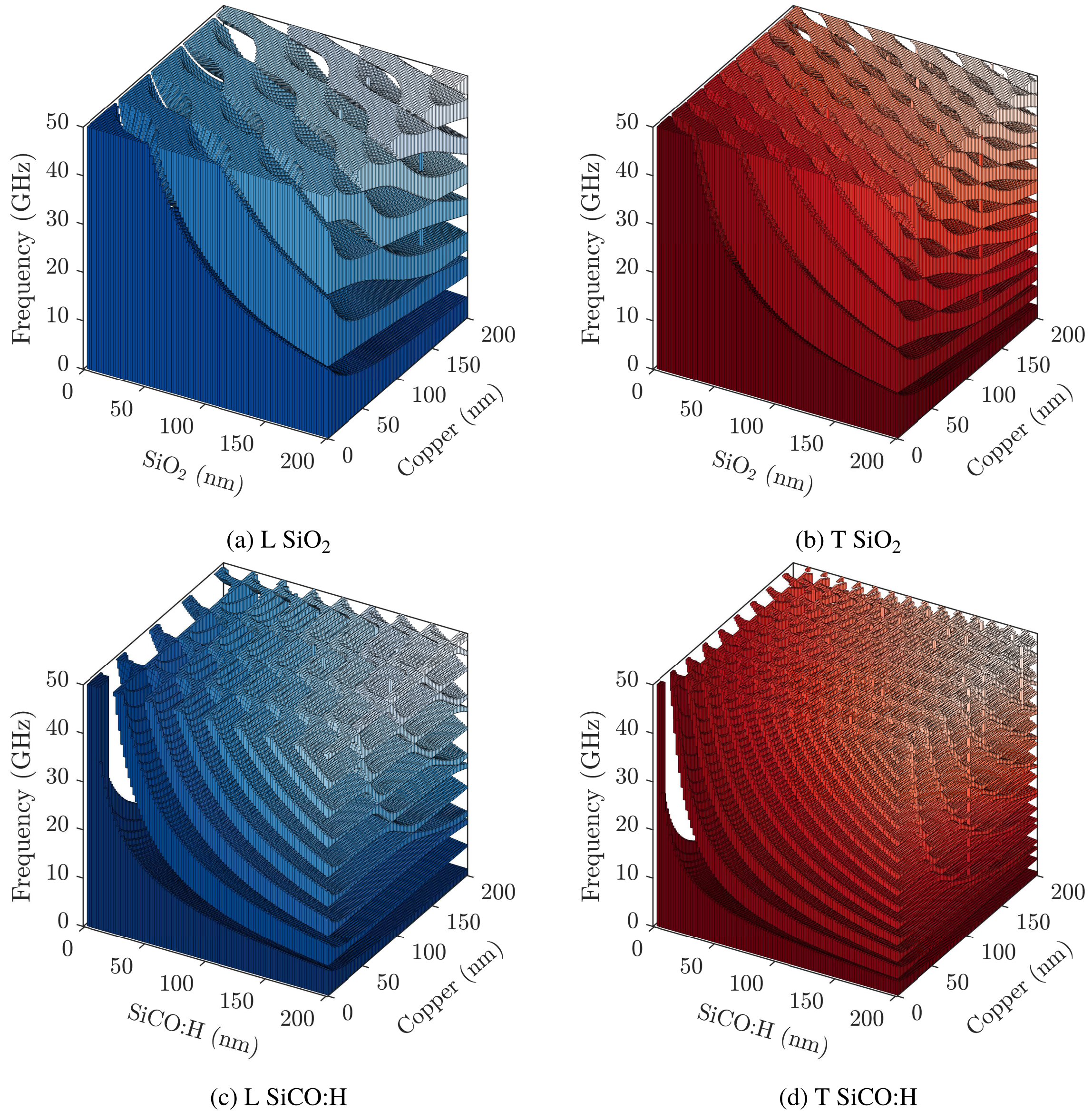

(a) L SiO_2

(b) T SiO_2

(c) L SiCO:H

(d) T SiCO:H

Figure 6.4: Evolution of phononic crystal bands with varying copper and SiO_2 layer thickness for (a) longitudinal and (b) transversal bands calculated with the interface response theory for vertical propagation along $\Gamma-Z$. The uninterrupted pillars for some configurations are artefacts of the calculation where the algorithm failed to find the roots of the equation.

a stronger attenuation within the band gap. Interestingly, a single copper and oxide layer pair already leads to a slight attenuation of incident waves. Also notable is the better performance of gaps with a larger bandwidth, and the largest attenuation is observed close to the centre frequency of each gap.

This analysis, however, is only valid for a specific BEOL thickness configuration. A preferably wide and non-polarised band gap is required to shield the RFT at the resonant frequency successfully. Assuming that the BEOL thicknesses can be freely chosen, the locations of all possible longitudinal and transversal band gaps are shown in Figures 6.4(a) and 6.4(b). Each pillar represents a certain thickness configuration, computed using the faster analytic method.

For the analysis, both the copper and SiO_2 thicknesses were swept from 5-200 nm. Within each pillar, a box indicates the existence of a band in that frequency range where either longitudinal or transversal waves may propagate through the stack. Interestingly for small copper and SiO_2 thicknesses, no phononic gaps, regardless of the frequency, are found. Similarly, for low frequencies, the investigated BEOL configurations do not exhibit a band gap, leading to the absence of gaps for many variations. For larger thicknesses and frequencies, however, phononic band gaps open up, repeating periodically. Here the longitudinal gaps in Figure 6.4(a) vary at a slower rate than transversal gaps in Figure 6.4(b), following the larger sound velocity, and thus an increased wavelength of the longitudinal waves. A few uninterrupted pillars can also be discerned, which are artefacts of the calculation as the algorithm failed to find the roots of the equation.

The same analysis is repeated for the modern low-κ BEOL stack, with the corresponding unit cell shown in Figure 6.1(b). As discussed in Section 2.1, the copper and SiCO:H layers are separated by a thin SiO_2 liner layer to prevent diffusion and increase structural integrity [Kavalieros et al. 2006; ITRS 2021]. Consequently, the unit cell features four layers and the interface response theory must be expanded [Djafari-Rouhani and Dobrzynski 1987; Dobrzynski 1990]:

$$\begin{aligned}\cos(\mathbf{k}a_u) = {} & C_1C_2C_3C_4 + \frac{1}{2}S_1S_2S_3S_4\left(\frac{F_1F_3}{F_2F_4} + \frac{F_2F_4}{F_1F_3}\right)\\ & + \frac{1}{2}C_1C_2S_3S_4\left(\frac{F_3}{F_4} + \frac{F_4}{F_3}\right) + \frac{1}{2}C_1C_3S_2S_4\left(\frac{F_2}{F_4} + \frac{F_4}{F_2}\right)\\ & + \frac{1}{2}C_1C_4S_2S_3\left(\frac{F_2}{F_3} + \frac{F_3}{F_2}\right) + \frac{1}{2}C_2C_3S_1S_4\left(\frac{F_1}{F_4} + \frac{F_4}{F_1}\right)\\ & + \frac{1}{2}C_2C_4S_1S_3\left(\frac{F_1}{F_3} + \frac{F_3}{F_1}\right) + \frac{1}{2}C_3C_4S_1S_2\left(\frac{F_1}{F_2} + \frac{F_2}{F_1}\right).\end{aligned} \tag{6.1.6}$$

The resulting bands for the SiCO:H-based BEOL are shown for longitudinal and transversal waves in Figure 6.4(c), respectively. The copper and SiCO:H thicknesses vary between 5-200 nm, while the liner layer thickness is fixed at 5 nm. Whereas the old SiO_2-based BEOL only had a few distinct band gaps in the investigated parameter range, the low-κ BEOL exhibits a larger number of phononic band gaps for both wave types. Furthermore, the gaps are separated by thinner bands leading to fewer forbidden regions for both longitudinal and transversal waves. This is caused by the much lower Young's modulus of SiCO:H in comparison to SiO_2, which leads to a larger acoustic impedance mismatch between the copper and oxide layers.

Assuming that the resonant mode of the RFT is exclusively radiating along $\Gamma{-}Z$ and the BEOL thicknesses can be chosen freely, the preceding results are used to find a viable BEOL phononic crystal configuration. Therefore, slices with a bandwidth of $f_{BW} = 1$ GHz, to allow for enough margin for the confinement, and a centre frequency matched to the resonant frequency of the RFT, are extracted from Figure 6.4. The 2D resonant frequency was simulated to $f_R = 30.847$ GHz

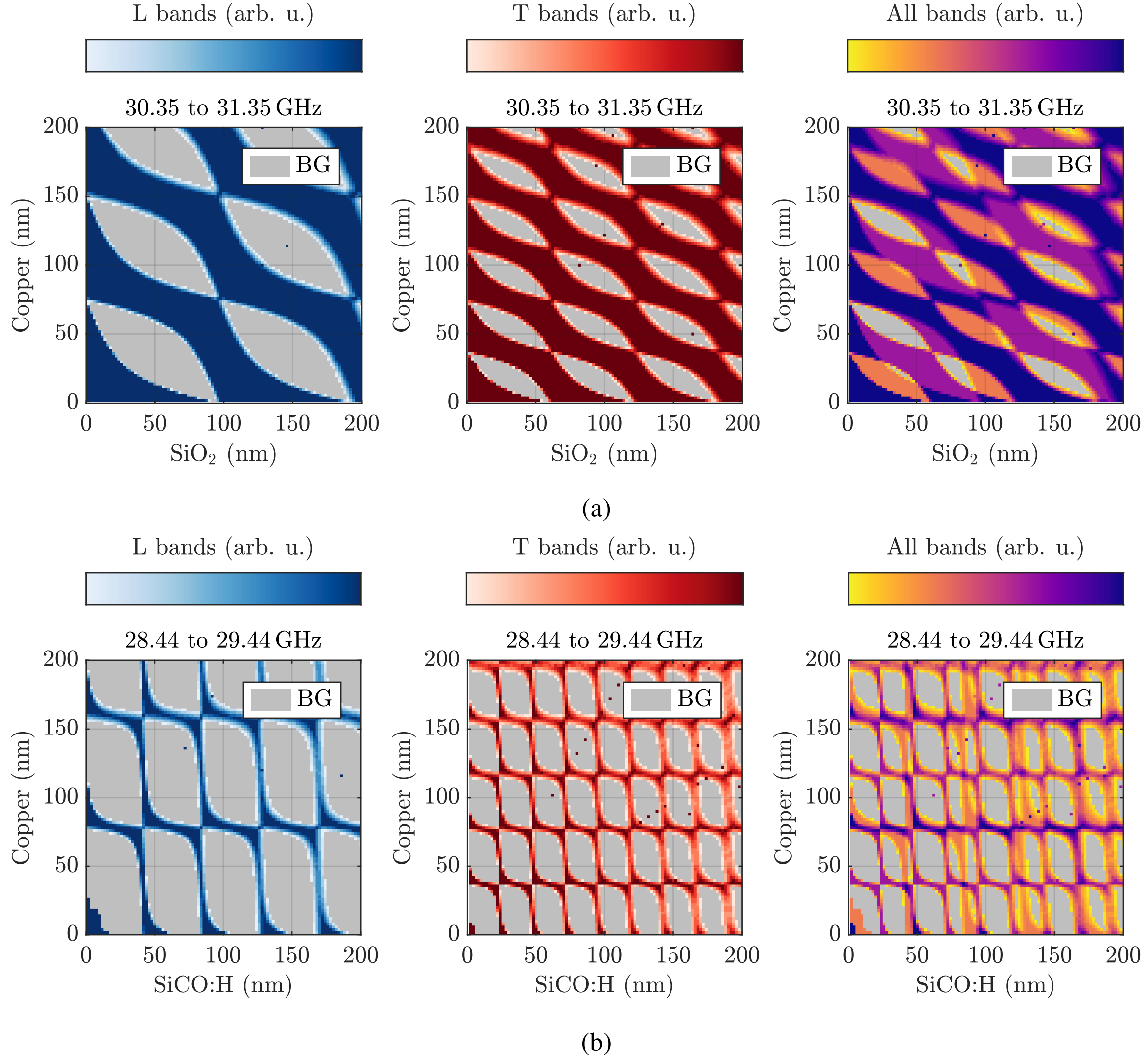

Figure 6.5: Extracted band gaps between 30.35-31.35 GHz for longitudinal and transversal and non-polarised waves propagating along $\Gamma-Z$. (a) For a SiO_2 and (b) for a SiCO:H-based BEOL.

for the SiO_2-based BEOL and f_R = 28.937 GHz for the SiCO:H based BEOL, as discussed in Section 5.4. The respective slices are plotted in Figure 6.5. The band gaps spanning at least the required frequency range are indicated in grey. The lighter colour around each gaps perimeter indicates a gap's existence, but their bandwidth is reduced as bands appear on either side of the spectrum. This leads to slight smearing of the band gaps with increasing layer thicknesses as the bands flatten, which is also visible in Figure 6.4. For longitudinally polarised waves, a band gap in the desired frequency range may be found for multiple BEOL layer configurations. The gaps repeat periodically for both layer thicknesses, which follows from the destructive interference at certain layer configurations. The same behaviour is also observed for transversal polarised waves, but the gaps are much smaller, and their repetition rate is higher due to the smaller shear wave velocity. It is possible to derive the non-polarised band gaps plotted in Figure 6.5(a) on the right by superimposing both polarisations. The number of gaps is strongly reduced, as both patterns of longitudinal and transversal waves must coincide to form a non-polarised band gap.

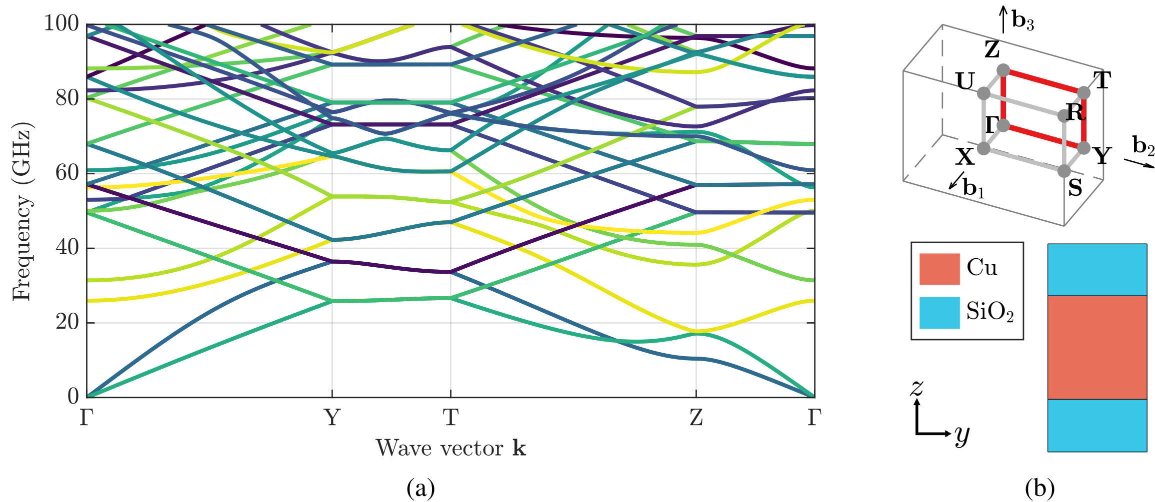

Figure 6.6: (a) The 2D band structure of a two-layer BEOL unit cell with a 50 nm thick copper and SiO_2 layer. (b) The respective unit cell and Brillouin zone for the FEM simulation.

Depending on the chosen BEOL stack, a matching band gap might be available, however, due to the broad extent of the individual bands, only a few very distinct options are possible.

The same applies to the SiCO:H-based BEOL (see Figure 6.5(b)), but due to the thinner bands the periodic pattern of the band gap changes more rapidly, which leads to fewer unsuited BEOL configurations. This behaviour can be observed for both longitudinal and transversal waves with a larger extent of the longitudinal gaps. Superimposing both the longitudinal and transversal solutions yields substantially more supported BEOL configurations which might be suitable for the confinement of the RFT mode.

Although suitable BEOL configurations for both variants can be found, the assumption of a pure vertical radiation pattern along Γ−Z is not entirely valid. As discussed for the FEOL mode of the RFT in Section 5.1.2, for the mode to propagate through the cavity its wave vector must be matched to the Y-point of the Brillouin zone. Therefore, the 1D assumption of the BEOL is insufficient as the incident wave has a non-vanishing contribution along the y-axis parallel to the gate.

6.2 The Two-Dimensional Phononic Crystal

To account for the lateral wave vector of the FEOL mode, the dimensions of the BEOL unit cell must be matched to the pitch of the underlying FinFETs, which was also required for the index guiding properties in Section 5.1.3. As the computation for non-perpendicular incident waves with the interface response theory is challenging the FEM, which is in excellent agreement with the analytic solution in the previous investigation, is used instead. The band structure is obtained by sweeping the wave vector of the Floquet-Bloch boundary conditions along the perimeter of the Brillouin zone, which is depicted in Figure 6.6(b). At each wave vector, an eigenmode simulation is carried out and the results are plotted in Figure 6.6(a). Since the eigenmodes are

computed for each wave vector separately, and no relation between adjacent wave vectors exists in the FEM, the band structure is originally unsorted and no bands can be identified. To assign each mode to its corresponding band, the individual eigenmodes are sorted and connected by exploiting the orthogonality of the eigenvectors for small enough wave vector steps during the simulation [Darinskii et al. 2007; Lu and Srivastava 2018].

Within the band structure the two exclusively horizontal or vertical propagating regimes along $\Gamma-\mathrm{Y}$ and $\Gamma-\mathrm{Z}$ can be seen. For lateral propagation along $\Gamma-\mathrm{Y}$ the BEOL is unpatterned, and thus exhibits no phononic crystal effects. This manifests in a continuum of possible modes since a possible supported eigenmode of the BEOL exists for each frequency and wave vector. Those modes are typically referred to as Lamb-waves, but they provide no shielding for the RFT [Hudeczek and Baumgartner 2020; Su and Ye 2009; Birgani et al. 2015; Birgani et al. 2017; Mizuno 2019; Giurgiutiu and Haider 2019; Pennec and Djafari-Rouhani 2016].

For vertical propagation along $\Gamma-\mathrm{Z}$, which has been discussed in the previous section, fewer polarised band gaps can be discerned compared to the 1D case in Figure 6.2. Here additional flat bands emerge above a frequency of approximately 50 GHz, which were not present in the previous 1D case. They result from a larger lateral extent of the Brillouin zone which leads to the folding of bands at the high symmetry points. Those folded bands extend throughout the complete band structure leading to a denser dispersion relation and less obvious band gaps.

The existence of the folded bands is problematic as they impede the performance of the phononic crystal. In Figure 6.7(a) the 2D solution within $\Gamma-\mathrm{Z}$ is computed with the FEM. Here the previously found purely polarised longitudinal or transversal bands in the 1D analytic calculations can be matched directly to the FEM solution, as indicated by the red and blue lines. However, the 1D interface response theory fails to capture the folded bands indicated in green as they only occur within the FEM simulation which captures a finite lateral extent. A subsequent transmission loss simulation of a finite stack with the lateral extend now matched to the FinFET pitch and eight BEOL layer repetitions align nicely with the theoretically predicted longitudinal and transversal band gaps. However, the folded bands indicated by the green shaded areas deteriorate the performance of the intersecting band gap by several decibels. Although their impact on the transmission loss appears only minor, the density of folded bands is expected to increase with a larger simulation volume encompassing either two, 14, or all 154 fins of the RFT. The high number of defect bands may thus overpower the polarised band gaps and entirely suppress any phononic crystal activity. In contrast to pure vertical propagation, as plotted in Figure 6.7(a), waves with a frequency below approximately 27 GHz for this configuration cannot propagate.

As mentioned earlier, the existence of band gaps matched to the propagation wave vector of the RFT mode at the Y point of the Brillouin zone is more important for the confinement. Here the BEOL provides several band gaps within $\mathrm{Y}-\mathrm{T}$ as all modes in that direction possess a matching wave vector, as indicated by the Brillouin zone in Figure 6.6(b). For this propagation direction, the transmission loss can also be computed with the FEM as plotted in Figure 6.7(b). Although

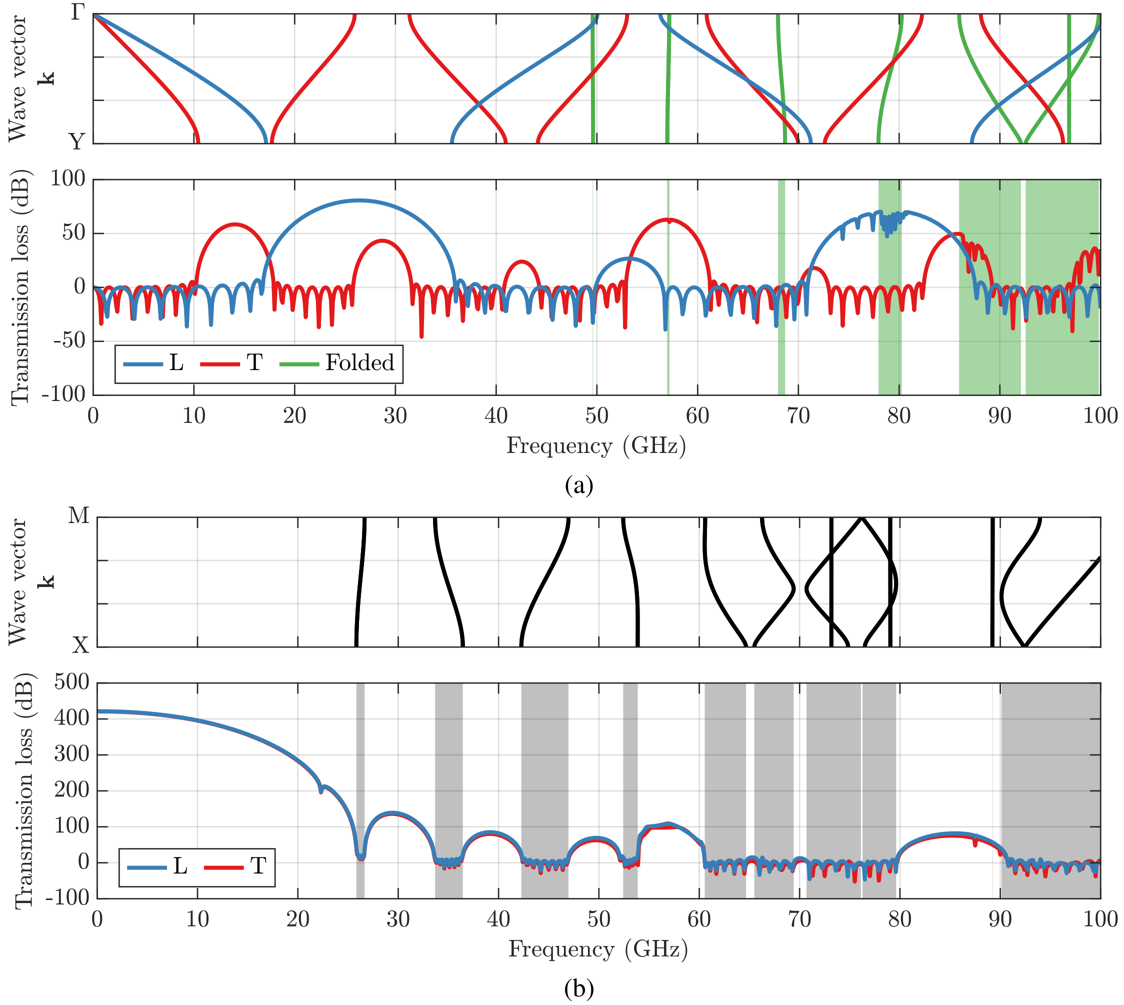

Figure 6.7: Simulated 2D band structure along (a) Γ−Z and (b) Y−T with the respective transmission loss for eight-layer repetitions.

the simulation was carried out for both longitudinal and transversal waves, both wave types produce an almost identical transmission loss. This follows from the mixed polarisation of the bands within Y−T, which cannot be classified as purely polarised bands as the polarisation changes between the high symmetry points [Achaoui et al. 2010; Muzar and Stotz 2019; Wang et al. 2015; Laude et al. 2009; Liu, Tsai, et al. 2014]. Nevertheless, the transmission loss spectrum matches nicely with the observed band gaps resulting in a strong attenuation of waves for the particular propagation directions covered by Y−T, regardless of their polarisation.

The observed band gaps within either Γ−Z or Y−T are also only applicable for the respective wave vectors, making them directional band gaps. For a band gap to be considered omnidirectional it must apply to all possible propagation directions within the Brillouin zone, which is impossible for the laterally unpatterned BEOL. Consequently, only the directions Γ−Z or Y−T may exhibit phononic crystal effects due to the periodic layering in those directions [Pennec and Djafari-Rouhani 2016; Khelif and Adibi 2016; Joannopoulos et al. 2008].

While the SiO_2 BEOL still offered several wide directional band gaps, suitable for the

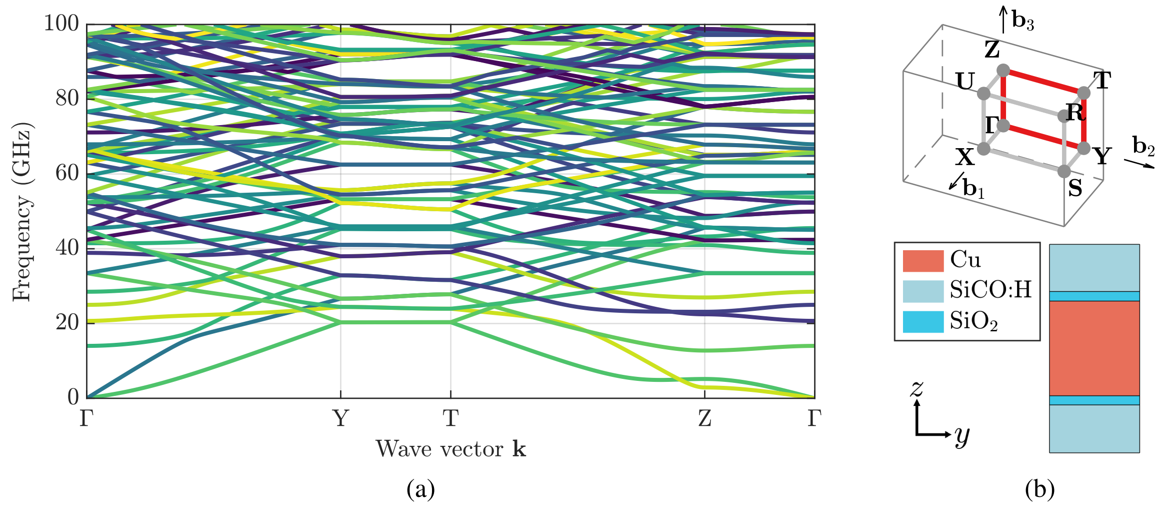

Figure 6.8: (a) The 2D band structure of a four-layer BEOL unit cell with a 50 nm thick copper and SiCO:H layer which are separated by 5 nm SiO_2 liner layers. (b) The respective unit cell and Brillouin zone for the FEM simulation.

confinement of the RFT, the band structure depicted in Figure 6.8 for the low-κ BEOL is much denser. Here the same behaviour is observed for the different possible propagation directions, however, the number of folded bands is strongly increased, making the existence of a matching band gap less likely.

To find a BEOL thickness configuration with a matching band gap the thickness sweeps from Section 6.1 are repeated with the FEM for bands within Y−T. The results are plotted in Figure 6.9(a) for SiO_2 and in Figure 6.9(c) for the SiCO:H-based stack. Both variants feature a large band gap, independent of the involved layer thicknesses, up to approximately 27 GHz for the SiO_2 and 18 GHz for the SiCO:H-based stack. Above the first band, the observed band gap again exhibits a periodic behaviour with the layer thicknesses, as already observed in the 1D case.

The respective slices with a bandwidth of $f_{BW} = 1\,\text{GHz}$, shown in Figure 6.9(b) and Figure 6.9(d), are matched to the resonant frequency of the RFT. Interestingly the band gaps of the SiO_2-based phononic crystal show almost no dependence on the oxide layer thickness in the investigated range up to 200 nm. For the copper layer thickness, a periodic behaviour is visible, with certain thickness configurations preventing the formation of a band gap, regardless of the oxide thickness. This behaviour was not observed for the vertical 1D case where almost no thickness existed preventing a band gap formation for all other thickness combinations with the other layer. For the low-κ BEOL the extracted slice features a periodic behaviour that depends on the metal and oxide configuration. Interestingly for both copper and SiCO:H, more combinations exist which prevent the formation of a band gap regardless of the choice of the other material thickness.

Although multiple viable BEOL configurations for the confinement of the RFT exist, the directional dependence remains a major drawback of the laterally unpatterned BEOL. To create an omnidirectional band gap periodic pattern must be present in all directions of the unit cell

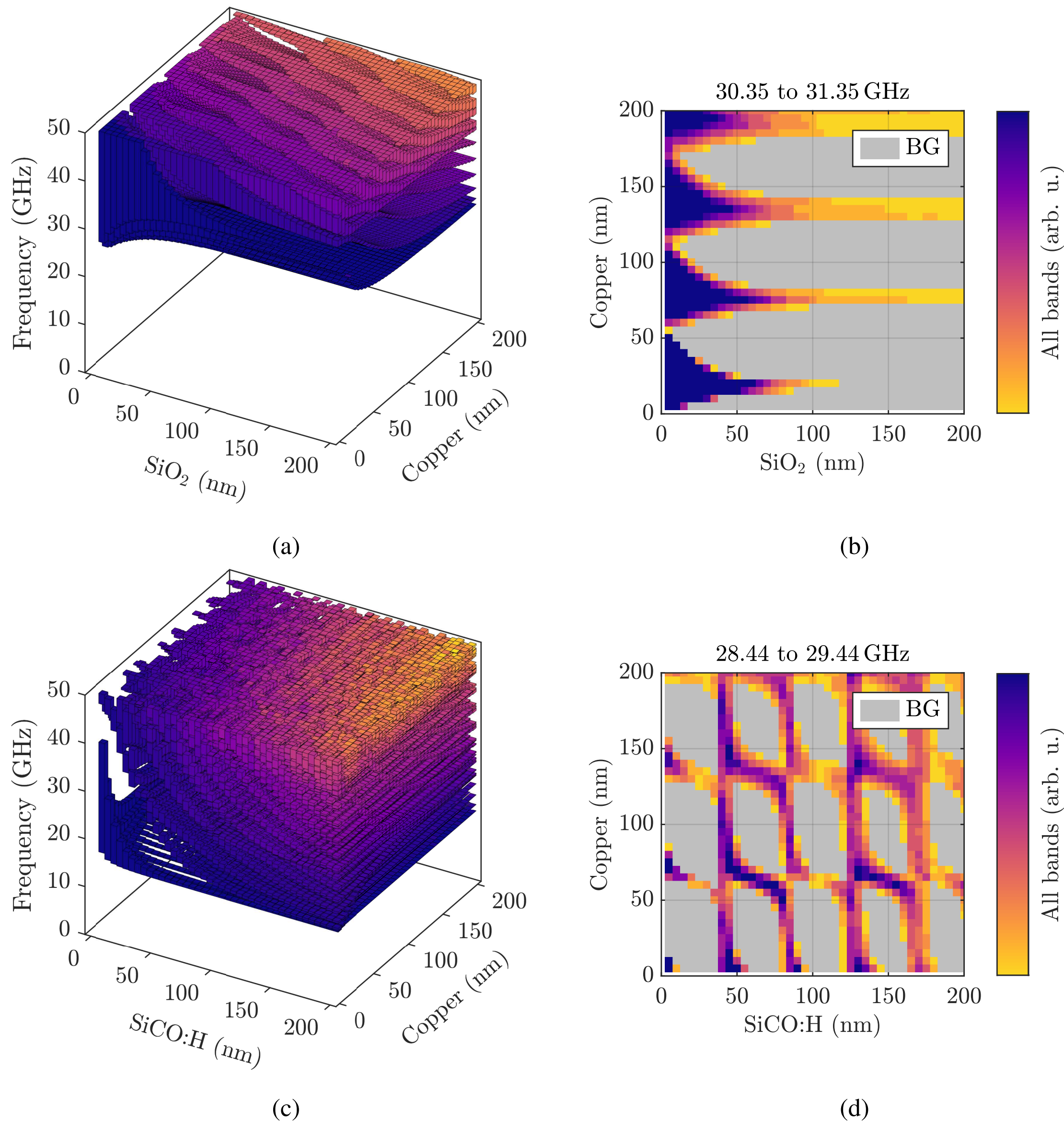

Figure 6.9: The evolution of bands with varying copper and oxide layer thickness for all bands calculated with the FEM for vertical propagation along Y−T. (a) For a SiO_2-based and (c) for a SiCO:H based BEOL. The extracted band gaps between (b) 30.35-31.35 GHz for the SiO_2 and (d) 28.44-29.44 GHz for the SiCO:H based BEOL.

[Khelif and Adibi 2016; Joannopoulos et al. 2008]. While uninterrupted metal plates can typically cover the whole RFT, the design rule check mandates strict lateral patterning rules for adjacent lines. One possibility is to create evenly spaced metal wires as illustrated in Figure 6.10(a), which are parallel to the channel directions, above the RFT. For those wires, minimum widths and spacings which the design rule check mandates must be maintained. The copper wires are embedded in SiCO:H and are covered by a 5 nm thick SiO_2 liner layer. An exemplary band structure for 75 nm thick copper wires with a width of 100 nm and an inter-wire spacing of 50 nm is plotted in Figure 6.11(a). Other than the previously laterally unpatterned stack, the resulting band structure features an omnidirectional band gap between approximately

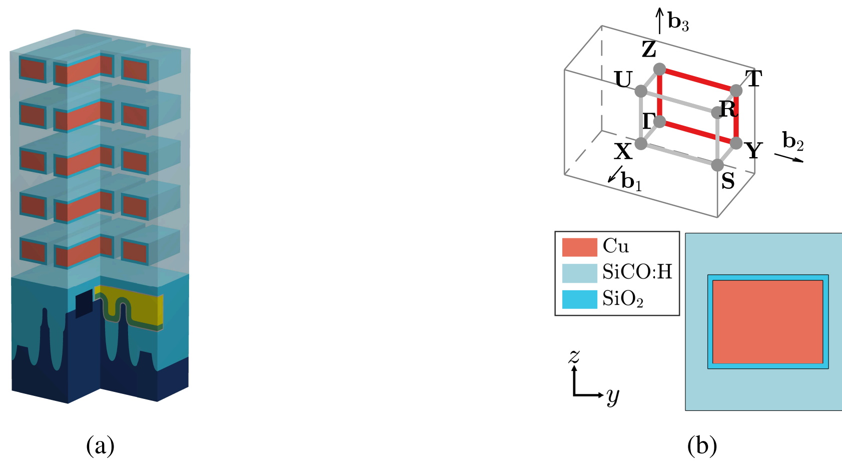

Figure 6.10: (a) A patterned BEOL stack with horizontal wires orthogonal to the RFT cavity. (b) The respective 2D unit cell of the BEOL and Brillouin zone.

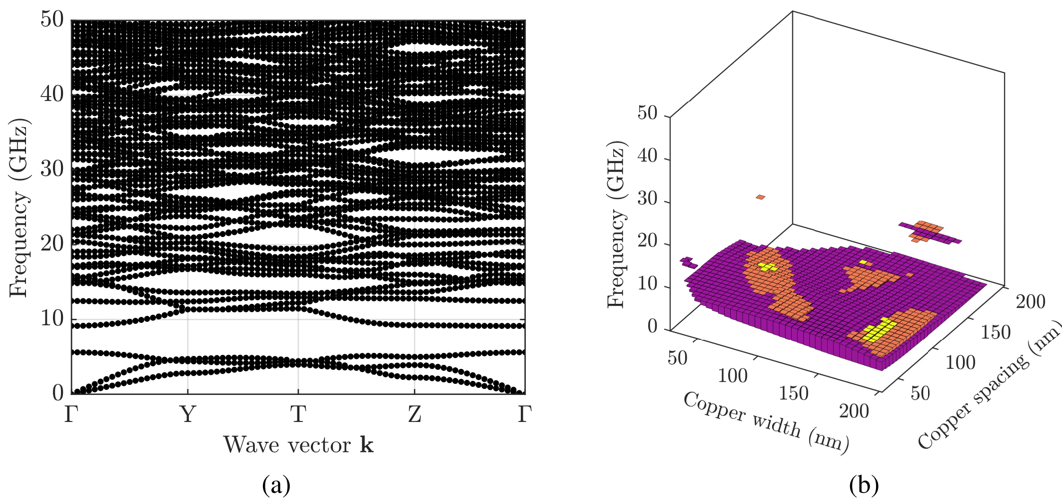

Figure 6.11: The band structure of the 2D unit cell depicted in Figure 6.10(b) is plotted in (a) for a copper and SiCO:H thickness of 75 nm. The copper wires are surrounded by a 5 nm thick SiO_2 liner layer and have a width of 100 nm and inter wire spacing of 50 nm. The possible full band gap configurations are shown in (b). Note that in this plot the band gaps are marked instead of the bands.

6.5-9.5 GHz. Within this gap, no wave propagates through the structure, independent of the polarisation or direction. This type of gap is preferable over a directional gap as any type of wave emitted or reflected from the cavity can be confined, and thus should lead to a larger Q-factor. However, further simulations are required to assess the impact.

The possible omnidirectional band gap frequencies for copper width and inter-wire spacings between 25-200 nm have been simulated with the FEM and are plotted in Figure 6.11(b). Note that in this plot the gaps are represented by the pillars, contrary to the previous representation in Figure 6.4 and Figure 6.9. For many configurations, a full band gap can be achieved. However, all of them are found around 10 GHz which is insufficient for the RFT which operates around 30 GHz. Moreover, metal slotting increases the number of bands above the omnidirectional band gap, reducing the chance for further suited directional band gaps.

Although other patterns could potentially shift the gaps to larger frequencies, they are unlikely to be supported by the foundry design rule check and have to be confirmed for the 30 GHz range [Khelif and Adibi 2016; Joannopoulos et al. 2008; Bahr et al. 2014]. Following the very strict design rule check rules, especially in the lower metal layers, the formation of an omnidirectional band gap within $\Gamma{-}\mathrm{Y}{-}\mathrm{T}{-}\mathrm{Z}{-}\Gamma$ which is matched to the RFT frequency, is therefore not feasible.

Consequently, the BEOL phononic crystal above the RFT must be fabricated with closed layers to enable at-least wider directional band gaps in the required frequency range and matched to the propagation of the RFT mode.

6.3 Combined Simulation of the Phononic Crystal and Resonant Cavity

In the previous section, directional band gaps in the layered stack were discussed for both SiO_2 and SiCO:H-based BEOLs. If the phononic gaps are matched to the resonant frequency of the RFT and modal wave vector, they are expected to greatly improve the Q-factor of the MEMS [Bahr et al. 2018; Bahr 2016; Goettler et al. 2010; Inomata et al. 2022; Liu, Tsai, et al. 2014]. While in the previous investigation the RFT was only simulated in the FEOL, and the BEOL was replaced by an oxide slab, they are now considered in a joint 2D simulation of the complete stack. This is necessary as modern low-κ oxides cannot provide sufficient confinement to the RFT through index guiding.

6.3.1 SiO_2-based Back-End-of-Line

Although SiO_2 proved to be a good material for high confinement of the RFT via index guiding, the RFT is now considered in conjunction with different BEOL stack configurations, and the impact on the performance is assessed. Analogously to the prior investigations the resonant eigenmodes and dispersion relation of the complete RFT structure are analysed using the FEM. Several suitable BEOL configurations with a well-matched band gap can be found from Figure 6.9(b). The chosen configuration features eight metal layer repetitions with 54 nm thick copper layers separated by 34 nm of SiO_2. The resulting dispersion relation along $\Gamma{-}\mathrm{Y}$ of the FEOL together with the BEOL is plotted in Figure 6.12 and marked by the coloured dots. Also indicated by thin grey lines are the four different sound cones, two each for the silicon substrate and the SiO_2 capping layer on top of the BEOL stack. The FEM solution of the individually considered infinite BEOL unit cell is superimposed in black. Plotted for reference is the analytic solution of the same stack for pure vertical propagation along $\Gamma{-}\mathrm{Z}$, which is indicated in blue and red for longitudinal and transversal modes, respectively. The folded bands not captured by the interface response theory are marked in green.

The resonant eigenmode of the RFT cavity is marked by an arrow and resides well within a phononic crystal band gap of the BEOL along $\mathrm{Y}{-}\mathrm{T}$. The second previously found guided

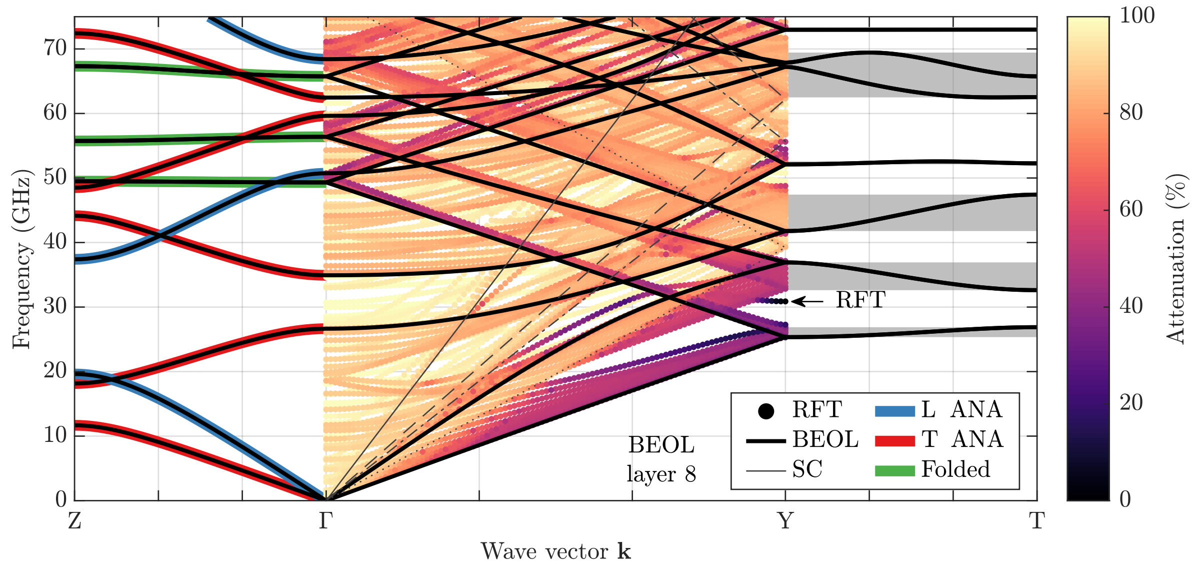

Figure 6.12: Band structure of a 2D RFT with eight BEOL copper layers which is superimposed with the band structure of the infinite BEOL unit cell as well as the analytic solution for longitudinal and transversal waves along Γ−Z. The copper layers have a thickness of 54 nm which are separated by 34 nm thick SiO_2 layers.

mode is covered by a larger number of additional guided modes in the band structure. The strongly increased number of eigenmodes throughout the whole spectrum, when compared to the identical structure without the BEOL in Figure 5.29(a), can be attributed to additional modes within the BEOL. Whereas the simulation without the BEOL features only two guided modes beneath the first shear sound cone of SiO_2, the dispersion relation of the complete structure has a larger amount of partially guided modes, which are indicated by their purple colour. Those modes occur close to the bands of the infinite BEOL simulation in a smeared-out fashion. They can be attributed to lateral modes propagating within the different layers of the BEOL rather than the FEOL. This allows them to remain partially guided even above the sound cones of silicon and SiO_2. The smearing of the bands is caused by the extent of the BEOL bands in Y−T, which is indicated by the grey-shaded areas.

The number of smeared-out bands correlates with the number of BEOL layer repetitions, as already observed for the transmission loss simulations. In Figure 6.13 the number of BEOL layers was swept, which did not affect the RFT mode. However, the number of BEOL modes increased as indicated by the circle. Note that one of the modes within the circle must be attributed to the asymmetric FEOL mode as shown in Figure 5.8(a) for a 3D simulation, which can be identified from its deformation profile. While each additional BEOL layer increases the number of possible supported modes in the structure, not all of them can be actuated for symmetry reasons or compatibility with the FEOL modes. More importantly, additional layers increase the transmission loss of the phononic crystal which manifests in the Q-factor of the RFT mode. The Q-factor increases with an increasing number of layers, as plotted in Figure 6.14. Interestingly for four or fewer BEOL layers, the Q-factor is lower than achieved through index guiding using a solid SiO_2 slab, which is indicated by a horizontal line. The Q-factor's slope

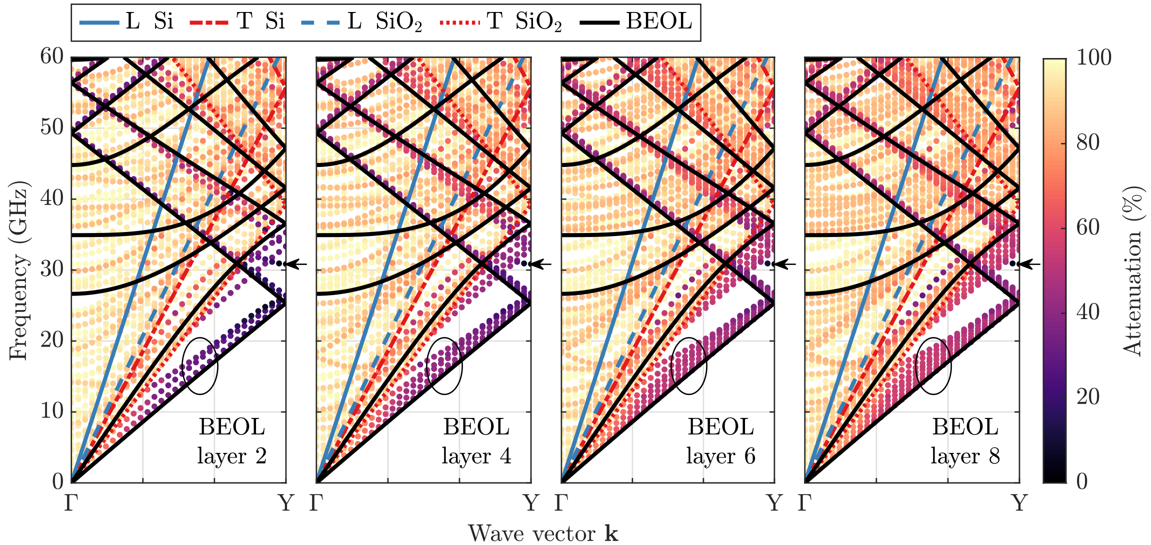

Figure 6.13: Band structure of a 2D RFT with an increasing number of BEOL layers from left to right. The copper layers have a thickness of 54 nm which are separated by 34 nm thick SiO_2 layers.

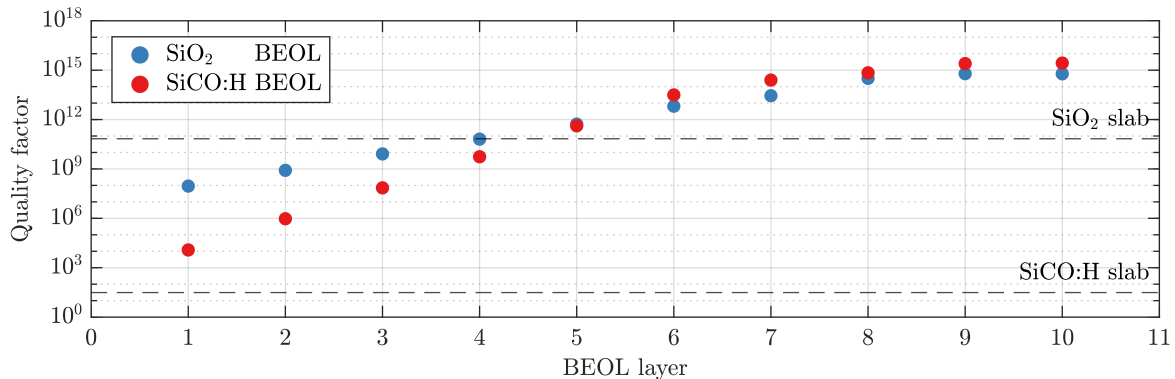

Figure 6.14: Dependence of the Q-factor on the number of copper layers within the BEOL phononic crystal. The Q-factors are calculated from the respective setups in Figure 6.12 for SiO_2 and Figure 6.18 for SiCO:H.

depends on the relative resonant frequency's position within the band gap. As shown for the transmission loss and the complex band structure, for example, in Figure 6.2, the attenuation of the band gaps decreases towards the edges. Consequently, the best phononic crystal performance is achieved for a band gap with a centre frequency close to the resonant frequency. Moreover, a wider band gap also results in an increased Q-factor as the transmission loss is larger than for a band gap with a lower bandwidth as shown in Figure 6.2. Five or more repetitions are required to improve the Q-factor further than achieved by only a SiO_2 slab without patterning. After approximately eight metal layers the Q-factor reaches 1×10^{15} with diminishing improvements with each additional layer. This trend implies that a phononic crystal on an older technology node might even reduce the performance. It also affects integrability as many of the metal layers above the RFT cannot be used for routing, which degrades the versatility. However, further investigation is required.

Note that the observed Q-factors of several trillion are unrealistic since no other damping mechanisms in the individual materials were considered. Consequently, the absolute values do

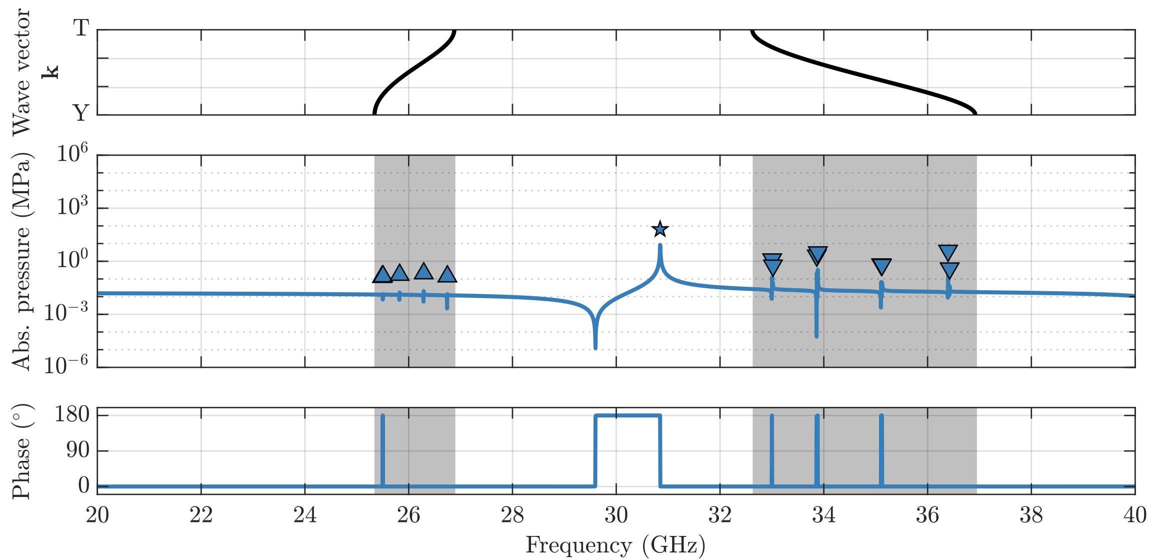

Figure 6.15: Frequency domain response of an RFT combined with a four-layer BEOL using the modal superposition technique. The copper and SiO_2 layers have a respectively 54 nm and 34 nm thickness.

not represent the actual performance but allow a relative comparison of different structures.

The frequency response is simulated for the complete undamped structure with four BEOL layers with a thickness of 54 nm and 34 nm for the copper and SiO_2, respectively. The BEOL layers were limited to four to maintain a reasonable degree of freedom (DOF) since the spectrum was simulated using the harmonic perturbation method to capture all involved eigenmodes in the investigated frequency range. Any artificial damping was omitted in this simulation to quantify the performance of the BEOL. The corresponding band structure of the BEOL within Y−T, pressure response, and phase are plotted in Figure 6.15. The spectrum exhibits a pronounced resonance at the frequency of the RFT, which is marked by a star. The respective deformation profile is shown in Figure 6.16(b), which is confined to the FEOL with a fast amplitude decay in the phononic crystal. In the absence of band gaps in the BEOL, which is marked by the grey shaded areas, spurious modes occur in the pressure spectrum. Here some modes of the RFT cavity can couple to supported modes of the BEOL, which results in spurious resonances as marked by triangles, and their deformation profiles are shown in Figures 6.16(a) and 6.16(c). Contrary to the RFT mode, these modes show a strong deformation with the BEOL stack as they radiate away from the cavity. Although their amplitude is small they pose a risk to the operation of the RFT as spurious modes in the close vicinity of the main resonance can lead to an energy loss [Harrington et al. 2010; Gokhale and Gorman 2018]

On the contrary, a BEOL configuration with 74 nm thick copper and 34 nm thick SiO_2 layers has no band gap at RFT's resonant frequency, which is visible in Figure 6.9(b). The respective frequency domain response is plotted in Figure 6.17. Rather than observing a single RFT resonance at the expected frequency of 30.847 GHz it is split into multiple resonances. They are marked by downward-facing triangles and are observed near each other. Their deformation profile, shown in Figure 6.16(e), has large displacements within the FEOL and the BEOL. Due

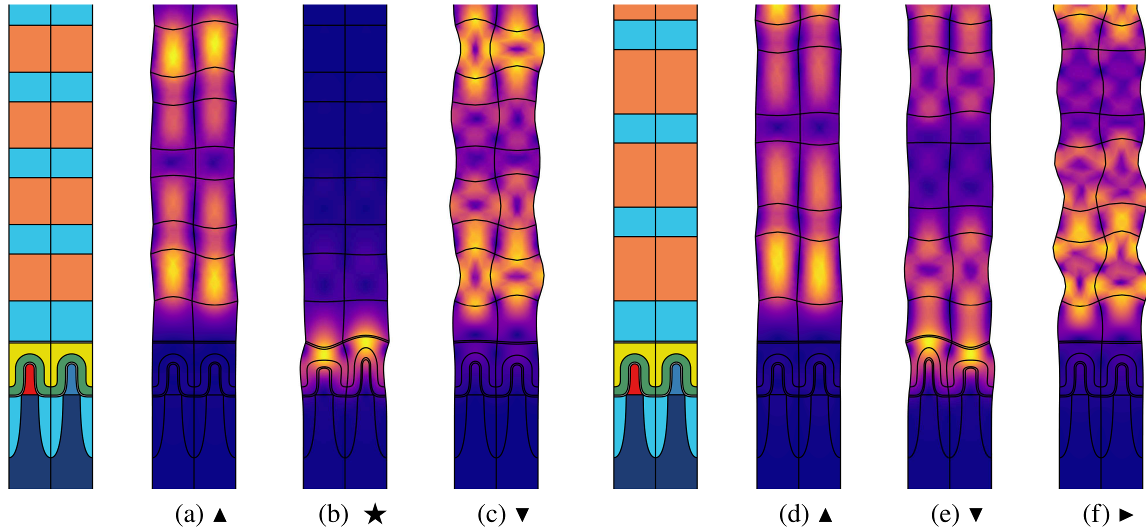

Figure 6.16: The displacement profiles for a 2D RFT with a four-layer BEOL with 54 nm thick copper and 34 nm thick SiO_2 layers are shown in (a) to (c) and correspond to the resonances from Figure 6.15. The modes shown in (d) to (f) correspond to a BEOL with 74 nm thick copper and 34 nm thick SiO_2 layers as Simulated in Figure 6.17. Note that the displacement amplitudes are normalised within each respective mode and not on the same scale for different modes.

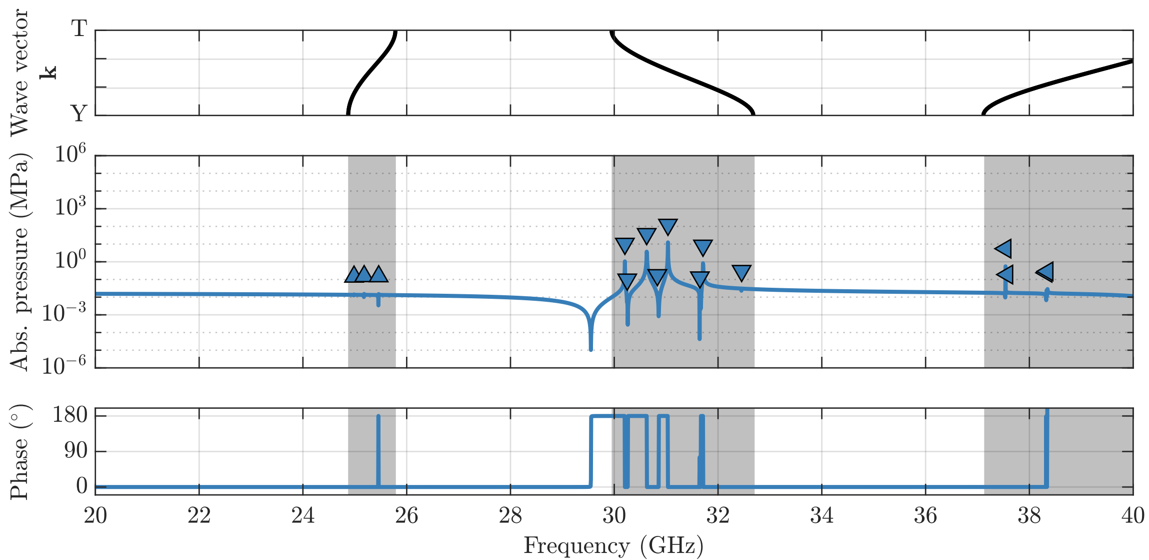

Figure 6.17: Frequency domain response of an RFT combined with a four-layer BEOL using the modal superposition technique. The copper and SiO_2 layers have a thickness of respectively 74 nm and 34 nm.

to the presence of a BEOL bands in this frequency range, which is highlighted by the grey area, the RFT mode can couple to the several support modes of the BEOL. Interestingly the largest observed peak pressure is almost identical to the previous case with a matching band gap, which follows from the SiO_2 capping layer on top of the BEOL. Although a FEOL mode can couple to the BEOL and radiate away, it is ultimately confined via index guiding at the top of the structure, leading to a reflection of the incident waves.

Also observed are a few weak BEOL modes, which are marked by upwards and sideways-facing triangles. They are again the result of a supported band where the cavity modes

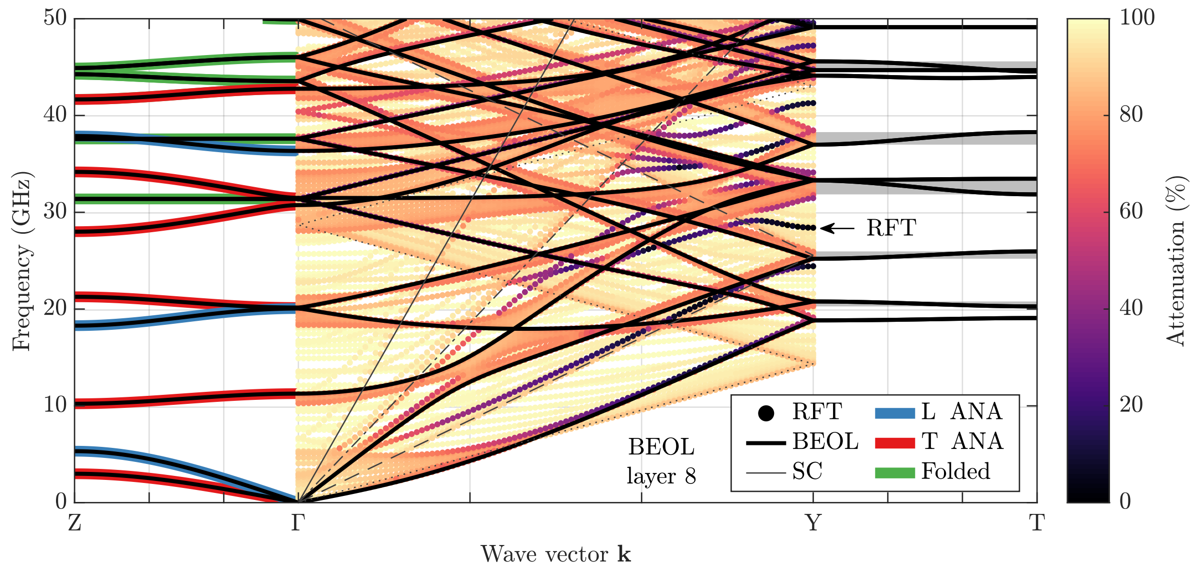

Figure 6.18: Band structure of a 2D RFT with eight BEOL copper layers which is superimposed with the band structure of the infinite BEOL unit cell as well as the analytic solution for longitudinal and transversal waves along Γ−Z. The copper layers have a thickness of 35 nm which are separated by 5 nm thick SiO_2 liner and 65 nm thick SiCO:H layers.

can couple to BEOL, which is also reflected by the deformation profiles in Figures 6.16(d) and 6.16(f).

This shows that a SiO_2-based BEOL phononic crystal is almost inconsequential to the performance of an RFT as the index guiding capabilities of the involved oxide layers already result in a well-confined FEOL mode. The addition of a BEOL phononic crystal only increases the risk of spurious modes in close vicinity to the RFT mode, impeding the performance rather than improving it. Also, a large number of successive metal layers is required to outperform the Q-factor obtained via index guiding, reducing the MEMS's vertical footprint.

6.3.2 SiCO:H-based Back-End-of-Line

While adding a phononic crystal mirror on an older technology node does not yield significant improvements it is essential for the RFT on more advanced nodes. The RFT cannot be confined on these nodes via index guiding of the low-κ oxide layer alone. Here the shear sound cone of SiCO:H is limiting the shielding to frequencies below 14.347 GHz, as listed in Table 5.2, which is insufficient for the approximately 30 GHz required by the RFT.

Following the foregone band gap analysis, shown in Figure 6.9(d), multiple suitable BEOL configurations which match the RFT frequency of 28.937 GHz can be found. One configuration has copper and SiCO:H layers with a thickness of 35 nm and 65 nm, respectively, while the SiO_2 liner layers are 5 nm thick. The resulting band structure of the RFT combined with an eight-layer BEOL is shown in Figure 6.18. It is again superimposed with the dispersion relation of the infinite BEOL, indicated by black lines, and the sound cones of both silicon and SiCO:H. Within Γ−Z the analytic solution for longitudinal and transversal modes are marked in blue and

red. The folded bands, identified with the FEM, are highlighted in green.

In the previous 2D simulation of the RFT with a solid SiCO:H slab, plotted in Figure 5.29(b), many unguided leaky modes exist above the shear sound cone. Since the RFT mode was also within the leaky region it is only poorly guided, which leads to a small Q-factor of 31. By adding of a phononic crystal with multiple band gaps, several previously leaky modes are now well confined within the structure which is indicated by black coloured dots at the high symmetry point Y in Figure 6.18.

Also, in this configuration, the BEOL introduces many additional modes which assimilate to the solution of the infinite BEOL simulation. The number of modes is again linked to the number of layers in the stack and they are smeared out by the extent of the bands within Y−T, as marked by the grey areas. Since the bands are more flat compared to the SiO_2-based BEOL the smearing is less pronounced. As previously found the SiCO:H based BEOL also introduces more additional bands when compared the SiO_2 based stack which leads to narrower band gaps.

Since a band gap well encloses the RFT mode, the Q-factor is improved, as plotted in Figure 6.14. A single BEOL layer already increases the Q-factor by several orders of magnitude over the Q-factor achieved by a SiCO:H slab. The Q-factor rises steadily with each additional layer, and, analogously to the SiO_2-based BEOL phononic crystal, levels off after approximately eight-layer repetitions. It also settles at a slightly increased Q-factor over the SiO_2 based phononic crystal, resulting from a better centring of the RFT mode within the respective band gap leading to higher confinement.

Although the configuration is similar, comparing this simulation to the band structure shown in [Bahr et al. 2018] several discrepancies are visible. The presented band structure is claimed to be simulated with a low-κ BEOL stack on top of the device. However, none of the respective BEOL bands occurs within the dispersion relation. Although the impact of the reduced sound cone frequency in SiCO:H is inconsequential, it still may be observed within the band structure simulation, as shown in Figure 6.18. In the data presented by Bahr et al., only the sound cone of silicon and none of the BEOL phononic crystal bands are discernible, raising concern about the band structure being simulated with the provided unit cell or undisclosed data post-processing.

Following the foregone frequency domain analysis, the effectiveness of the band gap is assessed for the in Figure 6.19. As shown in the band structure plot in Figure 6.18 the RFT is centred in a wide band gap manifests in a pronounced resonance which is marked by a star. The additional spurious modes, which couple to the BEOL modes, are indicated by triangles and diamonds. Also observed is an additional mode, close to one of the BEOL bands, which is marked by a circle. The respective deformation profiles are shown in Figures 6.20(a) to 6.20(d). The deformation profile of the RFT mode in Figure 6.20(c) is concentrated mainly to the FEOL of the device, which leads to a pronounced pressure response in the FinFET channels. Interestingly, the mode also exhibits strong deformations within the first SiCO:H layer before it is confined by the phononic crystal. This follows from the sound cone of the first SiCO:H layer, which may not shield against frequencies above 14.347 GHz. Consequently, the RFT mode can radiate into

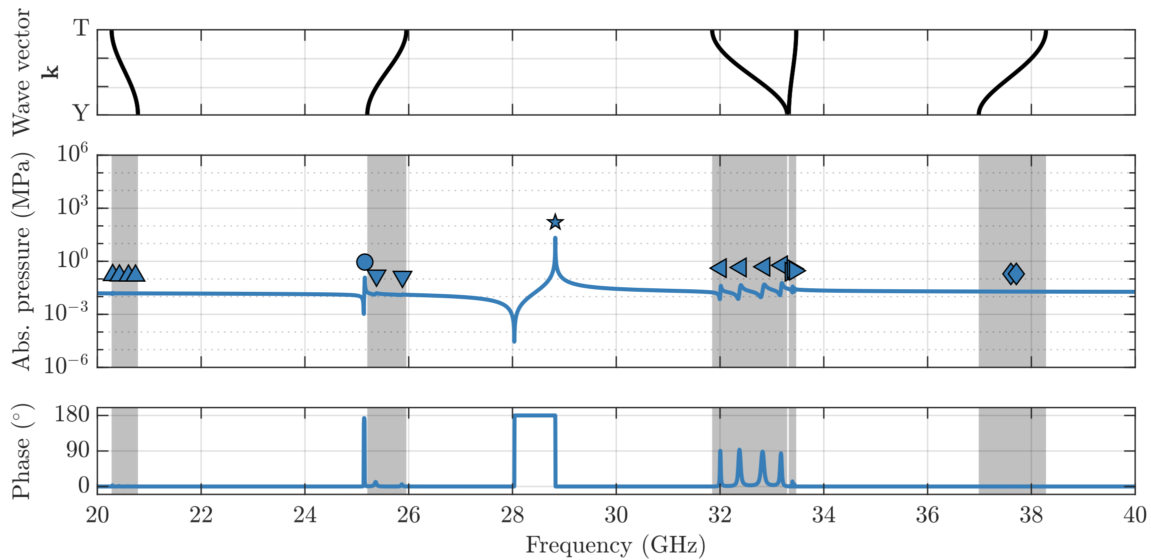

Figure 6.19: Frequency domain response of an RFT combined with a four-layer BEOL using the modal superposition technique. The copper and SiCO:H layers have a thickness of respectively 60 nm and 70 nm and are separated by 5 nm SiO_2 liner layers.

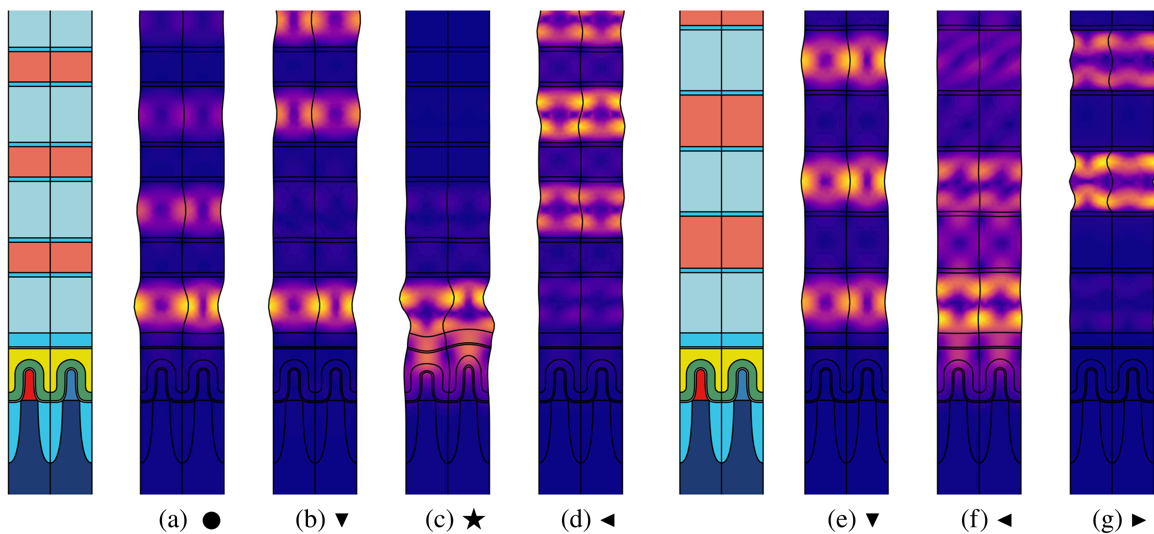

Figure 6.20: The displacement profiles for a 2D RFT with a four-layer BEOL with 35 nm thick copper and 65 nm thick SiCO:H layers are shown in (a) to (d) and correspond to the resonance from Figure 6.19. The modes shown in (e) to (g) correspond to a BEOL with 60 nm thick copper and 70 nm thick SiCO:H layers, as plotted in Figure 6.21. All layers are separated by 5 nm thick SiO_2 liner layers. Note that the displacement amplitudes are normalised within each respective mode and are not on the same scale for the different modes.

the first oxide layer of the BEOL, although a matching band gap exists. The RFT's performance is degraded as the mode is not fully confined within the FEOL but leaks into the intermediate space between the FEOL and BEOL.

The spurious BEOL modes in Figures 6.20(b) and 6.20(d) are mainly confined to the phononic crystal with small displacements within the FEOL. The additional observed mode in Figure 6.20(a) appears to be closely related to the BEOL modes with a frequency of 25.12 GHz. However, it shows a slightly increased deformation in the FEOL. The response, however, does

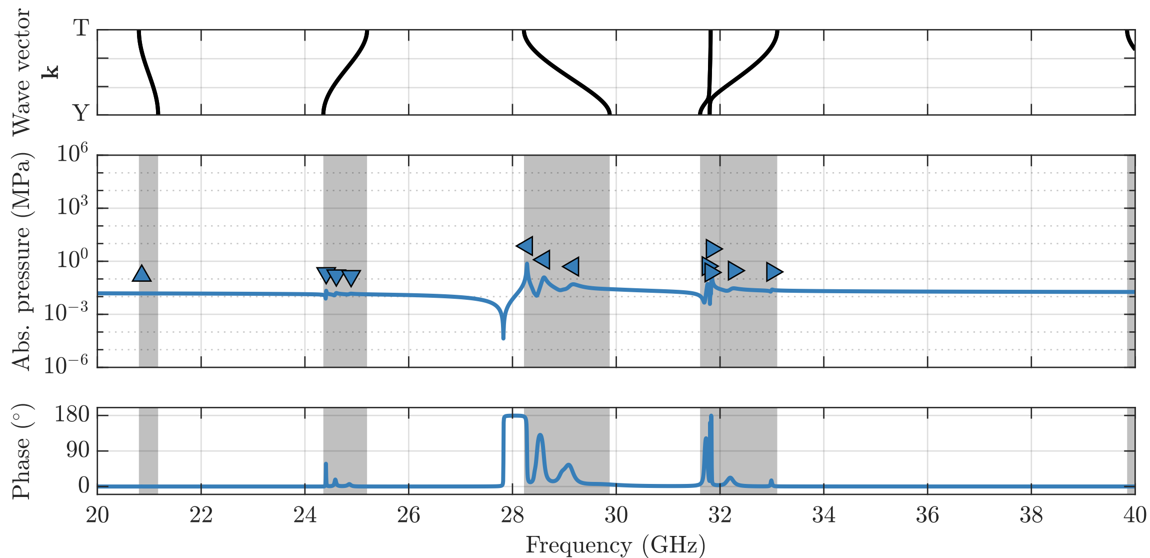

Figure 6.21: Frequency domain response of an RFT, combined with a four-layer BEOL, using the modal superposition technique. The copper and SiCO:H layers have a thickness of respectively 60 nm and 70 nm and are separated by 5 nm SiO_2 liner layers.

not belong to the second guided mode observed in Figure 6.18 at approximately 24.75 GHz since this mode cannot be excited for symmetry reasons.

Contrary to the SiO_2 BEOL, a mismatched band gap suppresses the RFT mode in a frequency domain simulation, as shown in Figure 6.21, for a BEOL with 60 nm thick copper and 70 nm thick oxide layers. The liner layers remain unchanged with a thickness of 5 nm. In the absence of a matching band gap no definite RFT mode can be discerned, but rather several resonances in the close spectral distance, as indicated by the left-facing triangles. Although the mode profile in Figure 6.20(f) is similar to the RFT mode it strongly couples to the BEOL, reducing the maximal pressure response. Furthermore, the frequency of the largest observed peak and anti-resonance are shifted towards the edge of the band by several megahertz.

As discussed in Chapter 5 both a large Q-factor and large pressures are required within the sense FinFET for optimal performance. Using an eigenmode simulation of the same structure, the Q-factor of the largest RFT-like mode was simulated to only 1141. In conjunction with the low observed kilopascal pressures, the transconductance is not expected to exceed the nanosiemens regime. This is still a strong overestimation of the result since the 2D simulation was shown to overestimate the pressure by approximately a factor of eight as listed in Table 5.5. A change from a 2-fin to a 14-fin unit cell results in another drop in the transconductance by a factor of seven.

Consequently, the presence of a matched phononic crystal band gap is mandatory as the simulated transconductance at a Q-factor of 50 000 falls already short of the reported value by three orders of magnitude. Although the general confinement principles of the BEOL were confirmed, many effects, such as mechanical anisotropy, have not been considered in this first 2D estimate.

Table 6.1: Vertical sound wave velocities along $\mathbf{k} = [001]$, in spatial coordinates, for selected copper orientations. The propagation direction $\mathbf{k}'$ is normalised in crystal coordinates. Also given are the explicit solutions for longitudinal and transversal waves [Ting 2006a; Hudeczek and Baumgartner 2020]. The density of copper is $\rho = 8960\,\mathrm{kg\,m^{-3}}$.

Orientation	Christoffel equation			Explicit expression		
	c_l (m s^{-1})	c_{t1} (m s^{-1})	c_{t2} (m s^{-1})	$\mathbf{k}'$	ρc_l^2	ρc_t^2
(001)	4330.1	2893.2	2893.2	$[001]^{-1/2}$	c_{11}	$c_{44}(\times 2)$
(011)	4949.5	2893.2	1619.5	$[022]^{-1/2}$	c_1^* [a]	$c_{44},\ c_{44} + Hk_3^2$ [b]
(111)	5972.1	3765.7	3765.7	$[333]^{-1/2}$	c_0^* [c]	$c_{44} + \frac{1}{3}H(\times 2)$ [b]

[a] $c_1^* = \frac{1}{2}(c_{11} + 2\gamma_1),\ \gamma_1 = c_{12} + 2c_{44}$
[b] $H = c_{11} - c_{12} - 2c_{44},\ k_3$ is the third vectorial component of $\mathbf{k}'$
[c] $c_0^* = \frac{1}{3}(c_{11} + 2\gamma_1),\ \gamma_1 = c_{12} + 2c_{44}$

6.4 The Three-Dimensional Phononic Crystal

In the previous 1D and 2D investigations all involved materials, including copper were assumed to be isotropic. This assumption is not valid as covered for silicon during the FEOL modelling of the RFT. Copper, which is used within the BEOL, is an even stronger anisotropic material. As discussed in Chapter 3, the sound velocities vary with the crystallographic direction. Consequently, the phononic crystal capabilities of the BEOL depend on the crystallographic orientation of the involved metal layers. Furthermore, all out-of-plane modes within the BEOL are suppressed in a 2D investigation, reducing the number of observed modes.

During fabrication, copper crystallises into grains in different phases, which changes the mechanical properties throughout the individual layers. The three most common orientations reported in the literature are (001), (011) and (111), with respective probabilities of 21 %, 14 % and 35 % [Basavalingappa et al. 2017]. The remaining 30 % are occupied by other orientations, however, at lower percentages of 3 % each, which are neglected for this analysis. In the following first-principles study, the individual copper sheets are assumed as monocrystalline for simplicity.

As covered in Section 3.7.4, an isotropic material supports the propagation of longitudinal and two transversal waves. In this case, the transversal wave velocities are identical and all three quantities are independent of the propagation direction. However, in an anisotropic material, the wave speeds depend on the direction of propagation. Only shear waves propagating along either ⟨100⟩ or ⟨111⟩ share the same velocities for both the fast and the slow shear wave. The transversal wave velocities differ for all other directions, with the largest velocity difference occurring along ⟨110⟩. This follows from the maximum and minimum shear modulus of copper discussed in Section 3.7.3.

The wave velocities for the different copper orientations can be obtained with the Christoffel equation (3.7.7) for an arbitrary propagation direction and are given in Table 6.1 for the three dominant copper orientations and vertical propagation. Because all three orientations are special configurations marking either a minimum, saddle point, or maximum of Young's modulus

along the direction of propagation (compare Figure 3.4), they can also be acquired by explicit analytic expressions, which yield identical results to the Christoffel equation [Ting 2006b; Hudeczek and Baumgartner 2021].

First, the case of vertical propagation for perpendicular incident waves is investigated. The band structure of all three crystallographic orientations is computed with the interface response theory (6.1.6) and it is also simulated with the FEM using a unit cell with a sufficiently small lateral extend to prevent premature Brillouin zone folding. The respective stack is fabricated from 50 nm thick copper and SiCO:H layers, which are separated by 5 nm liner layers. The analytical solution from (6.1.6) and the FEM simulation. Both results are compared in Figure 6.22. For all computed dispersion relations, in the first three columns of Figure 6.22, the analytic solution is given by coloured lines and the finite-element simulation results by grey dots. Here both solutions are aligned for real- complex-valued solutions for all three copper orientations.

As listed in Table 6.1 for the first orientation (001) in Figure 6.22(a), the two shear velocities are identical, leading to a two-fold degeneracy of the shear modes T_1 and T_2. Their polarisation directions

$$\mathbf{s}_{1,2} = \frac{1}{\sqrt{2}} \begin{bmatrix} \sin\phi \\ \cos\phi \\ 0 \end{bmatrix} \tag{6.4.1}$$

may point along any direction within the (001) plane, where ϕ is the polarisation angle. However, the orthogonality of both polarisations must be maintained at all times [Ting 2006a]. The longitudinal wave L is pseudo-polarised along the propagation direction. Also shown in Figure 6.22(a) is the transmission loss for a finite anisotropic BEOL with four copper layers, which matches well with the theoretically predicted band gap locations from the band structure calculation.

For a (011) oriented copper layer the fast and slow shear waves have different propagation velocities leading to a splitting of the shear modes in the dispersion relation shown in Figure 6.22(b). The same behaviour is also observed for the sound cones on certain silicon wafer orientations, as discussed in Section 5.1.3. Due to the special orientation of the copper layers, the polarisation directions are fixed along

$$\mathbf{s}_1 = \begin{bmatrix} 1 \\ 0 \\ 0 \end{bmatrix} \qquad \mathbf{s}_2 = \begin{bmatrix} 0 \\ -1 \\ 1 \end{bmatrix} \tag{6.4.2}$$

and both polarisations are again orthogonal [Ting 2006a]. Following the splitting of the transversal bands, the respective band gaps are only valid for the two distinct polarisation directions. Due to the changed mechanical response, the bands are also shifted compared to the prior investigated (001) orientation.

The respective transmission loss computed with the FEM, plotted in Figure 6.22(b), reflects

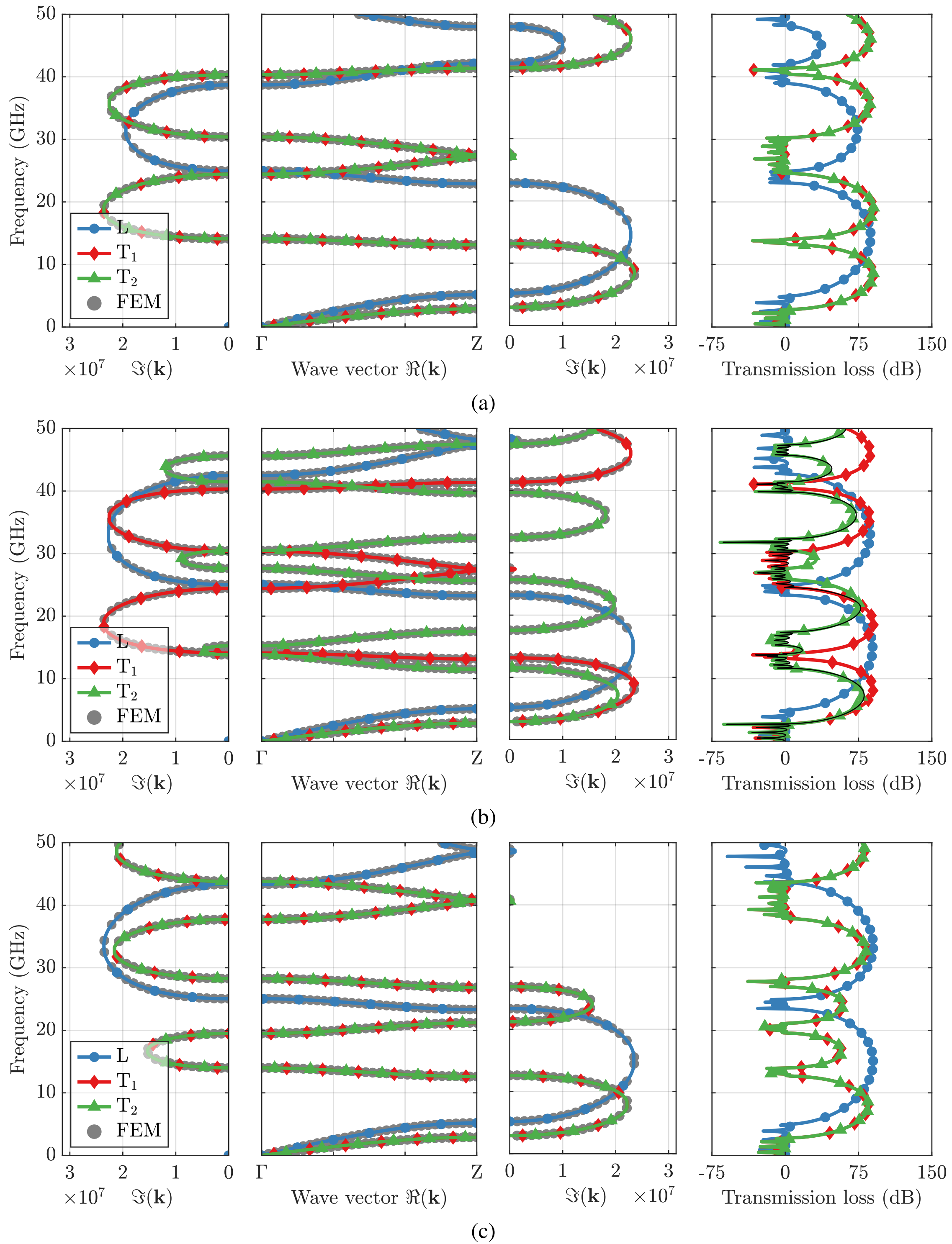

Figure 6.22: Comparison of the 1D band structures and transmission losses of a fully 3D BEOL, with 50 nm thick copper and SiCO:H layers, separated by 5 nm thick SiO_2 liner layers. The copper layers are oriented (a) (001), (a) (011) and (c) (111).

the split of the transversal bands and perfectly agrees with the band structure calculations. The separated transversal bands consequently lead to a reduction of the observed shear gap width.

In the case of a transverse wave, with a polarisation direction

$$\mathbf{s} = \frac{1}{\sqrt{2}} \begin{bmatrix} \sqrt{2} \\ 1 \\ -1 \end{bmatrix}, \tag{6.4.3}$$

which matches neither the polarisations of either T_1 or T_2. For this polarisation the effective shear gap reduces to the smallest common band gap of both bands, as indicated by the black line in Figure 6.22(b). Moreover, in the case of an unmatched polarisation the respective transmission loss of each gap is limited by the lower transmission loss of the two possible polarization directions [Hudeczek and Baumgartner 2020]. Hence, the primary crystallisation direction and the relative rotation of the copper layer concerning the underlying MEMS affect the width and strength of the band gaps.

For the band structure of the last copper orientation (111), as plotted in Figure 6.22(c), the splitting of the transversal modes is lifted again. Thus both transversal wave velocities coincide and their polarisation directions may again be along any direction orthogonal to the propagation direction while maintaining orthogonality between the waves. The corresponding transmission loss simulation also reflects this in Figure 6.22(c).

Following this analysis the band gap frequencies of both longitudinal and transversal gaps vary with the crystal orientation of the involved copper layers. However, it is unlikely that all copper layers will crystallise into the same orientation across the whole BEOL leading to changes in orientation between successive copper layers. The mechanical behaviour of such a structure is simulated for a three-layer stack, as shown in Figure 6.23. Each of the three copper layers A, B, and C feature one of the three main crystallographic orientations 1 → (001), 2 → (011) and 3 → (111). The previously discussed uniform variants are given by black dashed, dash-dotted and dotted lines, where all three-layers have the same orientations,. They are compared with all possible orientation combinations of the three involved copper layers.

The regions, which are common band gaps for all three uniform cases, are also band gaps for arbitrary combinations of copper crystal orientations in different layers. The order of the orientations in the different layers has almost no influence on the ultimate transmission loss. This follows from each BEOL unit cell layer having its own band gap frequencies. Hence, in case of mismatched band gap frequencies, all waves passing through any of the previous layers are partially blocked by the band gap of a successive layer, and consequently, the stack exhibits an averaged response [Jiménez et al. 2021]. Due to the partial blocking the overall strength of each gap is reduced and the averaged response might feature fewer suitable band gaps compared to a BEOL with only one orientation throughout the whole stack.

Following the worst-case assumption that all metal layers have distinct orientations while still being monocrystalline, finding a matching band gap is challenging. As shown for the transmission loss of a BEOL with mixed orientations, the band gaps follow the smallest common gaps. Consequently, by finding the possible band gaps for each orientation, a superposition of all

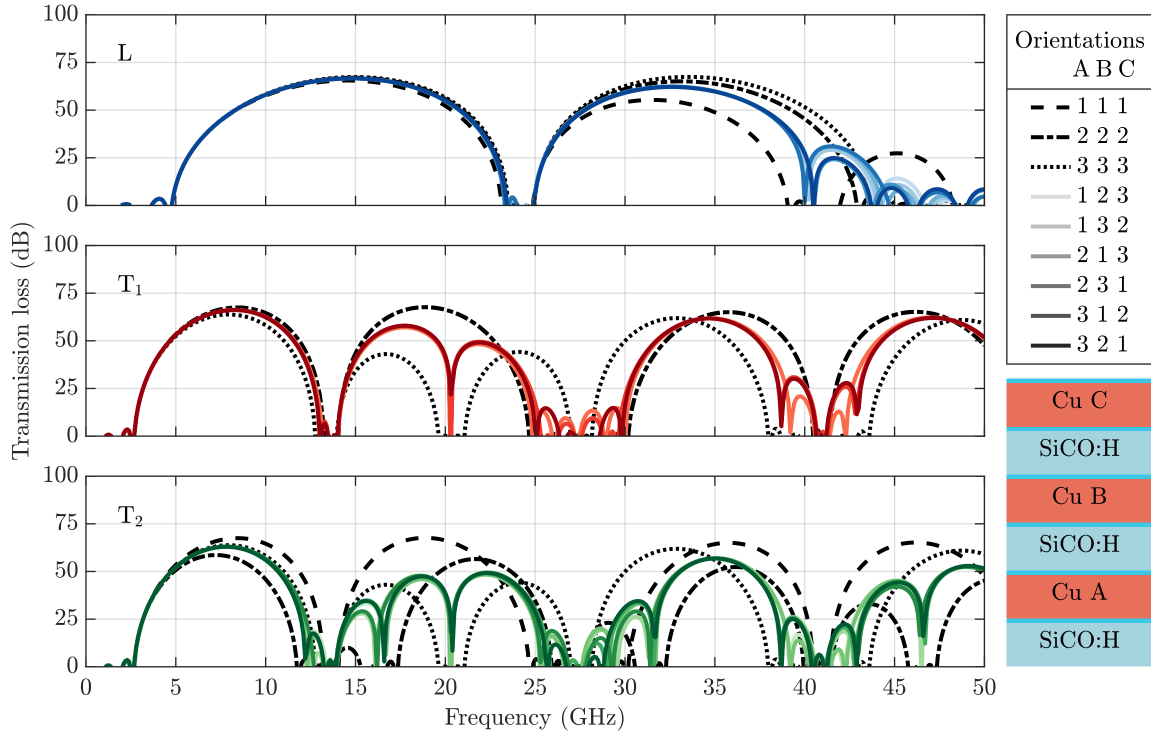

Figure 6.23: Transmission loss simulation for a three-layer stack with different copper orientations A, B and C along Γ−Z. The copper and SiCO:H layers have a thickness of 50 nm while the SiO_2 liner layer has 5 nm. Each copper layer may assume one of the following three crystallographic orientations: 1 → (001), 2 → (011) and 3 → (111).

results should yield the permanent gaps present regardless of the copper orientation. The overall pattern is very similar to the 2D approximation of copper (compare Figure 6.4), with a high periodicity of gaps that are separated by narrow bands, but an additional shear T_2 polarisation exists due to the three dimensional unit cell.

Assuming the resonant frequency $f_R = 30.922$ GHz of the RFT at its default configuration, the remaining vertical gaps are found by superposition of the three possible copper orientations (001), (011) and (111). The resulting gaps with a bandwidth of $f_{BW} = 1$ GHz are plotted in Figure 6.25. Shown in transparent black is the result of the isotropic 2D assumption using the same layer thicknesses. The longitudinal gaps do not vary strongly for the different copper orientations, especially at smaller layer thicknesses. The same was also observed for the transmission loss of the three-layer stack shown in Figure 6.23. Furthermore, the 2D approximation closely resembles the true band gap locations.

For the two shear waves T_1 and T_2 however, the speed of waves varies more between the different orientations, leading to a more pronounced shift of the observed band gaps. The overall size of the band gap, from a layer thickness point of view, is therefore reduced. The 2D approximation fails to capture the band's shift in a 3D simulation leading to larger band gaps with fewer variations.

Since the isotropic assumption was computed from the Voigt and Reuss averages it assumes the averaged locations of all bands from the different anisotropic copper orientations. This behaviour

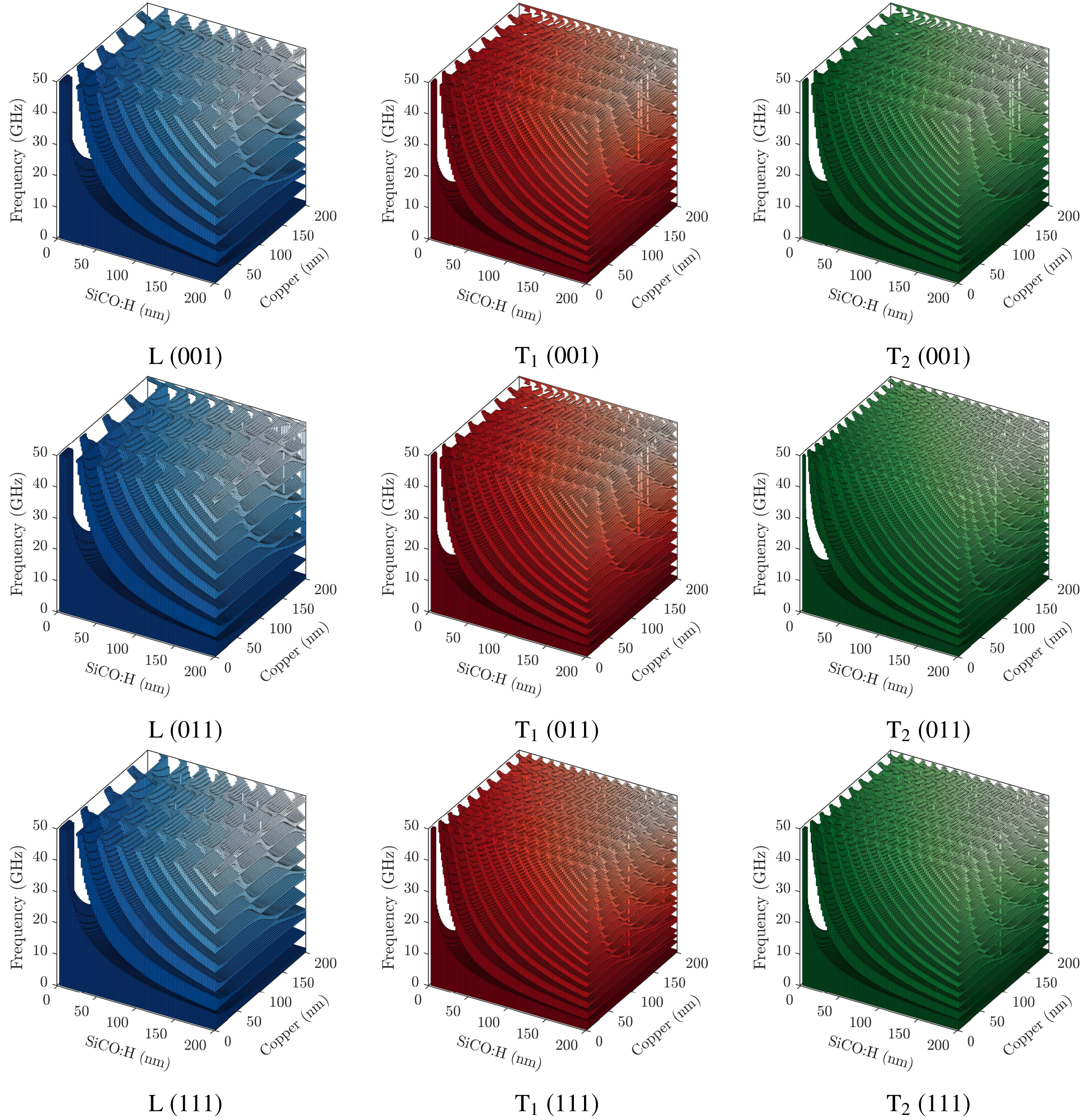

Figure 6.24: Evolution of bands with varying anisotropic copper orientations and SiCO:H layer thickness for longitudinal and transversal bands calculated with the interface response theory for vertical propagation along $\Gamma{-}Z$. The copper and SiCO:H layers are separated by a 5 nm thick SiO_2 liner layers. The uninterrupted pillars for some configurations are artefacts of the calculation where the algorithm failed to find the roots of the analytic equation.

is the consequence of the isotropic sound velocities, given in Table 5.3, which are in-between the extremal values for an anisotropic material. Therefore, the 2D isotropic simulation offers a good first-order approximation of the involved effects. However, a full 3D analysis is required to determine the band gap frequencies precisely.

As discussed in Section 6.2, band gaps for pure vertical propagation are inconsequential to the RFT performance, however, they allow a direct comparison of the involved effects using both analytical computations and finite-element simulations. To assess the full performance of the BEOL in 3D, including all folded bands, the BEOL phononic crystal must be modelled

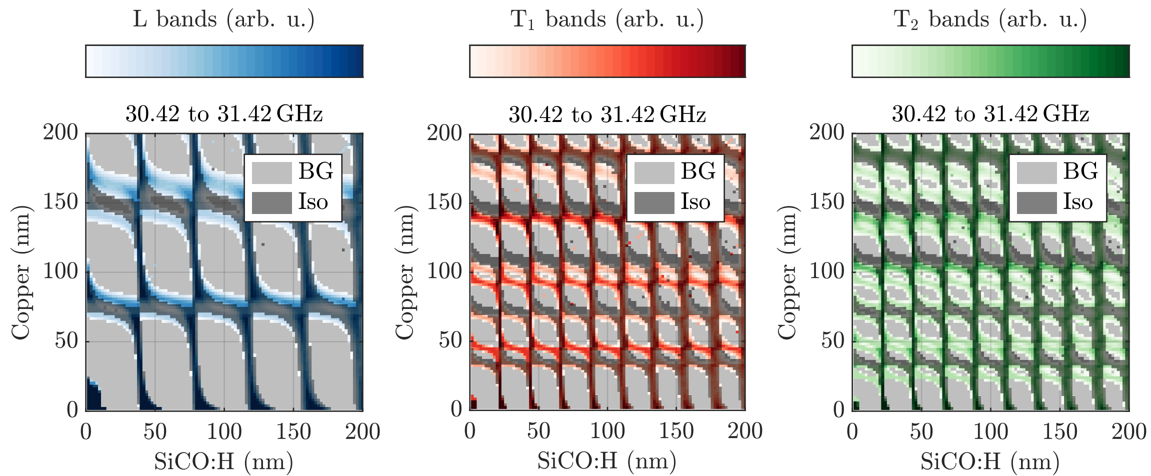

Figure 6.25: Comparison of the band gaps obtained with equivalent isotropic and anisotropic copper between 30.422-31.422 GHz for longitudinal and transversal waves and non-polarised waves propagating along Γ−Z. The anisotropic result is merged from the three predominant copper orientations (001), (011) and (111).

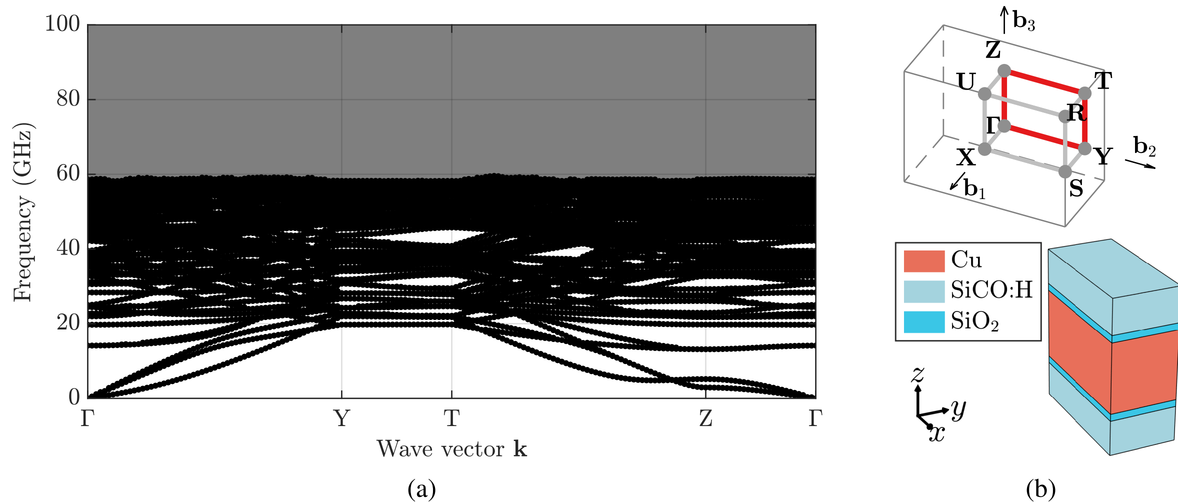

Figure 6.26: The simulated 3D band structure for a (001) oriented copper layer is shown in (a). The copper and SiCO:H layers have a thickness of 50 nm and are separated by 5 nm thick SiO_2 liner layers. (b) The corresponding unit cell and Brillouin zone for the FEM simulation. The simulation was capped at 150 modes as indicated by the shaded region.

with the lateral dimensions matched to both the FinFET and gate pitch. The corresponding unit cell and Brillouin zone for 50 nm thick copper and SiCO:H layers, with 5 nm liner layers, are sketched in Figure 6.26(b) and the resulting band structure for (001) oriented copper is shown in Figure 6.26(a). The computation was limited to the gate plane Γ−Y−T−Z−Γ, as only gaps at the high symmetry point Y are relevant. Due to the high computational effort, the number of modes was limited to 150, as indicated by the shaded area. Since the RFT frequency is within the computed range, this limitation can be disregarded. Whereas the 2D simulation of the same stack, shown in Figure 6.8, already featured a dense web of bands, the 3D simulation is even denser. Due to the finite extent along the gate and channel and the added second shear wave

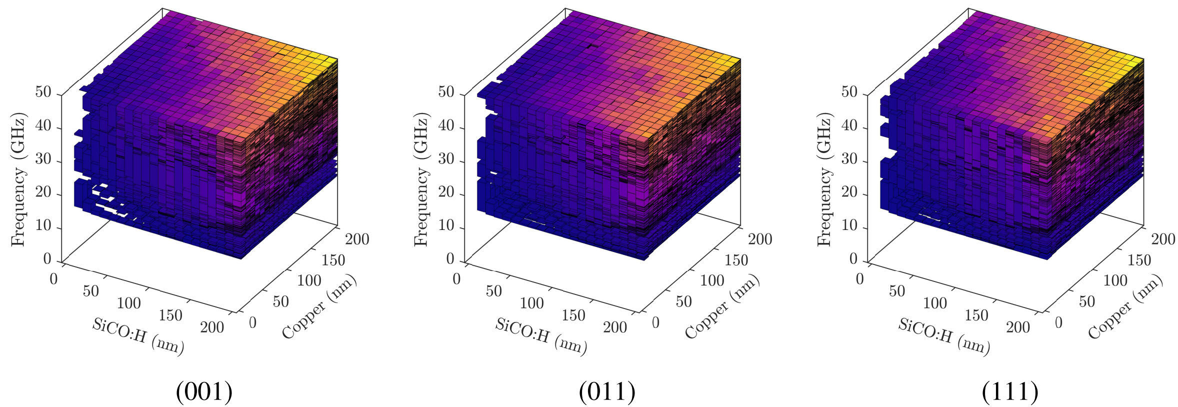

Figure 6.27: The evolution of bands with varying copper and SiCO:H layer thickness for all bands calculated with the FEM for vertical propagation along Y−T for the three main copper orientations (a) (001), (b) (011) and (c) (111).

velocity more folded bands occur. Consequently, no directional band gap occurs within the required direction Y−T.

This process is repeated for copper and SiCO:H thicknesses between 5-200 nm and all band gaps within Y−T are extracted. The results for the three predominant copper orientations are given in Figure 6.27. For all three orientations, the involved bands form a dense structure for almost any possible thickness configuration. Only at unrealistic small BEOL layer thicknesses for some band gaps exist, although not at the required frequencies. Moreover, as the superposition of all possible orientations must be considered no band gap can be found for any frequency above 20 GHz. Furthermore, approximately 30 % of the possible copper orientations have been neglected, which would add additional bands which need to be considered.

This has strong implications for the performance of the RFT. Although, as suggested by literature and discussed in Section 6.2, a laterally unpatterned BEOL exhibits suitable band gaps for monolithic MEMS confinement, they can only be confirmed with a 2D simulation [Bahr 2016; Bahr et al. 2018; Bahr et al. 2015]. To incorporate all involved mechanical effects, such as the anisotropic behaviour of copper, a 3D simulation is mandatory. In this simulation, no suited band gaps are present and the RFT mode cannot be confined. As also shown for the 2D simulations, the absence of a matching band gap strongly degrades the already small transconductance numbers of the RFT. This indicates that the RFT in its reported form is non-functional as mechanical confinement cannot be ensured and the transconductance will be small [Hudeczek et al. 2022].

6.5 Fundamental Limits of the Quality Factor

Another potential issue revolves around the Qf product of the proof-of-concept publication. With $Qf = 1.57 \times 10^{15}\,\mathrm{Hz}^{-1}$ it marks the highest ever reported figure of merit of silicon-based MEMS device [Bahr et al. 2018]. While the high resonant frequency depends on the small

FinFET size, which the previous simulations could confirm, the Q-factor of almost 50 000 remains debatable [Hudeczek et al. 2022]. In a MEMS the Q-factor is determined by the energy dissipation which can be caused by several effects [Ghaffari et al. 2013]. The Matthiessen's rule gives the inverse of the total Q-factor

$$\frac{1}{Q_{total}} = \sum_{i=1}^{n} \frac{1}{Q_i} = \frac{1}{Q_{PnC}} + \frac{1}{Q_{TED}} + \frac{1}{Q_{AKE}} + \frac{1}{Q_{LR}} + \cdots \tag{6.5.1}$$

where all n involved damping mechanisms Q_i are considered independent of each other [Brand et al. 2015; Chandorkar et al. 2008; Ghaffari et al. 2013; Ghaffari et al. 2015; Basu and Bhattacharyya 2011; Rodriguez et al. 2019; Zhou et al. 2018]. Therefore, the overall achievable Q-factor is limited by the largest source of damping or the smallest involved Q-factor $Q_{total} \approx Q_{min}$ of the system.

The effect of thermoelastic dissipation (TED) describes an intrinsic loss mechanism of all the involved materials, which is described by a coupling of temperature and strain gradients through the thermal expansion coefficient [Zhou et al. 2018; Lifshitz and Roukes 2000]. It relies on accurate data and analytic expressions for each geometry, typically only available for simple suspended single-material systems with a well-defined geometry. These expressions are inadequate to describe the RFT as it involves several materials and features a rather complex geometry. Typically it is inversely proportional to the temperature, requiring low temperatures to minimise the impact as the Q-factor is degraded with rising temperature [Kim et al. 2008; Chandorkar et al. 2008; Tabrizian et al. 2009; Ghaffari et al. 2015; Shao et al. 2019]. Assuming a well-designed MEMS, they can be typically disregarded from the analysis, but their actual role in the RFT requires further investigation as the measurement temperature of the RFT was not disclosed [Bahr et al. 2018].

However, another fundamental limit of the frequency product solely depends on the material properties through quantum mechanical phonon scattering, also known as the Akhiezer effect (AKE). The Akhiezer effect is expected to be the dominant source of damping for resonant frequencies $\omega_\tau \tau_l < 1$, where $\tau_l = 67.3\,\text{ps}$ is the relaxation time of longitudinal waves in silicon along the gate direction $\langle 110 \rangle$ [Lambade et al. 1995; Telichko et al. 2015]. For the Akhiezer effect, the Qf product is given by

$$Q_{\text{AKE}} f = \frac{\rho c_l^2 c_d^2}{6\pi \gamma^2 k T} \tag{6.5.2}$$

where the c_d is the Debye velocity, γ Grüneisen parameter of silicon, $k = 130 – 148\,\text{W}\,\text{K}^{-1}\,\text{m}^{-1}$ the thermal conductivity and $T = 300\,\text{K}$ the temperature [Stoffels et al. 2010; Goettler et al. 2010; Lambade et al. 1995; Tabrizian et al. 2009]. For the Grüneisen parameter γ several values are found in the literature as the quantity is difficult to assess accurately. It typically varies between 0.17–1.5 with the commonly used average $\gamma_{avg} = 0.51$ [Ghaffari et al. 2013; Brand et al. 2015;

Chandorkar et al. 2008; Lambade et al. 1995]. The Debye velocity

$$c_d^{-3} = \frac{2c_t^{-3} + c_l^{-3}}{3} \tag{6.5.3}$$

is calculated from the longitudinal and transversal sound wave velocities in silicon along the propagation direction [110] parallel to the gate. For a $(001)^{45}$ rotated wafer they are $c_l = 9130\,\mathrm{m\,s^{-1}}$ and $c_t = 4672\,\mathrm{m\,s^{-1}}$ which can be calculated using Christoffel's equation (compare (3.7.7) and Table 5.2) [Lambade et al. 1995].

The Akhiezer effect, as plotted in Figure 6.28 for the upper and lower limit as well as the average, imposes a fundamental limit on the Qf product [Ghaffari et al. 2013; Hamelin et al. 2019; Andriyevsky et al. 2017].

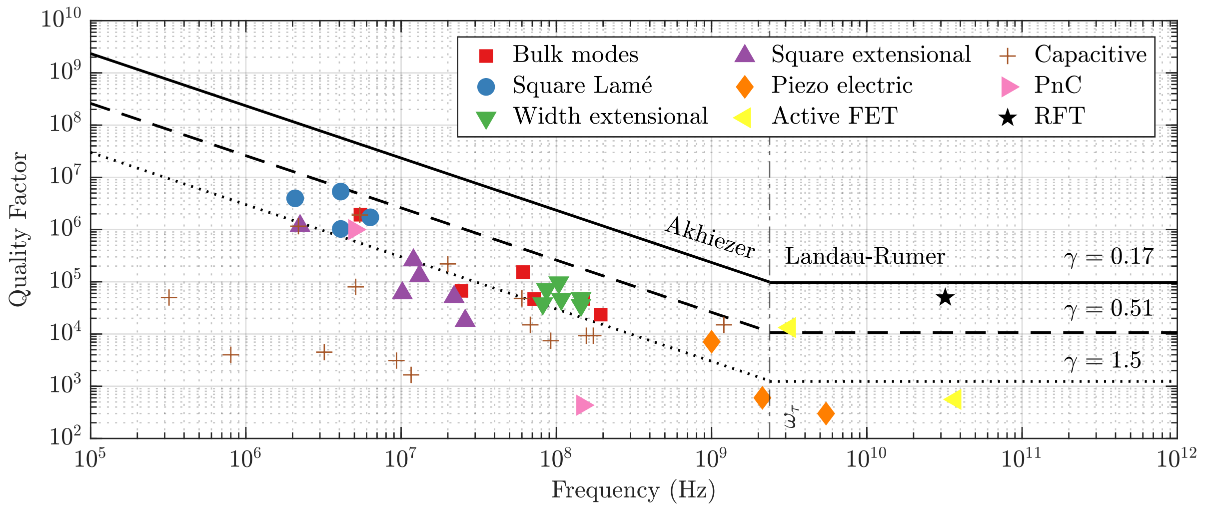

Figure 6.28: Comparison of several silicon-based MEMS figures of merit with the fundamental Q-factor limit of silicon. The reported value by Bahr et al. is marked by a star. All values are collected from [Ghaffari et al. 2013; Basu and Bhattacharyya 2011; Bahr et al. 2018; Yang, Hamelin, et al. 2018].

Several high-performing MEMS devices are marked, but most of them rarely exceed the average Qf product of $2.6 \times 10^{13}\,\mathrm{Hz}^{-1}$ for the Akhiezer effect at $\gamma = 0.51$. It should be noted that several of the devices are highly optimised structures with sub-ambient cooling to minimise thermoelastic dissipation. Furthermore, none of the highlighted devices is manufactured monolithically or in an unreleased manner. Therefore, the devices mainly suffer from anchor losses where they are attached to the substrate. However, it has been demonstrated that these losses can be successfully mitigated with the help of 2D phononic crystals, such as micro-machined holes in the support membrane leading to highly optimised structures with little losses [Ziaei-Moayyed et al. 2010; Hamelin et al. 2019; Yang, Hamelin, et al. 2018].

For frequencies above $\omega_\tau \tau_l > 1$, the Qf product is limited by the Landau-Rumer (LR) attenuation. In this region, the acoustic wavelength is smaller than the mean free phonon path. As a result of three-phonon interactions, the resulting acoustic attenuation is proportional to ω

leading to a constant Q-factor in this range [Tabrizian et al. 2009]. It is calculated via

$$Q_{LR}f = \frac{30\rho c_d^5 \hbar^3}{\pi^4 \gamma^2 k_b T^4} f \tag{6.5.4}$$

where k_b is the Boltzmann constant [Tabrizian et al. 2009; Telichko et al. 2015]. Again, the top-performing MEMS in Figure 6.28 rarely surpass the average Landau-Rumer attenuation. Although the MEMS should be limited by the Landau-Rumer attenuation, and may thus surpass the Akhiezer effect in this frequency range, Qf products above the continued Akhiezer effect are unreported [Brand et al. 2015].

It should be noted that all the previously discussed damping mechanisms are only valid for a pure monocrystalline silicon device. However, the RFT is made from several materials with different mechanical properties which all have to be considered. Here, the material properties of the metals and oxides might further reduce the upper limit [Gauster 1971; Joshi et al. 2018; Sanditov and Darmaev 2022].

In the instance of the RFT, assuming a perfectly designed and matched phononic crystal supporting a Q-factor of 49 000 or higher, the total Q-factor may consequently never surpass the limit imposed by the Akhiezer effect and Landau-Rumer regime [Goettler et al. 2010; Brand et al. 2015; Hamelin et al. 2019; Zhou et al. 2018; Rodriguez et al. 2019]. Although the fundamental Akhiezer effect limit in silicon for the average Grüneisen parameter has been theoretically achieved by using a phononic crystal in a free-standing structure [Goettler et al. 2010], or via measurements of a suspended crystal disk resonator cooled to 120 K [Hamelin et al. 2019], the verification within unreleased MEMS at room temperature is still missing. Assuming the average Grüneisen parameter as a baseline, a perfectly matched phononic crystal, and no temperature dependence of the Q-factor, the RFT is most likely limited to approximately 10 700 or a Qf product of $34.2 \times 10^{13}\,\mathrm{Hz}^{-1}$. The reported values in of $1.57 \times 10^{15}\,\mathrm{Hz}^{-1}$ by [Bahr et al. 2018] are thus highly improbable to be attained at the RFT frequency, adding to the controversial figures of merit, and consequently, its validity is challenged [Hudeczek et al. 2022].

Summary

The phononic crystal properties of a SiO_2 and SiCO:H-based BEOL stack were approximated by isotropic 1D and 2D simulations, which were followed by full 3D simulations. The periodic BEOL stack exhibits phononic crystal effects for a large acoustic impedance mismatch. They lead to the formation of forbidden frequency regions, known as band gaps, in the dispersion relation, which may shield the RFT from mechanical losses. Their frequency and shielding strength depend on the material composition of the BEOL and layer dimensions.

To shield the RFT from undesired losses, a 1D approach is not sufficient as the wave vector of the resonant eigenmode has to be considered. When the simulation is expanded to 2D suitable

band gaps within Y−T can be observed. However, additional folded bands emerge due to the unit cell's finite dimensions which reduces the likelihood of a matching band gap. Due to the only vertical patterning of the BEOL, the band gaps are only valid for specific propagation directions that must be matched to the RFT.

By designing the BEOL to possess a matching band gap, the RFT can be successfully shielded from undesired radiation losses. This is especially necessary for modern low-κ BEOL stacks since the guiding properties of the oxides are insufficient. However, in the absence of a matching band gap, resonant behaviour is suppressed or degraded due to the higher number of spurious modes.

To capture the anisotropic mechanical properties of the involved copper metal layers a 3D simulation is required. The phononic crystal will exhibit a different dispersion relation depending on the crystallographic orientation of the different copper layers. Since those layers crystallise statistically into different orientations, the overall perceived band gaps are reduced. When additionally considering the resonator's lateral dimensions, a large number of folded BEOL bands occur in the required propagation direction fully suppressing the formation of band gaps. Therefore, a laterally unpatterned BEOL stack with anisotropic materials such as copper is unsuited for the confinement of the RFT.

Lastly, the Q-factor is limited by several additional effects, such as the thermoelastic dissipation, Akhiezer effect and Landau-Rumer attenuation. Those impose an upper limit for the Q-factor, which solely depends on the involved material properties. Considering all additional damping mechanisms, the RFT's reported Qf product is deemed improbable.

7

Design and Characterisation of the Resonant Fin Transistor

Contents

7.1 Device Layout and Fabrication 149
7.2 Process Adaptations and DC Characterisation 155
7.3 Measurements of the Resonant Fin Transistor 161

To enable a successful fabrication of the micro-electro-mechanical-system (MEMS) on a fin field-effect transistor (FinFET) technology the layout of the resonant fin transistor (RFT) and required process adaptations are introduced. The RFT measurement setup is discussed. Various measurement results of the realised structures are presented and compared with the finite-element simulation data and data from the literature.

7.1 Device Layout and Fabrication

The RFT was built on a 16 nm FinFET technology node as part of several test chips. A fixed back-end-of-line (BEOL) stack with nine metal layers was used for all test chips. Here the metal layers one to four share the same thicknesses, while layers five to seven are about 10 % thicker. The last two metal layers, eight and nine, are so-called ultra-thick metals, used to connect to the wafer surface.

The RFT is fabricated on test chips as part of a shared reticle in a productive foundry flow. The electrical contacts to the RFT are realised with specialised 4-port radio frequency (RF) pads on the wafer surface, as sketched in Figure 7.1(a), which are used for on-wafer characterisation. In a typical productive wafer fabrication flow, the wafers are fabricated with bumps as they are later packaged for the final assembly. However, bumps provide several challenges for the on-wafer characterisation, especially in the high gigahertz regime where special RF measurement pads are preferred.

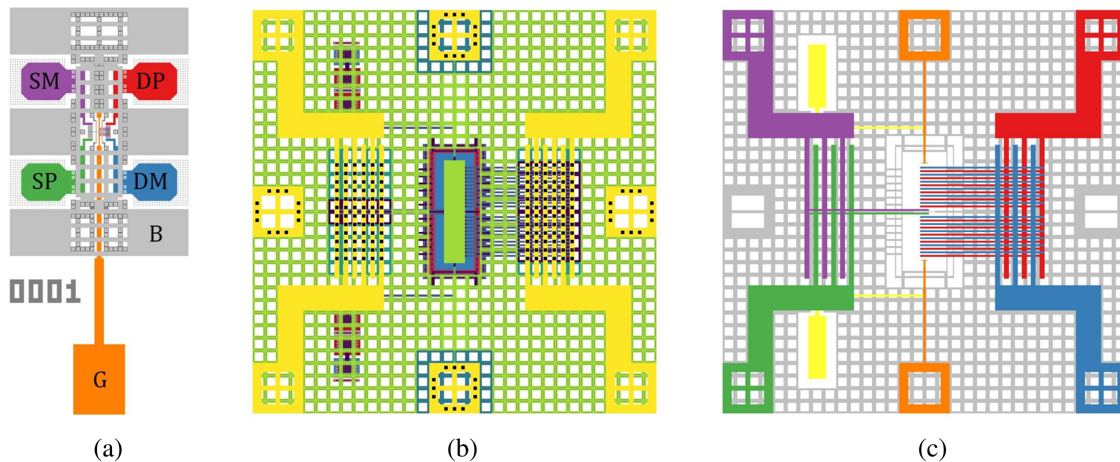

Figure 7.1: (a) 4-port GSGSG measurement pad structure. (b) Complete CMOS layout of the RFT with (c) the highlighted electrical nets.

As discussed in Chapter 2 and Chapter 5, the RFT follows a differential electrical wiring scheme for both the drive and sensing mechanism. Those are implemented as shielded differential RF contacts within the pad. The electrical drive signals plus and minus are highlighted in Figure 7.1(a) on the right side in red and blue, respectively. They are separated by a grounded metal shield indicated in grey. The same ground shield is also used to separate the drive and sense sides from any undesired mutual electrical coupling. On the left side, the sense phases plus and minus are respectively shown in green and purple. The constant gate voltage is supplied with a separated pad marked in orange.

At the centre of the pad is the RFT's main functional layout, referred to as the device under test (DUT). The overall top-view layout of the DUT and the respective electrical phases are shown in Figures 7.1(b) and 7.1(c). Starting from the highest metal layer of the BEOL, a strictly differential electrical wiring scheme is maintained, which seeks to minimise losses and potential cross-talk of the different phases [Pallas-Areny and Webster 1991; Zhao et al. 2016; Fan et al. 2003]. The device is also guarded from external electrical influences by a grounded metal shield, spanning all metal layers, which is marked in grey in Figure 7.1(c) [Kolding et al. 2000].

The coarse wiring on the highest metal layer M_8, which is required for the connection to the pads, is stepped down in size to the last layer M_1 for the fine pitch wiring of the cavity, as shown in Figures 7.2(a) to 7.2(h). To reduce the electrical resistance of the leads, broad or parallel connections are used where possible. Vertical vias interconnect all layers. Several vias are placed in parallel and are vertically aligned to reduce the wiring resistance. Also visible in Figures 7.2(b) to 7.2(g), in the centre of the layout, is the BEOL phononic crystal fabricated from closed metal plates, as discussed in Chapter 6. Since the fabricated RFT is part of a productive reticle the BEOL thicknesses are not ideal and two periodic regions exist. The different layer thicknesses of the BEOL are expected to imped the performance of the RFT, as discussed in Section 6.4.

On the lowest metal layer M_1 the BEOL wiring is connected to the mechanical cavity of the

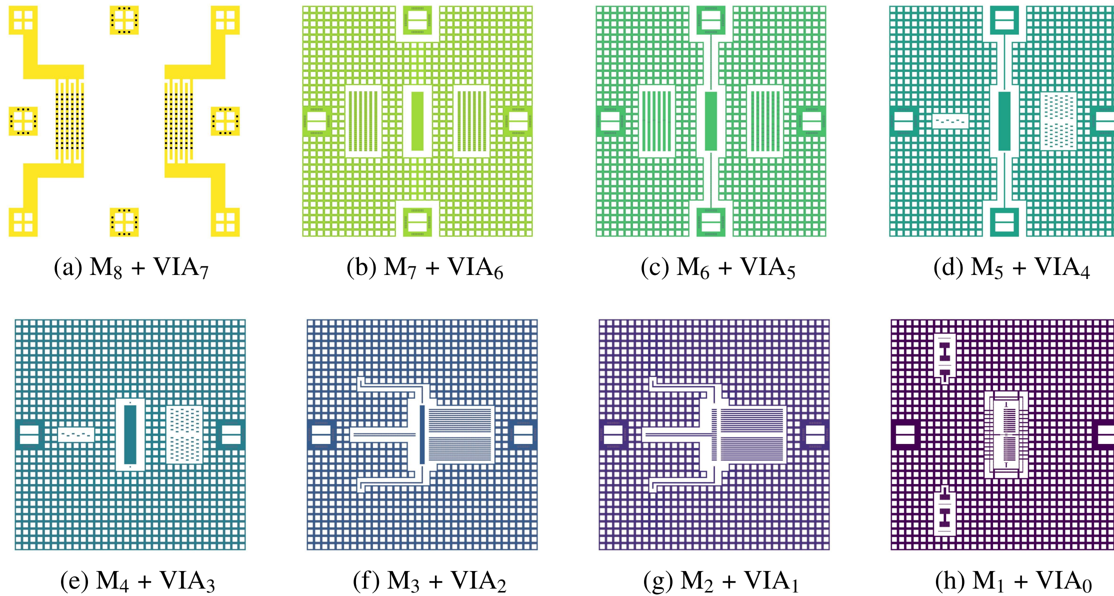

Figure 7.2: BEOL wiring for the metal layers (h) M_1 to (a) M_8, with the corresponding vertical interconnects VIA_0 to VIA_7 to the respective lower layer.

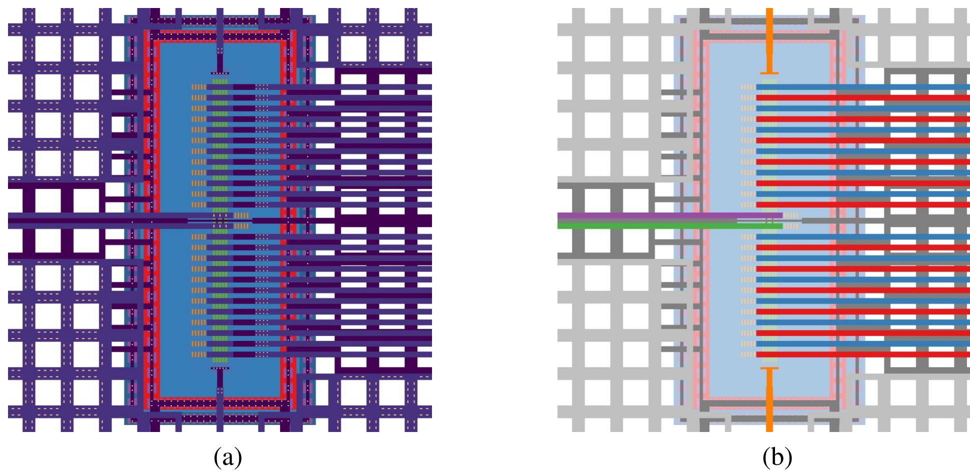

Figure 7.3: BEOL layout of the RFT (a) with the electrical nets highlighted in (b). The phases are marked as: drive-plus (DP) in red, drive-minus (DM) in blue, sense-plus (SP) in green, sense-minus (SM) in purple and gate (G) in orange. The metal shield surrounding the RFT, shown in grey, is grounded.

MEMS in the front-end-of-line (FEOL), which is shown in more detail in Figure 7.3(a). Here the differential arrangement of both drive and sense phases is highlighted in Figure 7.3(b) for an exemplary RFT with twelve 14-fin drive unit cells and four parallel gates. The cavity is also surrounded by a grounded guard ring, which provides a well-defined bulk reference potential [Dai and Ker 2016; Mikkelsen et al. 2004]. All connections within the BEOL adhere to the foundry's design rule check.

As discussed in Chapter 2 and Chapter 5, the ideal integration of the RFT cavity requires differential electrical contacts for every fin. Those, however, are typically only possible in special single-fin devices that must adhere to very strict design rule checks, which are not applicable for

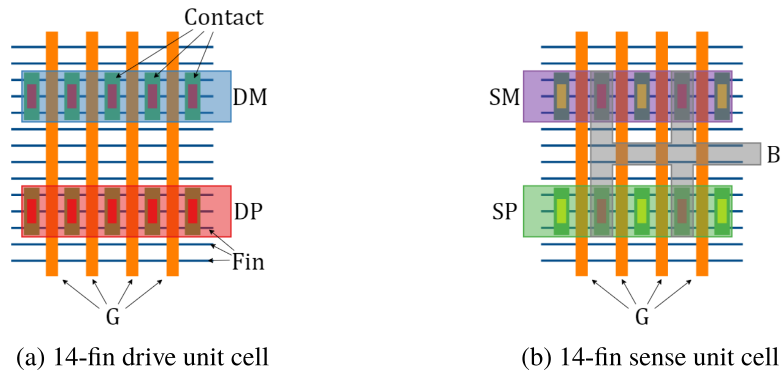

(a) 14-fin drive unit cell

(b) 14-fin sense unit cell

Figure 7.4: Top-down sketch of the (a) drive and (b) sense unit cell wiring analogous to the schematic shown in Figure 2.9.

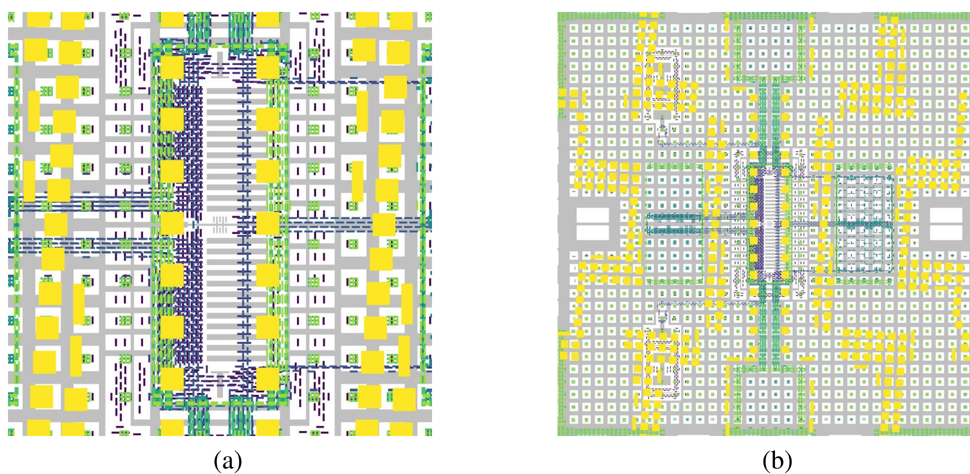

(a)

(b)

Figure 7.5: Filling structures in the BEOL around the (a) RFT core and (b) the full layout.

tens and hundreds of consecutive fins as required for the RFT [Bahr et al. 2018]. Therefore, the cavity is manufactured from several 14-fin drive unit cells and sense unit cell at the centre, as sketched in Figure 7.4. Rather than connecting each fin, two groups of three are jointly connected by a single contact. Both groups are separated by four intermediate electrically floating fins required for the cavity's mechanical waveguiding properties. The mechanical mode within the cavity is driven by electrostatic actuation by using field-effect transistors (FETs) connected as metal-oxide-semiconductor (MOS) capacitors. They are formed between the FinFET channel and the gate by shorting both the source and drain together, which is illustrated in Figure 7.4(a). To sense the modulated current, caused by the stress dependent mobility variation, the sense unit cell depicted in Figure 7.4(b) is wired as a pair of differential transistors.

Before the foundry can fabricate the design, additional filling structures must be added, both in the FEOL and BEOL, as sketched exemplarily for the BEOL in Figure 7.5. They are required to ensure an even mechanical response of the wafer surface during the several polishing stages in the CMOS process. As the involved metals and oxides respond differently during polishing, large oxide or metal areas may dish, which causes misalignments in the following lithography

Table 7.1: Possible layout variations of the RFT. NMOS and PMOS are abbreviated as N and P.

Parameter	Value
Drive unit cells	2-12
Sense unit cells	1
Gates	1-32
Type	N, P

Length	Pitch			
	P_1	P_2	P_3	P_+
L_1	N, P	N, P		
L_2	N, P	N, P		
L_3	N, P	N, P		
L_4		N, P	N	
L_+				N, P

steps [Schwalke 2000]. Therefore, metal dummy shapes are filled in-between the structures until a specific density across the whole layout is achieved. Although the fill is not in direct contact with the layout, as all individual shapes are electrically floating, it still may adversely impact the device performance, especially at elevated frequencies [Tsuchiya and Onodera 2009; Nan et al. 2007]. Due to the introduction of fill, the effective dielectric thickness between two metal traces is reduced by introducing electrically floating metal shapes, which increases coupling. Similarly, which is not shown, the FEOL is filled with dummy shapes. Hence, the performance of the device has to be considered after the filling routine was carried out, which is impossible due to computational constraints. However, it should be noted that fill requirements have to be met at all major foundries and are not exclusive to the used technology node.

As discussed in Chapter 5, several FinFET variants that impact the RFT performance are listed in Table 7.1. One aspect which strongly affects the quality factor (Q-factor) of the device is the number of drive unit cells. As discussed in Section 5.4.2, a larger number of drives for a finite two-dimensional (2D) cavity leads to a higher Q-factor. The upper limit of twelve drive cells was chosen not to exceed the active area limits of the process. Violating them can result in manufacturing problems and introduce risk for the integrity of other productive content on the wafer. Focusing on one sense cell allowed a larger number of drive cells. Also discussed was the impact of several parallel gates within the RFT cavity, where a larger gate count leads to a slightly increased mechanical transconductance. The RFT is manufactured as NMOS and PMOS, where the latter is expected to yield the largest mechanical transconductance due to the higher susceptibility of the hole mobility to external stress.

Both transistor types can be manufactured in several different gate lengths and pitches, as shown in Table 7.1 on the right. Note that for the shortest four gate lengths L_1 to L_4 the pitch is fixed to the prescribed value P_1 to P_3. For larger gate lengths L_+ the pitch P_+ between the centre of adjacent gates increases with the gate length to provide the required spacing. A change of the gate pitch was not specifically discussed in the theoretical analysis, however, the three available pitches only differ slightly and anyhow are forced to change at longer gate lengths, which is thus indirectly captured by the simulations. As found in the theoretical investigation of the performance, the reference gate length L_2 with pitch P_2 is expected to provide the largest transconductance. However, the deviations of the smaller length are almost negligible.

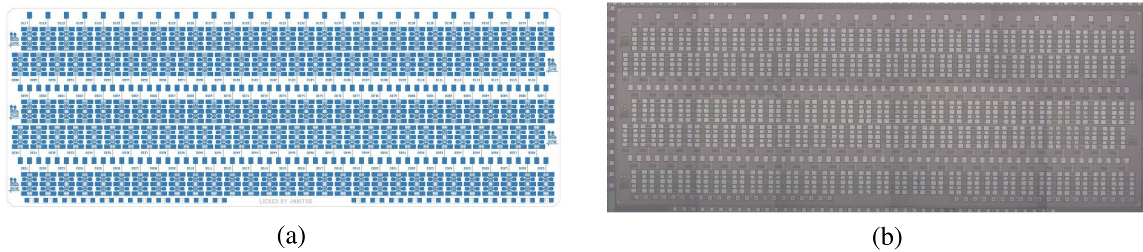

(a) (b)

Figure 7.6: (a) The layout of one complete chip with the RFT and process validation structures. (b) Respective die micrograph after fabrication.

Figure 7.7: Wafer photograph of the fabricated die within a reticle.

Therefore, all devices are fabricated with pitch P_2 as the largest mechanical transconductances were found for the gate lengths L_1 to L_4 in the theoretical investigation.

To account for as many of the available possibilities, the layout design process was automated using so-called parameterised cells, which allow an efficient generation of custom device layouts, which are not included in the standard process design kit offering of the foundry. Therefore, many customised layouts can be manufactured on each test chip, and modifications and design iterations can be implemented in a fast pace.

The different DUTs are combined into a single chip, as shown in Figure 7.6(a). The corresponding micrograph of the layout after fabrication is shown in Figure 7.6(b). Each chip may contain several hundred DUTs with typical sizes in the 5-30 μm^2 range. Each chip is part of a common reticle containing multiple other chips with different purposes and layouts. The reticle dimensions are defined by the size of the lithography masks used in the process. The mask set, containing all chips on the reticle, is stepped during the illumination across the wafer and creates identical copies of the chips. A 300 mm wafer may contain tens to a few hundred reticle shots. Since the RFT is co-fabricated with other chips for different purposes, it has to be ensured that the layout experiments do not endanger the other structures by manufacturability problems. An exemplary wafer photograph with multiple reticles is shown in Figure 7.7. In general, the electrical device performance is dependent on the location of each die on the wafer, as temperature variations during the material deposition processes lead to varying layer thicknesses [Su et al. 2016; Zhang et al. 2016; Li et al. 2018; Xu et al. 2016; Ebert et al. 2020].

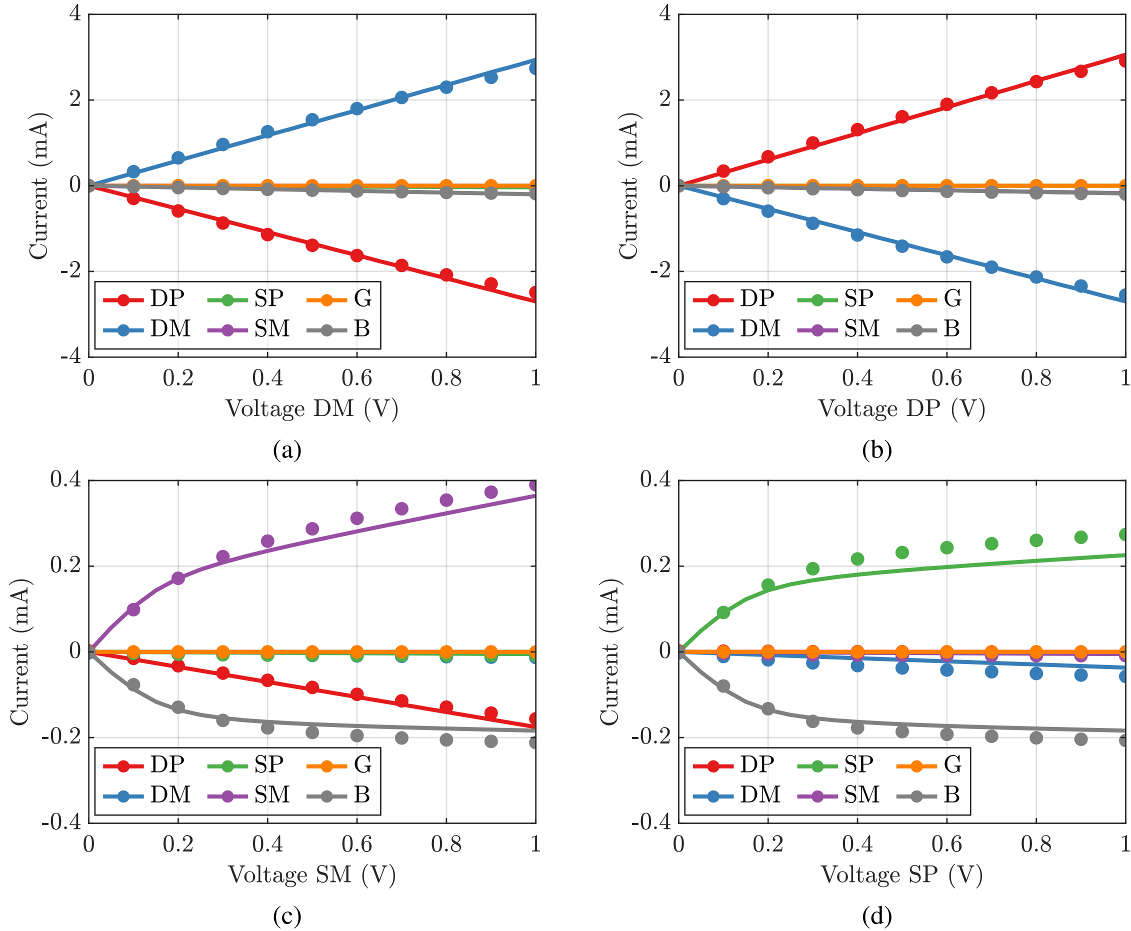

Figure 7.8: Phase-to-phase resistance of one NMOS RFT at $V_G = 0.8$ V. The signals are abbreviated as follows: drive-plus (DP), drive-minus (DM), sense-plus (SP), sense-minus (SM), gate (G) and bulk (B) in accordance with the wiring sketched in Figure 2.11(a) and Figure 7.1(c). Measured data is indicated by markers and simulated values by solid lines.

7.2 Process Adaptations and DC Characterisation

The first test chip was 6 mm × 5 mm with 145 different DUTs. To be fabricated, the foundry had to waive several design rule checks regarding contact placement in the FEOL. As a result, only NMOS devices could be fabricated in the first test chip. Their electrical integrity was tested with their direct-current characteristics, which yields information about potential wiring shorts in the BEOL or structural complications within the FEOL might prevent a successful operation. The RFTs are set to their on-state with $V_G = 0.8$ V and the voltage of each drive and sense pad was individually swept between 0 V and 1 V. The electrical currents of all five signal pads and the ground shield were measured during the sweeps. The results are plotted for an exemplary RFT with four drive cells, a gate length L_1, and one gate in Figure 7.8. For the voltage sweeps of both drive phases plotted in Figures 7.8(a) and 7.8(b) almost symmetric current flow between both phases, DP and DM, is observed. This indicates a conduction path within the FEOL or BEOL of the device, which is highly undesired as it prevents the actuation of the drive MOS capacitors. Furthermore, a small current at the bulk (B) and sense contacts is observed. Similar behaviour

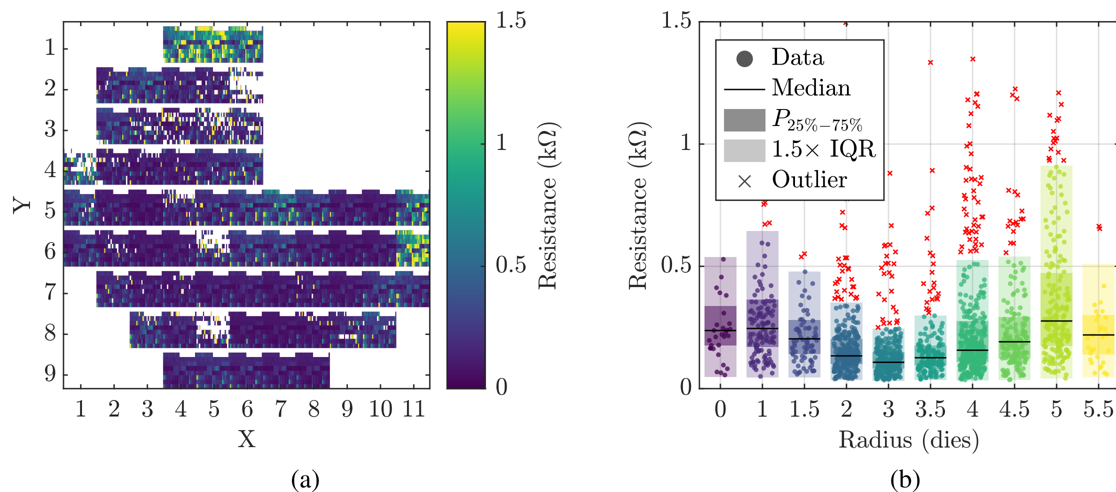

Figure 7.9: Phase to phase resistance of the RFT cavity for (a) a full wafer and (b) its statistical evaluation with radial die location. Each pixel in (a) marks a single DUT.

is observed for the voltage sweeps of the sense pads in Figures 7.8(c) and 7.8(d). Although a transistor-like behaviour is measured for both phases, additional leakage currents into the drive phases also occur. As expected, a portion of the current is flowing into the bulk (B) connection as one side of the differential sense unit is tied to the ground, however, this should account for almost the whole current flow. Interestingly the leakage current is directed to the directly adjacent drive phase, for example from sense-minus (SM) to drive-plus (DP) and sense-plus (SP) to drive-minus (DM). However, it is not equal between both sense phases, which hints at a varying resistance. The observed shorts were present for all manufactured DUTs and the three investigated wafers. Only the observed magnitude varies with the location on the wafer. To allow for a successful actuation of the mechanical eigenmode the root cause of the issue had to be resolved.

The resistance of the shorts is calculated from the slope of the leakage currents with $R = V/I$ leading to a resistance of 372 Ω between the drive phases drive-plus and drive-minus for the exemplary device in Figure 7.8. This resistance is mapped for all devices of a wafer, as shown in Figure 7.9. For the whole wafer the phase-to-phase resistance of ranges between 55 − 905 Ω, using the 25th and 75th percentile. The resistance variation across the wafer follows a doughnut shape with a clear radial dependence, as shown in Figure 7.9(b). This behaviour and value are indicative of a semiconductor short. A much lower resistance would be expected from metal shorts, additionally, no BEOL design rule check were waived, and mask inspection confirmed correct metal layouts without short. The resistance variation can be attributed to the processing of the epitaxial contacts deposited using metal-organic chemical vapor deposition (MOCVD). During fabrication within the metal-organic chemical vapor deposition reactor, the temperature varies across the wafer leading to an uneven thickness resulting in a distinct circular pattern [Su et al. 2016; Zhang et al. 2016; Li et al. 2018; Xu et al. 2016; Ebert et al. 2020].

Considering the required processing and device layout, a short occurs during epitaxial

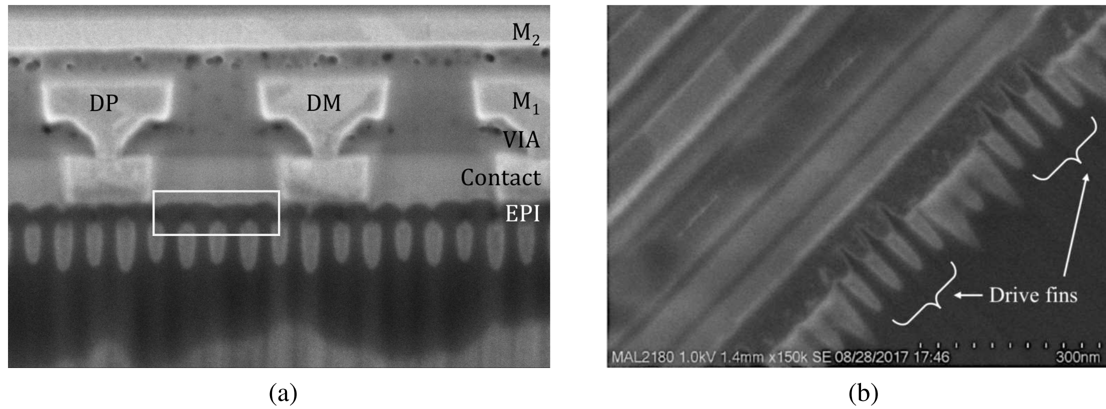

(a) (b)

Figure 7.10: (a) Shorted fin source-drain epitaxy between the marked drive connections compared to (b) the structure from Bahr et al. [Bahr et al. 2018].

processing of the RFT cavity's source-drain contacts (EPI). Consequently, the measured phase-to-phase resistances of a few hundred ohms is the result from several high-ohmic shorts which are connected in parallel in the cavity. The number of parallel shorts depends on the number of drives and parallel gates used in the RFT, with a larger device having a lower phase-to-phase resistance. Using the device geometry, the resistance of one epitaxial bridge spanning four fins is calculated to $3.19 - 18.67\,\mathrm{k\Omega}$ which hints at a strongly varying short. Assuming a brittle and uneven connection, however, the values are on the order of resistance values reported in the literature [Goeller et al. 1997; Eyoum and King 2004]. Using the calculated resistances in a direct-current spectre simulation of the cavity results in a similar response to the leakage currents, as shown by solid lines in Figure 7.8.

To fully confirm the origin of the short, the cavity was screened using a scanning electron microscope as shown in Figure 7.10(a). Comparing the structure to the cavity images published by Bahr et al. in Figure 7.10(b), the point of failure in the cavity, shown in Figure 7.10(a), is marked by a white box. Whereas in Figure 7.10(b) the individual drive fins are separated in Global Foundries process, as they have presumably been etched away, which is not the case for the process used in this work. To create a higher uniformity of the fins, which should aid performance, the fins were not removed by etching in this work, whereas in the proof of concept report of the RFT the fins were most likely etched (compare Figure 7.10(b)) [Bahr et al. 2018]. The raised epitaxial source-drain contacts of the individual fins are merged during fabrication, and thus form a semiconductor bridge between adjacent drive contacts in the cavity [Bhat et al. 2020].

Consequently, the process has to be modified to enable the fabrication of RFT. The epitaxial bridges may be suppressed by creating a special pattern on specific photomasks used in the process flow, which have been fabricated specifically for the RFT [Hudeczek et al. 2021]. The adaptation was tested on two wafers fabricated back to back with the same layout. The two wafers are called mask A and mask B, where the first is fabricated with the unmodified and the latter with the modified mask set, respectively. The modified mask set contains three different

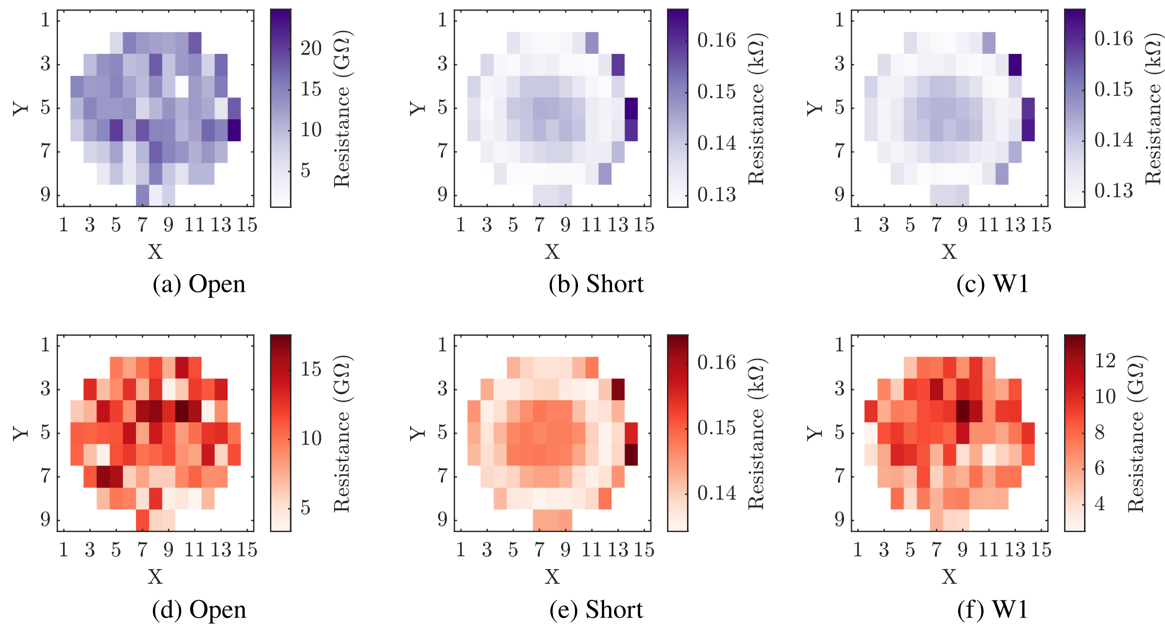

(a) Open (b) Short (c) W1

(d) Open (e) Short (f) W1

Figure 7.11: Phase-to-phase resistance wafer maps between drive-plus and drive-minus before the mask modification for (a) a deliberate open, (b) short and (c) a reference structure W1. The respective wafer maps after the process adaptation are shown in (d) to (f).

patterning schemes, referred to as W1, W2 and W3.

Both mask sets feature a structure designed as a forced electrical short (SH) and open (OP) to ensure successful implementation of the modification and asses the impact on the remaining wafer. The open is formed by actively suppressing the fin formation in between the phases, while the short is created using the old patterning scheme responsible for the shorting in the first place. The method used to create the forced open structure can not be applied to the RFT as the intermediate fins between the different drive phases are also suppressed beneath the gate, and consequently, the desired mechanical eigenmode will not emerge.

The test structures were created for both NMOS and PMOS devices as the epitaxial process differs for both device types. The measured resistances are shown for a PMOS device in Figure 7.11 for mask sets A and B, respectively. The forced open (compare Figures 7.11(a) and 7.11(d)) and short (compare Figures 7.11(b) and 7.11(e)) on both mask sets match the expected results. The open features a resistance in the gigaohm range, which is indicative of a complete electrical separation between the drive phases. The short resistance, however, is in the range of a few hundred ohms, indicating the previously observed merging of fins. The three test devices W1 to W3 on mask A are fabricated identically without modification, and thus they mimic the resistance of the forced short structure, as shown exemplarily for W1 in Figure 7.11(c).

The second mask set B, shown in Figures 7.11(d) to 7.11(f), features the same behaviour for the forced open and short reference structures. However, after the modification, the devices are now compared to the forced open, with resistances in the gigaohm range, as shown in Figure 7.11(f) for device W1. All acquired data for both NMOS and PMOS is shown in Figure 7.12. Note that

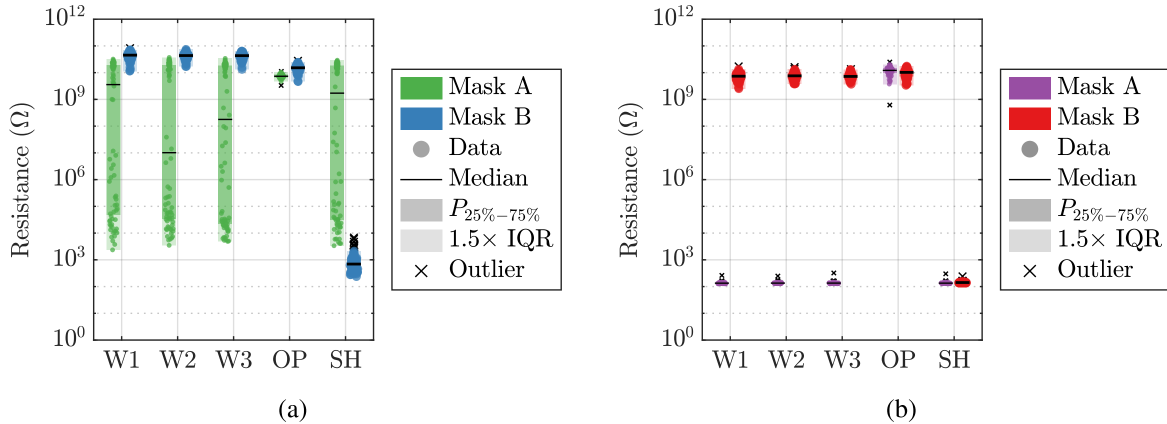

Figure 7.12: Comparison of the (a) NMOS and (b) PMOS RFT drive phase resistances between drive-plus and drive-minus before (Mask A) and after (Mask B) the process adaptation. A bad probe contact in (a) potentially skewed the NMOS data for Mask A during measurement.

during the measurements of the NMOS devices on mask A, a bad contact likely skewed the result. However, both device types have excellent isolation for the modified mask set B, indicating a successful implementation. The compatibility and cost of the process modification within the existing flow were of high importance. As the devised method does not rely on additional masks, the method can be applied at no additional cost to a productive foundry environment. The wafer processed with mask B showed unchanged device parameters for normal devices, which also shows that this is a viable low-cost concept to integrate the device.

The successful modification was also verified with a scanning electron microscope as shown in Figure 7.13. In Figures 7.13(a) and 7.13(b) the contact and gate cross-section of the fabricated and simulated RFT is shown before the process was modified. The cross-section of the new process are shown in Figures 7.13(c) and 7.13(d) for the contact and gate region.

Using the modified process a new test chip with the dimensions $6\,\mathrm{mm} \times 2.25\,\mathrm{mm}$ was designed and fabricated. It features 135 RF RFT devices with 10 de-embedding structures [Rumiantsev 2014]. The RF DUTs are distributed across three different CMOS compatibility splits (W1 to W3), resulting in 45 unique RFT cavity designs in the final layout iteration. An additional 20 non-RF structures were designed for NMOS and PMOS, allowing the process modification to be monitored within the foundry.

To confirm the electrical integrity of the DUTs several direct-current measurements are performed on the sense FinFETs and the drive MOS capacitors. The sense FinFET sense-plus and sense-minus, exhibit healthy drain current behaviour with a varying drain and gate bias as shown in Figure 7.14 for an exemplary NMOS and PMOS RFT. As both sense FinFETs yield identical currents, which indicates a good connection to the sense unit cell. Moreover, the PMOS has a slightly lower current at the same gate length and bias condition, as plotted in Figure 7.14(b), which was discussed during the theoretical modelling of the RFT in Section 5.5.

The successful connection to the MOS capacitors is confirmed by a forward bias of the bulk diode, located between the connected fins and the guard ring. As indicated by the arrow, the

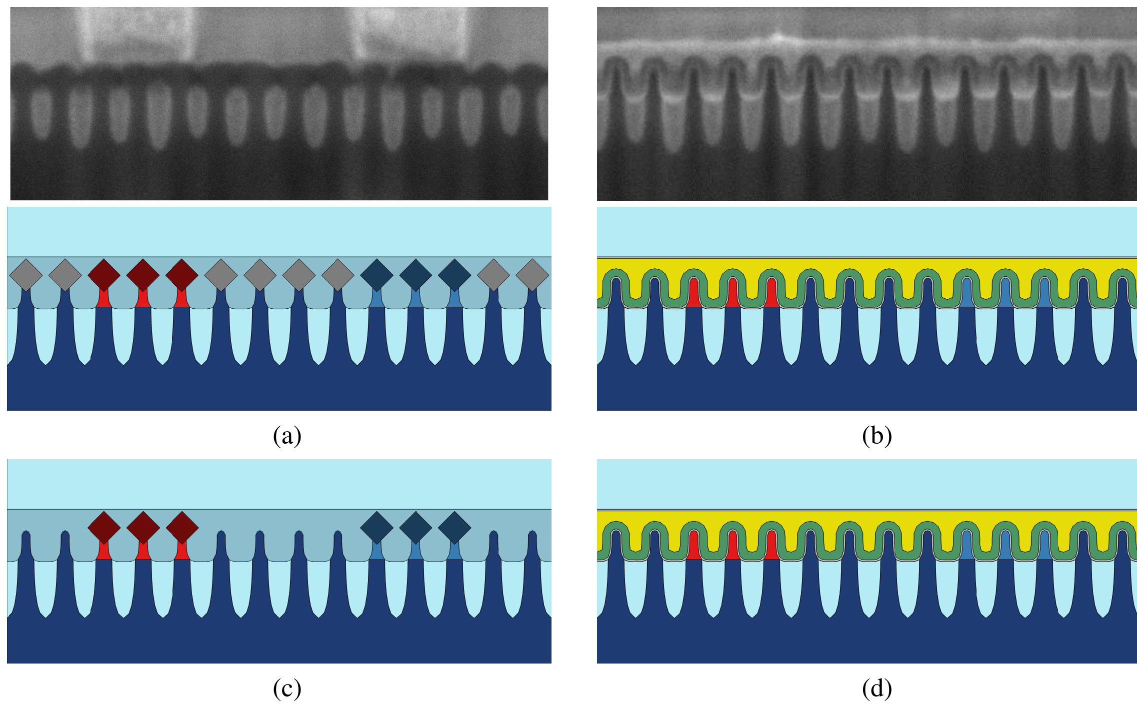

Figure 7.13: Cross-sections of the RFT in the (a) contact and (b) gate using the standard process. Cross-sections of the modified process in the (c) contact and (d) gate.

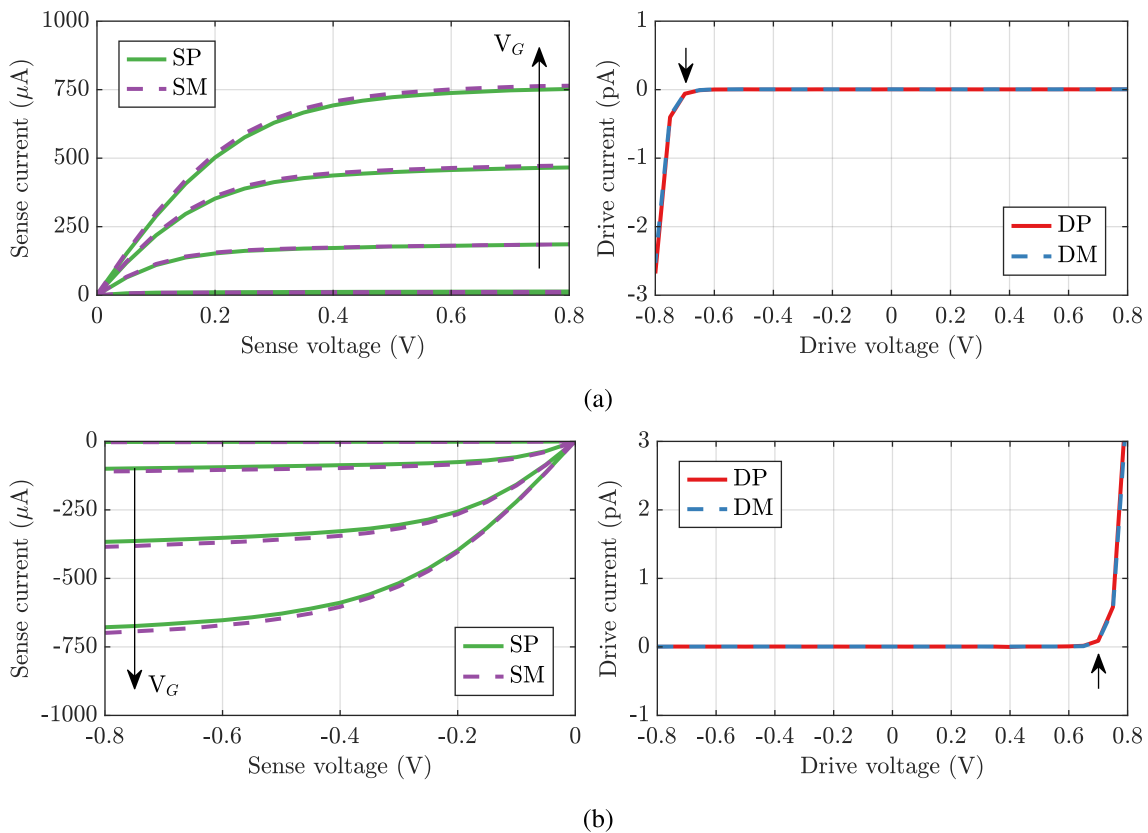

Figure 7.14: Exemplary measurement of the sense and drive connections for a (a) NMOS and (b) PMOS DUT.

diode opens at approximately ±0.7 V. Furthermore, as the process was adjusted according to Section 7.2, no shorts occurred between the different electrical phases and negligible electrical leakage was observed between the different ports.

7.3 Measurements of the Resonant Fin Transistor

The performance was assessed with the finite-element method (FEM) using a best-case approximation in the theoretical analysis. When the BEOL mirror was neglected and replaced by a SiO_2 slab, the simulated transconductance at a Q-factor 49 000 was 19.6 µS for the NMOS and 44.1 µS for the PMOS. On the other hand the modern low-κ SiCO:H cannot sustain a mechanical and must be replaced with a matched phononic crystal mirror in the BEOL. If a matched mechanical band gap exists in the BEOL, the resonant mode can be confined, and higher Q-factors might be achievable. However, the existence of a matched band gap could not be confirmed in a three-dimensional (3D) simulation as the anisotropic mechanical behaviour of copper and additional folded bands fully suppress their formation. Furthermore, the fundamental limit of the Q-factor, assuming a perfectly matched phononic crystal and no thermoelastic dissipation, is limited by Landau-Rumer attenuation to 10 708. This value, however, is largely overestimated as it assumes a monocrystalline silicon device, and consequently, the simulated transconductance figures cannot be reached.

The mechanical transconductance

$$G_m = |Y_{dd21} - Y_{dd12}| \tag{7.3.1}$$

of the MEMS is determined from full differential S-parameter measurements of the DUT and the resolution limit of the measurements is crucial to resolve the possible nano to micro siemens transconductances. They were performed with an N5225A parametric network analyser from Keysight with an integrated true-mode stimulus [Bahr et al. 2018; Weinstein and Bhave 2007]. The measurement setup is illustrated in Figure 7.15(a). The parametric network analyser is connected via ports 1 and 3 to drive phases drive-plus and drive-minus and ports 2 and 4 to sense phases sense-minus and sense-plus, respectively. The bias voltages for the drive, sense and gate are supplied by three 2636B Keithley source measure units. Since the RFT relies on differential actuation and sensing, the four individual ports are grouped in differential pairs, as sketched in Figure 7.15(b). The mixed-mode matrix describes the resulting S-parameters

$$S_{mm} = \begin{bmatrix} S_{dd11} & S_{dd12} & S_{dc11} & S_{dc12} \\ S_{dd21} & S_{dd22} & S_{dc21} & S_{dc22} \\ S_{cd11} & S_{cd12} & S_{cc11} & S_{cc12} \\ S_{cd21} & S_{cd22} & S_{cc21} & S_{cc22} \end{bmatrix} \tag{7.3.2}$$

where the four indices refer to the mode of sensing and stimulus at the receiving and transmitting

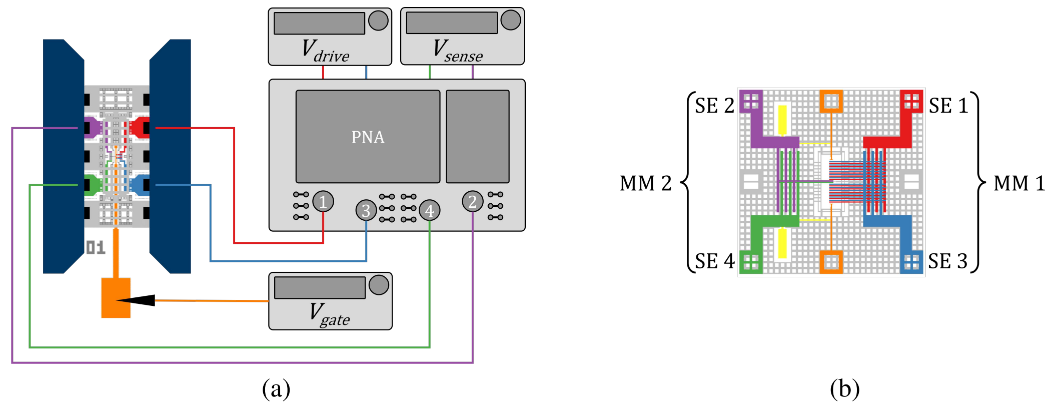

Figure 7.15: (a) The 4-port RF measurement setup with the PNA and direct-current sources. (b) The grouping of single-ended (SE) and mixed-mode (MM) ports on the RFT.

ports. Differential mode signals are denoted by d whereas common mode signals are indicated by c. The numeric subscripts indicate the port number analogously to the single-ended S-parameters [Fan et al. 2003; Huynh et al. 2010; Ferrero and Pirola 2006]. Consequently, the differential forward response of the RFT is described by S_{dd21}, where a differential stimulus and sense are performed on the drive (MM 1) and sense (MM 2) ports, respectively.

The measurements are calibrated and de-embedded to remove the impact of all undesired electrical effects of the probing apparatus and wiring [Rumiantsev 2014]. The calibration compensates for all influences from the parametric network analyser to the probe tips performed on commercially available substrates. However, as the probe pitch is too narrow only single-ended substrates are available, which only account for the direct connections between ports on opposing probes. For a full mixed-mode calibration, however, loopback through structures are necessary, which account for the return paths within the same probe. Consequently, a hybrid SOLR-LRRM calibration algorithm is used, which does not rely on the existence of loopback through structures, as they are inferred by the other measurements [Rumiantsev 2014; Hayden 2006]. After calibration the reference plane of the measurements is at the probe tips, and thus only effects of the pads, on-wafer wiring, and DUT are captured by the measurement.

It should be noted that although the hybrid SOLR-LRRM calibration yields good results in a mixed-mode application, minor imbalances in the calibration lead to ripples in the measurements. Those do not occur when the device is measured in a single-ended setup with the ports being actuated and measured in series. Therefore, all measurements are recorded using a single-ended approach and the resulting measurements are converted to mixed-mode parameters with the respective transformation matrices [Fan et al. 2003; Huynh et al. 2010]. The same approach was also used in all other resonant body transistor (RBT) and RFT publications [Bahr et al. 2018; Weinstein and Bhave 2010; Bahr et al. 2015].

An additional 4-port de-embedding procedure, carried out after the acquiring the calibrated measurement data, moves the reference plane from the probe tips closer to the actual DUT in the FEOL [Koolen et al. 1991; Rumiantsev 2014]. For this approach, two additional structures, an

electrically shorted and open layout without the RFT in the FEOL, are required. Both structures possess identical wiring to the RFT DUT. However, they are either shorted on the lowest metal layer close to the cavity or are not connected to the fin contacts. Using the measurements of both the open and the DUT, the capacitive impact of the pads and wiring is removed from the measurement. This procedure, using the impedance parameters of the measurement,

$$Y'_{DUT} = Y_{DUT} - Y_{OP} \tag{7.3.3}$$

is called open de-embedding. To also remove the inductive behaviour of the wiring, the short structure is required. After an initial subtraction of the open capacitance from the short measurement

$$Y'_{SH} = Y_{SH} - Y_{OP} \tag{7.3.4}$$

the inductive impact of the wiring can be removed from the DUT

$$Z''_{DUT} = Z'_{DUT} - Z'_{SH} \tag{7.3.5}$$

using the impedance parameters of the measurement. Note that the admittance, impedance and S-parameters may be transformed into one-another using the respective transformation matrices [Frickey 1994].

A different de-embedding technique allows the DUT to be de-embedded using both forward S_{dd21} and reverse S_{dd12} measurements of the same structure. This self-de-embedding is possible as the device may only function in the forward direction. Consequently, all electrical coupling of the wiring can be subtracted from the forward measurement as it is present and assumed to be identical in both directions [Weinstein 2009]. Consequently, the definition of mechanical transconductance (7.3.1) is self-de-embedded by construction [Bahr et al. 2018].

As the theoretically predicted transconductance is in the low nano to micro siemens range, the noise floor of the DUTs is first assessed for different parametric network analyser drive powers. All RFTs are biased at the default configuration of $V_G = 0.8\,\text{V}$, $V_{sense} = 200\,\text{mV}$, and $V_{drive} = 40\,\text{mV}$, as the best performance is expected at this bias condition, as shown in the theoretical analysis. Note that for the PMOS RFT all voltages are inverted. The mean transconductance is extracted from the measurements between 25-35 GHz of the eight best-performing DUTs, which is the expected range for the RFT frequency. The results are plotted for NMOS and PMOS devices in Figure 7.16 as blue and red solid lines. The power was increased from −26 dBm to −2 dBm as for higher powers the source of the parametric network analyser is not levelled and gives erroneous measurement results. With an increasing drive power, the measurement floor reduces, indicating that the background is not an active signal of the device. The shaded regions mark the standard deviation of the measurement floor for the best eight performing devices, approximately 1 μS for both NMOS and PMOS devices at the highest drive power.

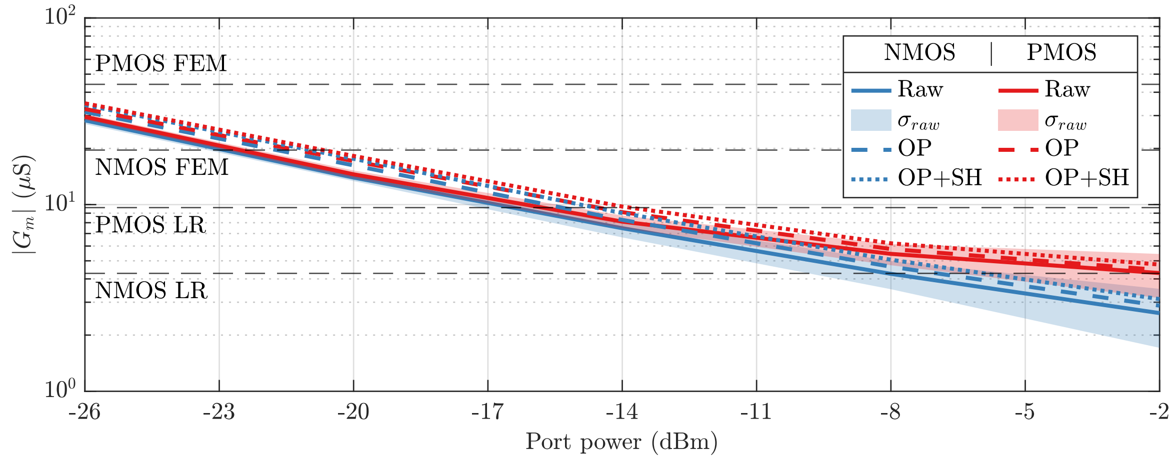

Figure 7.16: Measured transconductance for the ten theoretical best-performing NMOS and PMOS devices.

Table 7.2: Required Q-factors to reach the respective transconductances.

Type	FEM simulation		LR attenuation		Meas. floor	
	G_m (µS)	Q-factor	G_m (µS)	Q-factor	G_m (µS)	Q-factor limit
PMOS	44.1	49 000	9.6	10 708	4.3	4800 *
NMOS	19.6	49 000	4.3	10 708	2.6	6415 *

* This value is theoretically required to reach the specified transconductance detection limit and does not represent a measured quantity.

Furthermore, by using an additional open or open-short de-embedding the floor of the signal is slightly increased. As different structures have to be measured for the additional de-embedding, a degradation of the calibration accuracy and probe contact quality may adversely affect the ultimate result and slightly increase the noise floor. This shows that the self-de-embedding of the device offers the best performance while reducing chip area and measurement times.

Also indicated are the theoretical upper limits of the transconductance, which are set either by the FEM or the Landau-Rumer attenuation. Comparing the lowest possible measurement noise floor to theoretical values, as done in Table 7.2, highlights the RFT's inadequate performance. In the simulations, the transconductance achieved only a few ten micro siemens at a Q-factor of 49 000 which falls short of the reported value of 14 mS by three orders of magnitude. For the RFT to deliver a transconductance which is on par with the noise floor a Q-factor of 6400 and 4800 would be required for the NMOS and PMOS variants, respectively. Following the discussion of the fundamental limit of the Q-factor, which may not surpass 10 708, the transconductance is approximately a factor of two larger than required to protrude through the noise floor.

However, the likelihood of such Q-factors is very small as discussed in Section 6.5 since the device operates at room temperature and multiple materials are involved. Furthermore, in the simulations of the BEOL, possible matching mechanical band gaps in the phononic crystal were ruled out and therefore the Q-factor is reduced to immeasurably small values.

Subsequent measurements of the best-performing RFT between 15-40 GHz substantiated this assumption. To account for the possibility of a Q-factor in the ten-thousands, although it is not

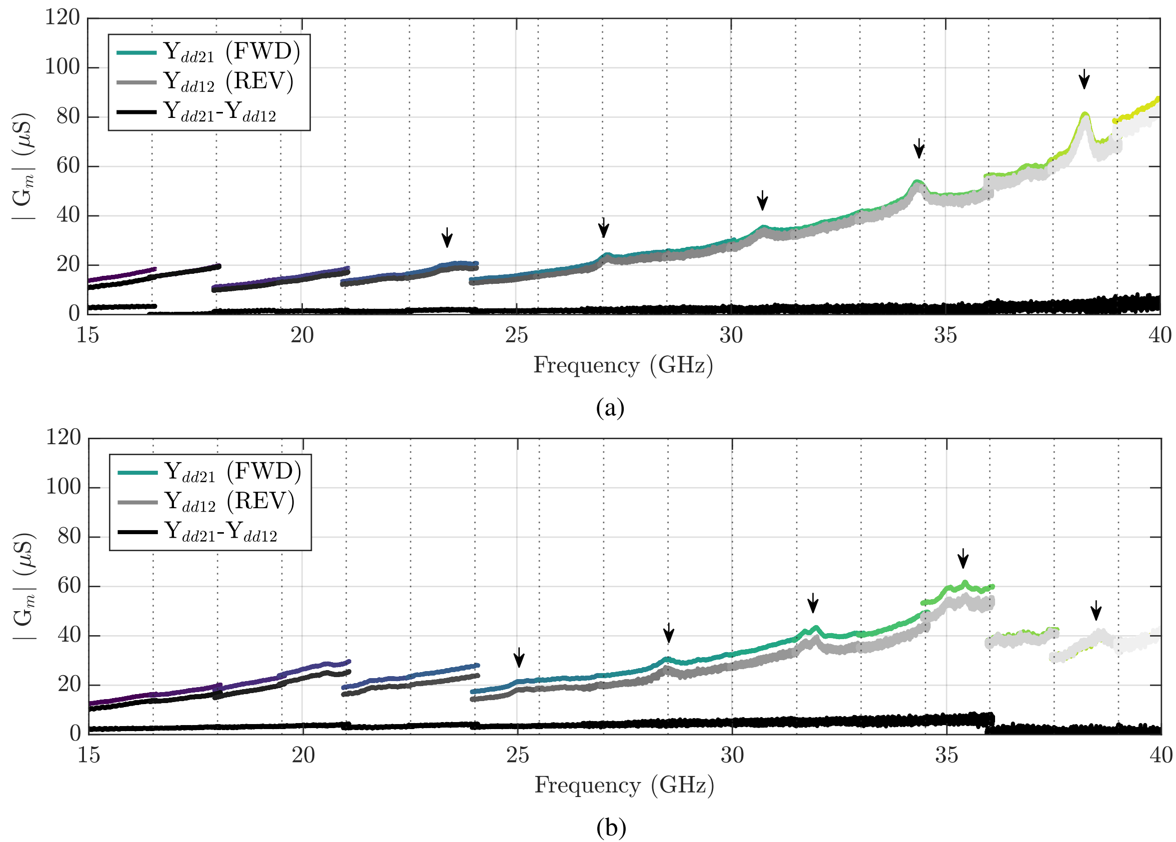

Figure 7.17: Measured transconductance for a (a) NMOS and (b) PMOS RFT.

supported by the theoretic investigation, the measurements were split into 1.5 GHz segments, each with 20 000 evenly spaced sample points. Furthermore, as discussed in the theoretical analysis of the device, the ramp-up behaviour at high Q-factors is slow. Each sample point was thus recorded with a time delay of 100 μs between the application of the continuous stimulus and the detection. To further reduce the noise of the measurements intermediate frequency bandwidth of the parametric network analyser is set to 500 Hz and the data is averaged across 20 consecutive measurements.

The measurements of the best performing NMOS and PMOS devices with a single-ended drive power of −2 dBm, which were identified by the simulations, are shown in Figure 7.17. Each features four parallel gates, 12 drive unit cells, and a gate length of 36 nm, which is considered the best-performing integration. For the NMOS the gate was biased at a constant voltage of $V_G = 0.8$ V, whereas the sense and drive bias voltages were 200 mV and 40 mV, respectively. For the PMOS the gate was biased at a constant voltage of $V_G = -0.8$ V, whereas the sense and drive bias voltages were −200 mV and −40 mV, respectively. The calculated transconductances are plotted for the forward (FWD) and the reverse (REV) direction as well as self-de-embedded (FWD-REV). The different segments are indicated by dashed vertical lines. Several small offsets between adjacent segments are observed which follow from changes in ambient temperature and possible degradation of the measurement pads.

Within the spectrum of both devices several resonance-like ripples, as marked by arrows, can

be observed. However, as they appear both in the forward and the reverse direction they are not caused by the RFT but rather by electrical coupling. Their even spacing by 3.5 GHz for the NMOS and 3 GHz for the PMOS indicates a higher harmonic behaviour of a wiring-induced effect occurring at a lower frequency. All ripples are consequently removed by the self de-embedding resulting in a flat response, marked in black.

The measurements were repeated on several hundred DUTs, distributed across several designs, wafers and chips. However, the reported resonance at approximately 32 GHz with a transconductance of 14 mS could not be observed which was predicted by the previous theoretical investigations.

Summary

The layout of the RFT was showcased on one example device designed using the parameterised cell approach to create large layout variations. The first test chip iteration highlighted a defect in the epitaxial processing of the intermediate fins, which resulted in an electrical shorting of the cavity. This issue was alleviated by a modification of the process, restoring compatibility and enabling a successful fabrication of the device, which was confirmed by scanning electron microscope and direct-current measurements.

Following the device fabrication, the mixed-mode measurement setup of the DUTs, with the required calibration and de-embedding, were discussed. The measurement conditions were optimised to achieve the highest possible resolution. This comprehensive evaluation included selecting the best device configurations from the 135 fabricated RFTs and also a optimisation of the bias and drive conditions, the measurement settings and the de-embedding procedure.

With these optimised conditions, a resolution limit in the micro to nano siemens range for the transconductance was achieved and no RFT resonance was observed. This characterisation data disproves a very large transconductance of 14 mS, as reported by Bahr et al. [Bahr et al. 2018]. From the theoretical investigations a signal in the range from 4.3-9.6 µS using the most optimistic assumptions would lead to a measurable result. However, no functional device could be identified.

Following these theoretical investigations and the limits from the characterisation results, the device performance is insufficient for practical circuit applications.

8

Conclusion and Outlook

The goal of this thesis was to improve the understanding of a novel monolithic complementary metal-oxide-semiconductor micro-electro-mechanical-system that promises exceptional performance. Therefore, a complete theoretical analysis using the finite-element method and subsequent characterisation of fabricated structures was carried out. Due to its direct compatibility with the standard complementary metal-oxide-semiconductor fin field-effect transistor process, it was a promising candidate to replace existing micro-electro-mechanical-system and coil-based solutions and alleviate many of the involved complications and drawbacks.

To enable a complete electromechanical modelling of the resonant fin transistor, the material properties of cubic anisotropic materials such as copper and silicon can be described by the generalised Hooke's law. In isotropic media, the response is independent of the interaction direction, which does not apply to anisotropic complementary metal-oxide-semiconductor materials such as copper and silicon. In those materials, all properties, such as Young's and the shear modulus and Poisson's ratio, exhibit a varying response that depends on the crystallographic orientation. From Young's and the shear modulus the wave velocities of longitudinal and transversal waves within bulk materials can be calculated, which are required to assess the index guiding properties of the silicon wafer.

With three-dimensional electromechanical finite-element simulations of the resonant fin transistor geometry, a compatible differential mechanical eigenmode at approximately 32 GHz within the front-end-of-line was confirmed. The frequency of the resonant mode is affected by the wafer orientation and geometrical properties, such as the gate length of the fin field-effect transistor, which enables the co-fabrication of resonant fin transistors with different resonant frequencies on the same wafer. To enable three-dimensional simulations with the finite-element method for such a complex nanostructure with the available compute infrastructure, it was necessary to reduce the degrees of freedom as far as possible. The usage of mirror planes is a common method to reduce the degree of freedom of the simulations, and the validity of this approach was studied in the presence of anisotropic mechanical materials such as silicon. For

the used wafer orientation the spatial symmetry planes coincide with the symmetry planes of the cubic silicon, enabling a reduction of the degrees of freedom by a factor of two. A physical silicon implementation needs to use a larger 14-fin unit cell due to lithography and processing limitations instead of the ideal 2-fin unit cell. The optimisation of the simulations enabled the simulation of this extended unit cell, and strong degradations in electromechanical coupling and peak pressure was found.

To analyse the electrical sensing the mechanical transconductance was modelled from the piezoresistive effect and the full stress tensors within the channels of the fin field-effect transistors. The variation of the carrier mobility in the presences of external stress was modelled using the empirical piezoresistive effect. Here a longitudinal compressive strain along the fin field-effect transistor channels of n-channel metal-oxide-semiconductor devices, and tensile strain for p-channel metal-oxide-semiconductor devices, resulted in improvement of the source-drain current. The piezoresistive effect and carrier mobility also depend on the dopant type and concentration, as well as the temperature. An increased temperature and doping concentration resulted in a reduced piezoresistive enhancement of the carrier mobility which ultimately lead to the p-channel metal-oxide-semiconductor outperforming the n-channel metal-oxide-semiconductor in the theoretical investigation.

In this work, the full strength of the piezoresistive effect is available, as advanced lightly doped transistors at room temperature on a stress-optimised industry standard (100)[45] wafer orientation are used. The optimum gate length for sensing was identified by simulations. A degradation of the mobility modulation was observed for the longer gate length leading to a reduced mechanical transconductance. Therefore, smaller gate lengths provide the required trade-off between mechanical actuation and carrier mobility variation leading to increased transconductance values.

Following the forgoing analysis, where lower pressure was obtained than reported in the literature, the mechanical transconductance is several orders of magnitude lower, with 44.1 μS and 19.6 μS for the p-channel metal-oxide-semiconductor and n-channel metal-oxide-semiconductor resonant fin transistor respectively. Both results contradict the reported transconductance of 14 mS by Bahr et al., which is contradictory as it requires previously unreported carrier mobility enhancements in excess of 750 % within silicon [Bahr et al. 2018].

The simulations showed that a SiO_2-based back-end-of-line provided good index guiding and high quality factors in simulations. State-of-the-art technologies, like the 16 nm fin field-effect transistor technology used in this work, transitioned to low-κ oxide materials like SiCO:H. This type of material class provided a much lower confinement for mechanical waves, leading to a drastic reduction of the quality factor.

One approach to mitigate this problem is to introduce a phononic crystal that uses the existing dielectric and metal layers for vertical confinement. The unpatterned back-end-of-line exhibits phononic crystal effects if the acoustic impedance between adjacent layers is mismatched which creates forbidden frequency regions where no mechanical wave can propagate. These

effects are modelled in one dimension for a purely vertical propagation along $\Gamma{-}Z$ with the finite-element method and analytically by the interface response theory for super-lattices, which are in perfect agreement. Several band gaps can be observed for longitudinal and transversal waves whose strength increases with a larger number of consecutive layers. Phononic band gaps in one-dimensional phononic crystals are, however, not sufficient for effective confinement due to the lateral wave vector of the excited mechanical modes of the resonant fin transistor.

A subsequent simulation of a laterally extended two-dimensional unit cell introduced additional bands by folding at the Brillouin zone edges, reducing the likelihood of wide band gaps, which is also reflected in the transmission loss. Moreover, in a low-κ SiCO:H back-end-of-line stack more bands are observed, further diminishing the shielding capabilities of the back-end-of-line. A verification of the phononic crystal shielding capabilities was carried out for a combined front-end-of-line and back-end-of-line in a two-dimensional simulation. Whereas the quality factor of the resonant fin transistor mode is improved with each additional layer in the presence of a matched phononic crystal band gap, no functionality is obtained in the absence of a matching band gap. The anisotropic effect of copper adds further complexity to the investigation of the band gaps considered in a three-dimensional simulation, where different orientations of the copper layers strongly influence the band gap formation [Hudeczek and Baumgartner 2021]. Assuming varying crystallographic directions and a back-end-of-line unit cell matched to the extent of the corresponding front-end-of-line unit cell no band gaps are found above a frequency of approximately 15 GHz regardless of the wave vector. The findings of the three-dimensional simulations carried out in this work contradict the measured and simulated results by Bahr et al., due to the use of an insufficient two-dimensional approximation in this publication [Bahr et al. 2018; Hudeczek and Baumgartner 2020].

The following analysis of the fundamental limits of the quality factor highlights another contradiction of the reported values. The total achievable quality factor of a micro-electro-mechanical-system is limited via Matthiesen's rule to the smallest quality factor of all involved damping mechanisms. These include intrinsic loss mechanisms such as thermoelastic dissipation, the Akhiezer effect, and Landau-Rumer attenuation. The latter is expected to be the dominant loss process which limits the Qf product to $34.2 \times 10^{13}\,\mathrm{Hz}^{-1}$ in silicon at the frequency of the resonant fin transistor. This limit remains unmatched by currently top performing and highly optimised micro-electro-mechanical-systems devices reported in literature to the current date. The resonant fin transistor is claimed to surpass this limit at room temperature by one order of magnitude with a Qf product of $1.57 \times 10^{15}\,\mathrm{Hz}^{-1}$.

To confirm the theoretical findings, the resonant fin transistor was fabricated on a 16 nm technology node, which resulted in an undesired shorting of the front-end-of-line cavity due to an incompatibility with the process. This issue was resolved by an adjustment of the involved process by a unique patterning of the lithography masks [Hudeczek et al. 2021]. This modification enabled a successful fabrication of the resonant fin transistor, as confirmed with a scanning electron microscope. Subsequent measurements of hundreds of devices under

test, with different layout parameters confirmed the theoretical findings in this work. Although the measurement accuracy allowed for the detection of resonances with a transconductance of a few tens of micro siemens the functionality of the resonant fin transistor could not be confirmed.

Following the work presented here, monolithically integrated complementary metal-oxide-semiconductor micro-electro-mechanical-system do not provide the anticipated performance gains, as the required stress levels cannot be achieved by dielectric transduction [Hudeczek et al. 2022; Hager et al. 2021]. A potential improvement of the figures of merit requires an exchange of the materials and integration improvements. Materials with piezoelectric or ferroelectric properties, which have proven successful operation in various applications, are potential candidates [Ptashnik et al. 2017; Liu et al. 2020; Shao et al. 2019; Gong and Piazza 2014; Piazza et al. 2007]. Here the concept of the resonant fin transistor could potentially be transferred to a GaN fin field-effect transistor process, which relies on a two-dimensional electron gas within the channel for conduction and potentially increased deformation when leveraging the piezoelectric effect [Im et al. 2014; Patwal et al. 2019; Patwal 2021]. This, however, does not alleviate the problem of a compatible back-end-of-line phononic crystal and the fundamental quality factor at the potentially large resonant frequency. Consequently, designs at much lower operating frequencies are necessary to be potentially confined by the back-end-of-line phononic crystal. Ultimately this approach voids the complementary metal-oxide-semiconductor compatibility and re-introduces the negative impact of the multi-chip approach. A rethinking of the integration of different devices in a single chip, as envisioned by the flip-chip technique or hyper-integration approach, is thus needed [Lu 2009].

Bibliography

Abdelaziz, B., K. Fouad and S. Kemouche (2014). "The Effect of Temperature and Doping Level on the Characteristics of Piezoresistive Pressure Sensor". In: *Journal of Sensor Technology* 04.02, pp. 59–65. DOI: 10.4236/jst.2014.42007.

Achaoui, Y., A. Khelif, S. Benchabane and V. Laude (2010). "Polarization State and Level Repulsion in Two-Dimensional Phononic Crystals and Waveguides in the Presence of Material Anisotropy". In: *Journal of Physics D: Applied Physics* 43.18, p. 185401. ISSN: 00223727. DOI: 10.1088/0022-3727/43/18/185401.

Alipour, A. and F. Zareian (2018). "Study Rayleigh Damping In Structures". In: *14th World Conference on Earthquake Engineering*. Vol. 14.

Ando, T. and T. Toriyama (2018). "Description of New Piezoresistance Tensor Equation for Cubic Single Crystal and Its Application to Multiaxial Stress". In: *Sensors and Materials* 30.9, p. 2101. DOI: 10.18494/sam.2018.1959.

André, N., T. P. Delhaye, M. Al Kadi Jazairli, B. Olbrechts, P. Gérard, L. A. Francis, J. P. Raskin and D. Flandre (2017). "Ultra-Low-Power SOI CMOS Pressure Sensorbased on Orthogonal PMOS Gauges". In: *22nd IMEKO TC4 International Symposum and 20th International Workshop on ADC Modelling and Testing*. Vol. 22, pp. 33–38. ISBN: 9781510849761.

Andriyevsky, B., W. Janke, V. Stadnyk and M. Romanyuk (2017). "Thermal Conductivity of Silicon Doped by Phosphorus: Ab Initio Study". In: *Materials Science-Poland* 35.4, pp. 717–724. DOI: 10.1515/msp-2017-0115.

Bachmann, H., W. J. Ammann, F. Deischl, J. Eisenmann, I. Floegl, G. H. Hirsch, G. K. Klein, G. J. Lande, O. Mahrenholtz, H. G. Natke, H. Nussbaumer, A. J. Pretlove, J. H. Rainer, E.-U. Saemann and L. Steinbeisser (1995). *Vibration Problems in Structures*. Birkhäuser Basel. DOI: 10.1007/978-3-0348-9231-5.

Bae, G., D.-I. Bae, M. Kang, S. Hwang, S. Kim, B. Seo, T. Kwon, T. Lee, C. Moon, Y. Choi, K. Oikawa, S. Masuoka, K. Chun, S. Park, H. Shin, J. Kim, K. Bhuwalka, D. Kim, W. Kim, J. Yoo, H. Jeon, M. Yang, S.-J. Chung, D. Kim, B. Ham, K. Park, W. Kim, S. Park, G. Song, Y. Kim, M. Kang, K. Hwang, C.-H. Park, J.-H. Lee, D.-W. Kim, S.-M. Jung and H. Kang (2018). "3nm GAA Technology Featuring Multi-Bridge-Channel FET for Low Power and High Performance Applications". In: *IEEE International Electron Devices Meeting*. Vol. 53. DOI: 10.1109/iedm.2018.8614629.

Baghelani, M., H. B. Ghavifekr and A. Ebrahimi (2011). "Analysis and Suppression of Spurious Modes of the Ring Shape Anchored RF MEMS Contour Mode Disk Resonator". In: *Microsystem Technologies* 17.10-11, pp. 1599–1609. ISSN: 09467076. DOI: 10.1007/s00542-011-1352-5.

Bahr, B. (2016). "Monolithically Integrated MEMS Resonators and Oscillators in Standard IC Technology". Dissertation. Department of Electrical Engineering. URL: https://dspace.mit.edu/handle/1721.1/105569.

Bahr, B., L. Daniel and D. Weinstein (2016). "Optimization of Unreleased CMOS-MEMS RBTs". In: *IEEE International Frequency Control Symposium*. DOI: 10.1109/fcs.2016.7563592.

Bahr, B., Y. He, Z. Krivokapic, S. Banna and D. Weinstein (2018). “32GHz Resonant-Fin Transistors in 14nm FinFET Technology”. In: *IEEE International Solid-State Circuits Conference*. Vol. 61, pp. 348–350. ISBN: 9781509049394. DOI: 10.1109/isscc.2018.8310327.

Bahr, B., R. Marathe and D. Weinstein (2014). “Phononic Crystals for Acoustic Confinement in CMOS-MEMS Resonators”. In: *IEEE International Frequency Control Symposium*. DOI: 10.1109/fcs.2014.6859980.

Bahr, B., R. Marathe and D. Weinstein (2015). “Theory and Design of Phononic Crystals for Unreleased CMOS-MEMS Resonant Body Transistors”. In: *Journal of Microelectromechanical Systems* 24.5, pp. 1520–1533. ISSN: 10577157. DOI: 10.1109/jmems.2015.2418789.

Bao, M. (2015). *Analysis and Design Principles of MEMS Devices*. 1st. Amsterdam Boston London: Elsevier. ISBN: 9780080455624.

Bao, M. and Y. Huang (2003). “Batch Derivation of Piezoresistive Coefficient Tensor by Matrix Algebra”. In: *Journal of Micromechanics and Microengineering* 14.3, pp. 332–334. DOI: 10.1088/0960-1317/14/3/003.

Bardeen, J. and W. H. Brattain (1948). “The Transistor, A Semi-Conductor Triode”. In: *Physical Review* 74.2 (2), pp. 230–231. DOI: 10.1103/physrev.74.230.

Basavalingappa, A., M. Y. Shen and J. R. Lloyd (2017). “Modeling the Copper Microstructure and Elastic Anisotropy and Studying Its Impact on Reliability in Nanoscale Interconnects”. In: *Mechanics of Advanced Materials and Modern Processes* 3.1. DOI: 10.1186/s40759-017-0021-5.

Basu, J. and T. K. Bhattacharyya (2011). “Microelectromechanical Resonators for Radio Frequency Communication Applications”. In: *Microsystem Technologies* 17.10-11, pp. 1557–1580. DOI: 10.1007/s00542-011-1332-9.

Bathe, K.-J. (2014). *Finite Element Procedures*. 2nd. Klaus-Jurgen Bathe. ISBN: 978-0-9790049-5-7.

Bauchau, O. A. and S. Han (2013). “Interpolation of Rotation and Motion”. In: *Multibody System Dynamics* 31.3, pp. 339–370. DOI: 10.1007/s11044-013-9365-8.

Bhat, T. S., S. Shintri, B. Chen, H.-C. Lo, J. Peng, Y. Qi, M. Willeman, S. K. Mishra, N. Yuksek and W. Z. Gao (2020). “Abnormal Silicon-Germanium (SiGe) Epitaxial Growth in FinFETs”. In: *IEEE Transactions on Semiconductor Manufacturing* 33.2, pp. 291–294. DOI: 10.1109/tsm.2020.2976123.

Bi, F. and B. Barber (2008). “Bulk Acoustic Wave RF Technology”. In: *IEEE Microwave Magazine* 9.5, pp. 65–80. DOI: 10.1109/mmm.2008.927633.

Birgani, P. T., S. Sodagar and M. Shishesaz (2017). “Generation of Low-Attenuation Lamb Wave Modes in Three-Layer Adhesive Joints”. In: *The International Journal of Acoustics and Vibration* 22.1, pp. 51–57. ISSN: 10275851. DOI: 10.20855/ijav.2017.22.1450.

Birgani, P. T., K. N. Tahan, S. Sodagar and M. Shishesaz (2015). “Theoretical Modeling of Low-Attenuation Lamb Wave Modes Generation in Three-Layer Adhesive Joints Using Angle Beam Transducer”. In: *Latin American Journal of Solids and Structures* 12.3, pp. 461–476. ISSN: 16797825. DOI: 10.1590/1679-78251143.

Bogue, R. (2013). “Recent Developments in MEMS Sensors: A Review of Applications, Markets and Technologies”. In: *Sensor Review* 33.4, pp. 300–304. DOI: 10.1108/sr-05-2013-678.

Brand, O., I. Dufour, S. M. Heinrich and F. Josse (2015). *Resonant MEMS*. Ed. by O. Brand, I. Dufour, S. M. Heinrich and F. Josse. Wiley-VCH Verlag GmbH & Co. KGaA. DOI: 10.1002/9783527676330.

Brannon, R. (2018). *Rotation Reflection and Frame Changes Orthogonal Tensors in Computational Engineering Mechanics*. IOP Publishing. DOI: 10.1088/978-0-7503-1454-1.

Brantley, W. A. (1973). "Calculated Elastic Constants for Stress Problems Associated with Semiconductor Devices". In: *Journal of Applied Physics* 44.1, pp. 534–535. ISSN: 00218979. DOI: 10.1063/1.1661935.

Brotherton, S. D., J. R. Ayres, A. Gill, H. van Kesteren and F. J. A. M. Greidanus (1987). "Deep Levels of Copper in Silicon". In: *Journal of Applied Physics* 62.5, pp. 1826–1832. DOI: 10.1063/1.339564.

BSIMCMG (2018). *BSIM-CMG Berkeley Short-Channel IGFET Model Common Multi-Gate*. Accessed 20.08.2018. URL: http://bsim.berkeley.edu/models/bsimcmg/.

Chandorkar, S. A., M. Agarwal, R. Melamud, R. N. Candler, K. E. Goodson and T. W. Kenny (2008). "Limits of Quality Factor in Bulk-Mode Micromechanical Resonators". In: *IEEE 21st International Conference on Micro Electro Mechanical Systems*. DOI: 10.1109/memsys.2008.4443596.

Chandrahalim, H., D. Weinstein, L. F. Cheow and S. A. Bhave (2007). "High-κ Dielectrically Transduced MEMS Thickness Shear Mode Resonators and Tunable Channel-Select RF Filters". In: *Sensors and Actuators A: Physical* 136.2, pp. 527–539. ISSN: 09244247. DOI: 10.1016/j.sna.2006.12.007.

Chen, H. C. and R. L. Taylor (1989). "Using Lanczos Vectors and Ritz Vectors for Computing Dynamic Responses". In: *Engineering Computations* 6.2, pp. 151–157. DOI: 10.1108/eb023769.

Chen, Z. (2015). "Thermal Tuning of Omnidirectional Reflection Bands in One-Dimensional Finite Phononic Crystals". In: *Journal of Applied Physics* 117.12, p. 124902. ISSN: 10897550. DOI: 10.1063/1.4915931.

Chopra, A. K. (2012). *Numerical Evaluation of Dynamic Response*. 4th. Prentice Hall, pp. 165–197. ISBN: 0-13-156174-X.

Chopra, A. K. and F. McKenna (2015). "Modeling Viscous Damping in Nonlinear Response History Analysis of Buildings for Earthquake Excitation". In: *Earthquake Engineering & Structural Dynamics* 45.2, pp. 193–211. ISSN: 1096-9845. DOI: 10.1002/eqe.2622.

Choudhary, V. and K. Iniewski (2013). *MEMS: Fundamental Technology and Applications*. Ed. by V. Choudhary and K. Iniewski. CRC Press, p. 478.

Chu, M., Y. Sun, U. Aghoram and S. E. Thompson (2009). "Strain: A Solution for Higher Carrier Mobility in Nanoscale MOSFETs". In: *Annual Review of Materials Research* 39.1, pp. 203–229. ISSN: 15317331. DOI: 10.1146/annurev-matsci-082908-145312.

Collaert, N., R. Rooyackers, F. Clemente, P. Zimmerman, I. Cayrefourcq, B. Ghyselen, K. San, B. Eyckens, M. Jurczak and S. Biesemans (2016). "Performance Enhancement of MUGFET Devices Using Super Critical Strained-SOI (SC-SSOI) and CESL". In: *IEEE Symposium on VLSI Technology*. DOI: 10.1109/vlsit.2006.1705212.

Comsol (14, 2018). *Comsol Blog Post Frequency Domain*. Accessed 14.10.2018. URL: https://www.comsol.com/multiphysics/mode-superposition.

Comsol (23, 2019). *Comsol Modal Super Position*. Accessed 23.08.2019. URL: https://www.comsol.com/blogs/part-1-modeling-the-harmonic-excitations-of-linear-systems/.

Dai, C.-T. and M.-D. Ker (2016). "Optimization of Guard Ring Structures to Improve Latchup Immunity in an 18 V DDDMOS Process". In: *IEEE Transactions on Electron Devices* 63.6, pp. 2449–2454. DOI: 10.1109/TED.2016.2549598.

Darinskii, A. N., E. L. Clezio and G. Feuillard (2007). “Frequency Degeneracy of Acoustic Waves in Two-Dimensional Phononic Crystals”. In: *Journal of Physics: Conference Series* 92.1, p. 012117. ISSN: 17426596. DOI: 10.1088/1742-6596/92/1/012117.

Date, E. H. F. and K. W. Andrews (1969). “Anisotropic and Composition Effects in the Elastic Properties of Polycrystalline Metals”. In: *Journal of Physics D: Applied Physics* 2.10, pp. 1373–1381. DOI: 10.1088/0022-3727/2/10/303.

Davis, J., R. Venkatesan, A. Kaloyeros, M. Beylansky, S. Souri, K. Banerjee, K. Saraswat, A. Rahman, R. Reif and J. Meindl (2001). “Interconnect Limits on Gigascale Integration (GSI) in the 21st Century”. In: *IEEE* 89.3, pp. 305–324. DOI: 10.1109/5.915376.

Dellinger, J., D. Vasicek and C. Sondergeld (1998). “Kelvin Notation for Stabilizing Elastic-Constant Inversion”. In: *Revue de l’Institut Français du Pétrole* 53.5, pp. 709–719. DOI: 10.2516/ogst:1998063.

Dennard, R., F. Gaensslen, H.-N. Yu, V. Rideout, E. Bassous and A. LeBlanc (1974). “Design of Ion-Implanted MOSFET’s with Very Small Physical Dimensions”. In: *IEEE Journal of Solid-State Circuits* 9.5, pp. 256–268. DOI: 10.1109/JSSC.1974.1050511.

Dhar, S., E. Ungersbock, H. Kosina, T. Grasser and S. Selberherr (2007). “Electron Mobility Model for ⟨110⟩ Stressed Silicon Including Strain-Dependent Mass”. In: *IEEE Transactions On Nanotechnology* 6.1, pp. 97–100. ISSN: 1536125X. DOI: 10.1109/tnano.2006.888533.

Dismukes, J. P., L. Ekstrom and R. J. Paff (1964). “Lattice Parameter and Density in Germanium-Silicon Alloys”. In: *The Journal of Physical Chemistry* 68.10, pp. 3021–3027. ISSN: 00223654. DOI: 10.1021/j100792a049.

Djafari-Rouhani, B. and L. Dobrzynski (1987). “Simple Excitations in N-Layered Superlattices”. In: *Solid-State Communications* 62.9, pp. 609–615. DOI: 10.1016/0038-1098(87)90200-6.

Dobrzynski, L. (1990). “Interface Response Theory of Continuous Composite Systems”. In: *Surface Science Reports* 11.5-6, pp. 139–178. DOI: 10.1016/0167-5729(90)90003-v.

Dobrzyński, L., A. Akjouj, Y. Pennec, H. Al-Wahsh, G. Lévêque, B. Djafari-Rouhani, I. Transmission, T. Book, et al. (2018). *Phononics: Interface Transmission Tutorial Book Series*. Elsevier. DOI: 10.1016/c2015-0-06475-9.

Doll, J. C. and B. L. Pruitt (2013). “Piezoresistance Fundamentals”. In: *Piezoresistor Design and Applications*. Springer New York, pp. 21–49. DOI: 10.1007/978-1-4614-8517-9_2.

Ebert, J. L., S. Ghosal and N. Acharya (2020). *Thermal Modeling of MOCVD Reactor*. URL: https://www.comsol.com/paper/thermal-model-and-control-of-metal-organic-chemical-vapor-deposition-process-51142.

Einstein, A. (1916). “Die Grundlage Der Allgemeinen Relativitätstheorie”. In: *Annalen der Physik* 354.7, pp. 769–822. DOI: 10.1002/andp.19163540702.

Eyoum, M.-A. and T.-J. King (2004). “Low-Resistance Silicon-Germanium Contact Technology for Modular Integration of MEMS with Electronics”. In: *Journal of The Electrochemical Society* 151.3, J21. DOI: 10.1149/1.1644143.

Fan, W., A. Lu, L. Wai and B. Lok (2003). “Mixed-Mode S-Parameter Characterization of Differential Structures”. In: *5th Electronics Packaging Technology Conference*. DOI: 10.1109/eptc.2003.1271579.

Fano, U. (1961). “Effects of Configuration Interaction on Intensities and Phase Shifts”. In: *Physical Review* 124.6, pp. 1866–1878. ISSN: 0031899X. DOI: 10.1103/physrev.124.1866.

Featherston, F. H. and J. R. Neighbours (1963). “Elastic Constants of Tantalum, Tungsten, and Molybdenum”. In: *Physical Review* 130.4, pp. 1324–1333. ISSN: 0031899X. DOI: 10.1103/physrev.130.1324.

Fedder, G., R. Howe, T.-J. K. Liu and E. Quevy (2008). “Technologies for Cofabricating MEMS and Electronics”. In: *IEEE* 96.2, pp. 306–322. ISSN: 00189219. DOI: 10.1109/jproc.2007.911064.

Felippa, C. A. (2004). *Introduction to Finite Element Methods*. University of Colorado.

Ferrero, A. and M. Pirola (2006). “Generalized Mixed-Mode S-Parameters”. In: *IEEE Transactions on Microwave Theory and Techniques* 54.1, pp. 458–463. DOI: 10.1109/tmtt.2005.860497.

Fischer, A. C., F. Forsberg, M. Lapisa, S. J. Bleiker, G. Stemme, N. Roxhed and F. Niklaus (2015). “Integrating MEMS and ICs”. In: *Microsystems & Nanoengineering* 1.1, p. 15005. ISSN: 2055-7434. DOI: 10.1038/micronano.2015.5. eprint: 1604.04843.

Fowler, A. and F. Ng (2021). *Glaciers and Ice Sheets in the Climate System*. Ed. by A. Fowler and F. Ng. Springer International Publishing. DOI: 10.1007/978-3-030-42584-5.

Frickey, D. (1994). “Conversions between S, Z, Y, H, ABCD, and T Parameters Which Are Valid for Complex Source and Load Impedances”. In: *IEEE Transactions on Microwave Theory and Techniques* 42.2, pp. 205–211. DOI: 10.1109/22.275248.

Gallon, C., G. Reimbold, G. Ghibaudo, R. Bianchi, R. Gwoziecki, S. Orain, E. Robilliart, C. Raynaud and H. Dansas (2004). “Electrical Analysis of Mechanical Stress Induced by STI in Short MOSFETs Using Externally Applied Stress”. In: *IEEE Transactions on Electron Devices* 51.8, pp. 1254–1261. ISSN: 00189383. DOI: 10.1109/ted.2004.831358.

Gambino, J. (2012). “Process Technology for Copper Interconnects”. In: *Handbook of Thin Film Deposition*. Elsevier, pp. 221–269. DOI: 10.1016/b978-1-4377-7873-1.00008-5.

Gao, A., K. Liu, J. Liang and T. Wu (2020). “AlN MEMS Filters with Extremely High Bandwidth Widening Capability”. In: *Microsystems & Nanoengineering* 6.1. DOI: 10.1038/s41378-020-00183-5.

Gao, A., R. Lu and S. Gong (2016). “Mitigation of AO Spurious Modes in AlN MEMS Resonators with SiO2 Addendums”. In: *IEEE International Frequency Control Symposium*. ISBN: 9781509020911. DOI: 10.1109/fcs.2016.7563550.

Garcıa, P. G. and J.-P. Fernández-Álvarez (2015). “Floquet-Bloch Theory and Its Application to the Dispersion Curves of Nonperiodic Layered Systems”. In: *Mathematical Problems in Engineering* 2015, pp. 1–12. DOI: 10.1155/2015/475364.

Gauster, W. B. (1971). “Low-Temperature Grüneisen Parameters for Silicon and Aluminum”. In: *Physical Review B* 4.4, pp. 1288–1296. DOI: 10.1103/physrevb.4.1288.

Ghaffari, S., S. A. Chandorkar, S. Wang, E. J. Ng, C. H. Ahn, V. Hong, Y. Yang and T. W. Kenny (2013). “Quantum Limit of Quality Factor in Silicon Micro and Nano Mechanical Resonators”. In: *Scientific Reports* 3.1. DOI: 10.1038/srep03244.

Ghaffari, S., E. J. Ng, C. H. Ahn, Y. Yang, S. Wang, V. A. Hong and T. W. Kenny (2015). “Accurate Modeling of Quality Factor Behavior of Complex Silicon MEMS Resonators”. In: *Journal of Microelectromechanical Systems* 24.2, pp. 276–288. DOI: 10.1109/jmems.2014.2374451.

Giurgiutiu, V. and M. F. Haider (2019). “Propagating, Evanescent, and Complex Wavenumber Guided Waves in High-Performance Composites”. In: *Materials* 12.2, p. 269. ISSN: 19961944. DOI: 10.3390/ma12020269.

Global Foundries (2021). *CMOS Nodes*. URL: https://gf.com/jishujiejuefangan/cmos.

Goeller, P. T., B. I. Boyanov, D. E. Sayers and R. J. Nemanich (1997). “Structure and Stability of Cobalt-Silicon-Germanium Thin Films”. In: *Nuclear Instruments and Methods in Physics Research Section B: Beam Interactions with Materials and Atoms* 133.1-4, pp. 84–89. DOI: 10.1016/s0168-583x(97)00458-8.

Goettler, D., M. Su, Z. Leseman, Y. Soliman, R. Olsson and I. El-Kady (2010). "Realizing the Frequency Quality Factor Product Limit in Silicon Via Compact Phononic Crystal Resonators". In: *Journal of Applied Physics* 108.8, p. 084505. DOI: 10.1063/1.3475987.

Gokhale, V. J. and J. J. Gorman (2018). "Identifying Spurious Modes in RF-MEMS Resonators Using Photoelastic Imaging". In: *IEEE Micro Electro Mechanical Systems*. Vol. 2018-Janua. January, pp. 779–782. ISBN: 9781538647820. DOI: 10.1109/memsys.2018.8346671.

Gong, S. and G. Piazza (2014). "Monolithic Multi-Frequency Wideband RF Filters Using Two-Port Laterally Vibrating Lithium Niobate MEMS Resonators". In: *Journal of Microelectromechanical Systems* 23.5, pp. 1188–1197. DOI: 10.1109/jmems.2014.2308259.

Graczykowski, B., S. Mielcarek, A. Trzaskowska, J. Sarkar, P. Hakonen and B. Mroz (2012). "Tuning of a Hypersonic Surface Phononic Band Gap Using a Nanoscale Two-Dimensional Lattice of Pillars". In: *Physical Review B* 86.8, p. 085426. ISSN: 10980121. DOI: 10.1103/physrevb.86.085426.

Graczykowski, B., M. Sledzinska, N. Kehagias, F. Alzina, J. S. Reparaz and C. M. S. Torres (2014). "Hypersonic Phonon Propagation in One-Dimensional Surface Phononic Crystal". In: *Applied Physics Letters* 104.12, p. 123108. ISSN: 00036951. DOI: 10.1063/1.4870045.

Graff, K. F. (1975). *Wave Motion in Elastic Solids*. New York: Dover Publications. ISBN: 9781621986461.

Grill, A. (2003). "Plasma Enhanced Chemical Vapor Deposited SiCOH Dielectrics: From Low-κ to Extreme Low-κ Interconnect Materials". In: *Journal of Applied Physics* 93.3, pp. 1785–1790. DOI: 10.1063/1.1534628.

Gross, D. and T. Seelig (2018). *Fracture Mechanics*. Springer International Publishing, pp. 13–17. DOI: 10.1007/978-3-319-71090-7.

Hager, E., R. Hudeczek, P. Baumgartner and H. Pretl (2021). "Modeling and Analysis of High-Q Resonant-Fin Transistors". In: *IEEE Transactions on Electron Devices* 68.9, pp. 4780–4786. DOI: 10.1109/ted.2021.3097302.

Hamelin, B., J. Yang, A. Daruwalla, H. Wen and F. Ayazi (2019). "Monocrystalline Silicon Carbide Disk Resonators on Phononic Crystals with Ultra-Low Dissipation Bulk Acoustic Wave Modes". In: *Scientific Reports* 9.1, pp. 1–8. ISSN: 20452322. DOI: 10.1038/s41598-019-54278-9.

Han, S. K., C. W. Wu and Z. Chen (2017). "Polarized Pass Band for Longitudinal Waves in Solid Phononic Crystals". In: *Journal of Physics Communications* 1.5, p. 055026. ISSN: 2399-6528. DOI: 10.1088/2399-6528/aa982c.

Harrington, B., M. Shahmohammadi and R. Abdolvand (2010). "Toward Ultimate Performance in GHZ MEMS Resonators: Low Impedance and High Q". In: *IEEE 23rd International Conference on Micro Electro Mechanical Systems*. DOI: 10.1109/memsys.2010.5442310.

Hashimoto, K. (2012). "Surface Acoustic Wave (SAW) Devices". In: *Ultrasonic Transducers*. Elsevier, pp. 331–373. DOI: 10.1533/9780857096302.3.331.

Hayden, L. (2006). "A Hybrid Probe-Tip Calibration for Multiport Vector Network Analyzers". In: *IEEE 68th ARFTG Conference: Microwave Measurement*. DOI: 10.1109/arftg.2006.8361674.

Healy, D., N. E. Timms and M. A. Pearce (2020). "The Variation and Visualisation of Elastic Anisotropy in Rock-Forming Minerals". In: *Solid Earth* 11.2, pp. 259–286. DOI: 10.5194/se-11-259-2020.

Hirose, A. and K. E. Lonngren (2010). *Fundamentals of Wave Phenomena*. SCITECH PUB. 384 pp. ISBN: 9781891121920.

Ho, S.-P. and Y.-L. Yeh (2006). “The Use of Enriched Hexahedral elemens With Bubble Functions for Finite Element Analysis”. In: *Transactions of the Canadian Society for Mechanical Engineering* 30.4, pp. 495–509. doi: 10.1139/TCSME-2006-0032.

Hodge, M. D., R. Vetury, S. R. Gibb, M. Winters, P. Patel, M. A. McLain, Y. Shen, D. H. Kim, J. Jech, K. Fallon, R. Houlden, D. M. Aichele and J. B. Shealy (2017). “High Rejection UNII 5.2GHz Wideband Bulk Acoustic Wave Filters Using Undoped Single Crystal AlN-on-SiC Resonators”. In: *IEEE International Electron Devices Meeting*, pp. 25.6.1–25.6.4. isbn: 9781538635599. doi: 10.1109/iedm.2017.8268460.

Hong, C.-H., H.-P. Kim, B.-Y. Choi, H.-S. Han, J. S. Son, C. W. Ahn and W. Jo (2016). “Lead-Free Piezoceramics - Where to Move On?” In: *Journal of Materiomics* 2.1, pp. 1–24. doi: 10.1016/j.jmat.2015.12.002.

Hopcroft, M. A., W. D. Nix and T. W. Kenny (2010). “What is the Young’s Modulus of Silicon?” In: *Journal of Microelectromechanical Systems* 19.2, pp. 229–238. doi: 10.1109/jmems.2009.2039697.

Hsu, J.-C. and F.-S. Lin (2018). “Measurement of Locally Resonant Band Gaps in a Surface Phononic Crystal with Inverted Conical Pillars”. In: *Japanese Journal of Applied Physics* 57.7S1, 07LB01. issn: 13474065. doi: 10.7567/jjap.57.07lb01.

Huang, C., R. Li and L. Chen (2014). “Anisotropic Elasticity and Abnormal Poisson’s Ratios in Super-Hard Materials”. In: *AIP Advances* 4.12, p. 127116. doi: 10.1063/1.4904100.

Huang, J.-Q., F. Li, M. Zhao and K. Wang (2015). “A Surface Micromachined CMOS MEMS Humidity Sensor”. In: *Micromachines* 6.10, pp. 1569–1576. doi: 10.3390/mi6101440.

Hudeczek, R. and P. Baumgartner (2020). “Polarization Independent Band Gaps in CMOS Back-End-of-Line for Monolithic High-Q MEMS Resonator Confinement”. In: *IEEE Transactions on Electron Devices* 67.11, pp. 4578–4581. doi: 10.1109/ted.2020.3025521.

Hudeczek, R. and P. Baumgartner (2021). “Mechanical Band Gap Formation in Anisotropic CMOS Back-End-of-Line Stacks for Monolithic High-Q MEMS Resonator Confinement”. In: *IEEE 51st European Solid-State Device Research Conference (ESSDERC)*. doi: 10.1109/essderc53440.2021.9631769.

Hudeczek, R., P. Baumgartner, R. Geiger and P. Riess (2021). “Resonant Fin Transistor (RFT)”. US11,201,151 and EP 3 886 320 A1.

Hudeczek, R., E. Hager, P. Baumgartner and H. Pretl (2022). “Performance Analysis of Resonant-Fin Transistors and Their Application in RF-Circuit Design”. In: *IEEE Access* 10, pp. 64388–64407. doi: 10.1109/access.2022.3182695.

Hui, Y., Z. Qian and M. Rinaldi (2013). “A 2.8 GHz Combined Mode of Vibration Aluminum Nitride MEMS Resonator with High Figure of Merit Exceeding 45”. In: *IEEE International Frequency Control Symposium and European Frequency and Time Forum*, pp. 930–932. isbn: 9781479903429. doi: 10.1109/eftf-ifc.2013.6702272.

Huynh, A., M. Karlsson and S. Gong (2010). *Advanced Microwave Circuits and Systems*. Ed. by V. Zhurbenko. InTech. doi: 10.5772/183.

Hwang, J.-K., S.-B. Hyun, H.-Y. Ryu and Y.-H. Lee (1998). “Resonant Modes of Two-Dimensional Photonic Bandgap Cavities Determined by the Finite-Element Method and by Use of the Anisotropic Perfectly Matched Layer Boundary Condition”. In: *Journal of the Optical Society of America B* 15.8, p. 2316. doi: 10.1364/josab.15.002316.

Im, K.-S., H.-S. Kang, J.-H. Lee, S.-J. Chang, S. Cristoloveanu, M. Bawedin and J.-H. Lee (2014). “Characteristics of GaN and AlGaN/GaN FinFETs”. In: *Solid-State Electronics* 97, pp. 66–75. doi: 10.1016/j.sse.2014.04.033.

Inomata, N., Y. Tonsho and T. Ono (2022). “Quality Factor Control of Mechanical Resonators Using Variable Phononic Bandgap on Periodic Microstructures”. In: *Scientific Reports* 12.1. DOI: 10.1038/s41598-021-04459-2.

Ionescu, A. M. (2010). “Resonant Body Transistors”. In: *IEEE 68th Device Research Conference*. June 2007, pp. 181–182. ISBN: 9781424478705. DOI: 10.1109/drc.2010.5551901.

Iqbal, F. and B. Lee (2018). “A Study on Measurement Variations in Resonant Characteristics of Electrostatically Actuated MEMS Resonators”. In: *Micromachines* 9.4, p. 173. ISSN: 2072666X. DOI: 10.3390/mi9040173.

ITRS (2021). *International Technology Roadmap for Semiconductors*. Semiconductor Industry Association. URL: https://www.semiconductors.org/resources/2009-international-technology-roadmap-for-semiconductors-itrs/.

Jaeger, R. C., S. Hussain, J. C. Suhling, P. Gnanachchelvi, B. M. Wilamowski and M. C. Hamilton (2013). “Impact of Mechanical Stress on Bipolar Transistor Current Gain and Early Voltage”. In: *IEEE Sensors*, pp. 31–34. ISBN: 9781467346405. DOI: 10.1109/icsens.2013.6688466.

Jaeger, R. C., J. C. Suhling, R. Ramani, A. Bradley and J. Xu (2000). “CMOS Stress Sensors on [100] Silicon”. In: *IEEE Journal of Solid-State Circuits* 35.1, pp. 85–95. DOI: 10.1109/4.818923.

Jaeken, J. W. and S. Cottenier (2016). “Solving the Christoffel Equation: Phase and Group Velocities”. In: *Computer Physics Communications* 207, pp. 445–451. DOI: 10.1016/j.cpc.2016.06.014.

Jaffe, H. and P. L. Smith (1957). “IRE Standards on Piezoelectric Crystals—the Piezoelectric Vibrator: Definitions and Methods of Measurement, 1957”. In: *Proc. IRE* 45.3, pp. 353–358. ISSN: 00968390. DOI: 10.1109/JRPROC.1957.278371.

Jiang, T., C. Li and Q. Han (2019). “Surface Acoustic Waves in 2D-Phononic Crystal of Laminated Pillars on a Semi-Infinite ZnO Substrate”. In: *Physics Letters A* 383.33, p. 125956. ISSN: 03759601. DOI: 10.1016/j.physleta.2019.125956.

Jiménez, N., J.-P. Groby and V. Romero-Garcıa (2021). “The Transfer Matrix Method in Acoustics”. In: *Topics in Applied Physics*. Ed. by N. Jiménez, O. Umnova and J.-P. Groby. Cham: Springer International Publishing, pp. 103–164. ISBN: 978-3-030-84300-7. DOI: 10.1007/978-3-030-84300-7_4.

Joannopoulos, J. J. D., S. Johnson, J. N. J. Winn and R. R. D. Meade (2008). *Photonic Crystals: Molding the Flow of Light*. Vol. 82. 26. AIP Publishing, p. 286. ISBN: 9780691124568. DOI: 10.1063/1.1586781.

Joshi, R., N. Bhatt, B. Thakore, P. Vyas and A. Jani (2018). “Grüneisen Parameter and Equations of States for Copper – High Pressure Study”. In: *Computational Condensed Matter* 15, pp. 79–84. DOI: 10.1016/j.cocom.2017.11.003.

Jurczak, M., N. Collaert, A. Veloso, T. Hoffmann and S. Biesemans (2009). “Review of FINFET Technology”. In: *IEEE International SOI Conference*, pp. 1–4. DOI: 10.1109/soi.2009.5318794.

Kanda, Y. (1982). “A Graphical Representation of the Piezoresistance Coefficients in Silicon”. In: *IEEE Transactions on Electron Devices* 29.1, pp. 64–70. DOI: 10.1109/t-ed.1982.20659.

Kanda, Y. and K. Matsuda (2007). “Shear Piezoresistance Coefficient Pi44 of N-Type Silicon”. In: *TechConnect Briefs* 3, pp. 153–156. ISSN: 1-4200-6184-4.

Kanda, Y. (1991). “Piezoresistance Effect of Silicon”. In: *Sensors and Actuators A: Physical* 28.2, pp. 83–91. DOI: 10.1016/0924-4247(91)85017-i.

Kaselow, A. (2004). “The Stress Sensitivity Approach: Theory and Application”. PhD thesis. Geowissenschaften. DOI: 10.17169/REFUBIUM-14552.

Kavalieros, J., B. Doyle, S. Datta, G. Dewey, M. Doczy, B. Jin, D. Lionberger, M. Metz, W. Rachmady, M. Radosavljevic, U. Shah, N. Zelick and R. Chau (2006). “Tri-Gate Transistor Architecture with High-k Gate Dielectrics, Metal Gates and Strain Engineering”. In: *IEEE Symposium on VLSI Technology*. DOI: 10.1109/vlsit.2006.1705211.

Khelif, A., Y. Achaoui, S. Benchabane, V. Laude and B. Aoubiza (2010). “Locally Resonant Surface Acoustic Wave Band Gaps in a Two-Dimensional Phononic Crystal of Pillars on a Surface”. In: *Physical Review B* 81.21, p. 214303. ISSN: 10980121. DOI: 10.1103/physrevb.81.214303.

Khelif, A. and A. Adibi (2016). *Phononic Crystals*. Ed. by A. Khelif and A. Adibi. Springer New York, pp. 1–245. ISBN: 9781461493938. DOI: 10.1007/978-1-4614-9393-8.

Kim, B., M. A. Hopcroft, R. N. Candler, C. M. Jha, M. Agarwal, R. Melamud, S. A. Chandorkar, G. Yama and T. W. Kenny (2008). “Temperature Dependence of Quality Factor in MEMS Resonators”. In: *Journal of Microelectromechanical Systems* 17.3, pp. 755–766. ISSN: 10577157. DOI: 10.1109/jmems.2008.924253.

Kim, J., D.-i. Cho and R. S. Muller (2001). “Why Is (111) Silicon a Better Mechanical Material for MEMS?” In: *Transducers - Eurosensors XV*. Springer Berlin Heidelberg, pp. 662–665. DOI: 10.1007/978-3-642-59497-7_157.

Knapp, M., R. Hoffmann, V. Lebedev, V. Cimalla and O. Ambacher (2018). “Graphene As an Active Virtually Massless Top Electrode for RF Solidly Mounted Bulk Acoustic Wave (SMR-BAW) Resonators”. In: *Nanotechnology* 29.10, p. 105302. ISSN: 13616528. DOI: 10.1088/1361-6528/aaa6bc.

Knowles, K. M. and P. R. Howie (2014). “The Directional Dependence of Elastic Stiffness and Compliance Shear Coefficients and Shear Moduli in Cubic Materials”. In: *Journal of Elasticity* 120.1, pp. 87–108. ISSN: 15732681. DOI: 10.1007/s10659-014-9506-1.

Kolding, T., O. Jensen and T. Larsen (2000). “Ground-Shielded Measuring Technique for Accurate On-Wafer Characterization of RF CMOS Devices”. In: *International Conference on Microelectronic Test Structures*. DOI: 10.1109/icmts.2000.844439.

Koolen, M., J. Geelen and M. Versleijen (1991). “An Improved De-Embedding Technique for On-Wafer High-Frequency Characterization”. In: *IEEE Bipolar Circuits and Technology Meeting*, pp. 188–191. ISBN: 0-7803-0103-X. DOI: 10.1109/bipol.1991.160985.

Kourani, A., R. Lu, A. Gao and S. Gong (2019). “A 300-500 MHz Tunable Oscillator Exploiting Ten Overtones in Single Lithium Niobate Resonator”. In: *IEEE International Frequency Control Symposium and European Frequency and Time Forum*. Vol. 1. ISBN: 9781538683057. DOI: 10.1109/fcs.2019.8856145.

Krishnaswamy, S. V., J. D. Adam and M. Aumer (2006). “P1J-4 High-Q FBARs Using Epitaxial AlN Films”. In: *IEEE Ultrasonics Symposium*. Vol. 1, pp. 1467–1470. ISBN: 1424402018. DOI: 10.1109/ultsym.2006.369.

Ku, W., T. Berlijn and C.-C. Lee (2010). “Unfolding First-Principles Band Structures”. In: *Physical Review Letters* 104.21, p. 216401. DOI: 10.1103/physrevlett.104.216401.

Lacaita, A. L., S. Levantino and C. Samori (2007). *Integrated Frequency Synthesizers for Wireless Systems*. Cambridge University Press. ISBN: 9780511541131. DOI: 10.1017/cbo9780511541131.

Lakin, K. (1981). “Equivalent Circuit Modeling of Stacked Crystal Filters”. In: *IEEE 35th Annual Frequency Control Symposium*, pp. 257–262. DOI: 10.1109/freq.1981.200482.

Lambade, S. D., G. G. Sahasrabudhe and S. Rajagopalan (1995). “Temperature Dependence of Acoustic Attenuation in Silicon”. In: *Physical Review B* 51.22, pp. 15861–15866. DOI: 10.1103/physrevb.51.15861.

Larson, M. G. and F. Bengzon (2013). *The Finite Element Method: Theory, Implementation, and Applications*. Springer Berlin Heidelberg. 416 pp. ISBN: 978-3-642-33286-9. DOI: 10.1007/978-3-642-33287-6.

Laude, V., Y. Achaoui, S. Benchabane and A. Khelif (2009). "Evanescent Bloch Waves and the Complex Band Structure of Phononic Crystals". In: *Physical Review B* 80.9, p. 092301. ISSN: 10980121. DOI: 10.1103/physrevb.80.092301.

Lee, J. W., D. Jang, M. Mouis, G. T. Kim, T. Chiarella, T. Hoffmann and G. Ghibaudo (2011). "Mobility Analysis of Surface Roughness Scattering in FinFET Devices". In: *Solid-State Electronics* 62.1, pp. 195–201. DOI: 10.1016/j.sse.2011.04.020.

Lee, K., I. Nam, I. Kwon, J. Gil, K. Han, S. Park and B.-I. Seo (2005). "The Impact of Semiconductor Technology Scaling on CMOS RF and Digital Circuits for Wireless Application". In: *IEEE Transactions on Electron Devices* 52.7, pp. 1415–1422. DOI: 10.1109/ted.2005.850632.

Lesieutre, G. (2001). "Damping in FE Models". In: *Encyclopedia of Vibration*. Elsevier, pp. 321–327. DOI: 10.1006/rwvb.2001.0021.

Li, J., Z.-y. Fei, Y.-f. Xu, J. Wang, B.-f. Fan, X.-j. Ma and G. Wang (2018). "Study on the Optimization of the Deposition Rate of Planetary GaN-MOCVD Films Based on CFD Simulation and the Corresponding Surface Model". In: *Royal Society Open Science* 5.2, p. 171757. DOI: 10.1098/rsos.171757.

Lifshitz, R. and M. L. Roukes (2000). "Thermoelastic Damping in Micro- and Nanomechanical Systems". In: *Physical Review B* 61.8, pp. 5600–5609. DOI: 10.1103/physrevb.61.5600.

Liow, T.-Y., K.-M. Tan, R. T. P. Lee, M. Zhu, K.-M. Hoe, G. S. Samudra, N. Balasubramanian and Y.-C. Yeo (2007). "Strain Enhancement in Spacerless N-Channel FinFETs with Silicon-Carbon Source and Drain Stressors". In: *IEEE 37th European Solid State Device Research Conference*. DOI: 10.1109/essderc.2007.4430901.

Liu, G. R. (2003). *The Finite Element Method : A Practical Course*. Oxford Boston: Butterworth-Heinemann. ISBN: 0750658665.

Liu, S. E., J. S. Wang, Y. R. Lu, D. S. Huang, C. F. Huang, W. H. Hsieh, J. H. Lee, Y. S. Tsai, J. R. Shih, Y.-H. Lee and K. Wu (2014). "Self-Heating Effect in FinFETs and Its Impact on Devices Reliability Characterization". In: *IEEE International Reliability Physics Symposium*. DOI: 10.1109/irps.2014.6860642.

Liu, T.-W., Y.-C. Tsai, Y.-C. Lin, T. Ono, S. Tanaka and T.-T. Wu (2014). "Design and Fabrication of a Phononic-Crystal-Based Love Wave Resonator in GHz Range". In: *AIP Advances* 4.12, p. 124201. ISSN: 21583226. DOI: 10.1063/1.4902018.

Liu, Y., Y. Cai, Y. Zhang, A. Tovstopyat, S. Liu and C. Sun (2020). "Materials, Design, and Characteristics of Bulk Acoustic Wave Resonator: A Review". In: *Micromachines* 11.7, p. 630. ISSN: 2072666X. DOI: 10.3390/mi11070630.

Loebl, H., C. Metzmacher, R. Milsom, P. Lok, F. van Straten and A. Tuinhout (2004). "RF Bulk Acoustic Wave Resonators and Filters". In: *Journal of Electroceramics* 12.1/2, pp. 109–118. ISSN: 13853449. DOI: 10.1023/b:jecr.0000034005.21609.91.

Lopez, J. L., J. Verd, J. Giner, A. Uranga, G. Murillo, E. Marigo, F. Torres, G. Abadal and N. Barniol (2009). "High Q CMOS-MEMS Resonators and Its Applications As RF Tunable Band-Pass Filters". In: *Transducers - International Solid-State Sensors, Actuators and Microsystems Conference*. DOI: 10.1109/sensor.2009.5285385.

Loubet, N., T. Hook, P. Montanini, C.-W. Yeung, S. Kanakasabapathy, M. Guillom, T. Yamashita, J. Zhang, X. Miao, J. Wang, A. Young, R. Chao, M. Kang, Z. Liu, S. Fan, B. Hamieh, S. Sieg, Y. Mignot, W. Xu, S.-C. Seo, J. Yoo, S. Mochizuki, M. Sankarapandian, O. Kwon, A. Carr, A. Greene, Y. Park, J. Frougier, R. Galatage, R. Bao, J. Shearer, R. Conti, H. Song, D. Lee,

D. Kong, Y. Xu, A. Arceo, Z. Bi, P. Xu, R. Muthinti, J. Li, R. Wong, D. Brown, P. Oldiges, R. Robison, J. Arnold, N. Felix, S. Skordas, J. Gaudiello, T. Standaert, H. Jagannathan, D. Corliss, M.-H. Na, A. Knorr, T. Wu, D. Gupta, S. Lian, R. Divakaruni, T. Gow, C. Labelle, S. Lee, V. Paruchuri, H. Bu and M. Khare (2017). “Stacked Nanosheet Gate-All-Around Transistor to Enable Scaling beyond FinFET”. In: *IEEE Symposium on VLSI Technology*. Vol. 5. 1, pp. 14–15. ISBN: 9784863486058. DOI: 10.23919/vlsit.2017.7998183.

Lu, J.-Q. (2009). “3D Hyperintegration and Packaging Technologies for Micro-Nano Systems”. In: *IEEE* 97.1, pp. 18–30. DOI: 10.1109/jproc.2008.2007458.

Lu, R., T. Manzaneque, Y. Yang and S. Gong (2018). “Lithium Niobate Phononic Crystals for Tailoring Performance of RF Laterally Vibrating Devices”. In: *IEEE Transactions on Ultrasonics, Ferroelectrics, and Frequency Control* 65.6, pp. 934–944. ISSN: 08853010. DOI: 10.1109/tuffc.2018.2804861.

Lu, Y. and A. Srivastava (2018). “Level Repulsion and Band Sorting in Phononic Crystals”. In: *Journal of the Mechanics and Physics of Solids* 111.November, pp. 100–112. ISSN: 00225096. DOI: 10.1016/j.jmps.2017.10.021. eprint: 1706.03857.

Luan, X., H. Qin, F. Liu, Z. Dai, Y. Yi and Q. Li (2018). “The Mechanical Properties and Elastic Anisotropies of Cubic Ni3Al from First Principles Calculations”. In: *Crystals* 8.8, p. 307. ISSN: 20734352. DOI: 10.3390/cryst8080307.

Lucklum, R., J. Li and M. Zubtsov (2010). “1D and 2D Phononic Crystal Sensors”. In: *Procedia Engineering* 5, pp. 436–439. DOI: 10.1016/j.proeng.2010.09.140.

Ma, J. L., Z. F. Fu, Q. Wei and H. M. Zhang (2013). “Uniaxial Stress Induced Electron Mobility Enhancement in Silicon”. In: *Silicon* 5.3, pp. 219–224. ISSN: 1876990X. DOI: 10.1007/s12633-013-9144-4.

Ma, J.-L., H.-M. Zhang, X.-Y. Wang, Q. Wei, G.-Y. Wang and X.-B. Xu (2011). “Valence Band Structure and Hole Effective Mass of Uniaxial Stressed Germanium”. In: *Journal of Computational Electronics* 10.4, pp. 388–393. DOI: 10.1007/s10825-011-0374-7.

Mainprice, D. and M. Casey (1990). “The Calculated Seismic Properties of Quartz Mylonites with Typical Fabrics: Relationship to Kinematics and Temperature”. In: *Geophysical Journal International* 103.3, pp. 599–608. DOI: 10.1111/j.1365-246x.1990.tb05674.x.

Mainprice, D. and M. Humbert (1994). “Methods of Calculating Petrophysical Properties from Lattice Preferred Orientation Data”. In: *Surveys in Geophysics* 15.5, pp. 575–592. DOI: 10.1007/bf00690175.

Man, C.-S. and M. Huang (2011). “A Simple Explicit Formula for the Voigt-Reuss-Hill Average of Elastic Polycrystals with Arbitrary Crystal and Texture Symmetries”. In: *Journal of Elasticity* 105.1-2, pp. 29–48. DOI: 10.1007/s10659-011-9312-y.

Manku, T. and A. Nathan (1993). “Electrical Properties of Silicon under Nonuniform Stress”. In: *Journal of Applied Physics* 74.3, pp. 1832–1837. DOI: 10.1063/1.354790.

Marfurt, K. J. (1984). “Accuracy of Finite-Difference and Finite-Element Modeling of the Scalar and Elastic Wave Equations”. In: *Geophysics* 49.5, pp. 533–549. DOI: 10.1190/1.1441689.

Martınez-Argüello, A. M., M. Martınez-Mares, M. Cobián-Suárez, G. Báez and R. A. Méndez-Sánchez (2015). “A New Fano Resonance in Measurement Processes”. In: *Europhysics Letters* 110.5, p. 54003. ISSN: 12864854. DOI: 10.1209/0295-5075/110/54003.

Masetti, G., M. Severi and S. Solmi (1983). “Modeling of Carrier Mobility against Carrier Concentration in Arsenic-, Phosphorus-, and Boron-Doped Silicon”. In: *IEEE Transactions on Electron Devices* 30.7, pp. 764–769. DOI: 10.1109/t-ed.1983.21207.

McGahay, V. (2010). “Porous Dielectrics in Microelectronic Wiring Applications”. In: *Materials* 3.1, pp. 536–562. DOI: 10.3390/ma3010536.

Meindl, J. D., J. A. Davis, P. Zarkesh-Ha, C. Patel, K. P. Martin and P. A. Kohl (2003). "Interconnect Opportunities for Gigascale Integration (GSI)". In: *Interconnect Technology and Design for Gigascale Integration*. Vol. 46. 2.3. Springer US, pp. 1–34. DOI: 10.1007/978-1-4615-0461-0_1.

Mendiratta, N. and S. L. Tripathi (2020). "A Review on Performance Comparison of Advanced MOSFET Structures below 45 Nm Technology Node". In: *Journal of Semiconductors* 41.6, p. 061401. DOI: 10.1088/1674-4926/41/6/061401.

Mensch, T. and P. Rasolofosaon (1997). "Elastic-Wave Velocities in Anisotropic Media of Arbitrary Symmetry-Generalization of Thomsen's Parameters ϵ, δ and γ". In: *Geophysical Journal International* 128.1, pp. 43–64. DOI: 10.1111/j.1365-246x.1997.tb04070.x.

Mikkelsen, J., O. Jensen and T. Larsen (2004). "Crosstalk Coupling Effects of CMOS Co-Planar Spiral Inductors". In: *IEEE Custom Integrated Circuits Conference*. Cd, pp. 371–374. ISBN: 0-7803-8495-4. DOI: 10.1109/cicc.2004.1358825.

Miller, J. M. L., A. Ansari, D. B. Heinz, Y. Chen, I. B. Flader, D. D. Shin, L. G. Villanueva and T. W. Kenny (2018). "Effective Quality Factor Tuning Mechanisms in Micromechanical Resonators". In: *Applied Physics Reviews* 5.4, p. 041307. DOI: 10.1063/1.5027850.

Mizuno, S. (2019). "Fano Resonances and Bound States in the Continuum in a Simple Phononic System". In: *Applied Physics Express* 12.3, p. 035504. ISSN: 18820786. DOI: 10.7567/1882-0786/ab032f.

Muramatsu, S. and M. Kitamura (1993). "Simple Expressions for Elastic Constants C_{11}, C_{12} and C_{44} and Internal Displacements of Semiconductors". In: *Journal of Applied Physics* 73.9, pp. 4270–4272. ISSN: 00218979. DOI: 10.1063/1.352807.

Muzar, E. and J. A. H. Stotz (2019). "Surface Acoustic Wave Modes in Two-Dimensional Shallow Void Inclusion Phononic Crystals on GaAs". In: *Journal of Applied Physics* 126.2, p. 025104. ISSN: 10897550. DOI: 10.1063/1.5056311.

Nan, L., K. Mouthaan, Y.-Z. Xiong, J. Shi, S. C. Rustagi and B.-L. Ooi (2007). "Impact of Metal Dummy Fills on the Performance of CMOS Inductors". In: *IEEE Conference on Electron Devices and Solid-State Circuits*. DOI: 10.1109/edssc.2007.4450109.

Narayanan, B., R. Kumar and P. Foo (2002). "Properties of Low-k SiCOH Films Prepared by Plasma-Enhanced Chemical Vapor Deposition Using Trimethylsilane". In: *Microelectronics Journal* 33.11, pp. 971–974. DOI: 10.1016/s0026-2692(02)00075-7.

Neihart, N. M., D. J. Allstot, M. Miller and P. Rakers (2008). "Twisted Inductors for Low Coupling Mixed-Signal and RF Applications". In: *IEEE Custom Integrated Circuits Conference*. DOI: 10.1109/cicc.2008.4672150.

Nguyen, C. (2007). "MEMS Technology for Timing and Frequency Control". In: *IEEE Transactions on Ultrasonics, Ferroelectrics and Frequency Control* 54.2, pp. 251–270. DOI: 10.1109/tuffc.2007.240.

Nguyen, C. T. (2005). "Vibrating RF MEMS Overview: Applications to Wireless Communications". In: *SPIE*. Ed. by M.-A. Maher and H. D. Stewart. January 2005, p. 11. DOI: 10.1117/12.608015.

Nitta, S. V., S. Purushothaman, J. G. Ryan, D. C. Edelstein, P. Andricacos, C.-K. Hu, T. M. Shaw, R. Rosenberg and J. R. Lloyd (2003). "Copper BEOL Interconnects for Silicon CMOS Logic Technology". In: *Interconnect Technology and Design for Gigascale Integration*. Springer US, pp. 35–65. DOI: 10.1007/978-1-4615-0461-0_2.

Nye, J. F. (1985). *Physical Properties of Crystals*. Oxford University Press. 352 pp. ISBN: 0198511655.

Oktyabrsky, S. (2022). *Lecture Notes*. URL: https://www.albany.edu/~soktyabr/NNSE508/.

Ostman, K., S. Sipila, I. Uzunov and N. Tchamov (2006). “Novel VCO Architecture Using Series Above-IC FBAR and Parallel LC Resonance”. In: *IEEE Journal of Solid-State Circuits* 41.10, pp. 2248–2256. ISSN: 00189200. DOI: 10.1109/jssc.2006.881567.

Pachkawade, V., M.-H. Li, C.-S. Li and S.-S. Li (2013). “A CMOS-MEMS Resonator Integrated System for Oscillator Application”. In: *IEEE Sensors* 13.8, pp. 2882–2889. DOI: 10.1109/jsen.2013.2259809.

Pallas-Areny, R. and J. Webster (1991). “Common Mode Rejection Ratio in Differential Amplifiers”. In: *IEEE Transactions on Instrumentation and Measurement* 40.4, pp. 669–676. DOI: 10.1109/19.85332.

Pardo, D., M. Paszynski, N. Collier, J. Alvarez, L. Dalcin and V. M. Calo (2012). “A Survey on Direct Solvers for Galerkin Methods”. In: *SeMA Journal* 57.1, pp. 107–134. DOI: 10.1007/bf03322602.

Parvais, B., A. Mercha, N. Collaert, R. Rooyackers, I. Ferain, M. Jurczak, V. Subramanian, A. D. Keersgieter, T. Chiarella, C. Kerner, L. Witters, S. Biesemans and T. Hoffman (2009). “The Device Architecture Dilemma for CMOS Technologies: Opportunities & Challenges of finFET Over Planar MOSFET”. In: *IEEE International Symposium on VLSI Technology, Systems, and Applications*, pp. 80–81. DOI: 10.1109/vtsa.2009.5159300.

Patel, C. and P. McCluskey (2012). “Modeling and Simulation of the MEMS Vibratory Gyroscope”. In: *IEEE 13th Conference on Thermal and Thermomechanical Phenomena in Electronic Systems*. DOI: 10.1109/itherm.2012.6231524.

Patwal, S. (2021). “2DEG Enhancement Via Epilayer Stress Engineering in AlN/GaN/AlN Heterostructure”. PhD thesis. Nanyang Technological University, Singapore. DOI: 10.32657/10356/153068.

Patwal, S., M. Agrawal, K. Radhakrishnan, T. L. A. Seah and N. Dharmarasu (2019). “Enhancement of 2D Electron Gas Mobility in an AlN/GaN/AlN Double-Heterojunction High-Electron-Mobility Transistor by Epilayer Stress Engineering”. In: *Physica Status Solidi (a)* 217.7, p. 1900818. DOI: 10.1002/pssa.201900818.

Pennec, Y., B. Djafari-Rouhani, J. O. Vasseur, A. Khelif and P. A. Deymier (2004). “Tunable Filtering and Demultiplexing in Phononic Crystals with Hollow Cylinders”. In: *Physical Review E* 69.4, p. 046608. DOI: 10.1103/physreve.69.046608.

Pennec, Y. and B. Djafari-Rouhani (2016). *Phononic Crystals*. Ed. by A. Khelif and A. Adibi. Springer New York, pp. 23–50. ISBN: 978-1-4614-9392-1. DOI: 10.1007/978-1-4614-9393-8.

Peroulis, D., P. R. Waghmare, S. K. Mitra, S. Manakasettharn, J. A. Taylor, T. N. Krupenkin, W. Zhu, G. D. Nessim, F. Marano, R. Guadagnini, F. Rodrigues-Lima, J.-M. Dupret, A. Baeza-Squiban, S. Boland, J. Y. Park, S. Oh, M. Madou, Y. K. Yap, B. Aslan, H. D. Han, G. Lopez-Berestein, A. K. Sood, M. S.-C. Lu, H. Qu, H. Xie, H. Xie, Y. Zhou, L. L. Howell, A. T. Conlisk, L. V. Zhigilei, A. N. Volkov, A. M. Dongare, Z. Yin, Y. Fan, S. T. Wong, V. V. R. Nandigana, N. R. Aluru, W. Li, H. Kwok and R. Wannemacher (2012). “CMOS MEMS Fabrication Technologies”. In: *Encyclopedia of Nanotechnology*. Springer Netherlands, pp. 441–449. DOI: 10.1007/978-90-481-9751-4_310.

Piazza, G., P. J. Stephanou and A. P. Pisano (2007). “One and Two Port Piezoelectric Higher Order Contour-Mode MEMS Resonators for Mechanical Signal Processing”. In: *Solid-State Electronics* 51.11-12, pp. 1596–1608. DOI: 10.1016/j.sse.2007.09.037.

Polunin, P., Y. Yang, J. Atalaya, E. Ng, S. Strachan, O. Shoshani, M. Dykman, S. Shaw and T. Kenny (2015). “Characterizing MEMS Nonlinearities Directly: The

Ring-Down Measurements". In: *Transducers - 18th International Conference on Solid-State Sensors, Actuators and Microsystems*. DOI: 10.1109/transducers.2015.7181391.

Popa, L. C. (2015). "Gallium Nitrid MEMS Resonators". PhD. Department of Physics, pp. 1–219.

Ptashnik, S. V., A. K. Mikhailov, A. V. Yastrebov, P. K. Petrov, W. Liu, N. M. Alford, S. Hirsch and A. B. Kozyrev (2017). "Ferroelectric Thin Film Acoustic Devices with Electrical Multiband Switching Ability". In: *Scientific Reports* 7.1. DOI: 10.1038/s41598-017-14895-8.

Qin, Z., Y. Gao, J. Jia, X. Ding, L. Huang and H. Li (2019). "The Effect of the Anisotropy of Single Crystal Silicon on the Frequency Split of Vibrating Ring Gyroscopes". In: *Micromachines* 10.2, p. 126. ISSN: 2072666X. DOI: 10.3390/mi10020126.

Qu, H. (2016). "CMOS MEMS Fabrication Technologies and Devices". In: *Micromachines* 7.1, p. 14. DOI: 10.3390/mi7010014.

Randjelović, D., A. Petropoulos, G. Kaltsas, M. Stojanović, Ž. Lazić, Z. Djurić and M. Matić (2008). "Multipurpose MEMS Thermal Sensor Based on Thermopiles". In: *Sensors and Actuators A: Physical* 141.2, pp. 404–413. DOI: 10.1016/j.sna.2007.10.043.

Rao, S. S. (2010). *The Finite Element Method in Engineering*. Oxford Elsevier: Butterworth-Heinemann. ISBN: 978-1-85617-661-3.

Razafimandimby, S., C. Tilhac, A. Cathelin and A. Kaiser (2013). "Tunable BAW Filters". In: *Integrated Circuits and Systems*. Springer US, pp. 207–231. DOI: 10.1007/978-1-4419-8798-3_8.

Reddy, P. R. and B. C. Mohan (2012). "Design and Analysis of Film Bulk Acoustic Resonator (FBAR) Filter for RF Applications". In: *International Journal of Engineering Business Management* 4.1, p. 28. ISSN: 18479790. DOI: 10.5772/54921.

Reggiani, S., M. Valdinoci, L. Colalongo, M. Rudan, G. Baccarani, A. Stricker, F. Illien, N. Felber, W. Fichtner and L. Zullino (2002). "Electron and Hole Mobility in Silicon at Large Operating Temperatures. I. Bulk Mobility". In: *IEEE Transactions on Electron Devices* 49.3, pp. 490–499. DOI: 10.1109/16.987121.

Reggiani, S., M. Valdinoci, L. Colalongo, M. Rudan and G. Baccarani (2000). "An Analytical, Temperature-Dependent Model for Majority- and Minority-Carrier Mobility in Silicon Devices". In: *VLSI Design* 10.4, pp. 467–483. DOI: 10.1155/2000/52147.

Reichardt, L., C. Sturm, F. Grunhaupt and T. Zwick (2012). "Demonstrating the Use of the IEEE 802.11p Car-to-Car Communication Standard for Automotive Radar". In: *IEEE 6th European Conference on Antennas and Propagation*. DOI: 10.1109/eucap.2012.6206084.

Robertson, J. (2005). "High Dielectric Constant Gate Oxides for Metal Oxide Si Transistors". In: *Reports on Progress in Physics* 69.2, pp. 327–396. ISSN: 00344885. DOI: 10.1088/0034-4885/69/2/r02.

Rochette, F., M. Cassé, M. Mouis, A. Haziot, T. Pioger, G. Ghibaudo and F. Boulanger (2009). "Piezoresistance Effect of Strained and Unstrained Fully-Depleted Silicon-on-Insulator MOSFETs Integrating a HfO2/TiN Gate Stack". In: *Solid-State Electronics* 53.3, pp. 392–396. DOI: 10.1016/j.sse.2009.01.017.

Rodriguez, J., S. A. Chandorkar, C. A. Watson, G. M. Glaze, C. H. Ahn, E. J. Ng, Y. Yang and T. W. Kenny (2019). "Direct Detection of Akhiezer Damping in a Silicon MEMS Resonator". In: *Scientific Reports* 9.1. DOI: 10.1038/s41598-019-38847-6.

Roesler, J. (2007). *Mechanical Behaviour of Engineering Materials*. Springer-Verlag Berlin Heidelberg. ISBN: 9783835100084.

Rose, J. L. (2014). *Ultrasonic Guided Waves in Solid Media*. Vol. 9781107048. Cambridge University Press, pp. 1–512. ISBN: 9781107273610. DOI: 10.1017/cbo9781107273610.

Rosenbaum, J. (1988). *Bulk Acoustic Wave Theory and Devices*. Artech House Inc. ISBN: 089006265X.

Ruby, R. (2007). "Review and Comparison of Bulk Acoustic Wave FBAR, SMR Technology". In: *IEEE Ultrasonics Symposium*. DOI: 10.1109/ultsym.2007.262.

Rumiantsev, A. (2014). "OnWafer Calibration Techniques Enabling Accurate Characterization of High-Performance Silicon Devices at the mm-Wave Range and Beyond". PhD thesis. Maschinenbau, Elektrotechnik und Wirtschaftsingenieurwesen.

Saitoh, M., A. Kaneko, K. Okano, T. Kinoshita, S. Inaba, Y. Toyoshima and K. Uchida (2008). "Three-Dimensional Stress Engineering in FinFETs for Mobility/On-Current Enhancement and Gate Current Reduction". In: *IEEE Symposium on VLSI Technology*. DOI: 10.1109/vlsit.2008.4588547.

Samsung (2021). *Technology Offerings*. URL: https://www.samsungfoundry.com/foundry/homepage/anonymous/technology300nm.do?_mainLayOut=homepageLayout&menuIndex=02.

Sanditov, D. S. and M. V. Darmaev (2022). "Elastic Moduli and the Grüneisen Parameter of Glass-Like Solids". In: *Glass Physics and Chemistry* 48.1, pp. 18–22. DOI: 10.1134/s1087659622010114.

Schwalke, U. (2000). "Challenges and Recent Developments in Device Isolation Technology". In: *30th European Solid-State Device Research Conference*. DOI: 10.1109/essderc.2000.194716.

Serrano, D. E. (2013). "Design and Analysis of MEMS Gyroscopes". In: *IEEE Sensors*. ISBN: 9781467346429. URL: http://ieee-sensors2013.org/sites/ieee-sensors2013.org/files/Serrano_Slides_Gyros2.pdf.

Setiono, A., J. Xu, M. Fahrbach, M. Bertke, W. Nyang'au, H. Wasisto and E. Peiner (2019). "Real-Time Frequency Tracking of an Electro-Thermal Piezoresistive Cantilever Resonator with ZnO Nanorods for Chemical Sensing". In: *Chemosensors* 7.1, p. 2. DOI: 10.3390/chemosensors7010002.

Setyawan, W. and S. Curtarolo (2010). "High-Throughput Electronic Band Structure Calculations: Challenges and Tools". In: *Computational Materials Science* 49.2, pp. 299–312. ISSN: 09270256. DOI: 10.1016/j.commatsci.2010.05.010. eprint: 1004.2974.

Shao, L., S. Maity, L. Zheng, L. Wu, A. Shams-Ansari, Y.-I. Sohn, E. Puma, M. Gadalla, M. Zhang, C. Wang, E. Hu, K. Lai and M. Lončar (2019). "Phononic Band Structure Engineering for High-Q Gigahertz Surface Acoustic Wave Resonators on Lithium Niobate". In: *Physical Review Applied* 12.1, p. 014022. DOI: 10.1103/physrevapplied.12.014022. eprint: 1901.09080.

Shi, L., W. Xuan, B. Zhang, S. Dong, H. Jin and J. Luo (2021). "Numerical Investigation of Phononic Crystal Based Film Bulk Acoustic Wave Resonators". In: *Nanomaterials* 11.10, p. 2547. DOI: 10.3390/nano11102547.

Shrikanth, S., K. M. Knowles, S. Neelakantan and R. Prasad (2020). "Planes of Isotropic Poisson's Ratio in Anisotropic Crystalline Solids". In: *International Journal of Solids and Structures* 191-192, pp. 628–645. DOI: 10.1016/j.ijsolstr.2019.10.014.

Sieberer, S., S. McWilliam and A. A. Popov (2019). "Nonlinear Electrostatic Effects in MEMS Ring-Based Rate Sensors under Shock Excitation". In: *International Journal of Mechanical Sciences* 157-158.October 2018, pp. 485–497. ISSN: 00207403. DOI: 10.1016/j.ijmecsci.2019.04.028.

Sjövall, P. and T. Abrahamsson (2008). "Substructure System Identification from Coupled System Test Data". In: *Mechanical Systems and Signal Processing* 22.1, pp. 15–33. DOI: 10.1016/j.ymssp.2007.06.003.

Smith, C. S. (1954). “Piezoresistance Effect in Germanium and Silicon”. In: *Physical Review* 94.1, pp. 42–49. ISSN: 0031899X. DOI: 10.1103/physrev.94.42.

Soares, D. and W. Mansur (2005). “A Frequency-Domain FEM Approach Based on Implicit Green’s Functions for Non-Linear Dynamic Analysis”. In: *International Journal of Solids and Structures* 42.23, pp. 6003–6014. DOI: 10.1016/j.ijsolstr.2005.05.047.

Sotto, M., I. Tomita, K. Debnath and S. Saito (2018). “Polarization Rotation and Mode Splitting in Photonic Crystal Line-Defect Waveguides”. In: *Frontiers in Physics* 6.AUG. ISSN: 2296424X. DOI: 10.3389/fphy.2018.00085.

Srivastava, A., B. Chatterjee, U. Rawat, Y. He, D. Weinstein and S. Sen (2021). “Analysis and Design Considerations for Achieving the Fundamental Limits of Phase Noise in mmWave Oscillators with On-Chip MEMS Resonator”. In: *IEEE Transactions on Circuits and Systems II: Express Briefs* 68.4, pp. 1108–1112. DOI: 10.1109/tcsii.2020.3030074.

Stillmaker, A. and B. Baas (2017). “Scaling Equations for the Accurate Prediction of CMOS Device Performance from 180 Nm to 7 Nm”. In: *Integration* 58, pp. 74–81. DOI: 10.1016/j.vlsi.2017.02.002.

Stoffels, S., E. Autizi, R. V. Hoof, S. Severi, R. Puers, A. Witvrouw and H. A. C. Tilmans (2010). “Physical Loss Mechanisms for Resonant Acoustical Waves in Boron Doped Poly-SiGe Deposited with Hydrogen Dilution”. In: *Journal of Applied Physics* 108.8, p. 084517. DOI: 10.1063/1.3499319.

Su, J., E. Armour, S. M. Lee, R. Arif and G. D. Papasouliotis (2016). “Uniform Growth of III-Nitrides on 200 mm Silicon Substrates Using a Single Wafer Rotating Disk MOCVD Reactor”. In: *Physica Status Solidi (a)* 213.4, pp. 856–860. DOI: 10.1002/pssa.201532708.

Su, Z. and L. Ye (2009). *Identification of Damage Using Lamb Waves*. Vol. 48. Springer London. ISBN: 9781848827837. DOI: 10.1007/978-1-84882-784-4.

Subramanian, V., B. Parvais, J. Borremans, A. Mercha, D. Linten, P. Wambacq, J. Loo, M. Dehan, C. Gustin, N. Collaert, S. Kubicek, R. Lander, J. Hooker, F. Cubaynes, S. Donnay, M. Jurczak, G. Groeseneken, W. Sansen and S. Decoutere (2006). “Planar Bulk MOSFETs Versus FinFETs: An Analog/RF Perspective”. In: *IEEE Transactions on Electron Devices* 53.12, pp. 3071–3079. DOI: 10.1109/ted.2006.885649.

Sun, G., Y. Sun, T. Nishida and S. E. Thompson (2007). “Hole Mobility in Silicon Inversion Layers: Stress and Surface Orientation”. In: *Journal of Applied Physics* 102.8, p. 084501. DOI: 10.1063/1.2795649.

Sun, Y., S. E. Thompson and T. Nishida (2007). “Physics of Strain Effects in Semiconductors and Metal-Oxide-Semiconductor Field-Effect Transistors”. In: *Journal of Applied Physics* 101.10, p. 104503. DOI: 10.1063/1.2730561.

Sviličić, B., E. Mastropaolo, R. Zhang and R. Cheung (2015). “Tunable MEMS Cantilever Resonators Electrothermally Actuated and Piezoelectrically Sensed”. In: *Microelectronic Engineering* 145, pp. 38–42. ISSN: 01679317. DOI: 10.1016/j.mee.2015.02.049.

Svitek, T., V. Vavryčuk, T. Lokajıček and M. Petružálek (2014). “Determination of Elastic Anisotropy of Rocks from P- and S-Wave Velocities: Numerical Modelling and Lab Measurements”. In: *Geophysical Journal International* 199.3, pp. 1682–1697. DOI: 10.1093/gji/ggu332.

Sze, S. M. (2014). *Physics of Semiconductor Devices*. Ed. by V. K. Jain and A. Verma. Springer International Publishing. ISBN: 978-3-319-03001-2. DOI: 10.1007/978-3-319-03002-9. eprint: 9809069v1.

Tabrizian, R., M. Rais-Zadeh and F. Ayazi (2009). “Effect of Phonon Interactions on Limiting the F.q Product of Micromechanical Resonators”. In: *Transducers - International Solid-State Sensors, Actuators and Microsystems Conference*. DOI: 10.1109/sensor.2009.5285627.

Tang, S., L. Chang, N. Lindert, Y.-K. Choi, W.-C. Lee, X. Huang, V. Subramanian, J. Bokor, T.-J. King and C. Hu (2001). “FinFET-A Quasi-Planar Double-Gate MOSFET”. In: *IEEE International Solid-State Circuits Conference*, pp. 118–119. DOI: 10.1109/isscc.2001.912568.

Telichko, A., B. Sorokin and G. Kvashnin (2015). “UHF Acoustic Attenuation and Quality Parameter Limits in the Diamond Based HBAR”. In: *IEEE International Frequency Control Symposium and European Frequency and Time Forum*. DOI: 10.1109/fcs.2015.7138799.

Thomas, T. Y. (1966). “On The Stress-Strain Relations For Cubic Crystals”. In: *National Academy of Sciences* 55.2, pp. 235–239. ISSN: 00278424. DOI: 10.1073/pnas.55.2.235.

Thompson, S., M. Armstrong, C. Auth, M. Alavi, M. Buehler, R. Chau, S. Cea, T. Ghani, G. Glass, T. Hoffman, C.-H. Jan, C. Kenyon, J. Klaus, K. Kuhn, Z. Ma, B. Mcintyre, K. Mistry, A. Murthy, B. Obradovic, R. Nagisetty, P. Nguyen, S. Sivakumar, R. Shaheed, L. Shifren, B. Tufts, S. Tyagi, M. Bohr and Y. El-Mansy (2004). “A 90-nm Logic Technology Featuring Strained-Silicon”. In: *IEEE Transactions on Electron Devices* 51.11, pp. 1790–1797. DOI: 10.1109/ted.2004.836648.

Ting, T. C. T. (2006a). “Longitudinal and Transverse Waves in Anisotropic Elastic Materials”. In: *Acta Mechanica* 185.3-4, pp. 147–164. DOI: 10.1007/s00707-006-0333-8.

Ting, T. C. T. (2006b). “On Anisotropic Elastic Materials for Which Young’s Modulus E(n) Is Independent of N or the Shear Modulus G(n,m) Is Independent of N and M”. In: *Journal of Elasticity* 81.3, pp. 271–292. ISSN: 03743535. DOI: 10.1007/s10659-005-9016-2.

Ting, T. C. T. and T. Chen (2005). “Poisson’s Ratio for Anisotropic Elastic Materials Can Have No Bounds”. In: *The Quarterly Journal of Mechanics and Applied Mathematics* 58.1, pp. 73–82. ISSN: 00335614. DOI: 10.1093/qjmamj/hbh021.

Tomar, M., V. Gupta and K. Sreenivas (2003). “Temperature Coefficient of Elastic Constants of SiO_2 Over-Layer on $LiNbO_3$ for a Temperature Stable SAW Device”. In: *Journal of Physics D: Applied Physics* 36.15, pp. 1773–1777. ISSN: 00223727. DOI: 10.1088/0022-3727/36/15/304.

TSMC (2021). *Logic Technology TSMC*. URL: https://www.tsmc.com/english/dedicatedFoundry/technology/logic/l_5nm.

Tsuchiya, A. and H. Onodera (2009). “Effect of Dummy Fills on Characteristics of Passive Devices in CMOS Millimeter-Wave Circuits”. In: *IEEE 8th International Conference on ASIC*. DOI: 10.1109/asicon.2009.5351449.

Turley, J. and G. Sines (1971). “The Anisotropy of Young’s Modulus, Shear Modulus and Poisson’s Ratio in Cubic Materials”. In: *Journal of Physics D: Applied Physics* 4.2, pp. 264–271. DOI: 10.1088/0022-3727/4/2/312.

Ungersböck, S.-E. (2007). “Advanced Modeling of Strained Cmos Technology”. en. PhD thesis. Institut für Mikroelektronik. DOI: 10.34726/HSS.2007.8326.

Ungersboeck, E., V. Sverdlov, H. Kosina and S. Selberherr (2006). “Strain Engineering for CMOS Devices”. In: *8th International Conference on Solid-State and Integrated Circuit Technology*. DOI: 10.1109/icsict.2006.306094.

Valle, J., D. Fernandez, O. Gibrat and J. Madrenas (2021). “Manufacturing Issues of BEOL CMOS-MEMS Devices”. In: *IEEE Access* 9, pp. 83149–83162. DOI: 10.1109/access.2021.3086867.

Vannucci, P. (2018). *Anisotropic Elasticity*. Springer Singapore. ISBN: 9783642002724. DOI: 10.1007/978-981-10-5439-6.

Verheyen, P., N. Collaert, R. Rooyackers, R. Loo, D. Shamiryan, A. D. Keersgieter, G. Eneman, F. Leys, A. Dixit, M. Goodwin, Y. Yim, M. Caymax, K. D. Meyer, P. Absil, M. Jurczak and S. Biesemans (2006). “25% Drive Current Improvement for P-Type Multiple

Gate FET (MuGFET) Devices by the Introduction of Recessed Si/sub 0.8/ge/sub 0.2/ in the Source and Drain Regions." In: *IEEE Symposium on VLSI Technology*. DOI: 10.1109/.2005.1469264.

Wang, W., L. C. Popa, R. Marathe and D. Weinstein (2011). "An Unreleased mm-Wave Resonant Body Transistor". In: *IEEE 24th International Conference on Micro Electro Mechanical Systems*, pp. 1341–1344. ISBN: 9781424496327. DOI: 10.1109/memsys.2011.5734682.

Wang, Y.-F., Y.-S. Wang and V. Laude (2015). "Wave Propagation in Two-Dimensional Viscoelastic Metamaterials". In: *Physical Review B* 92.10, p. 104110. ISSN: 1550235X. DOI: 10.1103/physrevb.92.104110.

Ward, R. M. (2012). "Modelling of Silicon-Germanium AlloyHeterostructures using Double GroupFormulation of k·p Theory". PhD thesis. Department of Physics.

Weinstein, D. (2009). "The Resonant Body Transistor". PhD. Cornell University. URL: https://ecommons.cornell.edu/handle/1813/14010.

Weinstein, D. (2018). *GHz CMOS-MEMS Resonators Motivation : Frequency Sources*. URL: https://nanohub.org/resources/28372/download/2018.03.08-Weinstein-BIRCK.pdf.

Weinstein, D. and S. A. Bhave (2007). "Internal Dielectric Transduction of a 4.5 GHz Silicon Bar Resonator". In: *IEEE International Electron Devices Meeting*. January 2008, pp. 415–418. ISBN: 978-1-4244-1508-3. DOI: 10.1109/iedm.2007.4418961.

Weinstein, D. and S. A. Bhave (2010). "The Resonant Body Transistor". In: *Nano Letters* 10.4, pp. 1234–1237. ISSN: 15306984. DOI: 10.1021/nl9037517.

Wikstrom, G., J. Peisa, P. Rugeland, N. Johansson, S. Parkvall, M. Girnyk, G. Mildh and I. L. D. Silva (2020). "Challenges and Technologies for 6G". In: *2nd 6G Wireless Summit*. IEEE, pp. 1–5. DOI: 10.1109/6gsummit49458.2020.9083880.

Wortman, J. J. and R. A. Evans (1965). "Young's Modulus, Shear Modulus, and Poisson's Ratio in Silicon and Germanium". In: *Journal of Applied Physics* 36.1, pp. 153–156. ISSN: 00218979. DOI: 10.1063/1.1713863.

Wu, G., Y. Zhu, S. Merugu, N. Wang, C. Sun and Y. Gu (2016). "GHz Spurious Mode Free AlN Lamb Wave Resonator with High Figure of Merit Using One Dimensional Phononic Crystal Tethers". In: *Applied Physics Letters* 109.1, p. 013506. ISSN: 00036951. DOI: 10.1063/1.4955410.

Xu, X., J. Zhong, H. So, A. Norvilas, C. Sommerhalter, D. G. Senesky and M. Tang (2016). "Wafer-Level MOCVD Growth of AlGaN/GaN-on-Si HEMT Structures with Ultra-High Room Temperature 2DEG Mobility". In: *AIP Advances* 6.11, p. 115016. ISSN: 21583226. DOI: 10.1063/1.4967816.

Yandrapalli, S., V. Plessky, J. Koskela, V. Yantchev, P. Turner and L. G. Villanueva (2019). "Analysis of XBAR Resonance and Higher Order Spurious Modes". In: 2019-Octob, pp. 185–188. ISSN: 19485727. DOI: 10.1109/ultsym.2019.8925993.

Yang, B. and M. Cai (2011). "Advanced Strain Engineering for State-of-the-Art Nanoscale CMOS Technology". In: *Science China Information Sciences* 54.5, pp. 946–958. DOI: 10.1007/s11432-011-4224-9.

Yang, J., B. Hamelin, S. Ko and F. Ayazi (2018). "Ultra-High Q Monocrystalline Silicon Carbide Disk Resonators Anchored Upon a Phononic Crystal". In: *Solid-State, Actuators, and Microsystems Workshop Technical Digest*. Transducer Research Foundation, pp. 83–86. ISBN: 9781940470030. DOI: 10.31438/trf.hh2018.22.

Yang, Q., W. Pang, D. Zhang and H. Zhang (2016). "A Modified Lattice Configuration Design for Compact Wideband Bulk Acoustic Wave Filter Applications". In: *Micromachines* 7.8, p. 133. ISSN: 2072666X. DOI: 10.3390/mi7080133.

Yang, S.-Y., H. Yang, E. Derunova, S. S. P. Parkin, B. Yan and M. N. Ali (2018). “Symmetry Demanded Topological Nodal-Line Materials”. In: *Advances in Physics: X* 3.1, p. 1414631. DOI: 10.1080/23746149.2017.1414631.

Yang, Y., R. Lu, T. Manzaneque and S. Gong (2018). “Toward Ka Band Acoustics: Lithium Niobate Asymmetrical Mode Piezoelectric MEMS Resonators”. In: *IEEE International Frequency Control Symposium*. May. ISBN: 9781538632147. DOI: 10.1109/fcs.2018.8597475.

Yu, D., Y. Zhang and F. Liu (2008). “First-Principles Study of Electronic Properties of Biaxially Strained Silicon: Effects on Charge Carrier Mobility”. In: *Physical Review B* 78.24, p. 245204. ISSN: 10980121. DOI: 10.1103/physrevb.78.245204.

Yu, L., Q. Yan and A. Ruzsinszky (2017). “Negative Poisson’s Ratio in 1T-Type Crystalline Two-Dimensional Transition Metal Dichalcogenides”. In: *Nature Communications* 8.1. DOI: 10.1038/ncomms15224.

Zeghbroeck, B. V. (2021). *Lecture Notes*. URL: http://ece-www.colorado.edu/~bart/book/.

Zhang, L., R. Barrett, P. Cloetens, C. Detlefs and M. S. del Rio (2014). “Anisotropic Elasticity of Silicon and Its Application to the Modelling of X-Ray Optics”. In: *Journal of Synchrotron Radiation* 21.3, pp. 507–517. ISSN: 16005775. DOI: 10.1107/s1600577514004962.

Zhang, Z., H. Fang, Q. Yao, H. Yan and Z. Gan (2016). “Species Transport and Chemical Reaction in a MOCVD Reactor and Their Influence on the GaN Growth Uniformity”. In: *Journal of Crystal Growth* 454, pp. 87–95. ISSN: 00220248. DOI: 10.1016/j.jcrysgro.2016.09.010.

Zhao, C., M. H. Montaseri, G. S. Wood, S. H. Pu, A. A. Seshia and M. Kraft (2016). “A Review on Coupled MEMS Resonators for Sensing Applications Utilizing Mode Localization”. In: *Sensors and Actuators A: Physical* 249, pp. 93–111. ISSN: 09244247. DOI: 10.1016/j.sna.2016.07.015.

Zhao, J.-g., X.-x. Huang, W.-f. Liu, W.-j. Zhao, J.-y. Song, B. Xiong and S.-x. Wang (2017). “2.5D Frequency-Domain Viscoelastic Wave Modelling Using Finite-Element Method”. In: *Geophysical Journal International* 211.1, pp. 164–187. DOI: 10.1093/gji/ggx273.

Zheng, F.-L., C.-S. Liu, J.-Q. Ren, Y.-L. Shi, Y.-B. Sun and X.-J. Li (2017). “Analytical Capacitance Model for 14 Nm FinFET Considering Dual- κ Spacer”. In: *Chinese Physics B* 26.7, p. 077303. DOI: 10.1088/1674-1056/26/7/077303.

Zhou, X., D. Xiao, Q. Li, Q. Hu, Z. Hou, K. He, Z. Chen, C. Zhao, Y. Wu, X. Wu and A. Seshia (2018). “Investigation on the Quality Factor Limit of the (111) Silicon Based Disk Resonator”. In: *Micromachines* 9.1, p. 25. ISSN: 2072666X. DOI: 10.3390/mi9010025.

Zhu, Y., N. Wang, C. Sun, S. Merugu, N. Singh and Y. Gu (2016). “A High Coupling Coefficient 2.3-GHz AlN Resonator for High Band LTE Filtering Application”. In: *IEEE Electron Device Letters* 37.10, pp. 1344–1346. ISSN: 07413106. DOI: 10.1109/led.2016.2602852.

Ziaei-Moayyed, M., M. F. Su, C. M. Reinke, I. El-Kady and R. H. Olsson (2010). “Silicon Carbide Phononic Crystals for High F.q Micromechanical Resonators”. In: *IEEE International Ultrasonics Symposium*, pp. 162–166. ISBN: 9781457703829. DOI: 10.1109/ultsym.2010.5935682.

Zienkiewicz, O. C., R. L. Taylor and J. Z. Zhu (2013). *The Finite Element Method: Its Basis and Fundamentals*. BUTTERWORTH HEINEMANN. 756 pp. ISBN: 978-1-85617-633-0.

Zizka, J., S. King, A. G. Every and R. Sooryakumar (2016). “Mechanical Properties of Low- and High-κ Dielectric Thin Films: A Surface Brillouin Light Scattering Study”. In: *Journal of Applied Physics* 119.14, p. 144102. ISSN: 10897550. DOI: 10.1063/1.4945672.

Acknowledgements

During the past years the whole world was facing challenging times. However, I was surrounded by a great group of people who supported me and my research in every imaginable positive way, whether we spent time together in the office or were separated during the pandemic. The new friendships and memories will always add to the great impression of this time. In the following, I would like to express my gratitude towards the people who had the most significant influence on my work:

I want to thank Prof. Thomas Eibert for the academic supervision of my thesis, his understanding and forbearance concerning the sometimes slow processes in a company, and the possibility of working on this thesis with the TUM.

I would like to thank Peter Baumgartner, my direct supervisor at Intel, for his unwavering support and guidance during the past years. I thoroughly enjoyed our many discussions and his constant challenges of my concepts which ultimately led to a vastly improved outcome of this work. His unmatched knowledge of the semiconductor processes and industry and his open and caring attitude resolved many roadblocks of this thesis.

I would like to thank Ehrentraud Hager from the JKU in Linz for the fantastic collaboration and friendship during the ups and downs of our mutual journey toward the doctoral degree. I am grateful for the lengthy discussions and disagreements during our shared publications which ultimately broadened my scientific horizon on many aspects far beyond the scope of my work.

I want to thank Richard Geiger for his constant support, especially in the early months of my thesis. I fondly remember our joint suffering during the long nights before the tape-outs and the continuous fights with our layouts, but somehow we always made it work in the end.

I would like to thank Philip Fisher for bridging the cultural and language barrier across the globe and sharing valuable insights into the working processes of a large semiconductor foundry.

I would like to thank Prof. Harald Pretl from the JKU in Linz for his support and advisory work during our publications and the early stages of the project.

I want to thank Zdravko Boos and Ofir Degani for their continued trust, internal advertisement, and financial support of my work.

I want to thank Carla Moran Guizan for her friendship and support and the remarkable discovery "That time is not infinite", which all doctoral students (or supervisors) have to discover at some point. I would like to also thank Mario Lauritano for the joyful moments in the office. For the many (and often too many) coffees and never-ending gossip during the lunch breaks.

I want to thank Hui Zhang, Alexander Bechthold, and Vase Jovanov for their great support in the laboratory and their patience when I broke (unfortunately utterly expensive) lab equipment.

I want to thank all the other people involved in my Thesis, being either minor details, large contributions, or just making the time on Campeon much more enjoyable. I want to thank Lukas Schramm for his support during the final stages of this thesis, Josef Sedlmeir for the nice discussion in the hallway, Jesenka Krüger for the many laughs and funny stories, and Dimitris Karavidas for teaching me why everything descended from the greeks. Thanks are also due to Michael Langenbuch, Gregor Bracher, Philipp Riess, and Sundaravadanan Anantha Krishnan, who helped me with countless problems during this time.

A great appreciation goes to all my friends who have endured my unavailability during these years. I want to thank them for all the good times and memories, either in person or online during the pandemic, especially Dennis Hoppe, Kilian Kellner, Simon Klimek, Alexander Baur, and Laurin von Lücken.

I want to finally thank my parents, Ernst and Sigrid for their unconditional support and appreciation of my doings, for which I am ever so grateful. I want to thank them for their strength and patience and for giving me the possibility to pursue my studies. Without You, I would not be where I am today.

Lastly, I want to thank Fiona for her never-ending support and love during those challenging times. Thank You for building me up when I was on the ground and pushing me when I lacked confidence. Thank You for all the vertical meters we have accomplished together, and for being the best counterweight I could hope for.

List of Publications of the Author

Hudeczek, **R.** and P. Baumgartner (2020). “Polarization Independent Band Gaps in CMOS Back-End-of-Line for Monolithic High-Q MEMS Resonator Confinement”. In: *IEEE Transactions on Electron Devices* 67.11, pp. 4578–4581. DOI: 10.1109/ted.2020.3025521.

Hager*, E., **R. Hudeczek***, P. Baumgartner and H. Pretl (2021). “Modeling and Analysis of High-Q Resonant-Fin Transistors”. In: *IEEE Transactions on Electron Devices* 68.9, pp. 4780–4786. DOI: 10.1109/ted.2021.3097302.
* Authors contributed equally to this work.

Hudeczek, **R.** and P. Baumgartner (2021). “Mechanical Band Gap Formation in Anisotropic CMOS Back-End-of-Line Stacks for Monolithic High-Q MEMS Resonator Confinement”. In: *IEEE 51st European Solid-State Device Research Conference*. DOI: 10.1109/essderc53440.2021.9631769.

Hudeczek, **R.**, P. Baumgartner, R. Geiger and P. Riess (2021). “Resonant Fin Transistor (RFT)”. US11,201,151 and EP 3 886 320 A1.

Hudeczek*, **R.**, E. Hager*, P. Baumgartner and H. Pretl (2022). “Performance Analysis of Resonant-Fin Transistors and Their Application in RF-Circuit Design”. In: *IEEE Access* 10, pp. 64388–64407. DOI: 10.1109/access.2022.3182695.
* Authors contributed equally to this work.